Department of Physics

Ultrafast Carrier Dynamics and Transport Properties in Semiconducting Nanowires

Tsokkou Demetra

A Dissertation submitted in partial satisfaction of
the requirements for the degree of Doctor of Philosophy
at the University of Cyprus

May 2012

PhD Candidate: Demetra Tsokkou

PhD dissertation title: Ultrafast Carrier Dynamics and Transport Properties in Semiconducting Nanowires

This PhD dissertation was submitted for the satisfaction of the requirements for the degree of Doctor of Philosophy at the Department of Physics and approved in May 29 by the examining committee.

Examining Committee:

Professor Andreas Othonos, Advisor

Assistant Professor Pavlos Savvidis

Assistant Professor Kyriacos Kalli

Associate Professor Fotios Ptochos, (chairperson)

Assistant Professor Grigorios Itskos

Dedicated to my family,

Abstract

Ultrafast Carrier Dynamics and Transport Properties in Semiconducting Nanowires

Demetra Georgiou Tsokkou, University of Cyprus, submitted in partial fulfilment of the requirements for the degree of Doctor of Philosophy

One-dimensional semiconducting nanowires (NWs) have great potential for applications in the fields of optoelectronic and sensor devices, mainly due to the remarkable electronic and optical properties that they exhibit. The key for the future of semiconducting NW-based devices is the detail understanding of their carrier relaxation and transport processes. The main objective of this research work is the detail understanding of ultrafast carrier dynamics in GaN, In_2O_3 and SnO_2 NWs, due to their attractive potential in various optoelectronic applications. This has been accomplished through the use of the powerful techniques of ultrafast transient differential absorption and THz spectroscopy.

Atmospheric pressure chemical vapour deposition has been utilized for the synthesis of GaN, In_2O_3 and SnO_2 NWs grown via the vapour–liquid-solid method. Optimization of these NWs has been accomplished through scanning electron microscopy, x-ray diffraction and steady state transmission spectroscopy. Transient differential absorption spectroscopy has been used as the key ultrafast characterization technique for the investigation of carrier dynamics on a sub-picosecond time scale in these NWs. Measurements as a function of various parameters including photon energy, incident pump fluence and probing wavelength provided invaluable information on carrier relaxation. It appears that defect-related states play a crucial role in the relaxation of the photogenerated carriers. Intensity dependent measurements revealed the role of Auger recombination in these nanostructures. Following the experimental findings, schematics of the band diagrams, which incorporate carrier dynamics are presented. Furthermore, THz transmission spectroscopies have been used to investigate the transport properties of SnO_2 NWs. A transient THz transmission spectroscopy based on the pump-probe technique has been developed for measuring the complex response function of the

nanostructures in equilibrium state or following excitation with ultrashort pulses. Analysis of the conductivity measurements in these NWs have been achieved using the Drude-Smith model. These measurements reveal localization of carriers in the NWs and strong suppression of long transport.

Περίληψη

Δυναμική των Φορέων και Ιδιότητες Μεταφοράς σε Ημιαγωγικά Νανονήματα

Δήμητρα Γεωργίου Τσόκκου, Πανεπιστήμιο Κύπρου, υποβάλλεται στα πλαίσια εκπλήρωσης απαιτήσεων για την απόκτηση Διδακτορικού τίτλου

Τα ημιαγωγικά νανονήματα παρέχουν εξαιρετικές προοπτικές για μελλοντική τους εφαρμογή σε οπτοηλεκτρονικές συσκευές και αισθητήρες αερίων, κυρίως λόγω των ηλεκτρονικών και οπτικών τους ιδιοτήτων. Για να γίνει εφικτή η εμπορευματοποίηση τέτοιων συσκευών, πρωταρχική ανάγκη είναι η ενδελεχής μελέτη των θεμελιωδών τους ιδιοτήτων, συμπεριλαμβανομένου της αποδιέγερσης των φορέων και των ιδιοτήτων μεταφοράς των νανονημάτων. Η οπτική φασματοσκοπία με τη χρήση υπερταχέων παλμών είναι η μοναδική τεχνική που προσφέρει τη δυνατότητα μελέτης της αλληλεπίδρασης μεταξύ ακτινοβολίας και ύλης με χρονική διακριτική ικανότητα femtoseconds καθιστώντας την ισχυρό εργαλείο για την κατανόηση των διαδικασιών αποδιέγερσης στα GaN, In_2O_3 και SnO_2 νανονήματα.

Η σύνθεση των GaN, In_2O_3 και SnO_2 νανονημάτων έχει γίνει χρησιμοποιώντας την τεχνική χημικής εναπόθεσης ατμών σε ατμοσφαιρική πίεση μέσω του μηχανισμού αέριας-υγρής-στερεάς φάσης. Η βελτιστοποίηση των χαρακτηριστικών των ημιαγωγικών νανονημάτων έχει πραγματοποιηθεί με τη χρήση των τεχνικών ηλεκτρονικής μικροσκοπίας σάρωσης, περίθλασης ακτίνων Χ και φασματοσκοπίας μετάδοσης. Η μελέτη και κατανόηση της δυναμικής των φορέων στα υπό μελέτη νανονήματα έχει πραγματοποιηθεί μέσω της μεθόδου της χρονικής εξέλιξης της απορρόφησης μεταβάλλοντας διάφορες πειραματικές παραμέτρους, την ένταση της δέσμης διέγερσης και το μήκος κύματος είτε της δέσμης διέγερσης, είτε της δέσμης ανίχνευσης. Η συσχέτιση των πειραματικών αποτελεσμάτων και η προσαρμογή θεωρητικών μοντέλων στα πειραματικά δεδομένα οδήγησαν στην εύρεση των μηχανισμών και των χρόνων αποδιέγερσης των φορέων. Από τα πειραματικά δεδομένα φανερώνεται η παρουσία και ο ρόλος των ενεργειακών καταστάσεων λόγω ατελειών. Επίσης, οι μετρήσεις της χρονικής εξέλιξης της απορρόφησης συναρτήσει της έντασης της δέσμης διέγερσης φανερώνουν την παρουσία του φαινομένου Auger σε αυτές τις νανοδομές.

Περαιτέρω, χρησιμοποιώντας τα πειραματικά αποτελέσματα που έχουν προκύψει, έχουν σχηματιστεί τα ενεργειακά διαγράμματα των GaN, In_2O_3 και SnO_2 νανονήματων.

Για τον προσδιορισμό των ιδιοτήτων μεταφοράς στα SnO_2 νανονήματα, η πειραματική διάταξη της τεχνικής φασματοσκοπίας THz μετάδοσης έχει κατασκευαστεί και ευθυγραμμιστεί. Μέσω αυτής της τεχνικής έχουν πραγματοποιηθεί πειράματα χρονικής εξέλιξης των φορέων, ενώ η καταγραφή της κυματομορφής του THz ηλεκτρικού πεδίου έδωσε τη δυνατότητα της μελέτης των οπτικών ιδιοτήτων και ιδιοτήτων μεταφοράς στα SnO_2 νανονήματα. Ανάλυση της αγωγιμότητας, αλλά και της φωτοαγωγιμότητας στα SnO_2 νανονήματα έγινε εφικτή μέσω του μοντέλου Drude-Smith και φανερώνουν τον χωρικό περιορισμό των φορέων στα νανονήματα.

Acknowledgments

None of this work would have ever materialized without the involvement of several key persons throughout the course of my research.

First and foremost, I would like to express my sincerest gratitude for providing guidance and for being supportive and patient along the way, of my supervisor Dr. Andreas Othonos. I would like to thank him for his constant encouragement and compelling enthusiasm, for having answers to all of my questions concerning experiments and explanation of experimental data and for giving me the opportunity to work in the fascinating area of ultrafast spectroscopy and explore many aspects of our measured NWs.

I would like to thank our collaborator Dr. Matthew Zervos for allowing me to use his laboratory - Nanostructured Materials & Devices Laboratory-, for introducing me to the field of NW synthesis and for training me in SEM technique.

I would like to express my thanks to Dr. Pavlos Savvidis, Dr. Kyriacos Kalli, Dr. Fotios Ptochos and Dr. Grigorios Itskos who have served on my thesis committee.

I would especially like to thank Dr. Stauri Christou, for supporting me during this course and for devoting her time to solve me endless questions concerning the field of surface chemistry.

Many sincere thanks to my colleagues and friends, Vaso Paraskeua, Dr. Domna Constantinou, Nico Christofi, Varvara Christou, Soulianna Kashiouri, George Georgiou and Constantino Papartyfonos, who have made my PhD experience so enjoyable.

Last, I am deeply grateful to my family for giving me the opportunity to pursue my goals, for believing in me and always giving me their full support through all these years at the University of Cyprus. Without their consistent encouragement I would not have to be able to complete this thesis.

List of Publications

The work in this thesis is, in part, based on the following publications:

- **D. Tsokkou**, A. Othonos, and M. Zervos, "*Carrier dynamics and conductivity of SnO_2 Nanowires by time-resolved terahertz spectroscopy*", Appl. Phys. Lett., **100** (2012) 133101
- **D. Tsokkou**, A. Othonos, and M. Zervos, "*Ultrafast time-resolved spectroscopy of In_2O_3 Nanowires*", J. Appl. Phys., **106** (2009) 084307
- **D. Tsokkou**, A. Othonos, and M. Zervos, "*Defect states of CVD grown GaN Nanowires: Effects and mechanisms in the relaxation of carriers*", J. Appl. Phys., **106** (2009) 054311
- Othonos, M. Zervos and **D. Tsokkou**, "*Tin Oxide Nanowires: The Influence of Trap States on Ultrafast Carrier Relaxation*", Nanoscale Res Lett., **4** (2009) 828

Other publications:

- H. E. Ruda, U. Philipose, A. Saxena, C. de Souza, S. Nair, J. Salfi, A. Shik, A. Othonos, E. Lioudakis, **D. Tsokkou**, L. Zhong and C. Fernandes, "*Optical Response of II-VI ZnSe Nanowires*" ECS Transactions **28** (3) (2010) 193
- Othonos, M. Zervos and **D. Tsokkou**, "*Femtosecond carrier dynamics in In_2O_3 nanocrystals*", Nanoscale Res. Lett., **4** (2009) 526–531
- M. Zervos, **D. Tsokkou**, M. Pervolaraki and A. Othonos, "*Low temperature growth of In_2O_3 and InN nanocrystals on Si (111) via CVD based on the sublimation of NH_4Cl in In*", Nanoscale Res. Lett., **4** (2009) 491–497
- Othonos, E. Lioudakis, **D. Tsokkou**, U. Philipose and Harry E. Ruda, "*Ultrafast time-resolved spectroscopy of ZnSe Nanowires: Carrier dynamics of defect states*", J. Alloys and Compounds **483** (2009) 600
- Othonos, **D. Tsokkou** and E. Lioudakis, "*Observation of quantum confinement effects with ultrashort excitation in the vicinity of direct critical points in silicon nano*films", Nanoscale Res. Lett., **2008** (2008) 837503

Table of Contents

List of Figures

List of Tables

Chapter 1

Introduction

The technological interest on the progressive reduction in the size of electronic and optoelectronic devices has establish the necessity for the development of the area of nanotechnology and nanoscience. *Semiconductor nanowires* (NWs) have attracted a great deal of interest over the past few years due to their potential application in the areas of electronics, optoelectronics, sensing and thermoelectrics, mainly because of the interesting properties that these structures exhibit in the nanometer scale. To fully understand the future potentials of these nanostructures, a deep insight into the fundamental optoelectronic properties is required. Some key interactions in materials and especially semiconductors occur on a picosecond or femtosecond time scales, making ultrafast spectroscopy an ideal technique to investigate these processes and in general these materials. These methods provide detail understanding on how carrier relaxation occurs following photoexcitation. Pump-probe techniques may provide information on carrier transport properties and carrier relaxation time constants. The main goal of this work is an in-depth investigation of the carrier relaxation processes in semiconducting GaN, In_2O_3 and SnO_2 NWs.

In this Chapter, a brief introduction to nanotechnology and nanoscience will be given followed by NWs synthesis. Furthermore, an overview of what is included in this and the following chapters is presented. Following this, various topics needed to give a clear view of the ultrafast spectroscopy, such as the nonlinear optics, the characteristics of ultrashort pulses; the sources of the amplified laser pulses and the pump-probe technique are described. Then, the methods used in this work for the ultrafast characterization are presented. Finally, carrier dynamics in semiconducting materials are discussed.

1.1 Nanoscience and Nanotechnology

The invention of silicon based transistor device made in 1947 at Bell Laboratories, by John Bardeen, Walter Brattain and William Shockley, has triggered a subsequent tremendous development in the area of technology and miniaturization. Since then, an enormous amount of applications in many sectors of everyday life have been attributed to optoelectronic devices, where semiconducting materials play a crucial role. Nowadays, billions of transistor devices are produced per second worldwide with consistently improved performance and characteristics.

In 1959, Richard Feynman presented his inspiring lecture titled, "*There's Plenty of Room at the Bottom*", where he has been wondering: "*Why cannot we write the entire 24 volumes of Encyclopedia Britannica on the head of a pin?*".[1] Back then, considering the known physical laws, he predicted that manipulation of nanoscale materials and atoms would offer new technological perspectives. At that time, his speech was completely theoretical and seemingly imaginary. It took more than twenty years for microscopes to be developed, to allow that pioneering vision to be realized and enable scientists to both see and manipulate matter at the atomic scale.

The last thirty years, major progress has been accomplished in the fields of *nanoscience* and *nanotechnology*. Specifically, nowadays these areas become a reality, emerging fast with evolutionary new products already on the horizon and with a variety of novel applications. The area of nanoscience involves research in discovering new structures and understand the behaviors and properties of nanomaterials with at least one of its dimensions been less than a few hundreds of nanometers (nm). Nanomaterials give rise to unique electrical, optical, magnetic, mechanical and chemical properties and thus are very promising as building blocks in diverse applications, in areas such as electronics, optoelectronics, sensing, thermoelectrics, catalysis and medical cures. Therefore, it is essential for the optical and electronic properties of these nanostructures to be extensively explored and a deep insight on their fundamental properties to be given. Ultrafast spectroscopic methods are ideal to be used for investigating the optoelectronic properties of many kinds of different materials due to the plethora of information extracted and therefore are of paramount

importance to be utilized in order to fully understand the future potentials of the nanostructures.

Nanoscience serves as the basis of nanotechnology, which includes the area of nanostructured material application in devices. The semiconducting device miniaturization, the possibility of developing complex organizational patterns, the potential for very high packaging densities and the requirement of reducing energy consumption are few of the perspectives in nanotechnology advancement.[2] For example, due to the miniscale size of nanostructures, manufacturers could fit millions more transistors on a single microprocessor. As a result, a significant increase in computer operation speed will be achieved.

The first requirement that is needed to be fulfilled in the area of nanotechnology is the development of simple, reproducible and controllable growth strategies for the synthesis of nanostructures. Several methods have been employed to synthesize nanosized structures with various morphologies and properties. An essential challenge in synthesis is to control the structure characteristics and achieve high yield of nanomaterials. Initially, synthesis was achieved using a *"top down approach"*. It includes lithographic technique and etching, where bulk material is selectively processed to form nanostructures. However, the spatial resolution of this approach is limited and true nanostructures are difficult to produce. Furthermore, the quality of nanostructures is usually poor, and in addition to the high cost associated with these techniques, the possibility for widely commercial use is limited. More recently *"bottom up approach"*, and especially chemical synthesis, has expanded the growth of nanostructures. The most widely used methods for chemical synthesis are the chemical vapor deposition (CVD) techniques and the molecular beam epitaxy. Advantages of these techniques are their simplicity, the improved synthesis control and the low cost, in comparison to top down techniques.

There are several reasons why nanomaterials are so technologically interested, especially due to the novel properties that they exhibit in the nanometer scale.[3] For example, bulk silicon (Si) is a poor photoluminescence emitter, due to its indirect energy band gap. As a consequence the application of Si in photonic devices is prohibited. This property changes in the case of Si nanocrystals with size on the order of a few nm.[4] Additionally, it is observed that one can control the emitted photon energy by changing the nanocrystal size. Such behavior is attributed to modifications in the electronic structure of the nanomaterial due to

quantum confinement effects. This effect is characterized by an increase in the energy band gap of the semiconducting nanostructure. As the nanostructure size decreases, it is expected that the energy levels become more discrete and widely spaced. These effects become evident, as the size of nanostructures becomes as small as the exciton Bohr radius of the material.[4–6] For most semiconductors, this characteristic quantity typically varies between few nm to some dozens of nm, while for metals is in the 1-2 nm range.

Another important consequence is the dramatic increase of the ratio of surface to volume of the material. Therefore, many properties of the nanomaterials are expected to be strongly influenced from the nanostructure surface. In any crystalline material, atoms at the surface usually have unsaturated bonds, such as dangling or impurity bonds, able to adsorb atoms from the environment. As a consequence of the large number of surface atoms in the nanostructures, new localized states are formed in the effective band diagram, the so called surface states. These states can strongly affect carrier dynamics in a material and usually act as non-radiative centers. The role of the surface has been investigated in the case of Si nanocrystals with diameter of few nm. It is found that for Si nanocrystals to photoluminescence, surface bonds have to be passivated.[7] No luminescence was observed for unpassivated Si nanocrystals following ultraviolet excitation. The increment in surface area is significant in applications where the surface to volume ratio assumes a critical role, such as in chemical catalysis[8] and sensing.[9]

Furthermore, lattice mismatch between the substrate and the material is an important drawback in the deposition of thin films. As a result, surface roughness and defects including dislocations, cracks, stacking faults and point defects are induced and do not give access to high purity materials. These defects often act as nonradiative recombination centers and the application of such materials results in electronic and optoelectronic devices with lower efficiencies. However, the smaller dimensions of nanostructures allow for largely lattice mismatch materials to grow on the substrate and higher crystalline materials are expected to grow. This will result in superior electronic properties and drastically enhance the device performances.

1.2 Nanowires

Nanomaterials are classified into different categories according to the number of dimensions that are spatially confined. One-dimensional (1-D) nanostructures are defined as the systems where the electrons and holes are confined in two dimensions.[10] 1-D nanostructures are the smallest structures that can efficiently transport electrical carriers. This property allows them to be used in applications where electrical conduction, rather than tunneling transport, is required.

Among 1-D nanostructures, NWs have attracted the greatest interest in recent years. NWs are solid, usually of cylindrical cross section that have diameter ranging from few to hundred of nm and length from one micron up to several tens of microns. In most cases, NWs are quasi-1-D structures, since their smaller dimension is in the nanoscale range, but generally they are too large to give rise to quantum confinement effects. Therefore, their band structure can be approximated by that of the bulk material.

Except from the usual cylindrical shape, NWs have also been grown in different shapes including: squared cross-section,[11] V-shaped,[12] T-shaped,[13] core-shell and axially modulated heterostructure NWs.[14] In the last ten years, a variety of inorganic elemental and compound NWs have been synthesized and their growth conditions have been extensively investigated. Such systems include Si,[15] germanium (Ge),[16] zinc oxide (ZnO),[17] indium oxide (In_2O_3),[18] tin oxide (SnO_2),[19] gallium oxide (Ga_2O_3),[20] aluminum nitride (AlN),[21] gallium nitride (GaN),[22] indium nitride (InN),[23] tin nitride (Sn_xN_y),[24] indium arsenide (InAs)[25] and gallium arsenide (GaAs).[25] In fact, there are only a few systems that have not been synthesized in the NW form. Even in the case of magnesium nitride (Mg_3N_2) that it has been very difficult to produce in bulk form, since it breaks down in the moisture of the atmosphere; Hu *et al.* solved the problem by growing Mg_3N_2 NWs inside carbon nanotubes.[26]

Some of the advantages that NWs exhibit in comparison to other species of nanostructures are the ease of growth and relative good control of their characteristics. Furthermore, NWs are usually easier to fabricate in high yield than the respective nanotubes and quantum dots. In addition, it is possible to precisely control doping in the synthesis of these nanostructures. A large lattice mismatch along the interface is tolerated, so

heterostructure NW are able to be synthesized, thus substrates with large difference atomic constants can be utilized. As a result, NWs generally have fewer defects than their thin film counterparts and possess superior optical properties.

Semiconducting NWs have attracted most of the interest amongst the different material NW structures, since they are expected to play an important role as interconnects and active components in fabricating electronic devices. NWs are being explored as building blocks for various important miniaturized photonic devices, including light emitting diodes (LEDs) with tunable wavelength and photodetectors. Additionally, since NWs are characterized by a large surface to volume ratio; they show high sensitivity to changes in the surface due to its surroundings making them ideal for application in sensing devices and catalysis, where the surface is the active area.

Different mechanisms responsible for the NWs growth have been proposed. The *vapor-liquid-solid mechanism* (VLS mechanism) was first reported to explain the growth of Si whiskers by Wagner and Ellis in 1974.[27] Whiskers have the same shape as NWs, but have larger diameters between 200 nm to few μm. In this process, a vapor phase reactant silicon iodide (SiI_2) and a liquid gold (Au) catalyst were used to produce Si whiskers. VLS process was the primary mechanism cited to describe the presence of a metal at the end of the NW. Much more recently, in 2004 another mechanism was proposed when metal particles were involved in the growth of NWs, the vapor-solid-solid mechanism (VSS mechanism) in order to explain the growth of GaAs and InAs NWs.[28,29] They have shown that the catalyst particle may exist in the solid phase when growth occurs. From in situ TEM images during growth of NWs via VSS mechanism, it was observed that the growth rate is at least one order of magnitude lower relative to the rate of NW growth via VLS mechanism.[16] Furthermore, there are cases that no metal is needed for the NW growth. In this case, two different mechanisms may be responsible, the vapor-solid mechanism,[2] where no catalyst is needed and the self-catalysis mechanism,[30] where the source material plays the role of the metal catalyst.

Nowadays, synthesis of NWs is most often achieved via the VLS mechanism, which is a catalyst assisted process.[2,30–32] As it is denoted by its name, in this model three different phases are involved. The source material is in vapor phase, the catalyst nanosized droplet is in liquid phase and the NW that grows in solid phase. Various types of NWs have been

synthesized using this approach. Some examples are Si,[33] Ge,[34] zinc selenide (ZnSe),[35] nitrides, as GaN[36] and AlN,[37] and oxides,[38,39] including ZnO, In_2O_3, Ga_2O_3 and SnO_2 NWs.

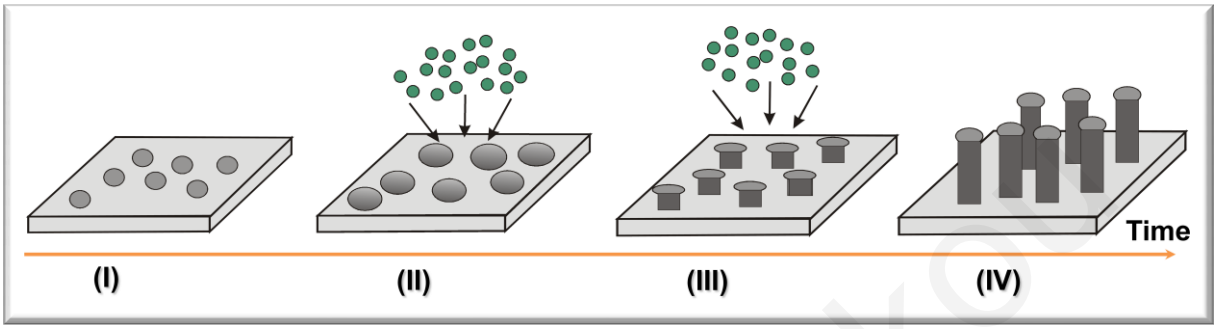

Figure 1.1. The different steps of the VLS mechanism are shown. In *Step I*, metal nanoparticles are deposited onto the substrate. In *Step II*, alloying occurs at elevated temperatures, as the source materials are absorbed by the nanoparticles. In *Step III*, supersaturation of the alloy droplets takes place and NWs start to grow at the edge of the nanoparticles. Finally in *Step IV*, NWs with appropriate length are formed and as the temperature decreases the metal catalyst solidifies at the NW edge.

The different steps that take place in the NW growth via VLS mechanism are shown in Fig. 1.1. In *Step I*, metal nanoparticles are deposited onto the substrate and serve as the nucleation sites for the NW growth. At elevated temperatures, alloying of the nanoparticles starts and atoms of the source materials in vapor phase are absorbed by the metal nanoparticle to form a liquid eutectic (*Step II*). As the eutectic continues to absorb source material atoms, it becomes supersaturated, since the concentration of absorbed source material exceeds the solubility in the metal catalyst. Then, nucleation occurs and NW growth in solid phase begins at the eutectic/NW interface (*Step III*). As the source material continues to be supplied into the system, the NW length will increase. As the system cools down, the alloy droplet solidifies at the end of the NW (*Step IV*). The NW diameter is mainly determined by the size of the metal nanoparticles[40] and therefore smaller nanoparticles result in thinner NWs, while their length depends on the growth rate and time.[41]

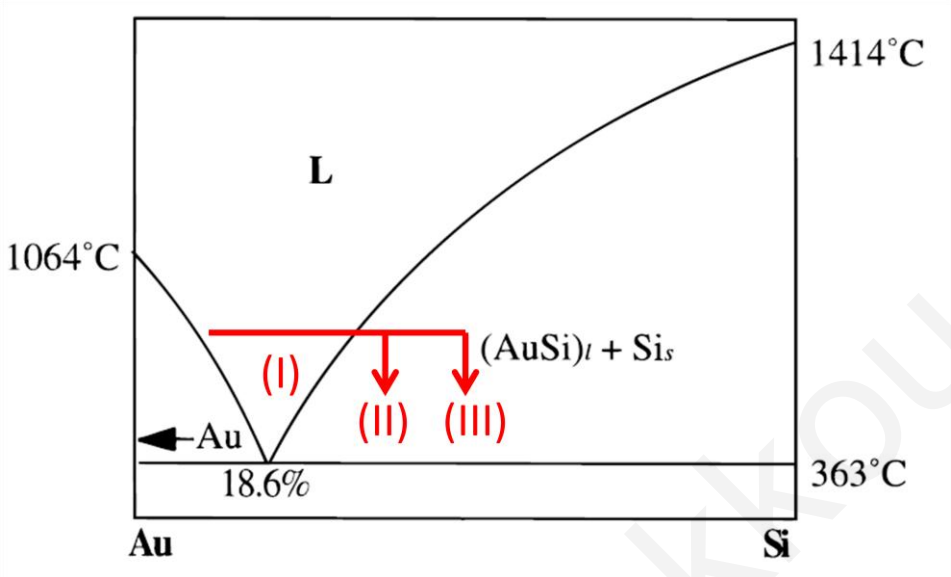

Figure 1.2. Phase diagram of Au:Si. Different stages of the VLS mechanism for Si NWs growth are also shown. A liquid alloy droplet is formed at a temperature above the eutectic point (I). As the concentration of Si increases, supersaturation (II) and growth of Si NWs (III) starts.[42]

A common procedure used to obtain metal nanoparticles is to deposit a metal thin film onto a substrate. When these films are annealed, small nanometer droplets of the metal are formed onto the substrate.[43] A disadvantage of this method is the uncontrolled agglomeration of the film resulting in nanoparticles with varying diameter randomly distributed on the substrate. The metal chosen as a catalyst should be physically active, but chemically stable. Therefore, to select an appropriate metal the equilibrium phase diagram between metal and source material can be initially consulted. As an example, the growth of Si NWs can be explained by using the phase diagram between Au and Si, which is shown in Fig. 1.2. A necessary condition is that the metal forms an alloy with the synthesized material in liquid phase and the synthesized material should also exist in solid phase at the same temperature.[44] The phase diagram of Au/Si has a eutectic point at 363 °C at about 18.6 % concentration of Si. When the growth temperature is above the eutectic point, Si is dissolved into the Au to form a liquid Au:Si droplet (*Step I*). As the concentration of Si into the alloying droplet increases (*Step II*), supersaturation occurs and solid Si NWs can grow (*Step III*) when the synthesis temperature is between the eutectic and the melting point of the material.

The most common catalyst choice is Au. This metal is chemically inactive, but it becomes physically active when small droplets with nanometer size are formed. Also, Au forms a eutectic with many materials at low temperatures. Catalytic growth can be achieved by using many different metals,[45] such as silver (Ag), transition metals nickel (Ni), indium (In), iron (Fe), etc. An advantage of using Au is that the probability of its incorporation in the NW is usually lower than for other metals.

1.3 Motivation and Thesis Organization

Despite all the potential applications that the semiconducting NWs may have and the fact that some sophisticated device structures based on NW systems have already been realized, many questions concerning the fundamental properties of these nanomaterials remain unanswered. Questions regarding the benefits of including semiconducting NWs in device performances rely heavily on our basic knowledge of semiconductor nanomaterials properties, such as electronic structure of the material, impact of defects and impurities on electronic properties, recombination mechanisms, relaxation carrier times and carrier transport. Given the potentials that the NWs may have in electronic and optoelectronic applications, it is necessary for the optical, electronic and transport properties of the NWs to be establish, before any further application of these nanostructures in devices. The objective of this research work is to provide an insight into the fundamental properties of GaN, In_2O_3 and SnO_2 semiconducting NWs using ultrafast spectroscopy.

The interesting properties of the GaN are well known. Group III-nitride compound semiconductors, especially GaN, InN and AlN, and their ternary or quaternary alloys, have proven to be useful for electronic and optoelectronic devices and have been investigated extensively over the past decade.[46–50] Most notably, the ability to tune the bandgap of GaN, which is a wide band gap semiconductor (E_g = 3.4 eV at room temperature) by alloying with In or Al is very promising for applications in solar cells. GaN epitaxial layers are an interesting material for optoelectronic devices emitting in blue and ultraviolet regions and

have already been utilized in commercial LEDs and lasers.[51–53] GaN is also promising for the fabrication of UV photodetectors due to its wide direct band gap.[54] In addition, GaN has been used in high temperature power electronic devices,[55] such as field effect transistors.[56,57] Electronic properties of GaN are strongly dependent on the structural and point defects formed in this material. In particular, yellow luminescence is often observed in GaN, which is detrimental for the device performance. In the case of NWs, the lattice mismatch between GaN and the substrate on which they are grown is not so much of a severe constraint, as in the case of homo- or heteroepitaxial growth of GaN. As a consequence, improved control on the formation of defects is feasible, which will potentially lead to nanodevices with enhanced performance and the possibility of direct integration with mainstream Si devices. It is expected that the miniaturization and efficiency improvement of blue light sources will lead to greater portability and broader applications. Although a lot of work has been done to characterize this material in the bulk form, work must still be done in nanometer scale to reveal its potential applications.

In_2O_3 and SnO_2 are considered important *n*-type wide band gap semiconductors. In_2O_3 has an energy band gap between E_G = 3.5–3.75 eV at room temperature, while SnO_2 has an energy gap at $E_G \approx 3.6$ eV. These metal oxides have received a great deal of attention over the past few years mainly due to its high transparency in the visible part of the spectrum and high electric conductance, which make them technologically important for the fabrication of optoelectronic devices, such in use in transparent conductive electrodes for solar cells, field effect transistors, and flat panel displays.[58–65] Moreover, metal oxide semiconductor sensors are the most promising devices among the solid state sensors. Furthermore, in recent years, the field of semiconducting metal oxides has benefited a great deal due to the development of 1-D nanostructures such as NWs and nanorods and their interesting properties arising from their small size and high surface-to-volume ratio.[10,66] For example, the large surface to volume ratio of atoms in NWs and nanoparticles is significant in order to observe changes in the electric conductivity, as gas molecules are adsorbed or desorbed from the nanomaterial surface. Therefore, SnO_2 and In_2O_3 NWs are of interest to the sensing communities, since they have demonstrated greater room temperature sensitivity and selectivity than their commercial thin film counterparts. In_2O_3 NWs are suitable for detection of toxic gases such as NO_2, NO, and NH_3.[67–69] On the other hand, SnO_2 NWs have been proposed for the detection of CO, NO

and C_2H_5OH.[70–72] Up to now SnO_2 NW-based nanodevices such as field effect transistors,[73] field emission devices,[74] ultraviolet sensors[75] and gas sensors[76–78] have been successfully fabricated in the laboratories. In view of these, there has been growing interest in the synthesis of In_2O_3 and SnO_2 NWs and the study of their fundamental electronic and optoelectronic properties.

The primary goal of this thesis is to give an insight onto the behavior of photoexcited carriers in semiconducting GaN, In_2O_3 and SnO_2 NWs. The synthesis conditions of In_2O_3, SnO_2 and GaN NWs using atmospheric pressure CVD and their structural and optical characteristics are also determined. Until now, there has been no detailed investigation using time resolved spectroscopic methods in these NWs, which can provide information on the dominant relaxation mechanisms, a detailed understanding on the nature of the electronic states and the carrier transport properties. In particular, time resolved absorption spectroscopy measurements were performed for the three systems to give an insight onto the behavior of photoexcited carriers and therefore we have undertaken a detailed investigation of the carrier dynamics and relaxation mechanisms in these semiconducting NWs.

The precise control on the density and uniformity of the SnO_2 NWs provided the mean of developing transient terahertz (THz) spectroscopy and its application to determine transport properties in NW systems. Therefore, a complex time resolved THz transmission optical setup had to be designed and aligned for these experiments. Next, many different sectors of the THz generation, propagation and detection in these experiments had to be conceived and taken into consideration, until satisfactory results for the obtained reference THz electric field including time duration and intensity, were achieved. From these measurements, the intrinsic conductivity and photoconductivity spectrums of the SnO_2 NWs were determined that give an insight on very important information, including mobility and carrier density. In addition, time resolved THz transmission spectroscopy was used as a complementary method to investigate carrier recombination mechanisms and times.

This thesis is organized in seven chapters, providing a theoretical background and further presenting and discussing extensively the experimental results. In Chapter 1, the minimum background necessary for an understanding of this work is given. Specifically in the next section, some aspects of ultrafast laser spectroscopy are reviewed. Given the importance of non-linear optical effects due to the high peak powers generated with ultrafast pulses, a

brief overview of this subject is presented. Following this, a brief introduction on ultrashort pulses generation and amplification is presented. Afterwards, a description of the various time resolved experimental methods used in this thesis, namely time resolved absorption spectroscopy, time resolved THz transmission spectroscopy and time domain THz transmission spectroscopy is given. Lastly, in an attempt to give the reader a more complete picture of the various processes that may occur following ultrafast short pulse excitation, the various recombination mechanisms that take place in semiconducting materials after the photoexcitation with ultrashort pulses are discussed.

Chapter 2 describes the experimental methods used in this thesis. Initially, atmospheric pressure CVD technique utilized to synthesize the samples is presented. Then, the different techniques used to characterize the NWs are discussed. This includes scanning electron microscopy (SEM), the x-ray diffraction (XRD) method and the steady state ultraviolet/visible/infrared (UV/VIS/IR) transmission spectroscopy. Finally, the experimental setups of time resolved absorption spectroscopy and time resolved THz transmission spectroscopy; key experiments for the ultrafast characterization of the NWs, are presented.

Chapter 3 covers the analytical tools required to interpret the experimental data obtained from ultrafast characterization. Initially, the interpretation for the experimental data from the time resolved differential absorption spectroscopy, as well as the rate equations used to extract the relaxation mechanisms are explained. Furthermore, the interpretation for the THz spectroscopy experiments, as well as the analysis followed for the derivation of the optical constants and intrinsic conductivity spectrum are presented. At the end of the chapter, the process followed on the time resolved THz spectroscopy data for the derivation of photoconductivity in the NWs is given.

The next three chapters present the results obtained from the various time resolved ultrafast measurements for each material under investigation. Chapters 4 and 5 are devoted to the synthesis and ultrafast characterization of GaN and In_2O_3 NWs, respectively. Each chapter contains the details of the process followed for the synthesis of the NWs via atmospheric pressure CVD and the important experimental parameters that influence the synthesis. Also, the experimental results from scanning electron microscopy (SEM), x-ray diffraction (XRD) and steady state transmission spectroscopy measurements used to characterize the samples and provide information about their morphology, crystal structure and transmission spectrum,

respectively are presented and discussed. Following this initial discussion, the main part of the chapter is devoted on ultrafast characterization of the NW system. Transient absorption measurements using a non-degenerate pump-probe technique with above and below band gap excitation are presented. The experimental results of these measurements are extensively discussed. Findings are explained in detail, in addition to the extraction of the various carrier relaxation times following photoexcitation of the carriers in the NW system.

Similarly, in chapter 6 the synthesis process and characterization of SnO_2 NWs are discussed. The results for carrier dynamics of SnO_2 NWs obtained from the time resolved absorption spectroscopy and time resolved THz transmission spectroscopy experiments are presented and explained. The optical constants for the SnO_2 NWs from time domain THz experiments are derived. Finally, time domain and time resolved THz transmission spectroscopy methods are used to calculate the intrinsic conductivity and photoconductivity spectrums of SnO_2 NWs in THz region, respectively. The results from these techniques are presented and analyzed.

Finally, chapter 7 summarizes the findings of the work of this thesis, along with an outlook and suggestions that could extend the experimental findings for future research.

1.4 Tools of Ultrafast Laser Spectroscopy

The availability of ultrafast laser pulses has opened new and extremely fascinating areas of scientific research. They gave access to time resolved spectroscopy measurements, which provide information on the carrier behavior in photoexcited materials in very small time scales that could not be achieved by other means. To help the reader comprehend the work that has been carried out is this thesis; different fundamental tools, which are involved with ultrafast laser spectroscopy are discussed.

Initially, nonlinear optical effects are described. These effects are important in ultrafast laser spectroscopy due to the high peak power achievable with ultrashort laser pulses. In general, nonlinear optical effects are present and have a non-trivial contribution when amplified ultrashort pulses interact with matter. Furthermore, one of the advantages of

nonlinear optical effects is their use in ultrafast spectroscopy to convert the fundamental pulses wavelength to other wavelengths. Following the basic introduction to nonlinear effects, the characteristics of ultrashort pulses and the amplifier laser systems are described. The principles of the pump-probe technique that the basic experimental arrangements of the ultrafast spectroscopy utilized here are also discussed.

1.4.1 Nonlinear Optical Effects

The invention of lasers was firstly demonstrated by Maiman in 1960[79] and has enable the observation of *nonlinear optical effects*.[80] Various new phenomena that could not be experimentally observed with the use of conventional optical sources were realized. Such effects include the generation of new frequencies that are not contained into the initial laser beam. In 1961, for the first time Franken *et al.* had observed a nonlinear optical effect.[81] They focused an intense beam from a Ruby laser onto a quartz crystal, resulting in a doubling of the initial frequency of the beam. This effect is known now as second harmonic generation.

Many different nonlinear optical effects are often needed for ultrafast spectroscopy measurements. Such effects take place in the generation of ultrashort pulses, the wavelength modification of the pulses, the generation and the detection of THz pulses, all needed for the purposes of this thesis. In this section, a brief description of the issues that concern the area of nonlinear physics follows.

Linear and nonlinear optical effects can be understood in terms of polarization, which is experienced by a dielectric medium as an optical beam propagates through it. In linear optics, the induced polarization in a medium is directly proportional to the external optical electric field and can be expressed as, $\vec{P} = \varepsilon_0 \chi \vec{\mathrm{E}}$, where ε_0 is the vacuum permittivity and χ is the electric susceptibility of a medium. In isotropic materials this relationship is scalar. In general, crystals are anisotropic (i.e. different directions have a different response) and linear susceptibility becomes a 3×3 matrix. The linear relation between polarization and electric field is valid only for low intensities of light. When higher intensities of light are used,

polarization dependence on the electric field acquires higher order terms as shown by equation 1.1,

$$P_i = \varepsilon_0 \left(\sum_j \chi_{ij}^{(1)} E_j + \sum_{jk} \chi_{ijk}^{(2)} E_j E_k + \sum_{jkl} \chi_{ijkl}^{(3)} E_j E_k E_l + \ldots \right) \tag{1.1}$$

where $\chi^{(1)}$ is the first order susceptibility responsible for linear effects and $\chi^{(i)}$ are the i^{th} order nonlinear susceptibilities ($i > 1$) and are described by tensors. For sufficiently high light intensities, the higher order terms may become important and are responsible for the nonlinear optical effects.

To understand few of the consequences arising from the equation shown above, let us consider the second order induced polarization of two plane waves ($E_1(t) = E_{01} e^{i\omega_1 t}$, $E_2(t) = E_{02} e^{i\omega_2 t}$) that propagate at the same direction, have the same polarization and different frequencies ω_1 and ω_2, both incident on a nonlinear medium. For second order nonlinear effects to occur, the crystal should be noncentrosymmetric - no inversion symmetry -, in order for the second order susceptibility not to vanish. For simplicity, the spatial dependence of the electric fields and the different values that second order susceptibility may have in different directions are ignored. Then, the second order induced polarization into the nonlinear medium is given by equation 1.2.

$$P^{(2)}(\omega_1, \omega_2, t) = \chi^{(2)} \begin{bmatrix} |E_1|^2 e^{2i\omega_1 t} + |E_2|^2 e^{2i\omega_2 t} + 2E_1 E_2 e^{i(\omega_1+\omega_2)t} \\ + E_1 E_2^* e^{i(\omega_1-\omega_2)} + E_1^* E_2 e^{-i(\omega_1-\omega_2)t} \\ + 2E_1^* E_1 + 2E_2^* E_2 \end{bmatrix} \tag{1.2}$$

It is observed that the induced polarization contains components oscillating at various frequencies. Therefore, the second order polarization will act as an electromagnetic radiation source at these frequencies. The first and the second terms in the above equation oscillate at frequencies twice the frequency of the initial components. This effect is referred as *second harmonic generation*. The third term is oscillating at a frequency equal to the summation of

the initial frequencies $(\omega_3 = \omega_1 + \omega_2)$, an effect known as *sum frequency mixing*. In the next two terms the resulted frequency is the difference between the two initial frequencies $(\omega_3 = \omega_1 - \omega_2)$, an effect referred as *difference frequency mixing*. The last two terms are independent of the frequency of the initial waves, so a static (dc) electric field is induced to the medium. This effect is called *optical rectification*.

However, only one of these frequency components is usually intensified in each case, since *phase matching condition* should also be fulfilled in nonlinear optical effects. This is crucial for an effective coupling to occur in the nonlinear crystal. For that, the initial and generated electric fields should be in phase as they propagate through the nonlinear medium, so that waves generated in different spatial points of the crystal to interfere constructively. For this to occur, the wave vector mismatch $\Delta\vec{k}$ between the generated and the initial waves should be zero. In this case the waves are phase matched. It can be achieved by properly selecting the polarization of the incident electric fields and the orientation of the nonlinear crystal. Thus, for different orientations of a crystal a different nonlinear effect may be intensified.

Usually, dispersion of the light occurs in most of the materials and different frequency components propagate with different phase velocities in the medium, since they experience a different refractive index $(u(\omega) = c/n(\omega))$. Consequently, the relative phase between the interacting waves will change and a phase mismatch is generated. An important parameter for a nonlinear effect to be evident in dispersive materials is the coherence length l_c ($= \pi/\Delta k$). It is the distance over the beams propagates in a medium before the phase difference between the initials and the generated waves becomes equal to π and then destructive interference will start to occur. Therefore, coherence length is the maximum nonlinear crystal thickness that can be tolerated for an efficient output to be produced, when nonlinear effects take place.

The phenomena described above are not the only ones that can be observed. Second order nonlinear phenomena are also the *optical parametric amplification* and *Pockel effect*. Optical parametric amplification may occur when a high intense beam at frequency ω_1 interacts with a weak beam at frequency ω_2 in a nonlinear medium. As $\omega_1 > \omega_2$ and phase matching condition is fulfilled, photons with frequency $\omega_3 = \omega_1 - \omega_2$ can be generated. On the other hand, Pockel effect, also called and linear electro-optic effect may occur when a dc

electric field and an optical beam are both present in a nonlinear crystal. The coupling of the two fields in a second order nonlinear crystal does not change the frequency of the optical beam, but causes a change in the amplitude and phase of the optical field that show a linear dependence on the dc electric field.

1.4.2 Ultrashort Pulses

Six years after the demonstration of the first laser, De Maria *et al.* produced the first pulses with sub-nanosecond time duration.[82] The development of pulsed laser sources was of paramount importance for measuring extremely short time intervals and study various fast processes. Due to the short duration of pulses and the fact that the time resolution of experiments that uses them reaches down to few femtoseconds, this field of research is known as *ultrafast science*.[83–85] Nowadays, ultrashort pulses with time duration below 10 fs are routinely achieved.[86] The shortening of ultrashort pulses increased the laser radiation power and gave the opportunity to generate high peak powers up to the petawatt (PWatt) regime.

For someone to realize what an ultrashort pulse is, a continuum plane wave with a sinusoidal electric field ($E(t) = E_0 e^{i\omega_0 t}$) and a pulse can be consider, as seen in the Fig. 1.3 (a). In time domain, the difference between an ultrashort pulse and a plane wave is that an ultrashort pulse contains only a few cycles of a sin wave, as it is seen on the right of Fig. 1.3 (a). In this case, a pulse with a Gaussian shape is taken into account, which closely approximates many real laser pulses. Thus, an ultrashort pulse (black line) is the product of a sin wave (grey dash line) and a pulse envelope function (red line), as described by the equation 1.3,

$$E(t) = E_0 e^{i\omega_0 t - \Gamma t^2} \tag{1.3}$$

where ω_0 is the central frequency of the pulse. Γ is the shape factor, which is related to the pulse duration $t_0 = \sqrt{2\ln 2\Gamma}$.

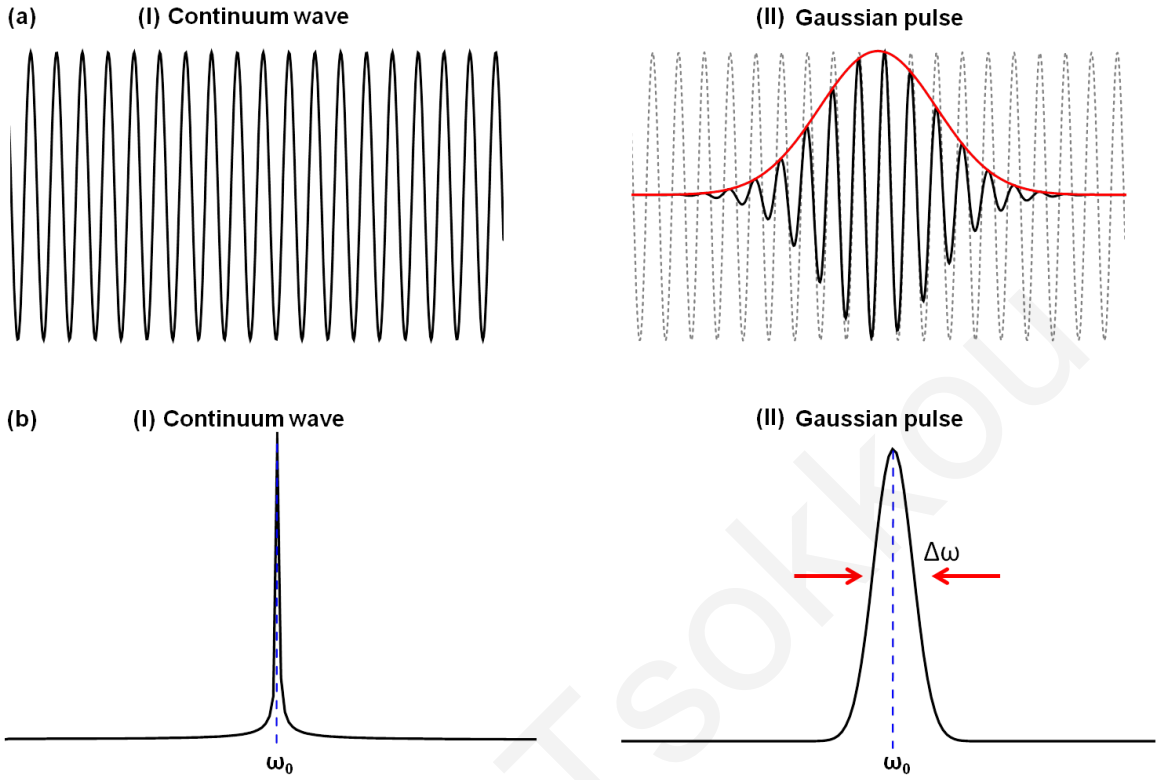

Figure 1.3. (a) Time evolution of the electric field of (I) a monochromatic plane wave and (II) a Gaussian pulse. On the right, a Gaussian pulse (black line) is shown to be the product of a plane wave (grey dash line) with a Gaussian pulse envelope (red line). (b) Frequency dependence of a (I) monochromatic plane wave and (II) a Gaussian pulse, derived after performing a Fourier transform on the time domain electric fields.

Due to the small duration of pulses new issues arise. The differences in time profiles of the two different beams have an impact on their spectral bandwidth. The time and frequency domain representations are related by Fourier transforms, given by the following equations 1.4.

$$E(t) = \frac{1}{\sqrt{2\pi}} \int_{-\infty}^{\infty} E(\omega) e^{i\omega t} d\omega \quad , \quad E(\omega) = \frac{1}{\sqrt{2\pi}} \int_{-\infty}^{\infty} E(t) e^{-i\omega t} dt \qquad (1.4)$$

Performing a Fourier transform at the time domain electric fields of a continuum plane wave and an ultrashort Gaussian pulse, different results arise as shown in the Fig. 1.3 (b). It is

seen that a delta function is obtained for the continuum plane wave, which corresponds to monochromatic waves ($E(\omega) = E_0\delta(\omega - \omega_0)$), whereas another Gaussian function is derived for a Gaussian ultrashort pulse $\left(E(\omega) = E_0 \exp\left(\frac{-(\omega-\omega_0)^2}{4\Gamma} \right) \right)$. This means that an ultrashort pulse has a much wider bandwidth. For example, for a pulse with duration of 100 fs, a bandwidth of approximately $\Delta\lambda \approx 10$ nm is required. Additionally, it can be shown that shorter pulses lead to a broader spectral bandwidth. This is derived also from the quantum mechanical uncertainty time-energy principle described by the equation 1.5.

$$\Delta E \cdot \Delta t \geq \hbar / 2 \tag{1.5}$$

Therefore, for an ultrashort pulse of a few femtoseconds the corresponding spectral width is a few hundreds of nm. The equality is valid for pulses with Gaussian time and spectral envelope.

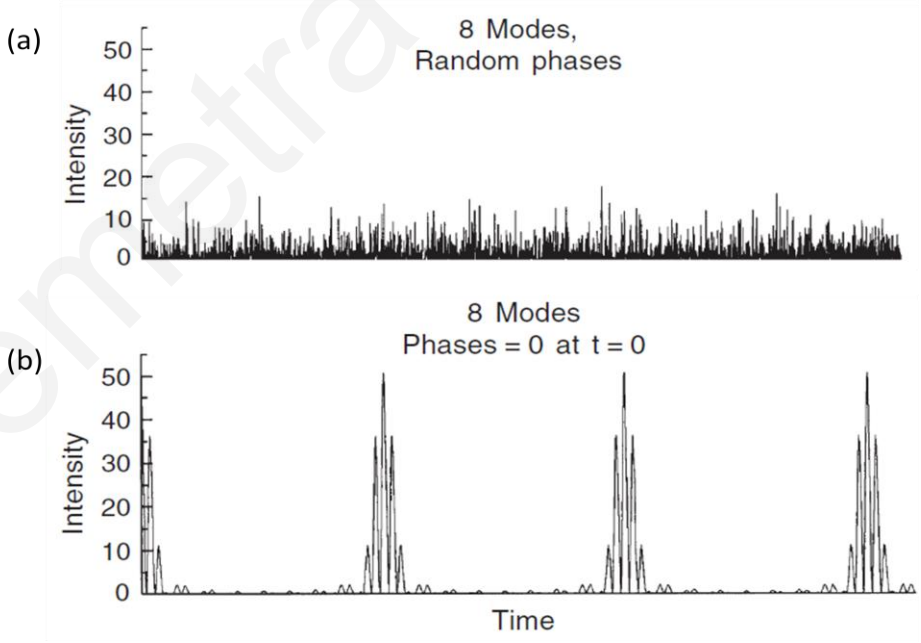

Figure 1.4. Time distribution of output intensity for eight modes (a) with random phases and (b) with the same phase.

Generation of ultrashort pulses is achieved in an oscillator cavity via *mode-locking technique*. This technique, given the choice of an appropriate gain medium, it provides the ability to generate pulses with duration as short as few femtoseconds.[87] The gain medium must have a broad bandwidth to allow a large number of longitudinal modes (~ 10^4 – 10^5 modes) to oscillate simultaneously into the cavity. Further, the set of allowed wavelengths depends on the oscillator cavity length, while successive modes have a frequency spacing of $\Delta\nu = c/2L$, that satisfies the condition of standing waves into a laser cavity.

The time distribution of intensity, when different modes interfere, depends essentially on the phase relations existing between them. An example of this is shown in the Fig. 1.4, where the interference of eight different modes is shown. The time distribution of the output intensity when different longitudinal modes with random distributed phases to each other are used, is shown in Fig. 1.4 (a). It is observed that the output intensity randomly fluctuates with time. To obtain femtosecond laser pulses, many different longitudinal modes should be phase-locked, i.e. the phase difference between adjacent modes has to be the same. This results in a constructive interference of the different modes that last for few femtoseconds, while they are destructively interfere elsewhere. An example of the output intensity of interference of eight modes with zero difference phases to each other is shown in Fig. 1.4 (b). If the modes maintain the same phase relation as they travel into the cavity, they will circulate and extract the optical cavity as pulses. When the number of different modes increases, the duration of the generated pulses becomes smaller and their intensity increases. Phase locking between different modes can be achieved, by introducing additional components into the oscillator cavity, such as acoustic-optic modulator -active mode locking-[88] or a saturable absorber -passive mode locking.[89]

Nowadays, generation of ultrashort pulses in a cavity oscillator is accomplished via *Kerr-lens mode-locking technique* (or self-mode locking technique),[90] which is a type of passive mode-locking. In this case, the nonlinear properties of the gain medium are taken in advantage to decrease losses of the stronger intensity peaks. Thus, for high intensities, Kerr effect that is a third order nonlinear effect, becomes apparent and is responsible for changes in the material refractive index, which becomes linearly dependent on the light intensity. For third order nonlinear effects to be observed, a centrosymmetric crystal should be chosen, so that second order susceptibility to be zero, since usually $\chi^{(2)} >> \chi^{(3)}$. Due to the Gaussian

spatial shape of the beam, its different parts experience a different refracting index as they propagate through the medium. Centre parts of the beam feel a larger refractive index which progressively decreases the outer parts of the beam. Therefore, the gain medium acts as a converging lens. The higher intensity parts of the beam will be strongly focused, while the weaker parts will experience a negligible focus. The intensity dependence of refractive index is also responsible for the shortening in the time pulse duration. Due to the finite duration of the pulse, the refractive index change is also time dependent. As a consequence, the pulse phase is temporally modified, which in turn broadens its spectrum and can result in pulses with shorter duration. This effect is called self-phase modulation.

1.4.3 The Source of Ultrafast Pulses

Ultrafast pulse sources are of primary importance for applications in such diverse fields as ultrafast optoelectronics and ultrafast spectroscopy. The most common source of ultrafast pulses for time resolved spectroscopy is an ultrafast amplifier laser system.

A typical ultrafast amplifier laser system consists of two laser cavities, a mode locked oscillator and a regenerative amplifier, as shown by a simplified schematic diagram in Fig. 1.5. The most common choice of a gain medium in an ultrafast laser cavity is a titanium-doped aluminum oxide (Ti:Sapphire – Ti^{3+}:Al_2O_3) crystal, because it exhibits an optical gain bandwidth over an exceptionally broad wavelength ranging from 650 nm to 1100 nm.[91] This broadband emission spectrum allows the generation of pulses in the femtosecond range, which has led to the commercialization of ultrafast mode-locked lasers in the early 1990s. Generally, a mode-locked oscillator consists of a laser cavity, where its gain medium is pumped by a continuous laser to achieve population inversion and emit radiation at wavelengths corresponding to its emission bandwidth. For a Ti:Sapphire mode-locked oscillator, a second frequency neodymium-doped yttrium vanadate (Nd:YVa) continuous laser with an output at 532 nm is a convenient choice, since Ti:Sapphire has a wide absorption band between 400-600 nm and a maximum at ≈ 500 nm.[91] Due to dispersion effects that are

created mainly in the laser crystal and optical components or self-phase modulation effects, the pulses do not have the desirable duration and need to be further compressed. Therefore, a sequence of prisms is included in the path of the optical cavity to compress the pulses. A slit is also placed within the optical cavity to produce lower loss in the mode-locked operation by blocking the weaker continuum outer part of the beam. In a Ti:Sapphire oscillator, pulses are centered at ≈ 800 nm, possess a few nJ in energy and have a repetition rate typically on the order of 100 MHz depending on the cavity length.

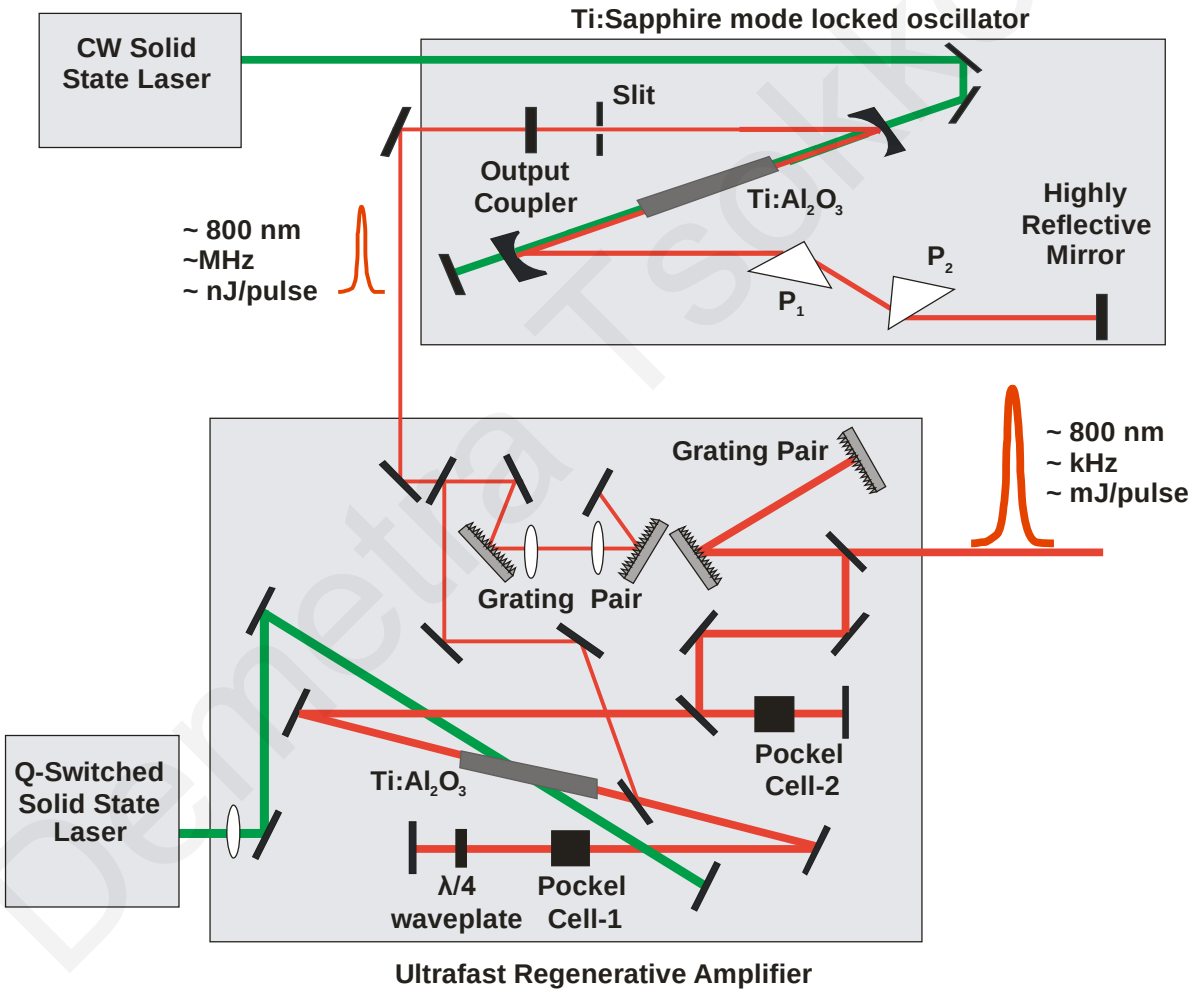

Figure 1.5. A schematic diagram of an ultrafast pulsed amplifier system consisted of a femtosecond mode-locked Ti:Sapphire oscillator pumped by a continuum solid state laser and a Ti:Sapphire regenerative amplifier pumped by a Q-switched solid state laser.

To take advantage of the non-linear optical effects in ultrafast laser spectroscopy, higher energy pulses are usually required; therefore pulses from the oscillator must be amplified by several orders of magnitude. A simplified diagram of the arrangement of different components that consists a regenerative amplifier is shown in Fig. 1.5. Amplification of pulses is similar to the process followed for pulses generation. Briefly, pulses are initially expanded in time to acquire time duration up to some hundreds of picoseconds to avoid damaging the gain medium and optical components in the amplifier. This process is achieved utilizing grating pairs in an antiparallel configuration to induce a chirp on the pulse, since different wavelength components will follow different paths. These temporally broad pulses are sent into the amplification stage in an optical cavity, where Pockel cells and polarizers are used to inject and reject pulses from the cavity. A medium that can support all the wavelengths contained into the initial pulse is required, thus Ti:Sapphire is used again as a gain medium. It is pumped by a Q-switched second harmonic neodymium-doped yttrium lithium fluoride (Nd:YLF) laser at 527 nm. The pulse circulates in the optical cavity for several times (around 20 passes), gaining additional energy in each round trip, until saturation gain occurs. When pulses are injected from the cavity, are compressed into their initial pulse width before leaving the amplifier. Compression of the pulses is usually achieved by an additional grating pair in a parallel configuration that compensates the chirp of the pulses. In a typical amplifier, pulses gain energy up to ~10^6 and the repetition rate is of the order of ~ kHz.

1.4.4 Pump – Probe Technique

For the investigation of very fast relaxation processes that occur in the femtosecond timescale, there is a lack of detectors with a fast enough response time. Only exception is streak cameras which have a time resolution of some hundreds of femtoseconds, but they are very costly. Therefore, to overcome this problem an experimental apparatus based on *pump-probe technique* seems to be the best choice.[92] All experimental setups used in this work for time resolved absorption or THz spectroscopy experiments are based on this technique, which

is schematically presented in Fig. 1.6. In this technique, a small part of the ultrashort pulses is used for detection purposes.

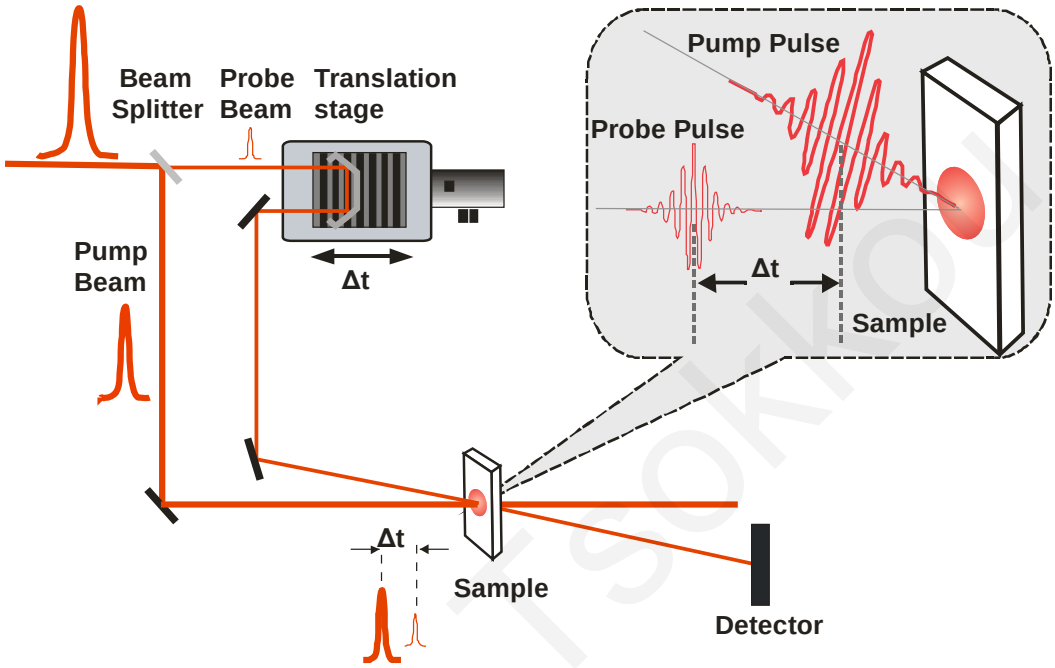

Figure 1.6. A schematic diagram of a typical non-collinear pump-probe configuration. In the inset of the figure, a pump beam incidents onto the sample to photoexcite the carriers, while the probe beam reaches the sample with a time delay Δt to detect the changes that pump beam has induced.

In a pump-probe configuration, the incident laser pulse is split into two pulses with different intensity, a *pump* and a *probe* pulse. Pump pulse possesses the majority part of the intensity of the initial pulse (~ 96 %) and is responsible for the excitation of the sample. On the other hand, probe pulse is much weaker than the pump pulse in order to ensure that it will not perturb the sample properties. It is used to detect the changes induced to the sample by the pump pulse.

The two pulses follow different optical paths and a translation stage with a retroreflector is placed in the pathway of the probe beam to induce an adjustable time delay Δt with respect to the pump pulse. The probe beam changes when interacting with the sample due to changes in the sample properties induced by the incident pump beam. The modifications depend clearly on the temporal delay Δt of the probe beam with respect to time

zero, which corresponds to the arrival time of the pump beam, because the sample response function is time dependent. For times $\Delta t < 0$, the probe beam reaches the sample before the pump beam and no changes are detected. For $\Delta t \geq 0$, the probe beam experiences the pump-induced changes on the sample. This modified probe beam is collected and measured by a photodetector.

In this type of experiments, a spatial overlap between pump and the probe pulses is important to ensure that the probe beam detects a uniformly excited area. Therefore, the pump pulse is spatially controlled to have a diameter at least twice the diameter of the probe beam. In the case that the two beams incident onto the sample in a different (same) angle, as seen in the Fig. 1.6, the setup configuration is named non-collinear (collinear). The time resolution of these experiments is limited by the pulse width, and therefore, time resolved measurements can be carried out with femtosecond resolution. Finally, a macroscopic parameter, such as the reflection or/and transmission signals, which changes due to the ultrafast excitation, are monitored using phase sensitive techniques.

1.5 Ultrafast Spectroscopic Techniques

In this section, the ultrafast spectroscopic techniques used to investigate the fundamental properties of semiconducting NWs in this work are presented. Time resolved absorption spectroscopy and time resolved THz transmission spectroscopy are described in different sections. The use of these techniques on semiconducting NWs will give a plethora of information on the behavior of photoexcited carriers in these materials.

1.5.1 Time Resolved Absorption Spectroscopy

Many kind of experiments based on the pump-probe technique have been proposed for investigating the ultrafast response of semiconducting materials. The main experimental method utilized in the investigation of ultrafast carrier dynamics is *time resolved absorption spectroscopy*. This method has been widely applied for the characterization of different types of materials over the past two decades including inorganic or organic compounds, metallic and semiconducting materials in bulk and more recently in nanostructures.[92–94] In this work, time resolved absorption spectroscopy is utilized to study the dynamic behavior of carriers in semiconducting NWs following femtosecond pulse excitation.

Here, the sample is excited by the pump pulse and the induced changes are detected by a delayed probe pulse in a non-collinear configuration. Transmission and reflection changes of the probe pulse are detected as a function of time delay between the two pulses, and subsequently are used to determine the temporal evolution of absorption change. Details about the experimental setup of this technique and the analysis of the experimental data are given in chapter 2.

Absorption changes in semiconducting material are induced due to strong resonant excitation, where carriers from the valence band are excited to higher energy states, such as conduction band and defect states. Since the pulse duration used is longer than the dephasing times of carriers in semiconducting materials, coherent effects –discussed in section 1.6– are neglected and the system response corresponds to the population of states by carriers. Quantitative information, such as relaxation times and qualitative information on the kind of transitions that take place or the kind of states that are involved can be obtained.

There are two types of time resolved absorption measurements that can be carried out. In its simplest form, *degenerate absorption change measurements* are taken, where the pump and probe pulses have the same wavelength. In this case, the pump beam excites carriers into higher energy states and the probe beam detects the evolution of carriers at the same states. More detail information of the carrier dynamics maybe obtained utilizing *non-degenerate absorption change measurements*, where the two pulses have different wavelengths. In the lateral case, the excited and detected states are located at different levels of the material

energy band structure. Thus, if a variety of different probe wavelengths are used, then the evolution of carriers from different states of the band diagram can be scanned and information about the photoexcited carrier relaxation over the whole band diagram can be obtained.

Time resolved absorption measurements may be carried out as a function of various parameters including photon energy to excite carriers in different energy levels, incident fluence of the pump beam to generate different density of photoexcited carriers and probing wavelength to detect carriers at different energy levels. The limit to the time resolution of these experiments is the temporal pulse width from the ultrafast laser.

The fundamental wavelength of the pulses from an ultrafast amplifier is often not convenient for the study of many semiconducting materials. Furthermore, it is necessary to have access to a very broad spectral range for both pump and probe pulses to obtain a complete information about the carrier dynamics of the semiconducting NWs investigated here. Thus, nonlinear optical effects are employed for the modification of the wavelength of both pump and probe pulses.

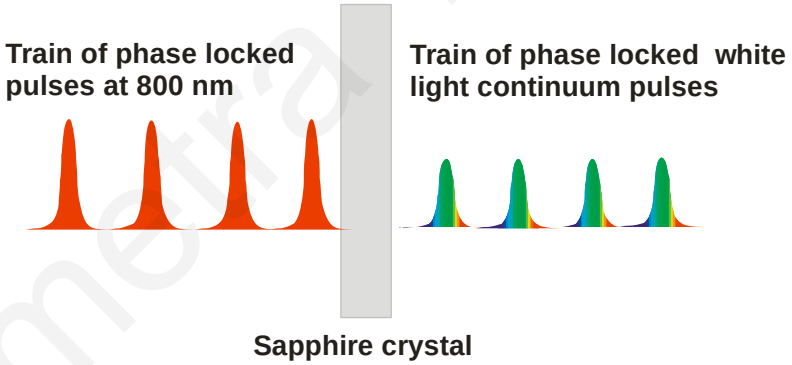

Figure 1.7. White light pulses generation on a quartz crystal.

A convenient choice that makes available wide range of wavelengths is the generation of *supercontinnum white light generation*.[95,96] For femtosecond pulses, white light can be easily created by strongly focusing a few μJ of energy into a variety of materials, such as quartz and sapphire, as it is shown in the Fig. 1.7. White light generation is based mainly on a nonlinear optical effect, known as self-phase modulation. As referred above, the temporal evolution of the refractive index of the nonlinear material when an ultrashort pulse propagates

through it, it causes phase modulation and results in the generation of new frequencies that broadens the bandwidth of the pulse. We should point out that more effects are present in white light generation, such as self-focusing and multi-phonon absorption, whose relative contributions depend on beam focusing and material parameters.

The modification of the pump pulse wavelength can be achieved via several nonlinear optical effects. For example, the easiest method to convert the initial wavelength of the optical near-IR pulses is to use a second harmonic crystal and generate pulses at 400 nm. Alternatively, in order to have the ability to modify the wavelength over a broad bandwidth of spectra, an *optical parametric amplifier* (OPA) is needed. Its operation is based on several non-linear optical effects, such as white light generation, optical parametric amplification and second harmonic generation.[97] When the beam is directed onto the OPA, a small part of the energy is used for the generation of white light continuum. The remainder energy is split into two parts. In the pre-amplification step, the first part of the beam is temporally and spatially overlapped with the white light continuum in a different nonlinear crystal. Using optical parametric amplification effect, two wavelengths from the white light continuum called "idler" and "signal" are amplified. The amplified output wavelength is determined by the angle between the beam and the axis of the crystal, which is tuned appropriately by rotating the nonlinear crystal. In the second amplification stage, the previous process is repeated in another nonlinear crystal for the "idler" and "signal" wavelengths to acquire sufficient energy. Then, by using one or two second harmonic generation crystals, wavelengths from the UV to the mid-IR region can be generated.

Finally, it is important to note that transient absorption spectroscopy gives information on radiative, but also non-radiative mechanisms that is not possible with other techniques, such as time resolved photoluminescence (PL). Therefore, carrier dynamics may also be investigated in indirect band gap semiconducting materials where radiative processes are not present.

1.5.2 Time Resolved and Time Domain Terahertz Transmission Spectroscopy

Time resolved terahertz (THz) *transmission spectroscopy* (TRTS) and *time domain THz transmission spectroscopy* (TDTS) are experimental techniques that use ultrashort pulses and their experimental arrangement is based on pump-probe configuration.[98] These techniques have attracted a lot of attention due to the variety of information that can be obtained for many different species of materials, such as semiconducting crystals, gases, solutions and superconductors. The generation and the detection of THz pulses use *difference frequency mixing* effect and *free-space electro-optic sampling* technique, respectively. These techniques are described below.

Measuring the photoconductivity in semiconducting NWs, is a challenging problem because of the inherent difficulty of attaching electrodes to nanometer sized objects, which is a difficulty that must be overcome when performing measurements with conventional techniques. On the other hand, THz spectroscopy is a non-conduct techniques ideally suited for probing the photoconductivity and charge transport properties in nanomaterials. In this work our main objective was the development of THz spectroscopy technique for the determination of transport properties in NW systems.

THz radiation covers frequencies, ranging between 0.3-10 THz (λ = 30 μm-1 mm), filling the gap between the far-IR and the microwave region. It started to extensively being explored only in the last few decades, due to lack of THz sources and detectors. Nowadays, there are two different methods that are widely applied for the generation of broadband THz pulses when using femtosecond pulses centered at 800 nm, via transient photoconductivity in narrow band gap semiconducting materials[99,100] and difference frequency mixing in non-centrosymmetric crystals.[101,102] The second method is mostly preferred when amplified laser systems are used since the potential of damaging the crystal, due to the high excitation fluences, is much lower. An additional advantage is that difference frequency mixing is a non-resonant method; therefore time duration of resulted pulses is independent of the material response time and is limited only by the width of the excitation laser pulse. Therefore, this method results in the generation of shorter pulses.

Difference frequency mixing, as referred in section 1.3, is a second-order nonlinear optical effect that occurs in noncentrosymmetric crystals. During this effect, difference frequency mixing between different frequency components v_1 and v_2 of the ultrashort pulse are combined, due to a generation of a nonlinear non-stationary polarization in the crystal that propagates in the nonlinear crystal with the group velocity of the pulse. Due to the frequency bandwidth of the ultrashort excitation beam, the pulses result in the THz region with time duration in the picosecond time scale. Evidently, THz pulses with larger frequency bandwidth can be achieved when broader spectrally optical pulses are used. Due to the small frequency difference between the different frequencies that are mixing, the process is sometimes called optical rectification. In first approximation, the spectrum bandwidth of THz pulses is identical to that of the optical pulses. This is true for a crystal with an infinitely thin thickness. Otherwise, dispersion effects in the nonlinear medium must be taken into consideration that eventually constrains the spectrum of THz pulses.

An important characteristic of a favorable crystal for THz pulse generation via difference frequency mixing is the high second order susceptibility to show strong nonlinear behavior. It has to exhibit a low absorption coefficient in optical and THz region, in order for resonant effects or optical phonon resonances not to take place, respectively. Lastly, phase matching condition is important to be fulfilled in the crystal.

The most convenient material choice to use for the generation of THz pulses by difference frequency mixing in time resolved THz spectroscopy is zinc telluride (ZnTe), which has a high second order nonlinear susceptibility, $\chi^{(2)} = 90\ pm/V$.[103] Furthermore, it exhibits a low absorption coefficient in the visible region due to its large band gap, $E_g = 2.4\ eV$ [104] and its high crystallinity. The bandwidth of THz pulses in a nonlinear crystal is mainly determined by the frequency bandwidth of optical pulses, although the upper frequency is confined by the transverse-optical phonon resonance at 5.3 THz,[105] which is a limited factor expected to constrain the bandwidth of the pulses below 4 THz. Also, ZnTe crystal shows excellent phase matching properties.[106] In the case of THz radiation and optical pulses at 800 nm, perfect phase matching occurs at frequencies near ~ 2 THz.[106] The coherence length is in the millimeter scale and remains high for frequencies below 3 THz.

Therefore, broadband THz pulses can be generated. THz pulses produced in a ZnTe crystal via difference frequency mixing have a bandwidth extending from 0.1 to 3 THz.

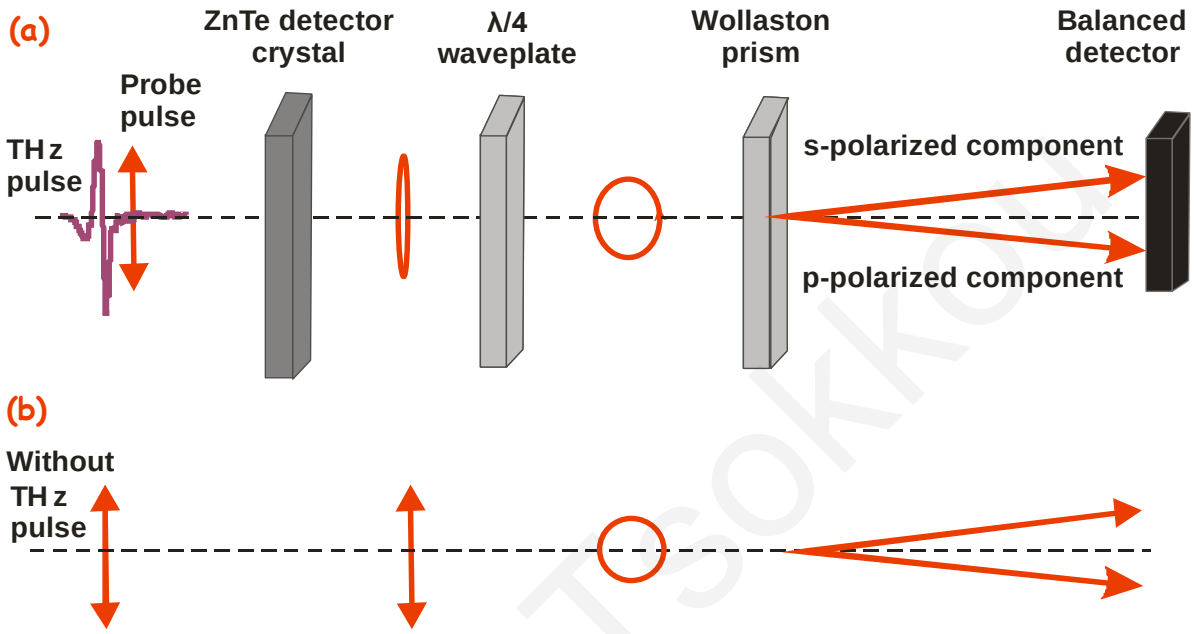

Figure 1.8. A scheme of the electro-optic sampling technique in a ZnTe crystal for the detection of THz pulses. Also, the changes in polarization of an initially linearly polarized optical pulse in (a) the presence and (b) the absence of THz pulse in different steps of the detection technique are shown.

To detect THz radiation pulses free space electro-optic sampling, a coherent detection technique is used.[106,107,108] An important advantage of this technique is that it provides information not only of the amplitude of the electric field, but it is also on the phase. The technique is based on the second order nonlinear effect called Pockel effect. For the THz detection two different beams, the THz pulse and a near-IR probe beam at 800 nm, incident onto a noncentrosymmetric crystal. Since THz pulse is significantly longer than the optical pulse, it can be approached as a static field biasing the crystal, inducing a change in the refraction index of the nonlinear crystal, which is proportional to the applied THz electric field. When the optical group velocity of the near-IR pulse matches the phase velocity of the THz pulse into the crystal, phase matching condition is fulfilled and the optical pulse experiences a constant electric field while propagating. The useful characteristics of a ZnTe crystal for THz generation, such as optical transparency, phase matching condition near 800

nm along with the high non-linearity, indicates that it is also a suitable material for the detection of THz pulses.

A schematic diagram of the detection technique is presented in Fig. 1.8. In this technique, a linearly polarized near-IR probe pulse at 800 nm and the generated THz pulse incident collinearly onto a ZnTe detector crystal. As a result of the birefringence induced in the crystal due to the presence of THz pulse, a phase shift between horizontal and the vertical parts of the initially linearly polarized near-IR beam is created and converts its polarization to slightly elliptical as shown in Fig. 1.8 (a). The phase shift on the near-IR beam, is described by the equation 1.6,[80]

$$\Delta\phi = \frac{\omega}{c}(n_y - n_x)d = \frac{\omega\, d}{c} n^3 r_{41} E_{THz} \qquad (1.6)$$

where ω the probe frequency ($\omega = \frac{2\pi\, c}{\lambda}$, λ = 800 nm), n = 3.22 the refractive index of ZnTe at 800 nm,[109] d the crystal thickness, c the speed velocity in vacuum and the electro-optic coefficient of ZnTe is $r_{41} = 4.04\ \ pm/V$.[110] To determine the phase change, a quarter wave plate that introduces a phase shift of π/2 between the two orthogonal components of the optical beam is used and the slightly elliptical polarization of the beam is converted to almost circular. Then, a Wollaston prism separates the initial beam into two orthogonal polarization components, which are subsequently directed into a balanced differential photodetector.

The magnitude and sign of the ellipticity induced by the THz field is recorded as a change in the voltage of the two orthogonal polarization components. For small changes in phase, which is usually valid for time resolved THz experiments, the difference voltage signal ($\Delta V = V_2 - V_1$) measured between the two polarization components is linearly proportional to the phase shift and consequently to the total THz electric field in the ZnTe crystal. The most frequently used sensor is the (110) oriented ZnTe crystal. In this case, the difference voltage between the polarization components ΔV is given by equation 1.7,[111]

$$\Delta V = V_0 \omega\, n^3 r_{41}\, E_{THz} \frac{d}{2c} (\cos a\ \sin 2\phi + 2 \sin a\ \cos 2\phi) \tag{1.7}$$

where V_0 is the voltage detected by each of the detectors when they are illuminated with the probe beam and no THz field is applied, α the angle between the THz polarization and the crystal axis and ϕ the angle between the probe polarization and the crystal orientation. By adjusting the arrival time between THz beam relative to the probe beam, time domain of THz electric field can be derived by using the expression described by equation 1.8,

$$\frac{\Delta V(t)}{V_0} \propto \frac{\omega\, n^3 E_{THz}(t)\ r_{41}\, d}{2c} \tag{1.8}$$

As it is seen in Fig. 1.8 (b), no birefringence is induced in the absence of the THz pulse and probe beam polarization is converted to circular when it propagates through the quarter wave plate. Therefore, the signal in the detector is zero since the two polarization components are equal.

In TRTS experiments three different pulses are needed, a pump pulse which excites the sample, a THz pulse that probes the changes caused by the pump pulse and the probe pulse, which is used for the detection of the THz pulse. In TRTS experiments, the properties of photo-excited materials are investigated. Different kind of experiments can be done to investigate either the carrier dynamics of the system or to study the temporal evolution of the photoconductivity with subpicosecond resolution.[112,113] To study the carrier dynamics of the semiconducting NWs, the change at the THz maximum signal due to the excitation of the sample by a pump pulse, is recorded as a function of time delays between the pump and THz pulses. Photoconductivity spectrums of a photoexcited sample can be derived by appropriate treating the experimental data -is explained in the chapter 3- when scanning the temporal signal of the changes induced in the THz electric field due to photoexcitation of the sample by the pump pulse in reference to the temporal signal of the THz electric field without pumping. From photoconductivity data, information on the transport properties of photoexcited carriers in the NW systems can be derived.

In TDTS experiments, only the THz and the probe pulses are used. In TDTS, the modifications in THz electric field as it propagates through an investigated material are measured, along with a reference THz pulse. The temporal behavior of the THz electric field is achieved by changing the temporal delay between the THz and the probe pulses. Analysis of these measurements gives access to the material optical and transport properties in THz region. Since a coherent detection method is used, it is able for complex refractive index, the refractive index and the absorption coefficient to be estimated in THz region. This is important because the data can be used further to calculate the complex intrinsic conductivity of the material, transport mechanisms can be studied, scattering times and carrier density of the material in equilibrium state can be estimated.

1.6 Carrier Dynamics in Semiconductors

Femtosecond laser pulse excitation provides the required temporal resolution for the time resolved spectroscopy measurements providing an important insight into the relaxation of photo-generated carriers. In the next few pages, a brief description of the processes following carrier excitation from ultrashort pulses is given.

When a semiconducting material is photo-excited, photon energy is transferred to the carriers, resulting in a generation of non-equilibrium carriers with elevated temperatures and with a well-defined phase relation among them and the electromagnetic field of the pulse.[114] These photogenerated carriers will undergo several stages of energy relaxation and spatial redistribution before they return back to equilibrium state. Table 1.1 summarizes the processes that take place in semiconducting materials following photoexcitation, along with their characteristic times. These processes are temporally resolved using various ultrafast spectroscopic techniques.

Relaxation Processes	Characteristic Times (s)
Carrier-carrier scattering	10^{-15}-10^{-12}
Intervalley scattering	$\geq 10^{-14}$
Intravalley scattering	$\approx 10^{-13}$
Carrier-optical phonon thermalization	$\geq 10^{-12}$
Optical phonon-acoustic phonon interaction	$\approx 10^{-11}$
Auger recombination	$\approx 10^{-10}$
Radiative recombination	$\geq 10^{-9}$
Non-radiative recombination	$\geq 10^{-6}$

Table 1.1. Relaxation processes and characteristic times that may occur in semiconducting materials after photoexcitation.[92]

The evolution of photogenerated carriers back to equilibrium may be divided into four different regimes, a) the *coherent regime*, b) the *non-thermal regime*, c) the *hot-carrier regime* and d) the *isothermal regime*.[92,115] It should be pointed out that different regimes might be temporally overlapped. Carrier relaxation times depend strongly on parameters such as the energy band structure, the carrier density and the lattice temperature. Schematic diagrams of the carrier distribution in coherent and non-thermal regimes are seen in Fig. 1.9. Relaxation mechanisms (*Mechanism I*-*V*) included in the hot-carrier and isothermal regimes, are shown in Fig. 1.10.

a) Coherent Regime

In coherent regime, the excitation of a semiconducting material via ultrashort pulses induces a macroscopic polarization of the system, which initially has a defined phase relationship with the electromagnetic field of the pulses. Then, a momentum relaxation starts on a femtosecond time scale via elastic and inelastic scattering between the carriers, which results in destroying the phase relations and correlation among carriers causing decoherence,

as seen in Fig. 1.9 (a). The dephasing or decoherence time is normally in the range of tens to hundreds of femtoseconds for semiconducting materials.

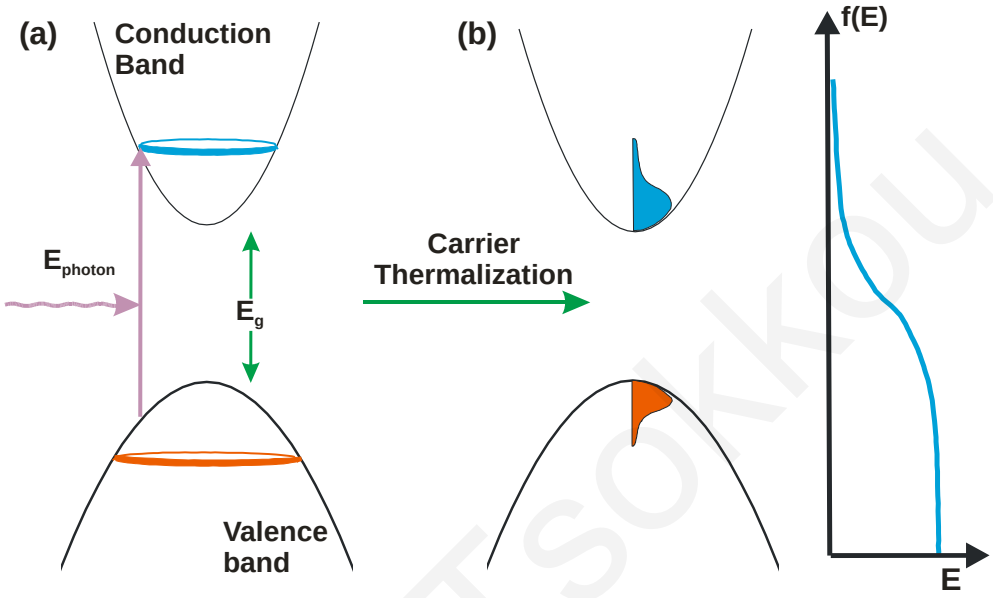

Figure 1.9. Carrier distribution of photo-generated carriers by an ultrashort pulse in (a) coherent regime and (b) non-thermal regime are shown. In non-thermal regime, the occupation probability of a state described by Fermi-Dirac distribution is included.

b) Non-Thermal Regime

Following the coherent regime, carriers will acquire excess energy resulting in a non-thermal distribution between carriers; therefore they cannot be described by Fermi-Dirac statistics with a defined temperature. In non-thermal, carrier-carrier and carrier-phonon scattering lead to redistribution of the carriers within the valence and the conduction band, causing thermalization between carriers. Then, carriers are characterized by a finite temperature and electrons can be described by Fermi-Dirac distribution in time ~10^{-13} s, as seen in Fig. 1.9 (b). The thermalization time depends on carrier concentration and the lattice temperature.

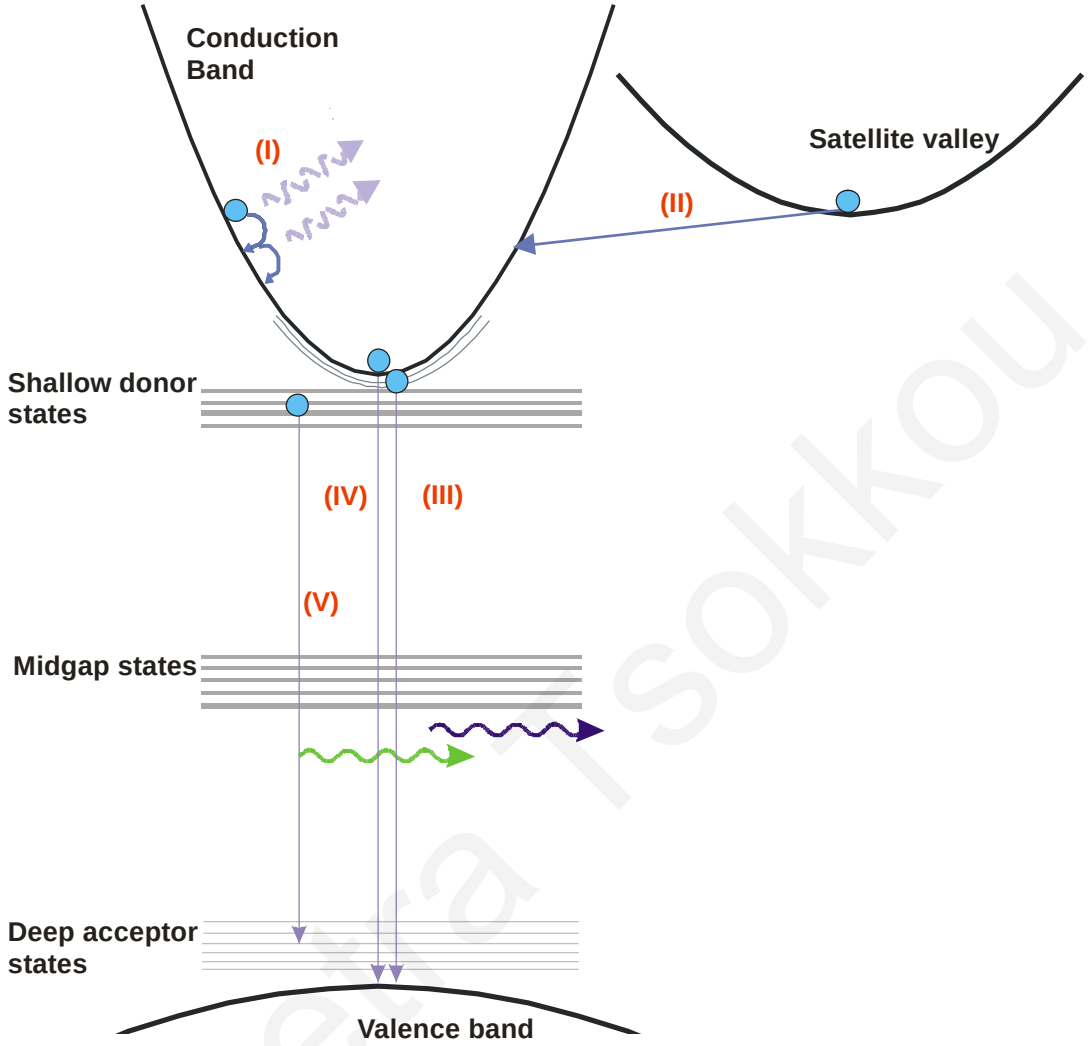

Figure 1.10. Different relaxation mechanisms are shown, *(I)* intraband relaxation, (*II)* interband transition, (*III)* excitonic recombination, (*IV)* band-to-band recombination and (*V)* donor-acceptor recombination.

(c) Hot-Carrier Regime

The processes that take place in non-thermal regime result in a thermalized distribution between carriers, carrier temperature is higher than that of the lattice, and carriers are called *"hot"*. Then in the hot-carrier regime, the carriers lose their excess energy through carrier-phonon interaction, which is an intravalley scattering process (*Mechanism I*). In

addition, intervallley scattering can be observed in this time scale denoted as *Mechanism II* in the Fig. 1.10. In the case of phonon scattering, optical phonons are emitted when subband spacing is above the longitudinal optical photon energy in times in the order of 1-2 ps. Alternatively, carriers may relax via emitting acoustic phonons, which are observed in much longer time scales between 10-100 ps.

(d) Isothermal Regime

Following the non-thermal regime, carriers and lattice are described by the same temperature, in isothermal regime the electron-hole pairs recombine through radiative or non-radiative processes and finally carriers return back to equilibrium. Excitonic recombination (*Mechanism III*) or band to band recombination (*Mechanism IV*) occur in the nanosecond regime for direct band gap semiconductors. In indirect band gap materials, carriers recombine via non-radiative processes in a time that reaches values in the microsecond (μs) or even millisecond (ms) range.

Additional states are formed due to defects, such as point defects (vacancies, interstitials and antisites) and planar defects (dislocation and stacking faults), which are usually positioned energetically below the gap. These states are assorted as shallow donor states, midgap states and deep acceptor states and affect significantly the recombination mechanisms in the material. The energy levels of different kind of states are denoted in the Fig. 1.10.

It is well known that the radiative efficiency of a direct band gap semiconductor from the band edge is suppressed at room temperature, predominantly due to increment of the non-radiative centres. Additionally, extrinsic radiative recombination can also be responsible for prohibiting band edge photoluminescence. These transitions usually take place between shallow donor states and deep level states (donor-acceptor recombination - *Mechanism V*). For radiative recombination processes from the band edge to occur at room temperatures, high quality crystals are required.

The efficiency of radiative recombination is also affected by the presence of Auger recombination, which is a non-radiative process and strongly depends on carrier density.[116] Auger recombination involves three free carriers where an electron leaves an energy state and

relaxes to a hole in a lower state, thereby transferring its energy to another electron. Therefore, Auger recombination rate *R* in the case of optically excited carriers is proportional to the cubic of carrier density, as described by, $R = C_{Auger} n^3$, where C_{Auger} is the Auger coefficient and *n* the carrier density. Clearly, Auger recombination becomes more important with increasing carrier densities. As pump fluence increases shorter relaxation times are observed due to the presence of Auger recombination, which eventually can lead to suppression of radiative recombination processes. Therefore, Auger effect is an important parameter that affects the performance of the materials in optoelectronic devices. Furthermore, surface states formed in nanostructures play a significant role in the carrier dynamics in nanomaterials and usually prohibit radiative recombination.

Chapter 2

Experimental Methods

The objective of this research work is the detail understanding of ultrafast carrier dynamics in three key semiconducting NW systems, namely GaN, In_2O_3 and SnO_2 NWs.

This work begins with the synthesis and structural characterization of the NWs under investigation providing a mean of controlling and optimization of the nanostructures. The NWs studied in this work have been grown using CVD and then studied structural using x-ray diffraction (XRD) technique. The morphology of the products deposited onto the substrate are studied using scanning electron microscopy (SEM), while optical measurements used to estimate the energy gap of these NWs carried out using steady state transmission spectroscopy.

The main objective of this research work has been accomplished using complex ultrafast characterization techniques, which are described in detail in this chapter. Time resolved absorption spectroscopy experimental setups with an optical parametric amplifier, have been designed and aligned thus providing ultrashort pulses at a wide spectral region for the photoexcitation of the samples. At the same time, white light continuum pulses have been utilized for probing the samples over a wide spectral bandwidth. Time domain and time resolved THz spectroscopy measurements have been accomplished following the designed and alignment of a complex optical setup. For these experiments, the initial beam is divided into three different components, to provide the pump beam, the THz beam and the probe beam. The different optical elements that consists each path and non-linear optical effects that take place in the different parts of the experimental setup are described.

2.1 Synthesis and Characterization Methods

Initially, in this chapter the experimental technique used for the NW growth will be discussed. Subsequently, characterization techniques are briefly described. In this work, morphology, crystallinity and optical properties of the NWs have been investigated by using scanning electron microscope (SEM) images, X-ray diffraction (XRD) studies and steady state transmission spectroscopy, respectively.

2.1.1 Atmospheric Pressure Chemical Vapor Deposition

Synthesis of In_2O_3, SnO_2 and GaN NWs was achieved via atmospheric pressure CVD (APCVD) at *Nanostructured Materials & Devices Laboratory* of the Department of Mechanical and Manufacturing Engineering at the University of Cyprus.

APCVD is widely used for the synthesis of thin films and nanostructures, such as NWs, nanotubes and nanocrystals and is a synthesis process in which chemical reactions play a crucial role. The reactions occur at elevated temperatures, as reactants are in vapor phase. Growth conditions, such as growth temperature, source materials and flow rates of gases are controlled properly to obtain products with specific characteristics. A horizontal CVD furnace system is used as the synthesis setup is made by *Atomate*. It is consists of a 25 mm quartz tube heated by resistive coils capable of reaching 1100 ^{o}C. A simplified scheme of the experimental apparatus is described schematically in Fig. 2.1.

For the NW synthesis, a proper source material in solid state (precursor) is selected and placed in a quartz boat next to the substrate, such as small pieces usually 8 mm x 8mm pieces of silicon, quartz or sapphire wafers. Afterwards, the quartz boat is introduced into the center of the quartz tube, next to the thermocouple that is used to detect the temperature at the center of the reactor. The quartz tube is surrounded by a zone heating element that offers temperature control of the system. The quartz tube has two vacuum seals one on each side to prevent gas leakage during growth. The operation of the reactor is computer controlled and

gives the ability to control and monitor simultaneously different deposition parameters, such as ramp rate, growth temperature, flow rates of introducing gases and duration.

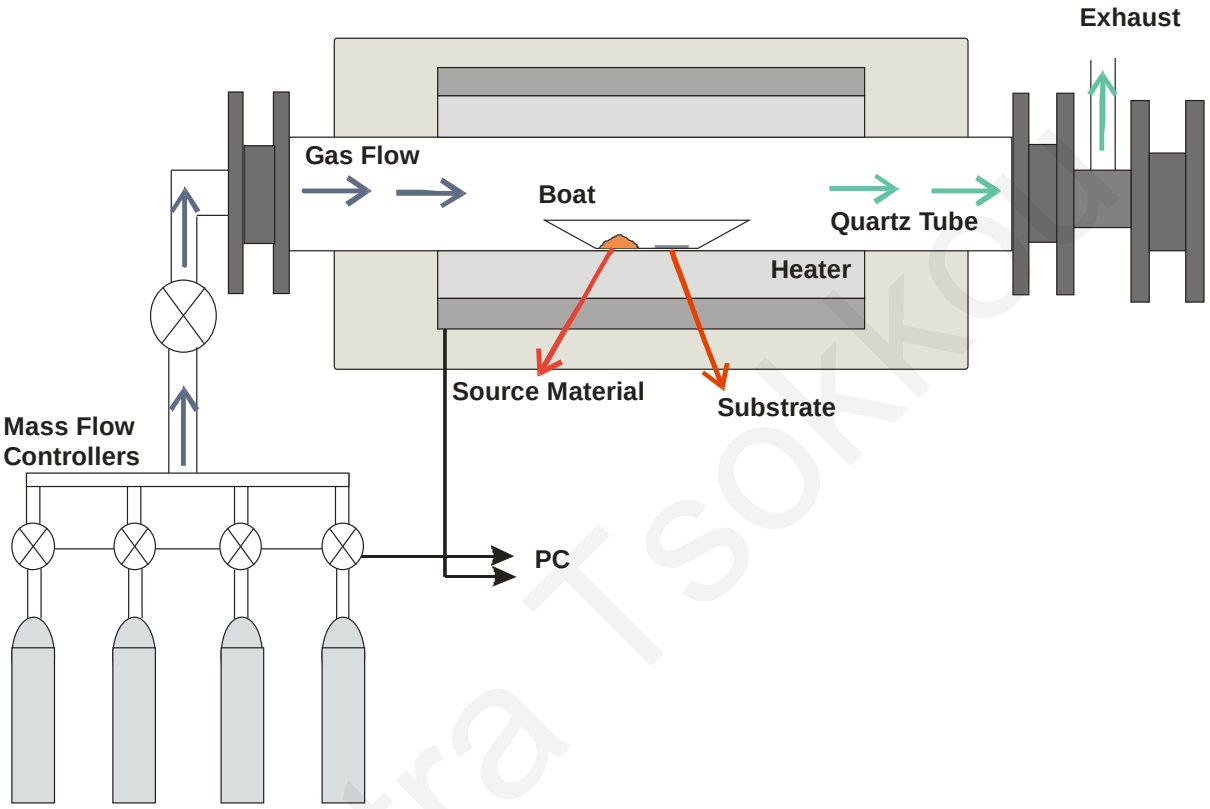

Figure 2.1. A simplified scheme of the horizontal APCVD furnace system used for the synthesis of nanomaterials.

Generally, in a synthesis process a high flow of a chemically inactive gas, usually argon (Ar) or nitrogen (N_2), is used as a carrier gas to eliminate oxygen and moisture from the tube before heating. Then, the furnace temperature is increased with a selected ramp rate under the continuous flow of a properly chosen gas. As the chamber temperature elevates, the source material melts and its vapor pressure increases. Finally, the system reaches an elevated growth temperature that remains constant for a specified time interval under the continuous flow of gases. During the growth process, a chemical reaction takes place between the evaporated source material and the introduced gases. The system is equipped with four mass flow controllers that can control and monitor independently the selection of desirable gases

and flow rates used in each step of the experiment. Typical gases used in the CVD system are argon (Ar), nitrogen (N), oxygen (O_2), ammonia (NH_3) and a mixture of nitrogen/hydrogen (N_2/5% H_2). The products are deposited onto the substrate in solid phase, while gaseous by-products are exhausted out of the tube on the other side of the system. Product characteristics, such as shape, size and density on the substrate, are optimized by changing the experimental parameters or the reaction chemistry, such as growth temperature, growth time, gases, gas flows and source material, until a satisfactory result is achieved.

APCVD has many advantages over other fabrication techniques, mainly because of the simplicity of operation and lower cost. Additionally, higher deposition rates are accomplished when using APCVD in compared with the MBE method. It is also significant that no ultra-high vacuum is needed. It has the capability of producing highly dense and pure materials and also offers flexibility of choosing different kind of precursors. The morphology of the products changes by controlling the growth parameters. Nevertheless, the main disadvantages of this technique are the high deposition temperatures and the fact that many precursors used are toxic or/and expensive.

2.1.2 Scanning Electron Microscopy

Scanning Electron Microscopy (SEM) is utilized for the structural sample characterization, especially the study of material morphology. SEM operation is similar to an optical microscope, although it uses a high energy electron beam, instead of photons, to accomplish larger magnifications. In the case of an optical microscope, magnification is limited to ≈ 1000x and spatial resolution reaches down to 0.2 μm. The use of electrons in the SEM microscope leads to an improved magnification up to ≈ 10000x corresponding to resolution of few nm. SEM is used to identify the deposited product structures, their homogeneity and density over a substrate. The SEM used in these experiments was a *Tescan Vega LSU* manufactured by Tescan.

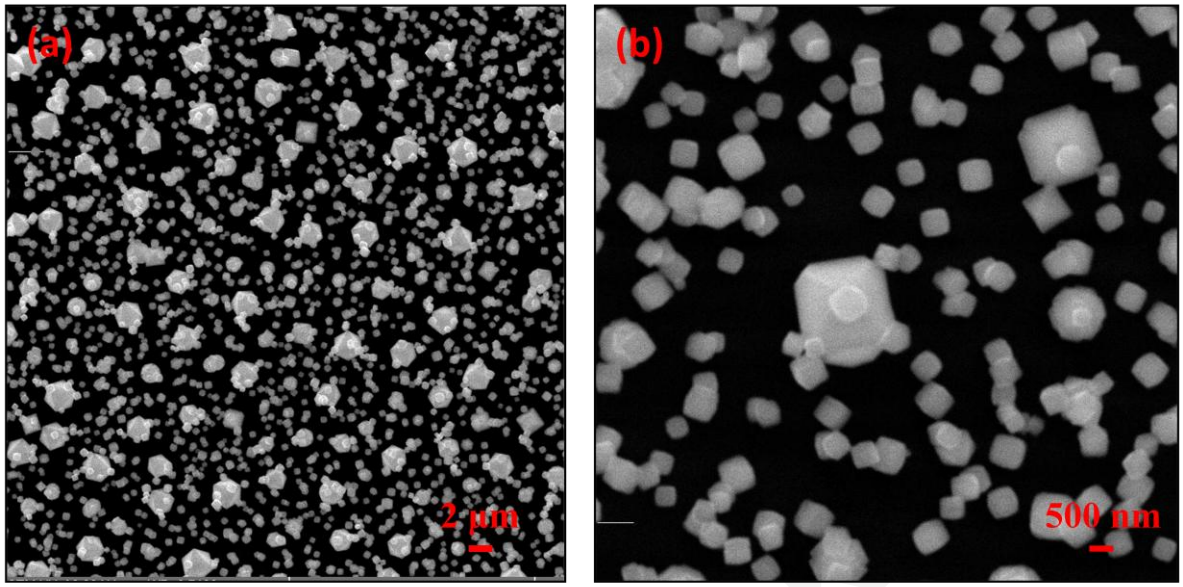

Figure 2.2. Typical SEM images of In_2O_3 nanocrystals on silicon substrate synthesized via APCVD.

Typical SEM images of In_2O_3 nanocrystals on Si substrate synthesized via APCVD at 900 ^oC under continuum flow of O_2 at 100 sccm are shown in Fig. 2.2. From the SEM image at the left (Fig. 2.2 a), it is revealed that there are two types of In_2O_3 nanocrystals observed with different size and density. From the SEM image shown in Fig. 2.2 b is depicted that smaller nanocrystals have a diameter of ≈ 500 nm and density 1 NCs/μm^2, while larger octahedrons are almost 2 μm and density 0.01 NCs/μm^2.

2.1.3 X-Ray Diffraction

Structural characterization of the NWs under investigation has been accomplished using X-Ray Diffraction (XRD). XRD serves for the identification of unknown materials and determination of the crystal structure. Additionally, it is used to identify different components and their proportion in mixtures. X-ray diffraction measurements were performed by using a *SHIMADZU XRD 6000*, X-ray diffractometer. Typical scanning incidence angles had a range between 10-80^o at a rate of angle step between 0.01-0.02^o.

2.1.4 Steady State Transmission Spectroscopy

Steady state transmission spectroscopy is used for the characterization of optical properties of materials. This method is attractive due to its simplicity of operation. In a semiconducting material the transmission spectrum is useful for the determination of its band gap.

In this work, a *Perkins-Elmer 950* UV/VIS/IR spectrometer is used for the steady state transmission measurements performed. In this spectrometer system, a continuum deuterium and tungsten halogen lamps are used as light sources in the UV and VIS/IR region, respectively. The spectrometer is equipped with a double grating monochromator to select a convenient wavelength for the excitation of the sample. Afterwards, the transmitted signal is directed onto the detector and the transmission spectrum can be recorded for different wavelengths between 190 nm and 3300 nm.

The absorption coefficient of a semiconducting material, which is a function of wavelength, can be extracted from the transmission signal $T(\lambda)$. When light normally incidents on a thick sample transmission signal $T(\lambda)$ is related to absorption coefficient $\alpha(\lambda)$ via a simple relation as described by equation 2.1,[117]

$$T(\lambda) = (1 - R(\lambda))^2 \exp(-a(\lambda)\ d) \tag{2.1}$$

where $R(\lambda)$ is the reflectance signal and d the thickness of the material. Furthermore, near the high absorption region ($\alpha \geq 10^4$ cm^{-1}), the absorption coefficient has the frequency dependence shown by equation 2.2, which is used to estimate the optical band gap of the semiconducting material.

$$a(v) \propto (hv - E_g)^n \tag{2.2}$$

A plot of $\alpha^{1/n}$ with respect to hv and extrapolation to a straight line at $\alpha^{1/n} = 0$, provides the optical band gap. Generally, n is equal to 2 for an indirect band gap and 1/2 for a direct band gap semiconductor.

2.5 Ultrafast Characterization

The characterization of semiconducting NWs using ultrafast spectroscopic techniques aims to study their fundamental optical and electronic properties, which will reveal the required information for the potential application of NW-based devices. The experimental methods used in this work are, the *time resolved absorption* and *time resolved THz transmission spectroscopy*. These techniques are based on a variation of the known pump-probe configuration. The sources of amplified pulses along with the characteristics of each beam used in each case are presented. The important optical elements included and processes that take place in each experimental setup are briefly described.

2.5.1 Time Resolved Absorption Spectroscopy

Transient absorption changes were determined using two different ultrafast amplifier laser systems in typical supercontinuum non-collinear pump-probe configuration. A simplified scheme of the experimental configuration for the non-degenerate absorption change measurements is shown in Fig. 2.3.

The first system consists of a Self Mode-Locked Ti:Sapphire Oscillator (*Mira*), a commercially available Coherent system, generating 20 fs IR pulses, having a centre wavelength at ≈ 790 nm. Pulse energy is approximately ≈ 5 nJ at a repetition rate of 100 MHz. This oscillator is pumped by a continuum frequency doubled Nd:YVO_4 laser, *(Verdi-V6* manufactured by *Coherent*), that provides 5 Watt and operates at 532 nm. Additionally, a Regenerative Amplifier (*Legend*) is used to amplify the pulses approximately 10^6 times. Their energy per pulse reaches ≈ 0.5 mJ with time duration of ≈ 45 fs pulses at a repetition rate of 5 kHz. A solid state Q-switched nanosecond Nd:YLF Laser (*Evolution 30 Coherent*) is used as a pump for the regenerative amplifier.

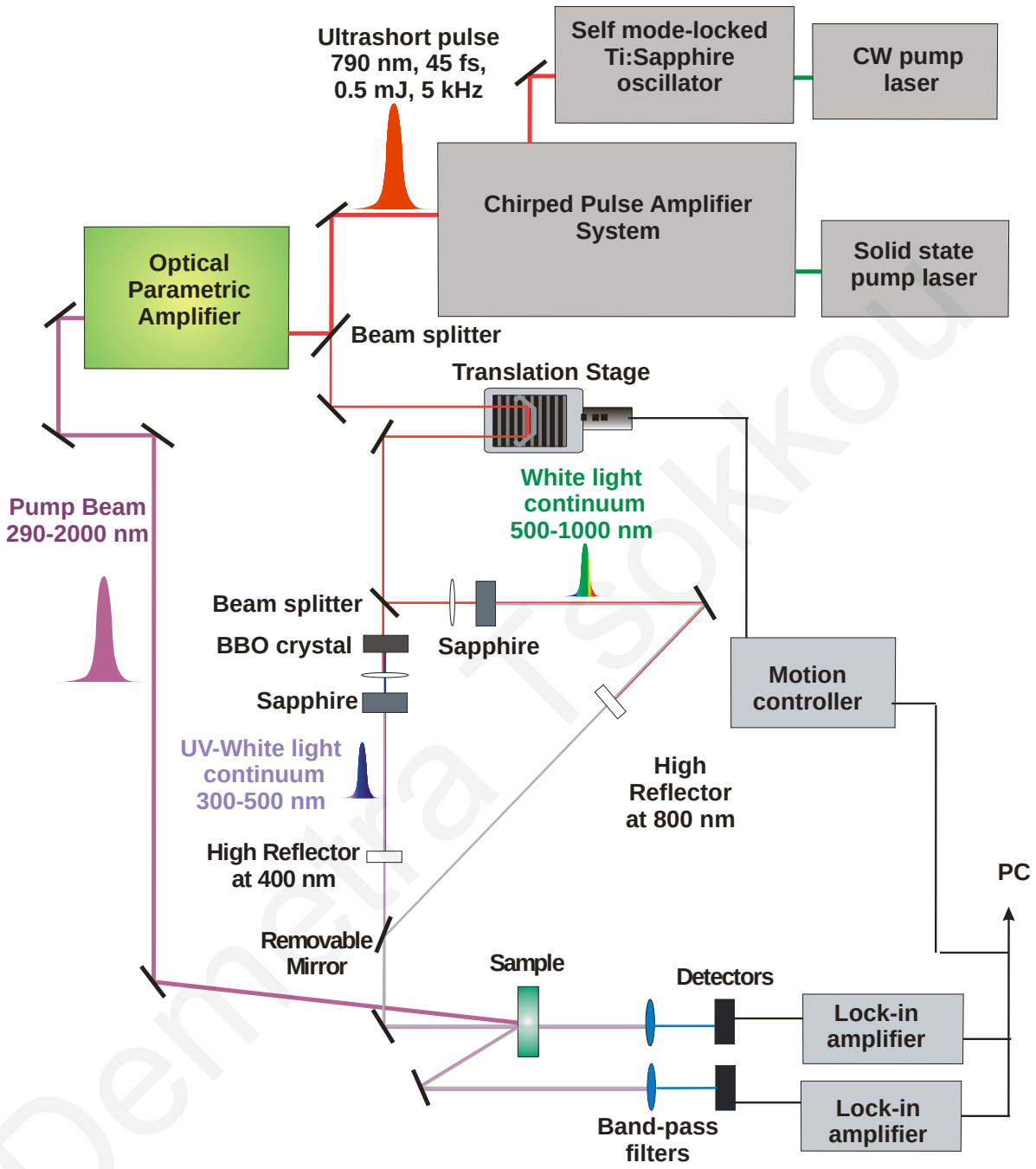

Figure 2.3. Experimental configuration for non-degenerate time resolved absorption measurements.

As shown in Fig. 2.3, a beam splitter is utilized to divide the output beam produced by the amplifier system into two components, that eventually produced the pump and the probe beams. The larger part of the output energy is directed into an Optical Parametric Amplifier

(OPA), which converts the wavelength of the pump beam through nonlinear processes. The OPA provides pulses within a wide spectral region ranging from UV (290 nm) to the far IR region (1800 nm). For the experiments in this research work, OPA was used to generate excitation pulses in the UV region which is located above band gap for the materials under investigation. Furthermore, ultrathin reflective filters were utilized for intensity dependent measurements.

The probe beam at 800 nm, corresponding to a very small part of the fundamental intensity, is used to generate a supercontinuum white light for transient non-degenerate absorption measurements.[95,96] This was accomplished through a strong focus of the beam on a 1 mm sapphire plate. Two different setups are used in order to broaden the range of selected probing wavelengths. The first setup is used to generate the continuum white light in the region between 500 and 1000 nm. The second one produces wavelengths in UV region between 300 and 500 nm. This is accomplished through the additional second harmonic crystal that initially converts the probe wavelength to 400 nm and then utilizing this second harmonic to produce the white light.

The variation of the relative delay time between pump and probe pulses was accomplished using a computer controlled translation stage with 0.1 μm step resolution, which was placed in the pathway of the probe beam. Its optical travel range was 25 cm, proving time resolved measurements upto 1.5 ns following optical excitation. The desired probing wavelength was selected using band-pass filters. The transmission and reflection change induced on the probe beam by the incident pump beam were detected by Si photodiodes. These signals were measured using lock-in amplifiers with reference to an optical intensity modulator (an optical chopper) of the pump beam, in order to enhance signal to noise ratio. In this configuration, the lock-in amplifiers measure only the components that are modulated at the pump modulation frequency, whereas signal from different frequency components is rejected. The output of the lock-in amplifier is digitally recorded using a Labview based program that controls various experimental parameters including the translation stage movement.

A second ultrafast amplifier system uses a similar apparatus to produce excitation pulses in the visible region at 400 nm with time duration of 100 fs and a repetition rate of 1 kHz. A continuous solid state laser (*Millenia Spectra Physics*) producing 5 W at 532 nm was

used to pump a femtosecond mode-locked oscillator (*Tsunami Spectra Physics*). A continuous power of 4.5 W is needed to pump the gain medium of the oscillator producing ultrashort pulses at 800 nm, with pulse energy of 0.7 nJ/pulse, repetition rate of 100 MHz, and time duration of 100 fs. These pulses are directed onto a regenerative amplifier (*Spitfire Spectra Physics*). The regenerative amplifier is pumped by a Q-switched doubled frequency Nd:YLF laser (*Empower Spectra Physics*) operating at 527 nm wavelength with 1 kHz repetition rate, and 15 W of average power. The resultant pulses are amplified up to ~10^6 times and reach energy of 1 mJ/pulse at 800 nm, with time duration of 120 fs and repetition rate at 1 kHz. In this setup, a nonlinear BBO crystal is used in order to double the pump wavelength via second harmonic generation, while the probe pulses are used to generate continuum white light in the region between 500-100 nm.

2.5.2 Time Resolved and Time Domain Terahertz Transmission Spectroscopy

A THz spectrometer system based on an optical rectification and free electrooptic sampling has been designed and developed. The source of excitation was a Ti:Sapphire ultrafast amplifier producing 120 fs pulses at a repetition rate of 1 KHz and centered at 800 nm. A simplified schematic diagram of the experimental arrangement is shown in Fig. 2.4.

In this experimental configuration, the initial incident beam is separated into three beams each following a different optical path. Therefore, the apparatus consists of three different pathways: the optical excitation, the THz generation and the THz detection branches.

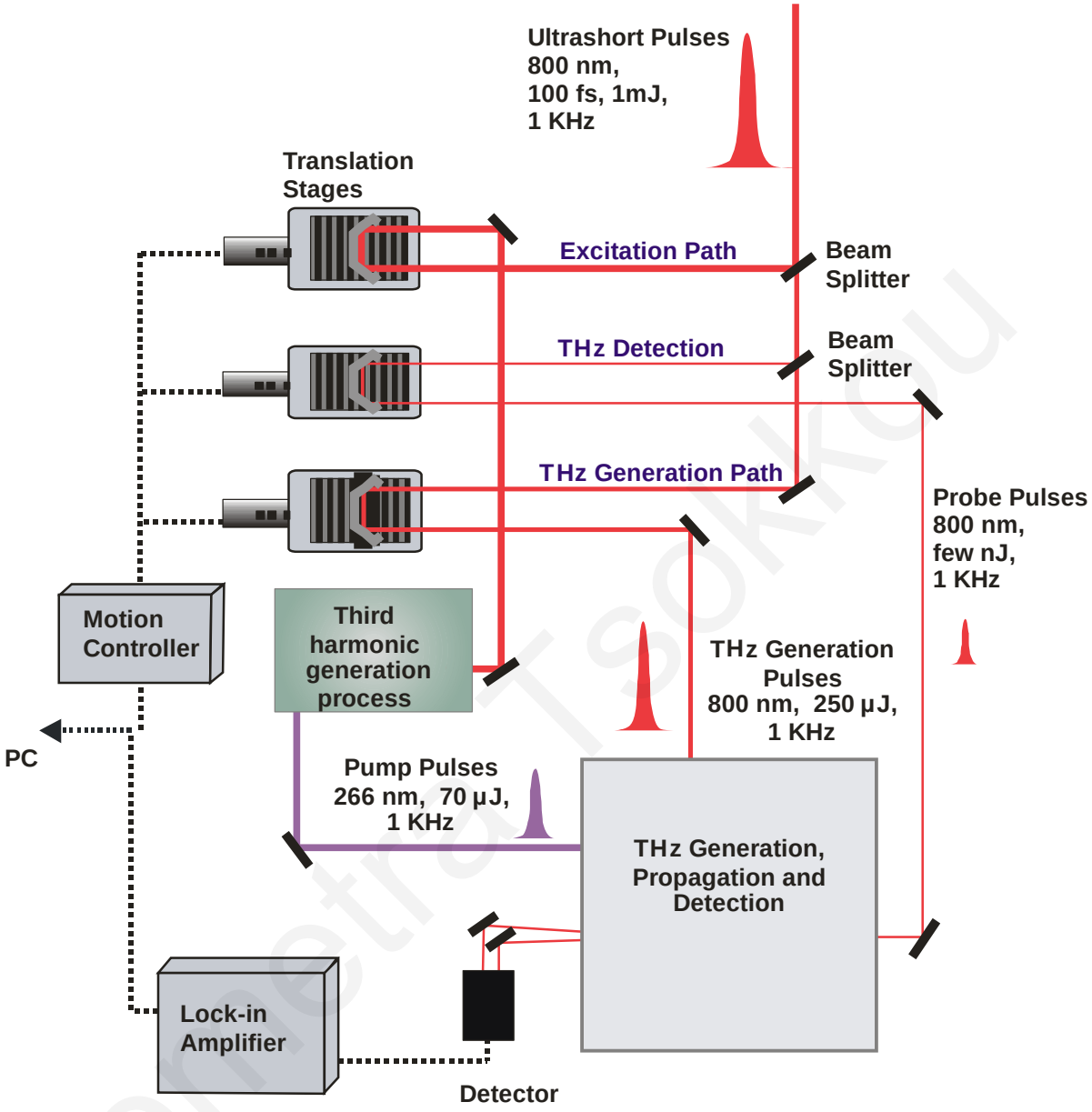

Figure 2.4. A simplified schematic diagram of experimental configuration for the time resolved UV-pump terahertz-probe optical setup. The initial incident beam is divided into three components; Pump beam, THz beam and the Probe beam. Each of the optical paths is controlled by a different motorized translation stage with sub-micron resolution.

In more detail, the initial beam is directed onto a beam splitter (75:25) to separate the fundamental beam into two parts. The majority of the intensity is used for the excitation of the sample and possesses approximately 75% of the initial beam intensity. The residual intensity

(25%) passes through a second beam splitter (96:4) and is divided into two parts. The beam with the higher intensity (24%) is used for the generation of picosecond THz pulses, while the weaker part is responsible for the detection of the THz beam and is called the probe beam.

(a) Optical excitation path

In the optical excitation path, non linear crystals are used to convert the wavelength of the fundamental beam into that of the excitation beam via nonlinear optical effects. For the investigation of wide band gap semiconductors, UV pulses are needed to excite the carriers above the band gap. Therefore, the initial wavelength of near-IR pulses has to be converted into the UV region using a third harmonic frequency mixing process, which is a two-step process. Two different nonlinear crystals, namely a second harmonic BBO (β-BaB_2O_4) crystal in combination with a third harmonic BBO crystal are used to convert the initial beam wavelength.

First, a BBO crystal is used to double the incoming IR beam and generate pulses at 400 nm. After the first BBO crystal, the resultant beam consists of 400 nm and the fundamental IR at 800 nm light, as it is shown in Fig. 2.5. A highly reflective mirror at 800 nm is used to separate the different wavelength components. Following that, a half wave plate is placed in the path of the visible light (400 nm) to change its polarization. The two resultant beams follow different pathways and are directed onto a second BBO crystal, which favors sum frequency mixing between 800 nm and 400 nm, to produce UV pulses at 266 nm. Since the two different beams have to travel the same distance before they interfere into the second crystal, two mirrors directing the beam at 800 nm are placed on a small translation stage to make easier the achievement of temporal and spatial overlap between the two pulses. The UV generated pulses from this configuration have energy up to 70 μJ/pulse.

Additionally, a focusing lens is used before the beam incidents on the sample to control the diameter of the pump beam at the excitation point. For TRTS measurements, the diameter of pump beam is adjusted to be between 3-4 mm. This setup offers easy access for three different pumping wavelengths namely 266 nm, 400 nm and 800 nm ranging from the UV into IR region.

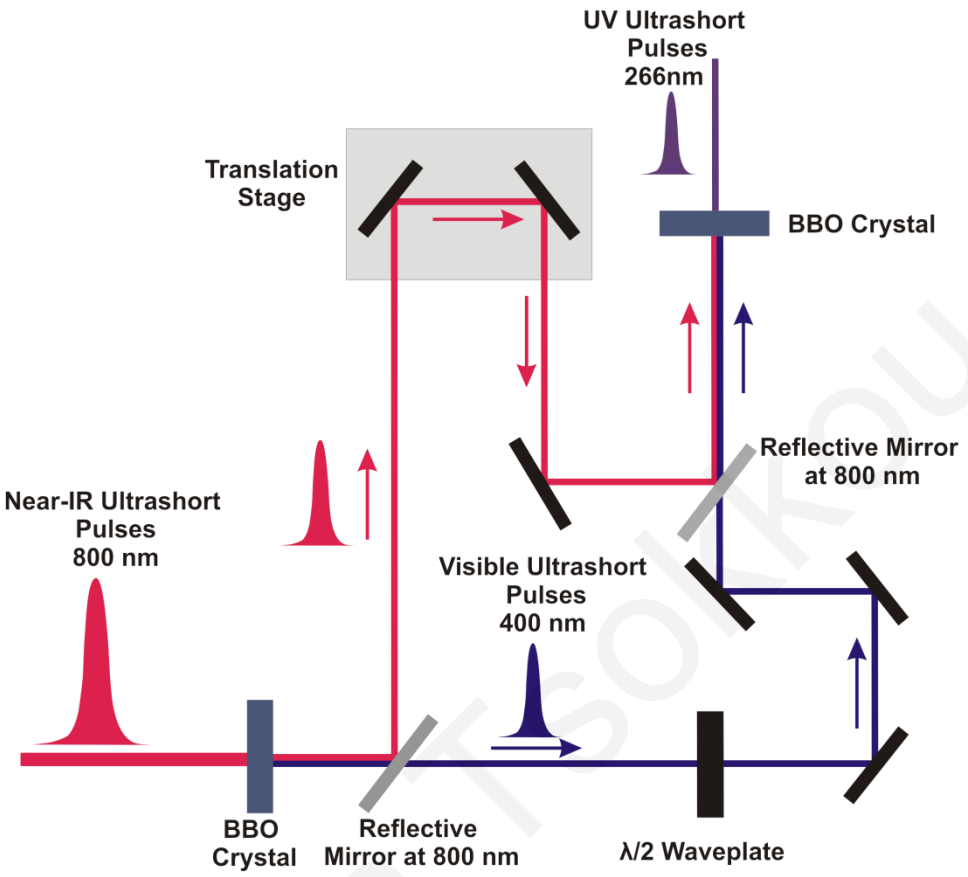

Figure 2.5. Experimental configuration of UV pulses generation by using third harmonic frequency mixing effect.

(b) THz generation path

The main parts of the THz generation path are the terahertz generation crystal and the 90^0 off-axis parabolic mirrors, as seen in Fig. 2.6. A focusing mirror is placed in front of the THz generator crystal to reduce the diameter of the optical beam that incidents onto the crystal to approximately 4 mm. The crystal utilized for the generation of the THz radiation is a 0.5 mm <110> oriented ZnTe, where difference frequency mixing takes place. The choice of the crystal orientation is made in order to maximize the THz emitted signal.

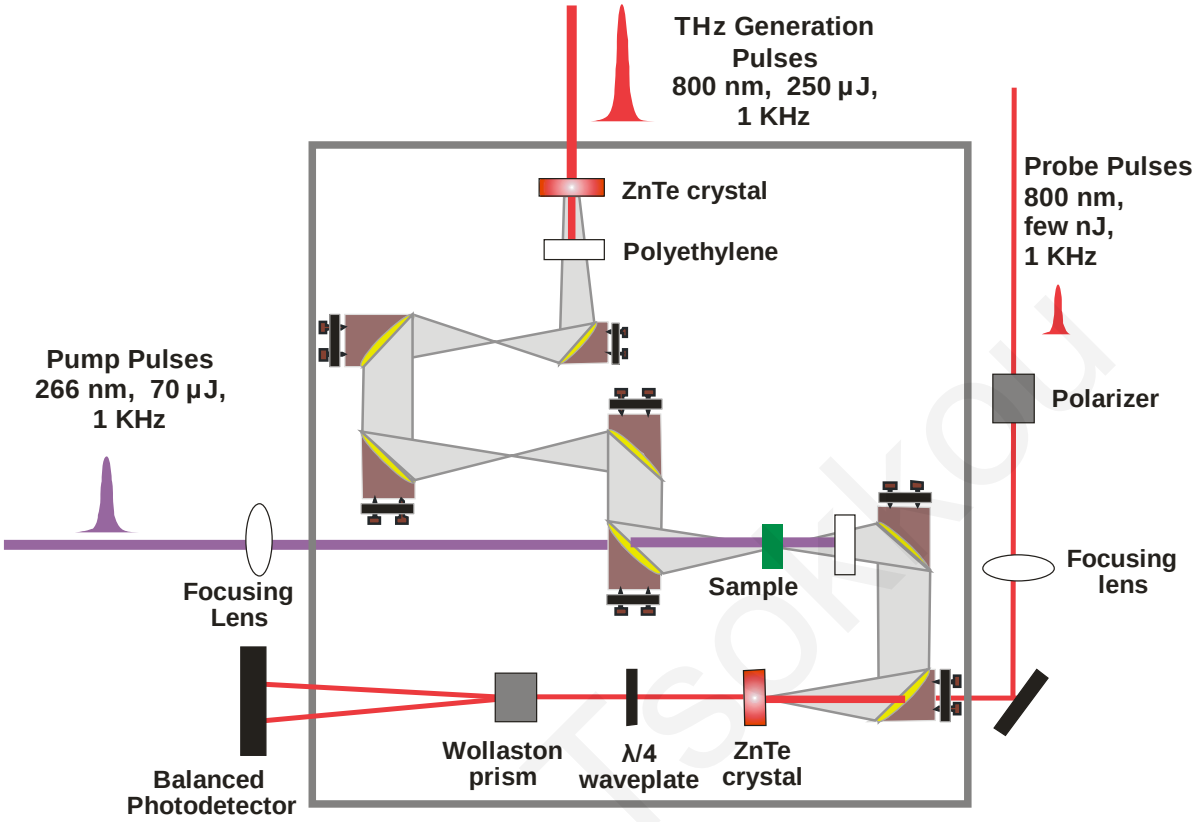

Figure 2.6. Experimental configuration of generation, propagation and detection of THz pulses in a transmission configuration.

The spot size of the beam is significantly larger than that used in optical pump-probe experiments in order to avoid damaging the ZnTe crystal, that occurs for optical fluences above 3 mJ/cm^2.[118] The intensity of the optical beam was measured in front of the ZnTe crystal and found to be equal to 250 µJ/pulse. Therefore, this energy corresponds to fluence that incident onto the sample equals to ~ 2 mJ/cm^2, which is below the damage threshold of the crystal. Behind the nonlinear crystal a high density polyethylene is positioned to block any residual fundamental light transmitted through the ZnTe crystal that may damage the optical elements in the setup.

Alignment of the 90^0 off-axis parabolic mirrors, which are used to direct and focus the THz beam onto the sample, is quite tricky. To achieve this, a continuous-wave (CW) He-Ne laser operating at 632 nm was used. Initially, the beam of the CW laser was coincided spatially with the IR beam, as it is directed onto the ZnTe crystal. Next to the laser, a

telescope was placed to enlarge the initial beam diameter to make possible the detection of the THz beam trajectory and the spatial points that will incident onto the off-axis parabolic mirrors. It is of paramount importance that off-axis parabolic mirrors are correctly oriented and that THz beam incidents onto the mirror center, in order to be reflected under a 90^0 angle. In this way, a tightly focused THz beam will result, with no aberrations that will lead to widened pulses.

Following the ZnTe generation crystal in a close distance, a 90^0 Au-coated off-axis parabolic mirror is used to focus the generated THz radiation. In order to collect efficiently the THz signal emitted by the ZnTe crystal, the first parabolic mirror must have small focal length. Then, few 90^0 Au-coated off-axis parabolic mirrors are used so that THz pulses are collimated and then focused again onto the sample in a convenient arrangement, as it is seen in Fig. 2.6.

To achieve a good temporal overlap between excitation and THz pulses and at the same time excite the sample area uniformly, a small hole was created on the last Au-coated off-axis parabolic mirror placed before the sample, so that the two beams incident collinearly onto the sample. Furthermore, previous studies have shown that it is crucial for the pump beam diameter to be at least twice larger than the diameter of THz beam for uniform excitation.[119] Pump beam is focused to have a diameter between 3-5 mm and the THz beam diameter between 1-2 mm. Finally, the THz beam transmitted through the sample is recollimated and focused by a pair of off-axis parabolic mirrors onto a 0.5 mm <110> ZnTe detector crystal.

(c) THz detection path

The third part of the fundamental beam is used as a gated beam for determining the electric field of the THz pulse via free-space electro-optic sampling technique. After the sample, two additional 90^0 off- axis parabolic mirrors are utilized to focus the THz beam onto the ZnTe detector crystal. Additional to the THz beam, a probe beam is also focused onto the crystal through a small hole that was drilled in an off-axis non-parabolic mirror to allow collinear propagation of the beams. The diameter of the probe beam is adjusted at about ~ 250 μm and its energy is few nJ/pulse. Before the probe beam is directed onto the crystal, it passes

through a polarizer to ensure the linear polarization of the beam, which is important for good signal to noise measurements to be carried out.

In order to determine the spatial and temporal overlap between the optical and THz beams, an intensity autocorrelation technique was used. The ZnTe detector crystal was replaced by a non-linear BBO crystal, while the polyethylene is removed and a small amount of optical beam intensity in the THz propagation path is allowed to reach the non-linear crystal. The probe beam is delayed with respect to the THz beam. When the two beams temporal coincide, second harmonic effect will take place and a weak signal at twice the frequency of the optical IR beam is produced. In this way, the spatial and temporal overall was determined.

Given that the probe beam duration is much shorter than the THz beam, the time domain of the THz pulse can be scanned by adjusting the optical delay between the two pulses. Passing through the electro-optic crystal, the linearly vertically polarized probe beam becomes elliptically polarized. After a quarter-wave plate and a Wollaston prism, the voltages of the two orthogonal polarized signals are collected by a balanced photo-detector. The detector is connected with a lock-in amplifier that is phase-locked to an optical chopper, which modulates either the pump or THz beam, depending on the kind of measurement. Before a measurement is performed, in the absence of the THz beam, the quarter wave plate is rotated appropriately to minimize the difference voltage signal of the two photodiodes.

A part of the experimental arrangement can be seen in the Fig. 2.7. It includes the generation, the propagation and the detection of the THz beam. Blue line corresponds to the pathway of the THz beam, with red line the pathway of the probe beam as it passes through the last 90^0 off-axis parabolic mirror, until it reaches the detector and with violet line the path of the pump beam until incidents onto the sample.

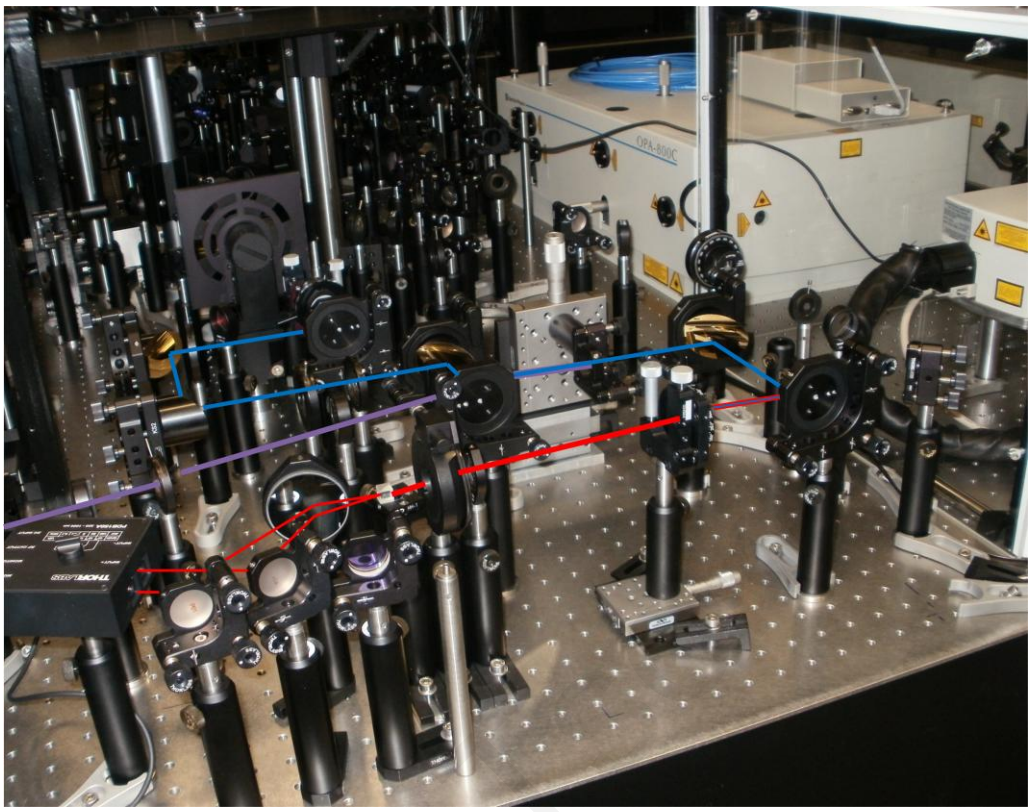

Figure 2.7. A photo of the time resolved THz transmission experimental setup. The parts of generation, propagation and detection of the THz pulses are evident. Blue line depicts the trajectory of the THz pulse from the generation crystal to the detection crystal. Violet line follows the pathway of the pump beam until it reaches the sample and the red line shows the trajectory of the probe beam after it passes through the off-axis parabolic mirror until it reaches the balanced photo-detector.

In each path, a different computer controlled motorized translation stage is placed to allow independent and efficient control of relative time delay difference between the pulses that can be seen in the Fig. 2.8. The mechanical precision of the movement is 0.1 μm and the maximum measured time delay reaches up to 660 ps.

In order to prevent any effect of the measured signal due to THz absorption by water vapor found in the atmosphere, the parts of the experimental arrangement including the steps of THz pulses generation and detection needs to be introduced into a nitrogen dry purged box, as it is will be evident in the next chapter.

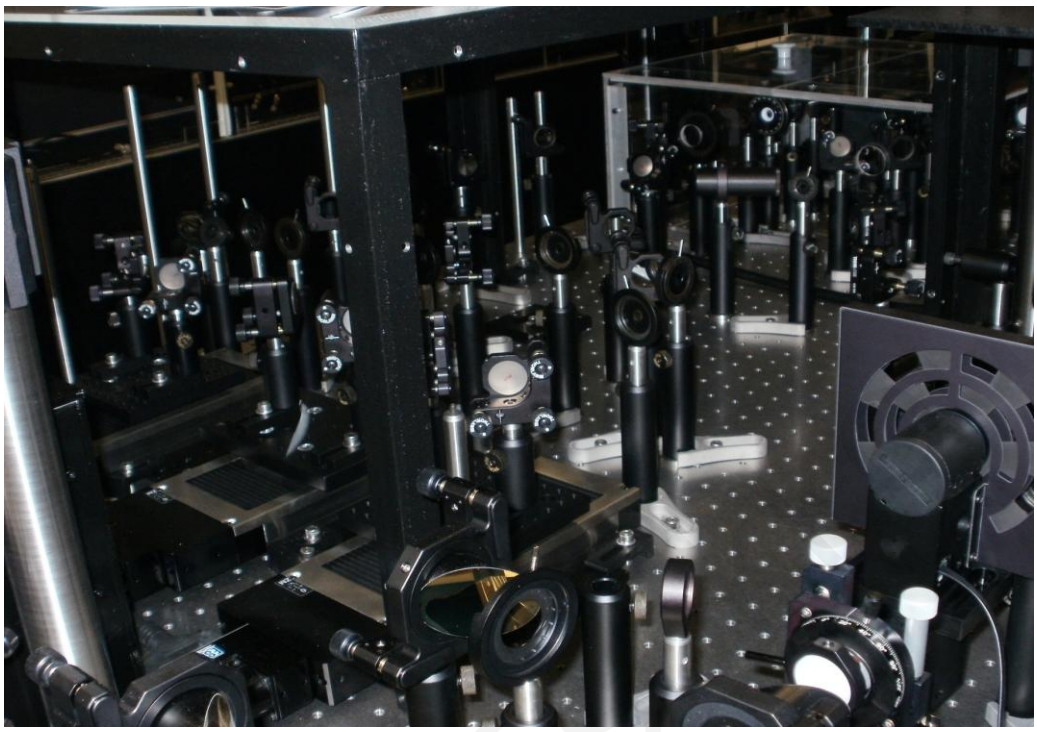

Figure 2.8. A different photo of the experimental setup. It shows the three different translation stages responsible to control the time difference between the three pulses.

Chapter 3

Analysis of Ultrafast Spectroscopy Measurements

The experimental data obtained from the ultrafast spectroscopy measurements need further manipulation to obtain useful information regarding ultrafast carrier dynamics in the NWs under investigation in this work.

In the first part of this Chapter, the analysis followed in the time resolved absorption spectroscopy measurements is presented. The effects of "*state filling*" and "*free carrier absorption*" detected in these experiments and the way that they are related to the carrier relaxation in semiconducting materials, are discussed. Furthermore, carrier relaxation dynamics and the differential rate equation used to fit the experimental data for low carrier densities to obtain the carrier relaxation times and the number of mechanisms that take place, are described. These experiments are also used to determine the existence of various energy states and the presence of many body effects.

Next, the mathematical analysis for the experimental data obtained from the time domain and time resolved THz transmission spectroscopy used to extract the complex dielectric function, is described. Initially, the time domain and frequency domain data of the reference THz electric field detected are presented and discussed. Then, the steps followed to determine the complex refractive index or intrinsic conductivity from time domain THz transmission spectroscopy, in the case of (a) bulk and also (b) nanostructured materials, are presented. Moreover, the Drude-Smith model used to explain the experimental data of complex conductivity is discussed. In the last section of this Chapter, the mathematical analysis used to obtain photoconductivity from the experimental data is also described.

3.1 Analysis of Time-Resolved Absorption Change Measurements

Time resolved absorption measurements investigate the response of semiconducting materials following photoexcitation through the contributions of differential reflectivity and transmission at different time delays Δt between the pump and probe pulses. These changes are attributed to modifications in the material dielectric function related to the generation of photoexcited carriers and their subsequent relaxation.

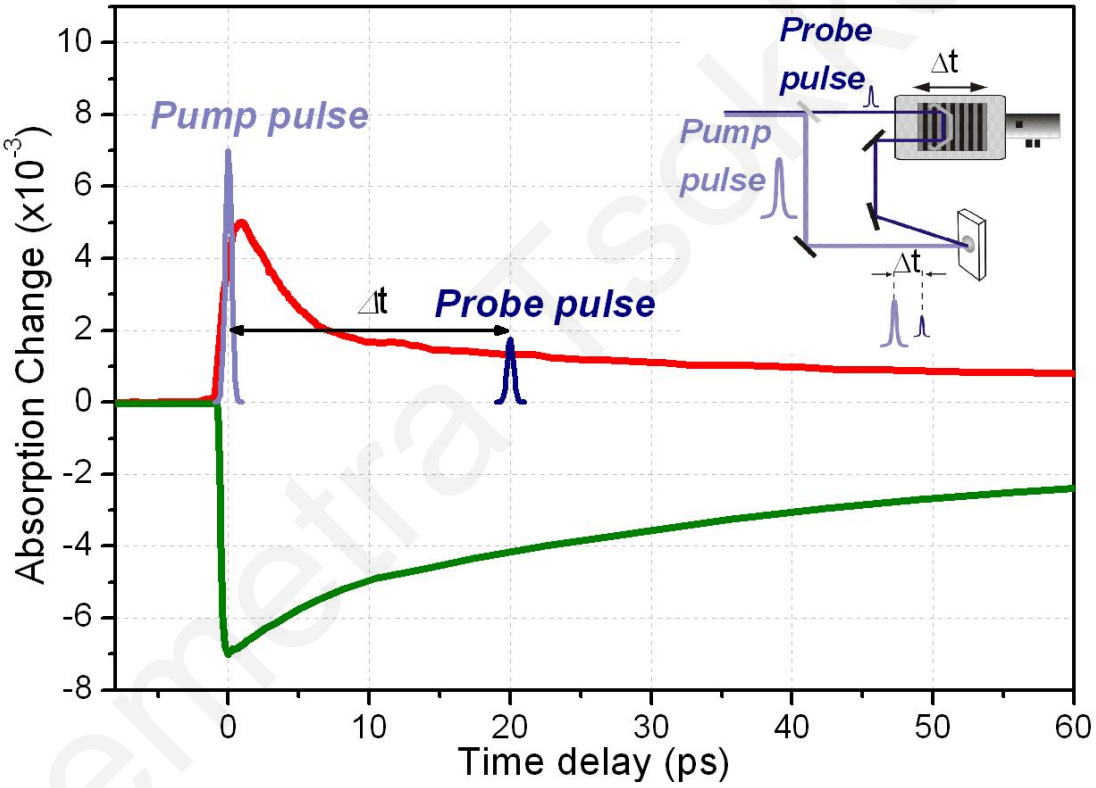

Figure 3.1. Typical graphs of the temporal evolution of absorption change signal following short pulse excitation. Green line is attributed to the detection of state filling effects in these experiments, while the red line denotes the detection of free carrier absorption effects. In addition, the pump pulse that incidents onto the sample at time delay Δt = 0 ps and the probe beam that reaches the sample with a time delay Δt induced by a motorized translation stage can be seen in the inset of the figure, where a simplified configuration of the pump-probe technique is shown.

The temporal variation in the photo-induced absorption extracted is a direct measure of the photo-excited carrier dynamics within the probing region. Differential absorption change $\Delta A(t)$ is related to transmission change $\Delta T(t)$ and reflectance change $\Delta R(t)$ signals at different delay times between the pulses as described by the equation 3.1,

$$\frac{\Delta A(t)}{A_0} = -\frac{(\Delta T(t) + \Delta R(t))}{A_0} \qquad (3.1)$$

where $\Delta A(t)$ is the absorption change induced by the pump beam at time delay $\Delta t = t$ and A_0 is the absorption of the sample in the absence of any excitation.

Typical graphs of the evolution of absorption change signal as a function of the delay time between the two pulses are shown in Fig. 3.1. The pump pulse that incidents onto the sample at time Δt = 0 ps is also included, along with the probe beam that incidents onto the sample at a delay time Δt. Absorption change induced on the probe beam is measured at different delay times Δt before and after photoexcitation of the sample. The time delay Δt between the two pulses is achieved using a motorized translation stage, as seen in the inset of the Fig. 3.1. Generally, an initial fast increase or decrease is observed in the differential absorption signal, which is usually followed by a much longer recovery towards equilibrium. Positive or negative sign of the absorption change is assigned to "*free-carrier absorption*" or "*state filling*" effects, respectively. In both cases, when many body effects are negligible, the time evolution of the signal corresponds to the population recovery from the excited states to the ground states.

A negative change in the photo-induced absorption is the result of the occupation of energy states by photo-generated carriers in what is known as *state filling*,[120] shown with a green line in Fig. 3.1. A simplified picture of this effect in a semiconductor material is depicted in Fig 3.2 at different time delays between the excitation and the probe pulses. In this schematic picture, the excitation pulse has photon energy larger than the band gap of the semiconducting material. Therefore with the arrival of the pump pulse carriers will be generated in the conduction band. At time delay very close to Δt = 0 ps (depending on the response of the material) most of the carriers will be generated near the excitation region, conserving energy and momentum. Clearly, selecting the probe beam to have the same

wavelength as the excitation pulse, it will sense the maximum change in the absorption. Furthermore, with the appropriate selection of the probe pulse wavelength it is possible to follow the energy relaxation of the photogenerated carriers as they move toward equilibrium.

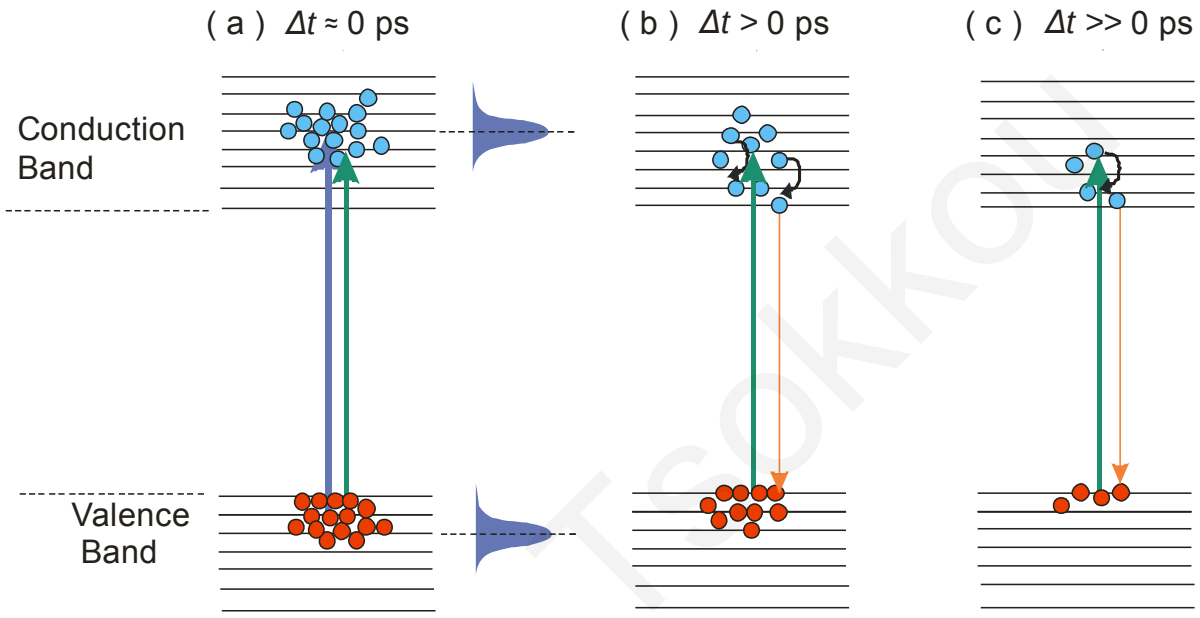

Figure 3.2. Schematic diagram of carrier evolution in a semiconducting material, to explain state filling effects. (a) At Δt = 0 ps, the pump beam excites a number of electrons into the conduction band and at the same time the probe pulse incidents onto the sample and tries to excite more carriers from the valence band states. (b) At Δt > 0 ps, a number of carriers leave the conduction states and thus there are more available states for carriers to be excited by the probe beam. (c) At times Δt >> 0 ps, only a small number of carriers still exists in conduction band states and evidently a larger number of carriers can be excited by the probe beam.

At times $\Delta t < 0$ ps, the probe beam arrives earlier than the pump beam, because it follows a shorter path. Given that no carriers have been excited yet, no change in the absorption signal has been induced and therefore the differential absorption is zero.

Optical absorption is determined by the transition rate given by the Golden Fermi rule, seen in equation 3.2. Golden Fermi rule gives the transition rate W_{if} of an electron to leave its initial state i, as it absorbs a photon with energy E_{fi} (= E_f - E_i) and be excited to a final state f.

$$W_{if} = \frac{2\pi}{\hbar} M_{fi}^{2} \rho(E_{fi}) \tag{3.2}$$

It is observed that the transition rate W_{if} depends on the strength of the coupling between the initial and final states, which is described by the matrix element of interaction M_{if} $\left(M_{if} = \int \Psi_f^* V \Psi_i d^3 r \right)$. Furthermore, the transition rate is dependent on the density of the available states $\rho(E_{fi})$ for the transition to occur. Following excitation of carriers, the available states for transitions to occur are reduced, due to the occupation of the conduction band states and consequently the absorption of incident light is smaller.

At times $\Delta t > 0$ ps but close to zero, the probe beam (green line) also arrives and tries to excite more carriers from the valence band into higher energy states. At this time, there are fewer available energy states in the conduction band due to occupation of the upper states. Therefore, the probe beam propagates through the sample suffering less absorption and the absorption change signal appears to be negative. At times $\Delta t > 0$ ps, some photoexcited carriers will relax into lower states or even recombine into states in the valence band, so fewer carriers will remain in the probed states as seen in Fig. 3.2 (b). Therefore, a larger number of states will be available, and more carriers from the valence band will absorb photons from the probe beam. Consequently, the probe beam will undergo larger absorption and the final signal will appear to be less negative. For times $\Delta t >> 0$ ps (Fig. 3.2 (c)), only a small fraction of photogenerated carriers (or no carriers) will exist in the probed state and the observed signal returns back to zero, since the absorption of the probe pulse is approximately the same as before excitation.

On the other hand, an observed positive change in the absorption described with a red line in Fig. 3.1, is attributed to *free-carrier absorption* effects, which is a consequence of the secondary excitation of free carriers by the probe beam from the probed states into higher energy states.[121] The amplitude of this absorption depends on the coupling efficiency between these energy states and the number of carriers present in the lower coupled energy states. A similar schematic diagram of that shown for the state filling effect is seen in Fig. 3.3, when free carrier absorption effects are detected. At time delays $\Delta t > 0$ ps but close to zero, a large

number of carriers will be present in the probed states and will be excited into even higher states, by absorbing photons from the probe beam, as seen in Fig. 3.3 (a). Therefore, absorption change appears to be positive. At larger times, a number of carriers leave the probed states, and the probe beam will suffer less absorption, leading to a less positive signal (Fig. 3.3 (b)). At $\Delta t >> 0$ ps, only few carriers remain into the detected states and the absorption change becomes almost zero (Fig. 3.3 (c)).

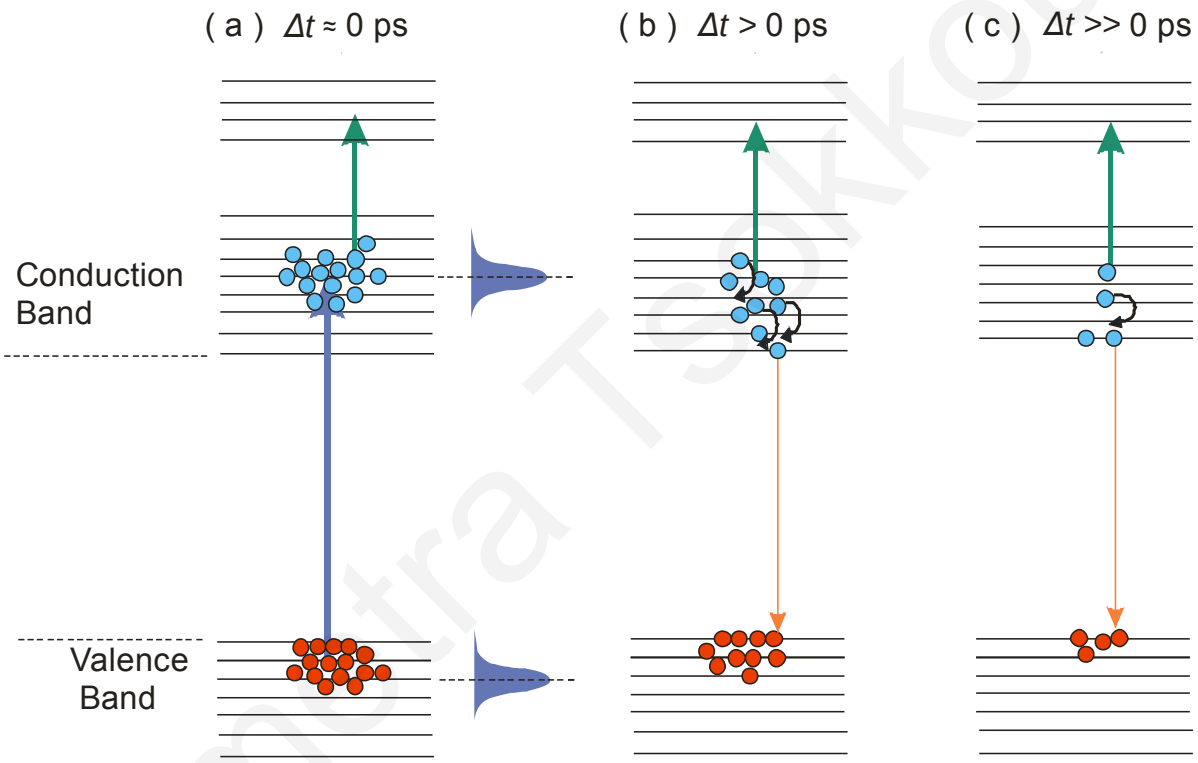

Figure 3.3. Schematic diagram of carrier evolution in a semiconducting material, which explains free carrier absorption effects. (a) At $\Delta t = 0$ ps, the pump beam excites a large number of electrons into the conduction band and at the same time the probe beam causes secondary absorption of carriers at higher energy states. (b) At $\Delta t > 0$ ps, a number of carriers leave the detected states and therefore fewer carriers are further excited by the probe beam. (c) At times $\Delta t >>$ 0 ps, only a small number of carriers still exist in conduction band states and therefore a small number of carriers or no carriers will be further excited by the probe beam.

Normally, state filling is the dominant contribution when probing above the band edge, whereas free-carrier absorption is the dominant process when probe photon energy is

smaller than the band gap. The reason is that there are not available energy states at energy levels below the band gap (assuming an ideal pure semiconductor). Therefore, absorption of the probe pulse from the photoexcited carriers to higher energy states becomes significant. In most cases both effects are present, while the sign of the overall absorption change is determined by the dominant effect.

Here we should point out that in most cases the band diagram of a typical semiconducting material is more complex than that shown in Figs. 3.2 and 3.3. Point or structural defects induce modifications in the band diagram of the semiconductors and energy states are likely to be formed within the band gap, as has been referred in the section 1.6. These additional states affect significantly the recombination mechanisms.

For low carrier densities where many body effects are negligible, the absorption change signal corresponds to the carrier density occupying the probed states. In the case where the photogenerated carriers relax through a single relaxation mechanism, carrier density evolution *n(t)* may be described by the differential rate equation 3.3.

$$\frac{dn}{dt} = -n\ \frac{1}{t_1} \tag{3.3}$$

Therefore, the carrier density evolution *n(t)* and consequently absorption change is described by exponential decay, $n(t) = N_0 e^{-t/t_1}$. When fitting the experimental results to an exponential equation, carrier lifetime t_1 is extracted. Usually, more relaxation mechanisms are involved and carrier evolution can be reproduced by multi-exponential time dependence decays, as it is described by the generalized equation 3.4,

$$\frac{\Delta A}{A} \propto n(t) = \sum_{i=1}^{m} c_i\ e^{-t/t_i} \tag{3.4}$$

where *m* is the total number of relaxation processes occurring in the sample until it returns back to equilibrium state and t_i is the relaxation time for *i* mechanism. In the case where the normalized absorption change signal is used, c_i is a weight number, which its square

represents the percentage of carriers that leave the state through *i* mechanism and should satisfy the following equation 3.5.

$$\sum_{i=1}^{m} |c_i|^2 = 1 \tag{3.5}$$

As mentioned previously, experiments can be performed for different pump photon energies; thus carriers can be excited into different energy states. At the same time, different energy states in the band diagram can be accessed using different probing wavelengths, thus providing a more comprehensive picture of the carrier dynamics. A further insight into the carrier dynamics may be achieved using intensity measurements. This type of experiments may reveal the presence of many body effects, which are strongly dependent on the photo-excited electron density, such as band gap renormalization[122] and Auger effects.

3.2 Analysis of Time Domain Terahertz Transmission Spectroscopy Measurements

To derive useful information from THz spectroscopy measurements, mathematical analysis is needed to manipulate the experimental data to extract quantitative results for the investigated materials. The models used to obtain the optical and transport properties from the TDTS measurements, in the case of bulk materials and NWs are discussed.

3.2.1 Reference THz Electric Field Measurements

Typical measurements of THz electric field waveforms $E_{ref}(t)$ – reference signal – carried out are shown in Figs. 3.4 and 3.5. These signals are obtained when the pump beam is blocked and the optical chopper modulates the THz beam. Changing the temporal delay between the THz and the probe pulses, the time domain of the THz electric field is scanned.

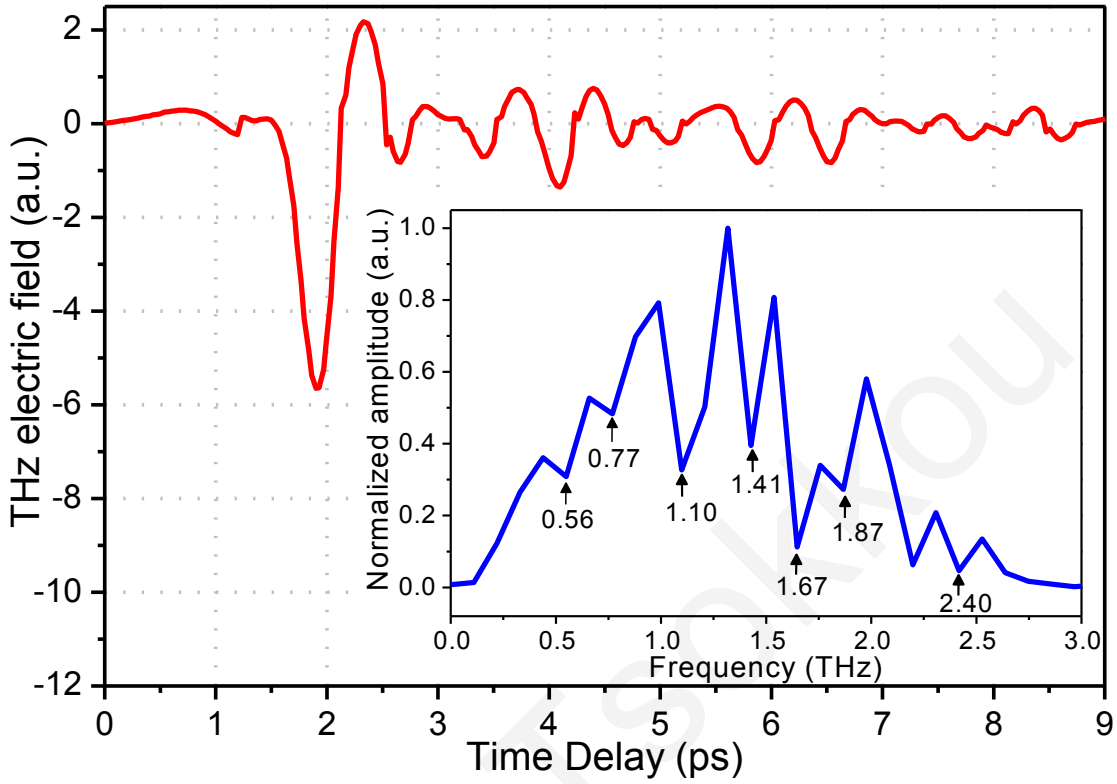

Figure 3.4. Typical THz electric waveform $E_{ref}(t)$ measured in the presence of atmosphere water. Pulses are generated in a 0.5 mm <110> ZnTe generator crystal via optical rectification and detected in another 0.5 mm <110> ZnTe detector crystal via free-space electro-optic sampling technique. Normalized frequency domain THz spectrum $E_{ref}(v)$ calculated by discrete fourier transform on the time domain THz signal is seen in the inset of the figure. The arrows denote the water absorption lines.

The THz electric field shown in the Fig. 3.4 is the measured signal taken in atmosphere, while the THz waveform seen in the Fig. 3.5 has been measured when the THz system was purged with nitrogen. Comparing the two signals, it is clearly evident that the presence of atmosphere water causes distortions on the THz pulse waveform and affects its maximum amplitude. The contribution of water absorption in the THz signal is confirmed in the resulted frequency domain signals shown in the inset of the Figs. 3.4 and 3.5 that are further discussed below. It is worth to be mentioned that the oscillatory tail in the time domain THz electric field in the absence of atmospheric water is a result of the probe beam dispersion into the non-linear detection crystal[123] and phase mismatching between the THz and probe beams.[124]

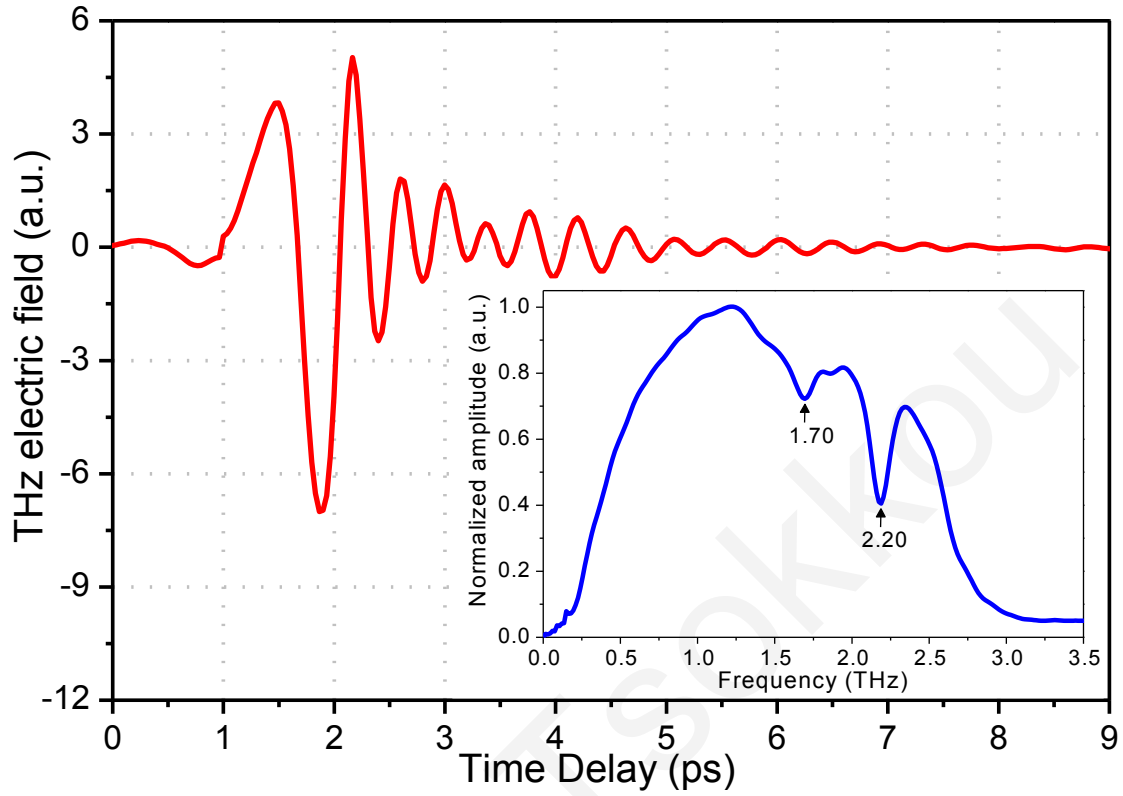

Figure 3.5. Typical THz electric waveform $E_{ref}(t)$ measured in the presence of nitrogen. In the inset of the figure, the normalized frequency domain THz spectrum $E_{ref}(v)$ is shown. It is seen that only the main absorption peak of water is still evident (1.70 THz), while the absorption peak at 2.20 THz is due to the polyethylene.

The measured temporal THz electric field consists of a set of discrete data points $E_n(t)$, therefore to obtain the frequency domain data $E_n(\omega)$, discrete Fourier transform has to be applied to the time domain data. This is defined as follows,

$$E_n(\omega) = \sum_{n=1}^{N} E_n(t) e^{-i\omega nt} \tag{3.6}$$

where N is the total number of data points in the time domain signal. The fourier transform yields the frequency spectrum of the complex electric field $E_n(\omega, \varphi)$, including the amplitude $E_n(\omega)$ and the phase $\varphi_n(\omega)$ ($E_n(\omega,\varphi) = E_n(\omega)e^{i\varphi(\omega)}$). Analysis of the time domain signal is achieved with the development of a simple analysis software using "FORTRAN".

Normalized frequency dependence of amplitude when performing a discrete fourier transform to the time domain THz signals of Figs 3.4 and 3.5, are shown in the insets of the Figs. 3.4 and 3.5, respectively. Strong absorption lines observed at frequencies 0.56 THz, 0.77 THz, 1.10 THz, 1.41 THz, 1.67 THz, 1.87 THz and 2.40 THz taken in ambient air are consistent to water vapor absorption lines in the THz region and agree with the values reported in literature.[125] These absorption lines are attributed to rotational transitions of water molecules and are denoted by arrows in the normalized frequency domain THz spectrum. This is expected when the THz pulse travels distances larger than few centimeters in atmosphere where humidity is present. In these experiments, the distance between the generation and detection crystals is over 1 m.

Here we should point out that two absorption peaks at 1.70 THz and 2.20 THz remain in the THz spectrum, when the system is purged with nitrogen, which can be seen in the inset of the Fig. 3.5. The peak at the lower frequency is one of the main water absorption peaks and is attributed to residual atmospheric water in the metallic box. The second peak at 2.20 THz is an absorption line of the high density polyethylene, which is placed twice in the pathway of the THz beam to block the optical and UV beams, due to lattice translational mode of polyethylene.[126] The amplitude shows that the pulse frequency spectrum content is centered around 1.2 THz and the signal does not diminish for frequencies up to 3 THz. From these measurements, it is obvious that atmosphere water must be eliminated from the system in order to minimize its contribution into the signal for further measurements to be taken.

To assure that reliable results are obtained when discrete fourier transform is performed in THz electric field waveform, it is important that a small step Δx in the movement of the translation stage is chosen. For a selected step there is an upper frequency of the spectrum that can be detected called Nyquist frequency and is defined as: $\nu_f = 1/2\Delta t$, where $\Delta t = 2\Delta x/c$. This characteristic frequency has to be larger than the expected THz bandwidth. Otherwise, any signal present at higher frequencies than Nyquist frequency will be "aliased" to lower frequencies, meaning that the signal obtained for frequencies larger than ν_f will be shifted at frequencies below ν_f . Using a step of Δx = 5 μm, which is the case of the spectrums shown above, frequencies up to 15 THz can be detected, which is sufficient for the bandwidth observed in our measurements.

Furthermore, the spectral resolution $\Delta\nu$ of the THz signal is determined by the total length of the time domain measurement. The following equation quantifies the spectral resolution, $\Delta\nu = 1/N\Delta t$, where N is the total number of data points and Δt (= $2\Delta x/c$) the time step. For the rest of measurements, the experiments were carried out with a step of $\Delta x = 2\ \mu m$, that corresponds to a time step of 13.3 fs.

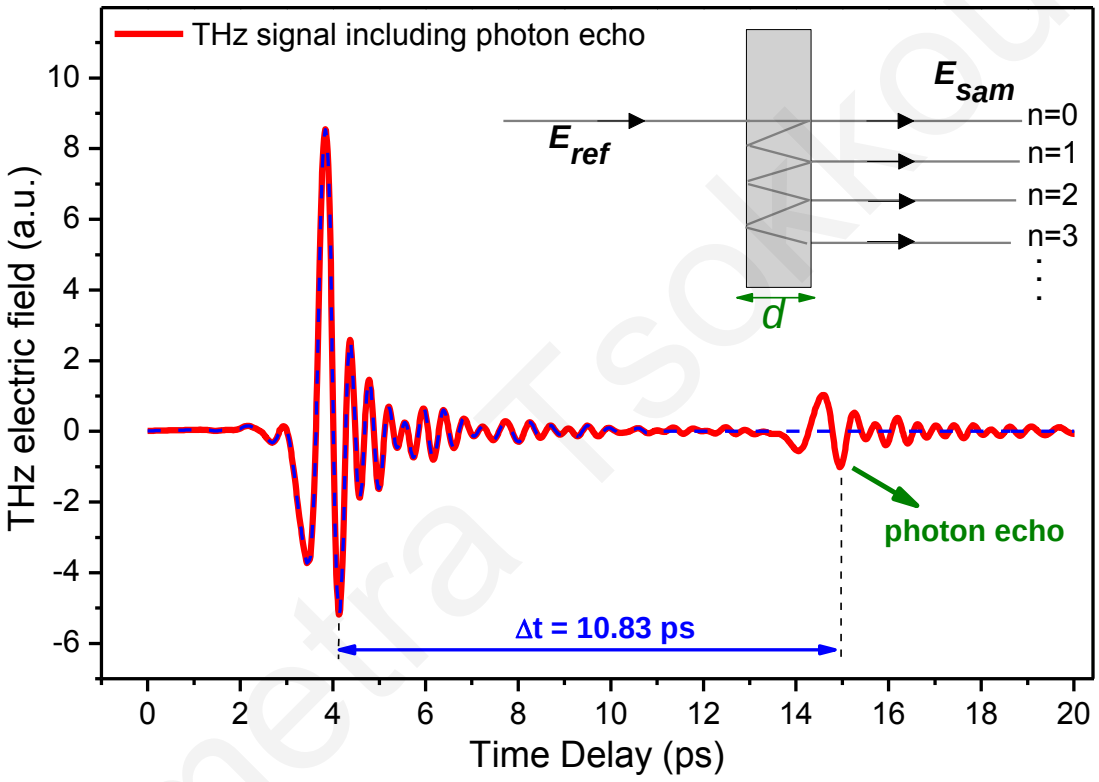

Figure 3.6. Reference THz electric waveform $E_{ref}(t)$ measured in the presence of nitrogen for times up to 20 ps. Photon echo due to internal reflections of the THz beam in the ZnTe generation crystal is also observed at larger times. In the inset of the figure, a scheme of internal reflections of the THz beam in the crystal is shown.

In Fig. 3.6, a measurement of the THz electric field waveform for times up to 20 ps is shown. It is observed that in addition to the main part of the pulse detected at early times, a second THz pulse is detected at times about $t \approx 15$ ps. This is caused by the reflections of the THz pulse in the ZnTe generator crystal back and front surfaces and is referred as photon echo of the pulse. Multiple reflections are expected in this kind of experiments, since the THz

wavelength is comparable to the crystal size. The second pulse is much weaker and has almost an identical shape with the main pulse. The photon echo recorded corresponds to the first reflection of the signal into the crystal with n = 1, as it is shown in the inset of Fig. 3.6. Given the refractive index of ZnTe and the time difference between the two pulses Δt, $(\Delta x = c\ \Delta t / 2n)$, the thickness of the crystal can be estimated. In Fig. 3.6, the two signals have a time difference of Δt = 10.83 ps, corresponding to a thickness equal to d = 0.5 mm, which agree very well with the manufactured specifications of the crystal.

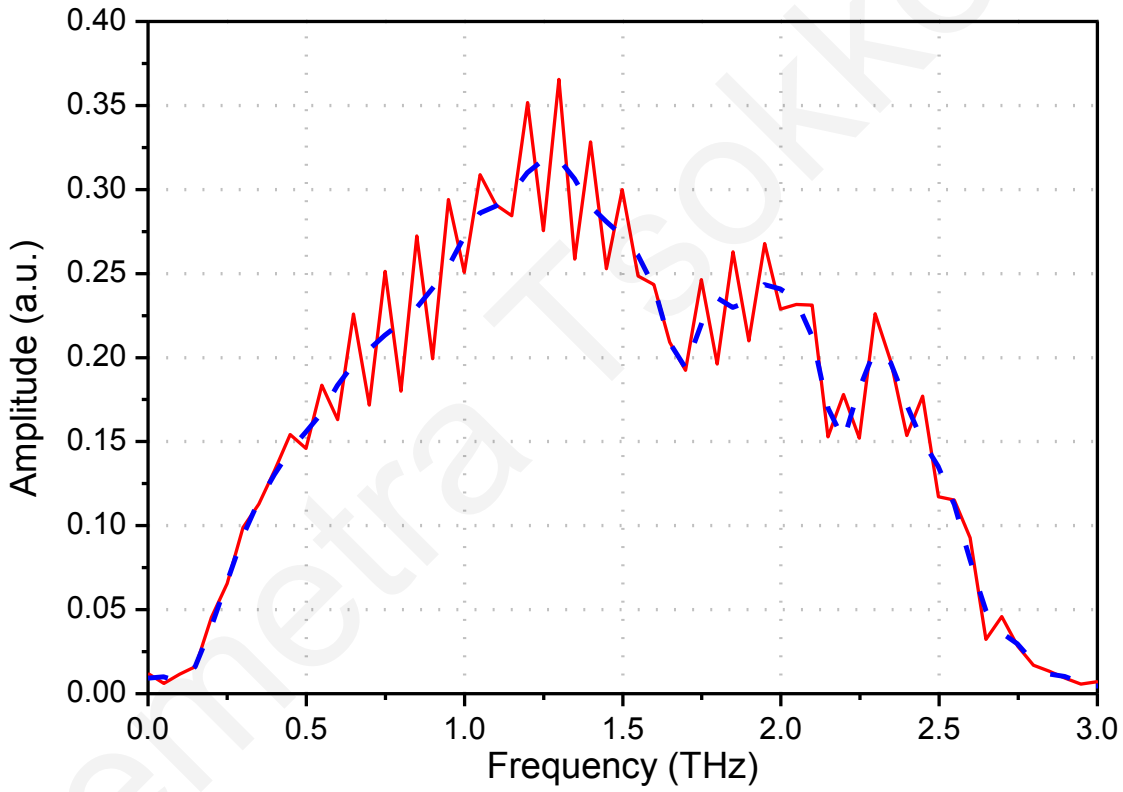

Figure 3.7. Frequency-dependent THz amplitude $E_{sam}(v)$ measured without sample in the presence of nitrogen including the photon echo (red line) and b) when photon echo signal is ignored (blue line).

The amplitudes of the THz signal with and without the photo echo signal are shown in the Fig. 3.7, with red solid and blue dashed line, respectively. Clearly the amplitude signal, when photo echo is included, is distorted and periodic oscillations are apparent. These structures disappear when the data points in the temporal THz signal, due to photon echo are padded to zero. This is acceptable because no significant contribution of the main part of the

THz pulse is expected at those times. For very thin crystals (d < 0.1 mm) a more careful manipulation of the data has to be done, since the signal of the multiple reflections will overlap with the main part of the pulse.

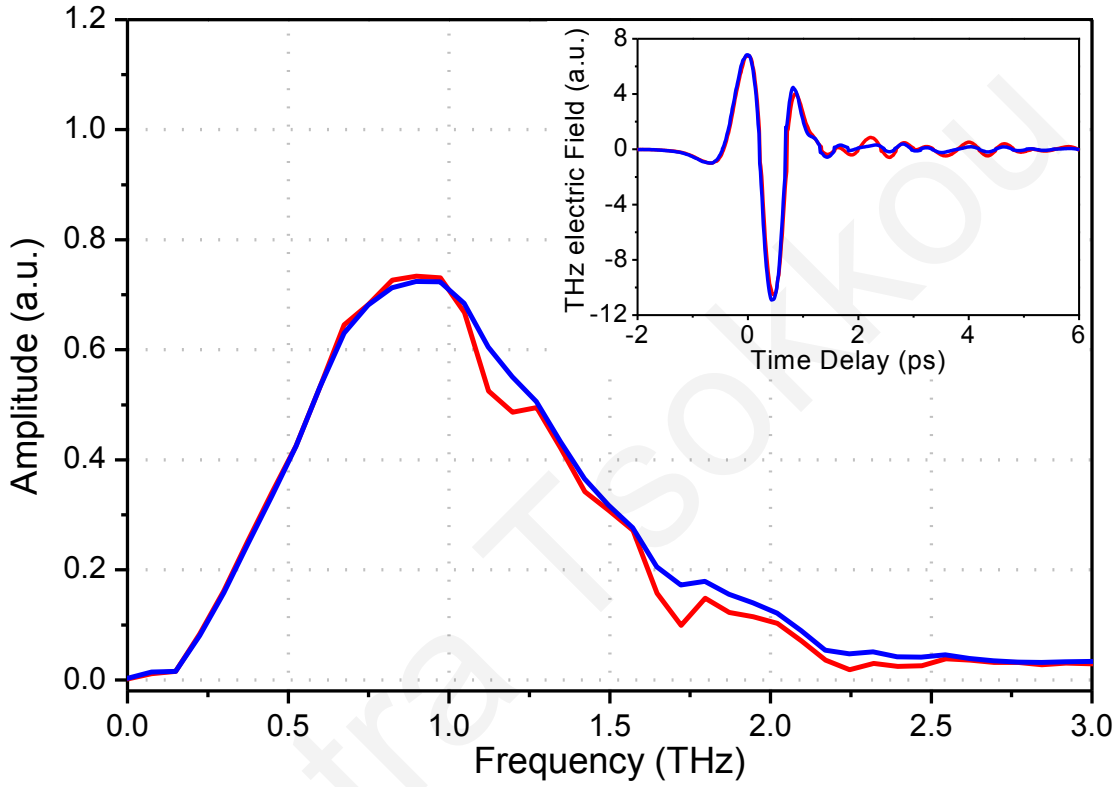

Figure 3.8. Amplitude of THz reference pulse after purging the metallic box with nitrogen for (a) 20 min (red line) and (b) 40 min (blue line) using the nitrogen generation system. In the inset of the figure, the time domain data of the THz electric field are shown.

To improve the THz signal and reduce further the influence of atmosphere water, a nitrogen gas generation system was used to provide a continuous flow of nitrogen into the metallic box. For the experimental data shown previously, the system was purged by using a dry nitrogen pressured gas bottle. Two spectrums of the reference THz signal taken at 20 min and 40 min after the introduction of nitrogen from the gas generation system, are shown in the Fig. 3.8. It is observed that in the signal taken at 20 min, the main absorption peaks of water at 1.10 THz and 1.70 THz are still evident. However, the water absorption peaks are almost eliminated when the nitrogen runs into the system for 40 min. In addition, for these

experiments the polyethylene films were replaced by thinner ones, so the absorption line at 2.2 THz becomes weaker. The small changes in the frequency spectrum shape as can be seen when comparing with Figs. 3.8 and 3.5, and their corresponding time domain data, are due to realignment of the experimental arrangement. A higher peak of the THz peak is achieved at the second case, as seen in the inset of the Fig. 3.8, but some of the higher frequencies are not detected. We believe that since the higher frequencies travel at the center of the THz beam, in accordance with Gaussian beam propagation, some losses are observed through the holes in the off-axis parabolic mirrors.

3.2.2 Calculation of Intrinsic Complex Optical Constants in Bulk Materials

Time domain THz spectroscopy (TDTS) is a method used to obtain the equilibrium properties of a sample and investigate its complex optical constants in THz region. This is possible since the THz pulse electric field is measured and not just its intensity. In this section, the mathematical analysis used for the calculation of complex optical constants, the real refractive index $n(\omega)$ and the absorption coefficient $a(\omega)$ for bulk materials, is developed.

In this method, two different measurements are required. For all measurements, the pump beam is blocked to prevent sample photo-excitation and the THz beam is chopped, in order to scan the THz electric field. Initially, a reference measurement of the THz electric field $E_{ref}(t)$ is taken. A second measurement is required, where the modified THz electric field transmitted through the sample $E_{sam}(t)$ is obtained.

For the frequency dependent spectrum, discrete Fourier transformation is performed on the time-domain to obtain the spectral amplitude $E(\omega)$ and phase component $\phi(\omega)$ of the THz electric field. The ratio between the frequency domain results obtained for both signals are necessary to interpret correctly the experimental data and to eliminate the influence the frequency response of the detector $D(\omega)$. According to equation 3.7, the ratio of complex spectra gives the transmission function of the sample $T(\omega)$.

$$T(\omega)=\frac{E_{sam}(\omega)\ e^{i\phi_{sam}(\omega)}D(\omega)}{E_{ref}(\omega)\ e^{i\phi_{ref}(\omega)}D(\omega)}=\frac{E_{sam}(\omega)\ e^{i\phi_{sam}(\omega)}}{E_{ref}(\omega)\ e^{i\phi_{ref}(\omega)}} \tag{3.7}$$

In the case of bulk materials, it is straightforward to calculate the frequency-dependent complex refractive index $\bar{n}(\omega)$ ($\bar{n}(\omega)=n(\omega)+ik(\omega)$), and subsequently absorption coefficient ($a(\omega)=\frac{2\pi}{\lambda_0}k(\omega)$). The transmitted reference electric field $E_{ref}(\omega)$ -empty sample holder- and the electric field after the propagation into the sample $E_{sam}(\omega)$ are determined by equations (3.8a) and (3.8b) respectively,

$$E_{ref}(\omega)=e^{\frac{i\omega d}{c}}E_0 \tag{3.8a}$$

$$E_{sam}(\omega)=t_{air-sam}t_{sam-air}e^{\frac{i\omega\,\bar{n}d}{c}}\sum_{k=0}^{\infty}\{r_{sam-air}^2\exp(2i\omega d\,\bar{n}/c)\}^k E_0 \tag{3.8b}$$

where d the sample thickness, $t_{ij}\left(=\frac{2\bar{n}_i}{\bar{n}_i+\bar{n}_j}\right)$ and $r_{ij}\left(=\frac{\bar{n}_i-\bar{n}_j}{\bar{n}_i+\bar{n}_j}\right)$ are the Fresnel transmission and reflection functions between i and j mediums, respectively.[127] Then, the transmission function for an air/film system is derived, according to equation 3.9.

$$T(\omega)=\frac{4\bar{n}}{(\bar{n}+1)^2}\exp\left(\frac{i\omega\,\bar{n}\,d}{c}\right)\sum_{k=0}^{m}\left[\frac{\bar{n}-1}{\bar{n}+1}\exp\left(\frac{i\omega\,\bar{n}\,d}{c}\right)\right]^{2k} \tag{3.9}$$

The equation 3.9 consists three terms and is valid for plane parallel samples. The first term describes the Fresnel losses at the front and back surfaces of the sample in the case of normal incidence. The second term describes the change in phase as the THz beam propagates across the sample. The last term describes the contribution of multiple reflections of the THz pulse in the sample, where m is the number of reflections taken into consideration. Neglecting absorption losses at the front and back surfaces of the sample, the complex refractive index in

the first term of the above equation is replaced by the real refractive index. However, in the case of thick films, signals from the main pulse and photon echoes are well separated in time and therefore the term of internal reflections is ignored (*m=0*). Then, the equations that describe the real part of refractive index and absorption coefficient take the simple form seen in equations 3.10a and 3.10b, respectively.

$$n(\omega) = \frac{c(\phi_{sam}(\omega) - \phi_{ref}(\omega))}{\omega\, d} + 1 \tag{3.10a}$$

$$\alpha(\omega) = -\frac{2}{d}\ln\left(\frac{E_{sam}(\omega)}{\mathrm{E}_{ref}(\omega)}\frac{(1+n)^2}{4n}\right) \tag{3.10b}$$

One can then derive the complex dielectric constant and conductivity. The frequency dependence of the complex dielectric constant $\varepsilon(\omega)$ ($= \varepsilon_1(\omega) + \varepsilon_2(\omega)$) is equal to the square of the complex refractive index ($\bar{n}_{NW}^2 = \varepsilon_{NW}$). Also, the dielectric constant is related to the complex conductivity as shown in equation 3.11,

$$\varepsilon(\omega) = \varepsilon_\infty + \frac{i\sigma(\omega)}{\omega\varepsilon_0} \tag{3.11}$$

where ε_∞ is the high frequency dielectric constant and ε_0 the permittivity of vacuum.

3.2.3 Calculation of Intrinsic Complex Conductivity in Nanowires

A different process has to be followed to calculate the complex intrinsic conductivity in the THz region, when considering thin samples. This is attributed to the fact that the THz signals from multiple reflections of the beam that originates from the sample surfaces are temporally overlapped. Given the thickness of the NW sample, the calculation of equilibrium

optical properties for the NWs is accomplished using the procedure followed in the case of thin films.[128,129]

Fig. 3.9 schematically shows the two measurements that needs to be carried out, firstly through the system air/substrate and then through the air/NWs/substrate. In the latter case, a two layer system has to be handled, since the NWs are placed onto a substrate. In this case, the reference measurement is the THz electric field that propagates through the air/substrate $E_{ref}(\omega)$. The refractive index of the substrate n_2 and its thickness d_2 are known. Then, the THz electric field through air/NWs/ substrate $E_{sam}(\omega)$ is measured. In this process an assumption is used, that the NWs form a thin film on the substrate with thickness d_1. Further, it is taken into account that the THz pulse incidents onto the sample at a normal incidence.

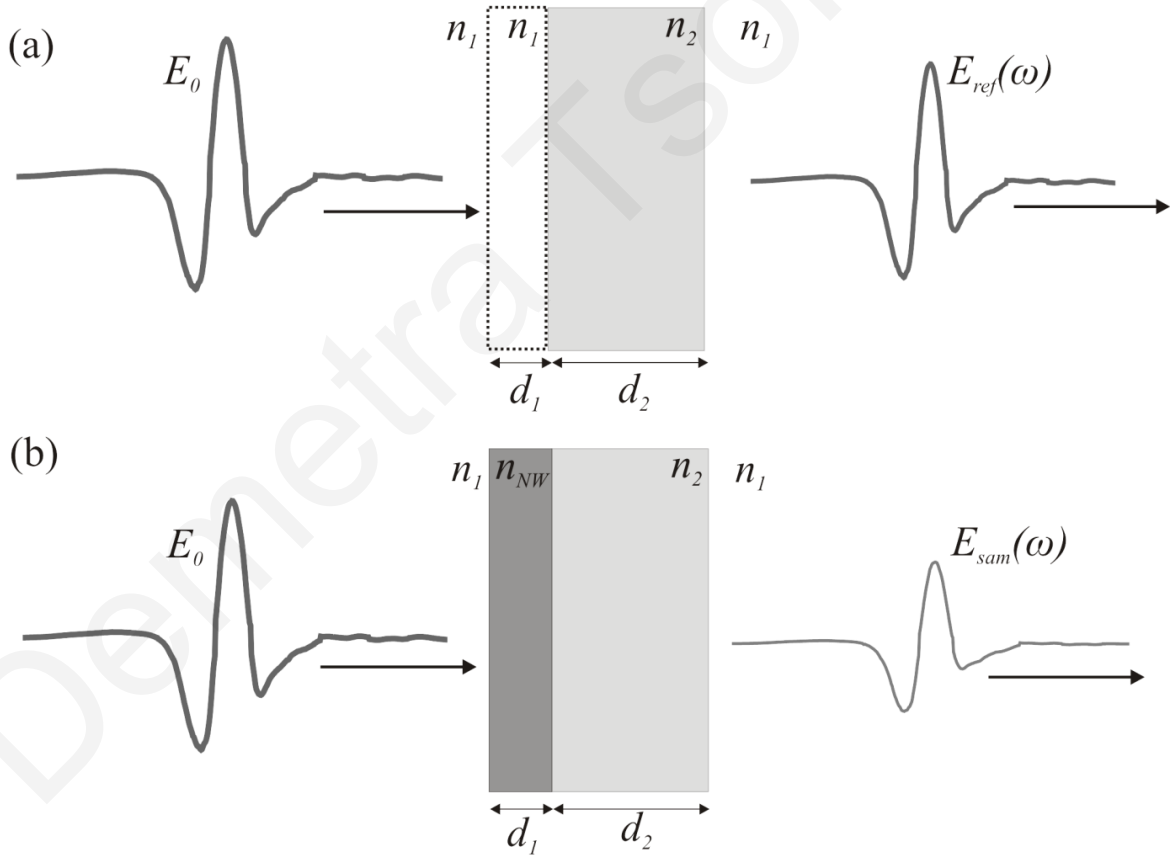

Figure 3.9. A schematic diagram of the method used for a time domain THz transmission measurement of the THz transmission signal through (a) a thick substrate (reference measurement) and (b) the NW thin film deposited on a thick substrate (sample measurement).

The complex refractive index of the NWs is $n_{NW} = n + ik$, where n is the real refractive index of NWs and k the extinction coefficient. The transmitted reference electric field $E_{ref}(\omega)$ and sample electric field $E_{sam}(\omega)$ are determined by equations 3.12a and 3.12b, respectively.

$$E_{ref}(\omega) = t_{12}t_{21}\, e^{\frac{i\omega(n_1 d_1 + n_2 d_2)}{c}} E_0 \tag{3.12a}$$

$$E_{sam}(\omega) = t_{1NW}t_{NW2}t_{21}\, e^{\frac{i\omega}{c}(n_{NW} d_1 + n_2 d_2)} \sum_{k=0}^{\infty} \{r_{NW2} r_{NW1} e^{2i\omega d_1 n_{NW}/c}\}^k E_0 \tag{3.12b}$$

Fabry-Perot term, due to multiple reflections of the THz field at the front and back surfaces of the substrate, is not included since the main part of the pulse and first echo are well temporally separated and no signal of the main THz pulse is expected at these times. On the other hand, Fabry-Perot term $\left(= \sum_{k=0}^{\infty} \{r_{NW2} r_{NW1} e^{2i\omega d_1 n_{NW}/c}\}^k \right)$ has to be considered in the case that THz pulse propagates through the NW film, since the small thickness of the layer ensures that signal from the main part of the pulse and the echoes are completely overlapped. In this case, the geometrical series is summed up to infinity. Taking the ratio between the sample and the substrate signal and using the approximation valid for thin films, $n\omega d/c << 1$, the transmission function $T(\omega)$ is calculated, as described by equation 3.13.

$$T(\omega) = \frac{E_{sam}(\omega)}{E_{ref}(\omega)} = \frac{E_s(\omega)\phi_s(\omega)}{E_r(\omega)\phi_r(\omega)} = 1 + \frac{i\omega d_1}{c(1+n_2)}(n_{NW}^2 - 1) \tag{3.13}$$

Using that the frequency dependence of complex dielectric constant $\varepsilon(\omega)$ $(\varepsilon(\omega) = \varepsilon_1(\omega) + \varepsilon_2(\omega))$ is equal to the square of the complex refractive index ($n_{NW}^2 = \varepsilon_{NW}$), the real and imaginary parts of the dielectric constant are given by the following equations 3.14a and 3.14b, respectively.

$$\varepsilon_1(\omega) = \frac{c}{\omega d_1}\frac{E_s}{E_r}(1+n_2)\sin(\phi_s - \phi_r) + 1 \quad (3.14a)$$

$$\varepsilon_2(\omega) = \frac{c}{\omega d_1}\frac{E_s}{E_r}(1+n_2)(\cos(\phi_s - \phi_r) + 1) \quad (3.14b)$$

Then, the refractive index *n(ω)* and extinction coefficient *k(ω)* are found as described in equations 3.15a and 3.15b, respectively.

$$n(\omega) = \frac{1}{\sqrt{2}}(\varepsilon_1(\omega) + (\varepsilon_1^2(\omega) + \varepsilon_2^2(\omega))^{1/2})^{1/2} \quad (3.15a)$$

$$k(\omega) = \frac{1}{\sqrt{2}}(-\varepsilon_1(\omega) + (\varepsilon_1^2(\omega) + \varepsilon_2^2(\omega))^{1/2})^{1/2} \quad (3.15b)$$

Further, the complex conductivity is calculated by using the equation 3.11, shown in the previous section.

3.2.4 Model for Conductivity Interpretation – Drude-Smith Model

It is well known that conductivity of semiconductors is determined by the number of carriers in the conduction band and their mobility. For the interpretation of the derived complex conductivity data, several models have been used to determine the scattering time and the mobility of carriers.

The most common approach for electron transport is the *Drude model*, a classical model that explains the behavior of free carriers in semiconductors.[130] In the Drude model, electrons are considered free to move into the lattice, meaning that their wavefunction is delocalized and are elastically scattered with the positive ionic cores. Scattering effects are considered to randomize the momentum of charge carriers. This model has been extensively applied to investigate the behavior of free carriers in bulk semiconducting systems. In a

material with a Drude model response, the real part of conductivity $\left(\sigma_1 = \frac{\sigma_{DC}}{1+\omega^2\tau^2}\right)$ is expected to show a maximum at $\omega=0$ that decreases monotonically for larger frequencies, whereas the imaginary part $\left(\sigma_2 = \frac{\sigma_{DC}\omega\tau}{1+\omega^2\tau^2}\right)$ is positive and shows a maximum at $\omega = \tau^{-1}$.

In several situations, and especially in the case of nanostructures, Drude model cannot explain the behavior of electrons, since they cannot be considered as completely free. Thus modifications have to be taken into consideration to improve the fitting. Therefore, additional parameters are included to the conventional model which describes *semi-free carriers*. The model usually used was proposed by Smith,[131] to explain localization of carriers in nanomaterials. This model incorporates additional terms, which includes non-randomization of the carrier momentum after a collision. Therefore, an assumption is made that an electron has a memory of velocity from previous collisions. Then, the probability that an electron will experience 'n' collisions in a time interval [0, t] is described by Poisson distribution, as given by equation 3.16,

$$p_n(t) = \left(\frac{t}{\tau}\right)^n \frac{\exp\left(-\frac{t}{\tau}\right)}{n!} \tag{3.16}$$

where τ is the average time between successive collisions. The current density $j(t)$ is given by equation 3.17.

$$j(t) = j(0)\exp(-t/\tau)\left[1+\sum_{n=0}^{\infty} c_n\left(\frac{t}{\tau}\right)^n / n!\right] \tag{3.17}$$

Since the complex conductivity $\sigma(\omega)$ is the Fourier transform of the current density $\left(\sigma(\omega) = \int_0^{\infty} j(t)e^{i\omega t}dt\right)$, conductivity yields to obey the relation 3.18,

$$\sigma(\omega) = \frac{\sigma_0}{1 - i\omega\tau}\left[1 + \sum_{n=1}^{\infty} \frac{c_n}{(1 - i\omega\tau)^n}\right] \tag{3.18}$$

where c_n is named *persistence of velocity* and represents the fraction of the initial velocity retained after n collisions. In practice, only the term n = 1 is considered, as had been suggested by Smith. This means that only the last collision influences the velocity after a collision.

Value of persistence of velocity can vary between 0 and -1, giving different responses to the observed real and imaginary parts of conductivity as seen in Fig. 3.10. In the case that c_1 = 0, Drude model is recovered. Further, it is observed that as c_1 increases a suppression of real part of conductivity is observed. For $c_n > -0.5$, the real part of conductivity suppresses, since lower values are observed at low frequencies that increases for higher frequencies. On the other hand, the imaginary part of conductivity is negative for low frequencies and becomes positive for higher frequencies. Negative imaginary conductivity is associated with backscattering of carriers after a collision, which prohibits the long range carrier transport.

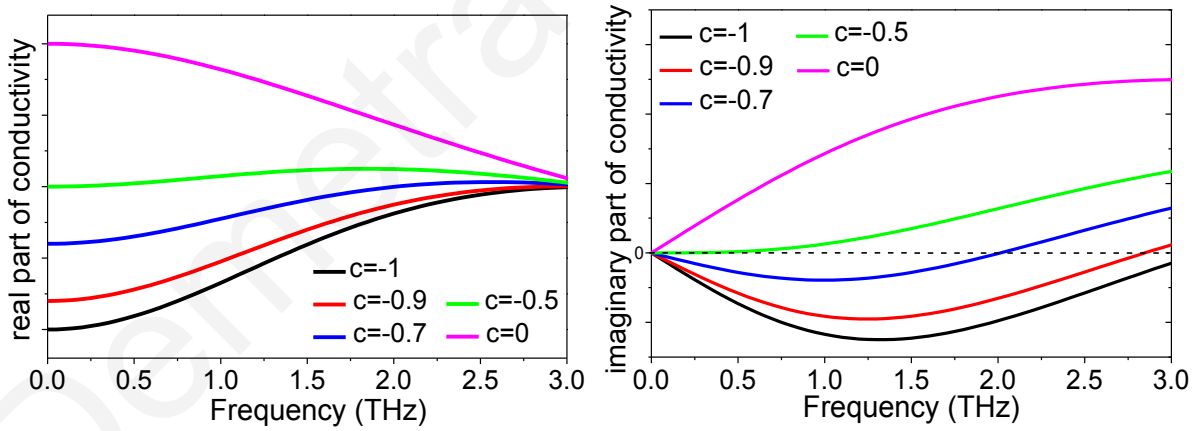

Figure 3.10. (a) Real and (b) imaginary parts of conductivity following the Drude-Smith model for different values of the persistence of velocity between 0 and -1, using a specific scattering time equal to 50 fs.

3.3 Analysis of Time Resolved Terahertz Transmission Spectroscopy Measurements

When TRTS measurements are taken to calculate the photoconductivity spectrum of the semiconducting NWs in the THz region, a different model has to be applied than that used usually for the case of thin films. In what follows, the process for obtaining the photoconductivity in NWs is described.

3.3.1 Calculation of Photoinduced Complex Conductivity in Nanowires

For photoconductivity measurements to be performed, two different measurements have to be taken. Initially, the modified THz electric field as propagated through an unexcited NWs/substrate sample is needed. For this measurement the pump beam is blocked and the chopper modulates the THz beam. Then, the pump beam is used to photoexcite the sample and the changes induced to the THz electric field have to be detected. For that, the chopper is placed to modulate the pump beam.

Since the investigated layer is a mixture (composite) of air and NWs, the filling factor f_s, defined as the volume covered with NWs, is introduced to get a more reliable equation to calculate the photoconductivity in NWs. This procedure has been similarly applied in the case of extracting photoconductivity in GaAs NWs, although in this process the contribution of quartz substrate was ignored.[112] The ratio between the measured difference THz electric field ΔE in the presence and absence of pump beam and the THz electric field through the unexcited sample E is defined as,

$$\frac{\Delta \mathrm{E}}{\mathrm{E}} = \frac{f_s(E_S^* - E_S)}{f_s E_S + (1 - f_s)E_{air}} \tag{3.19}$$

where $E_{S^*(S)}$ is the THz electric field after transmission through the photoexcited (non-excited) sample/substrate and E_{air} is the THz electric field taken in air. By rearranging the equation shown above, it can be written in the form 3.20.

$$\frac{\mathrm{E}_S^*}{\mathrm{E}_S} = \frac{\Delta E}{E}\left(1+\frac{(1-f_s)}{f_s}\frac{E_{air}}{E_S}\right)+1 \tag{3.20}$$

It is revealed that one has to calculate the ratio E_S^*/E_S. The term E_{air}/E_S can be defined by the transmission Fresnel constants using the refractive index of NWs in the THz region that are determined from the time domain THz spectroscopy measurements.

To develop a model that calculates the optical properties, a system consisted of air/NWs/quartz substrate is considered. The modifications in the electric field due to the propagation of the THz pulse into the unexcited and excited sample is defined as described by equations 3.19a and 3.19b respectively,

$$E_S = t_{air-NW}\ t_{NW-s}t_{s-air}e^{i\omega d\ n_1/c}e^{i\omega d_2 n_2/c}E_0\sum_{k=0}^{\infty}\{r_{NW-s}r_{NW-air}e^{2i\omega d_1 n_1/c}\}^k \tag{3.21a}$$

$$E_S^* = t_{air-NW^*}\ t_{NW^*-s}t_{s-air}e^{i\omega d\ n_{NW}^*/c}e^{i\omega d_2 n_2/c}E_0\sum_{k=0}^{\infty}\{r_{NW^*-s}r_{NW^*-air}e^{2i\omega d_1 n_{NW}^*/c}\}^k \tag{3.21b}$$

where (*) presents the photoexcited state, $d_{1(2)}$ is the thickness of NW layer (substrate), $n_{1(2)}$ is the refractive index of the NWs (substrate), respectively. The last term presents the Fabry-Perot term, due to multiple reflections of the beam into the sample. By substituting the Fresnel coefficients and rearranging the terms of the above equation, it can be written in the following form,

$$\frac{E_S^*}{E_S} = \frac{n_1^*\left(\ (n_2+n_1)(n_1+1)-(n_1-n_2)(n_1-1)\ e^{2i\omega\ n_1 d_1/c}\ \right)}{n_1\left(\ (n_2+n_1^*)(n_1^*+1)-(n_1^*-n_2)(n_1^*-1)\ e^{2i\omega\ n_1 d_1/c}\ \right)} \tag{3.22}$$

The sample thickness is on the order of nm, therefore it is reasonable to use the approximation for the thin film limit ($n\omega d_1/c << 1$). Thus, the exponential can be written in the form $e^{i\omega d_1 n_1/c} \approx 1 + i\omega d_1 n_1 / c$. Then, the ratio E_S^* / E_S can take the simple form described by equation 3.23.

$$\frac{E_S^*}{E_S} = \frac{1 + n_2 - (n_1^2 + n_2) i\omega d_1 / c}{1 + n_2 - (n_1^{*2} + n_2) i\omega d_1 / c} \tag{3.23}$$

By rearranging the terms in the above equation, the complex refractive index of the photogenerated NWs can be derived, that it give access to the complex refractive index and the complex photoconductivity. In this case, the complex conductivity is given by the equation 3.24,

$$\sigma = \omega\varepsilon_0 \left(i(\varepsilon_\infty + n_2) + \frac{c}{\omega\, d_1 \dfrac{E_S^*}{E_S}} \left(1 - \frac{E_S^*}{E_S}\right)(1 + n_2) - i \frac{n_1^2 + n_2}{\dfrac{E_S^*}{E_S}} \right) \tag{3.24}$$

where ε_0 is the permittivity of free space and ε_∞ the high frequency dielectric constant of the investigated material.

Chapter 4

Carrier dynamics in GaN Nanowires

This Chapter is devoted to the study of the carrier dynamics in GaN NWs. Initially, an overview of the strategies followed for the growth of these NWs is introduced. The optimum experimental conditions for the synthesis of GaN NWs using APCVD method via nitridation of metal Ga at elevated temperatures are given. Experimental results revealed that GaN NWs growth is a catalyst assisted process. The results of the characterization of these NWs via SEM and XRD methods are also presented.

In the main part of this Chapter, the experimental results obtained from the time resolved absorption spectroscopy experiments for GaN NWs are presented and discussed. For these NWs, carrier dynamics have been investigated using ultrashort excitation pulses with photon energies corresponding to energy levels above and below the energy band gap of GaN. Measurements were performed for several probing wavelengths from the UV to the IR spectral region. Time resolved absorption change measurements reveal a large number of defect states located within the band gap. These transient measurements also reveal the location of the *U* valley within the energy diagram of the GaN NW system. Intensity measurements of transient absorption for different probing wavelengths are also presented. The results reveal that Auger recombination is important for carriers located in defect states. We should point out that the relaxation of carriers from shallow donor states and midgap states in GaN NWs has been resolved and carrier relaxation times from these states have been estimated. A band diagram for GaN NWs has been suggested for GaN NWs based on our experimental results.

4.1 Synthesis of GaN Nanowires

In the following pages, a brief introduction on the synthesis of GaN NWs via CVD reported by different groups is given. Following that, analysis of the experimental results of the optimum growth conditions and the characterization of GaN NWs will be presented.

4.1.1 Overview for GaN Nanowires

The fundamental properties of GaN and their intriguing modifications expected to be observed at the nanometer scale have attracted a great deal of attention on the synthesis and optimization of GaN NWs. The first reports for GaN NWs growth have been with carbon nanotubes or porous alumina membrane acting as a template, thus spatially confining the NW growth.[132,133] In 1997, Han *et al.* have synthesized GaN NWs using carbon nanotubes through a gas reaction of Ga_2O with flowing ammonia (NH_3) at 1173 ^oC. Two years later, Cheng *et al.* used the same source materials to fabricate GaN NWs in porous alumina membrane. Since then, GaN NWs have been synthesized with several diverse methods, such as CVD,[22] metalorganic CVD,[134] molecular beam epitaxy,[135] but also via the arc discharge method,[136] pyrolysis[137] and pulsed laser ablation.[138]

The most challenging and frequently used synthesis method is CVD. The first fabrication of GaN NWs with this method was reported by Tang *et al.*, in 2000.[139] In this process, a mixture of Ga, SiO_2 and Fe_2O_3 was used as a source material. At high temperature, (T = 950 ^oC), Ga reacts with SiO_2 to form Ga_2O that subsequently reacts with NH_3 to form GaN NWs. In this process, iron (Fe) acts as a catalyst and the growth is achieved via the VLS mechanism. In the following years, various parameters that affect the GaN NWs growth via CVD and their characteristics have been studied. Such parameters are the growth temperature, the starting material, the gas flow and the catalyst choice.

The most usual choice for source materials is the metal gallium (Ga), [22,139–141] although Ga_2O_3 film[142] and mixtures of Ga/GaN powder[143] have also been reported. A common issue when using these precursors is that the synthesis of GaN NWs is achieved at temperatures

higher than 900 ^{o}C. This is attributed to the reduced vapor pressure of Ga at lower temperatures.[144] Additionally, several studies note that the synthesis of GaN NWs is achieved only for a narrow range of temperatures. Different ways to decrease the growth temperature have been suggested. Chang and Wu used gallium acetylacetonate as a source material.[144] This compound starts to vaporize at a temperature between 130-185 ^{o}C and then it reacts in vapor phase with NH_3 to form GaN. In this case, the GaN NWs grow via a catalyst assisted process. More recently, Yu *et al.* have used a mixture of Ga and calcium fluoride (CaF_2), to synthesize GaN NWs at 650 ^{o}C on a Ni-coated Si substrate.[145] CaF_2 is an inert salt with a high melting point (1360 ^{o}C) and therefore does not chemically react with NH_3. However, it acts as a dispersant. It is known that the vapour pressure of a material at a specific temperature depends also on the droplet size. Therefore, when metal Ga is dispersed to CaF_2, smaller Ga droplets are formed, the vapor pressure of the metal increases and the NW formation is observed at a lower temperature.

In most cases, synthesis of GaN NWs is achieved via the VLS mechanism. A plethora of metals have been successfully used as catalysts.[22] Transition metals such as Fe,[22] indium (In),[22,146] cobalt (Co)[22] and especially nickel (Ni)[140, 144,145] are suitable. However, controversial studies exist when Au is used. Zhang and Zhang have reported that Au is inappropriate for the synthesis of GaN NWs.[141] They assumed that responsible for this is the low solubility of nitrogen in Au nanoparticles. Few years later, Cai *et al.* have synthesized GaN NWs in high yield using direct nitridation of Ga with NH_3 at 950 ^{o}C on an Au-coated Si substrate.[140] After that, several groups have used this metal for the growth of GaN NWs.[147,148]

There is a drawback when using transition metals as catalysts for GaN NWs. Transition metals have a low defect formation energy that result in the contamination of metallic elements into the NW. A computational study has reported that for the formation energy of Ni substitution is ~ 1.2 eV in GaN, whereas Au substitution requires higher defect formation energy ~ 4 eV.[149] This significantly affects the optical and electronic properties of the resulted NWs, since defects can form several energy states below the band gap that act as trap states and affect the performance of the material into the electronic devices.

4.1.2 Optimum Growth Conditions

Taking into account the experimental conditions followed by different groups for the GaN NW growth, a sequence of experiments was carried out with the main objective been a high yield of GaN NWs with desirable characteristics. Experimental conditions were carefully adjusted in different growth experiments, including growth temperature, ramp rate, use of catalyst and flow rates of gases until a high yield of straight GaN NWs was obtained.

Considering the experimental results on the synthesis of GaN NWs, the optimum conditions for growth of GaN NWs were derived and are referred in detail below. A table (Table 4.1) is also shown that summarize the growth conditions of GaN NWs. For our optical experiments, straight GaN NWs were used.

Step	Name	Gas flow (sccm)	Temperature (^oC)	Duration (min)
1	**System Purging**	500 Ar	25	10
2	**Rise of Temperature**	100 Ar	25 → 950	61
3	**Growth Process**	75 Ar, 25NH_3	950	60
4	**System Cooling**	75 Ar 25NH_3	950 → 25	60

Table 4.1. Summary of growth conditions for GaN NWs using APCVD.

GaN NWs were grown, initially, on *n* type Si (111) and then on sapphire (Al_2O_3) and quartz (SiO_2) via APCVD through direct nitridation of metal Ga with NH_3. Initially, a thin film of Au with thickness of ≈ 0.5 nm was deposited on Si (111) or Al_2O_3 via sputtering at a slow rate 5 Å/ s using an Ar ion plasma under a pressure $10^{-4} mBar$. Before the deposition of Au film, the substrates were cleaned in hydrogen fluoride (HF), rinsed in ionized water and dried with nitrogen. The Au-coated substrate was placed in an alumina boat and then 0.3 g of

pure metal Ga (Aldrich 99.99%) was carefully positioned in the boat ≤ 5 mm upstream from the sample.

The boat was then loaded at the center of the 25 mm quartz tube directly above the thermocouple used to measure the heater temperature. Initially, the tube was flushed with 500 sccm of Ar and 500 sccm of N_2/5% H_2, for 10 min in order to eliminate residual oxygen and moisture contained in the reactor. Afterwards, the temperature of the furnace was increased to 950 °C with a ramp rate of 15 ^{o}C/min, under a steady flow of 100 sccm of N_2:5%H_2. Subsequently, the temperature was maintained at 950 °C for 1 h and NH_3 was allowed to flow at 25 sccm using a reduced flow of 75 sccm of N_2:5%H_2. At the end of the growth period, the reactor was allowed to cool down to room temperature in flows of 25 sccm of NH_3 and 75 sccm of N_2:5%H_2 for 1h. Upon removal from the reactor the Si or Al_2O_3 substrates were covered with a white-blue colored layer.

Based on the above experimental results, growth of GaN NWs is critically dependent on the vapour pressure of the Ga that depends not only on the temperature, but also by the flow rate of NH_3 since it affects the evaporation rate of Ga during the process. In agreement with previous investigations on GaN NWs, high growth temperatures ≥ 900 °C are necessary for the growth of GaN NWs by direct nitridation of metal Ga with NH_3. NWs were also obtained at 900 °C, but their density was higher at 950 °C. We also found that the addition of H_2 to the gas flow, during the temperature ramp and growth step, is crucial to prevent the oxidation of Ga from residual O_2 in the reactor. In addition, when NH_3 was included during the temperature ramp, it leads to the nitridation of the Ga upstream, which in turn reduced the Ga vapor pressure at the growth temperature.

No GaN NWs were obtained on silicon or sapphire alone confirming that the GaN NWs is a catalyst assisted process. VLS mechanism is usually referred as the responsible mechanism for the synthesis of GaN NWs, although modifications to this model have been also proposed when Au is used as a catalyst. Kuo *et al.* proposed that an Au-Ga alloy is formed, instead of an Au-Ga-N alloy, due to the low solubility of N into the Au.[148] They suggest that the reaction between Ga and N occurs at the liquid/solid interface between Au:Ga droplet and the GaN. Recently, Zervos and Othonos suggested that when H_2 gas was used during the growth process, the hydrogen not only eliminates oxygen from the Ga droplet surface and increase vapor pressure of Ga to promote the GaN NWs growth, but also reacts

with Ga to form GaH_2, which has low formation energy and is a gas at the growth temperature.[150] Due to this the formation of an amorphous GaN layer is avoided onto the substrate.

4.1.3 Characterization of GaN Nanowires

Following the synthesis of GaN NWs, SEM and XRD measurements were performed and the results are shown below.

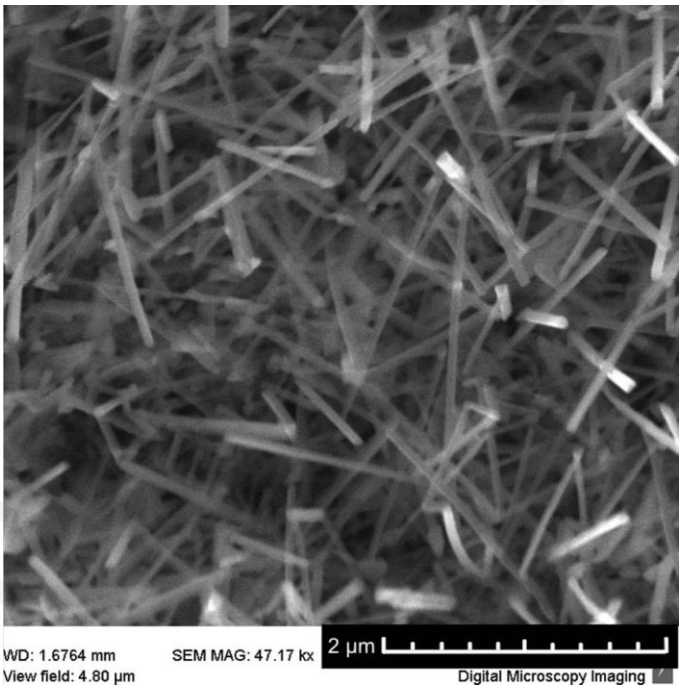

Figure 4.1. SEM image of the GaN NWs on Au/Al_2O_3 substrate.

Typical SEM images of the high density GaN NWs grown on 0.5 nm Au/Al_2O_3 are shown in Figs. 4.1 and 4.2. From SEM image shown in the Fig 4.1, the diameter and the length of GaN NWs are evident. Straight wires with uniform diameters of 100 nm and lengths up to a few

microns are observed. A second SEM image (Fig. 4.2) reveals the dense and uniform coverage on the substrate.

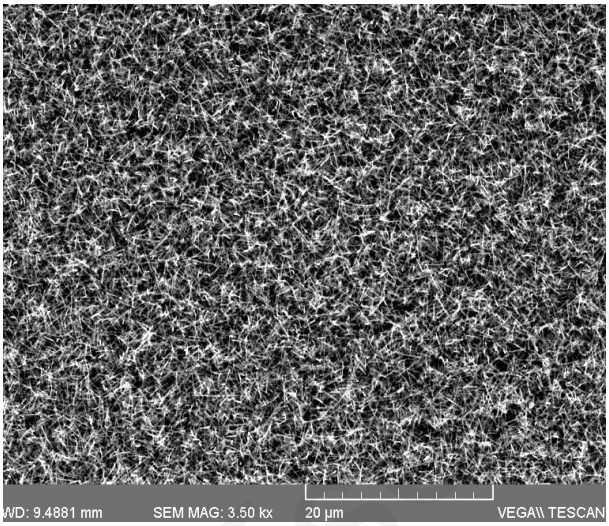

Figure 4.2. SEM image of the GaN NWs on Au/Al_2O_3 substrate.

Fig. 4.3 shows the XRD pattern of the GaN NWs grown on sapphire where the peaks correspond to the (100), (002), (101), (110), and (112) crystallographic planes of the hexagonal wurtzite structure of GaN with lattice constants a = 0.318 nm and c = 0.518 nm.[139] No diffraction peaks of other phases or other materials, such as Ga_2O_3 or elements, such as Ga were identified.

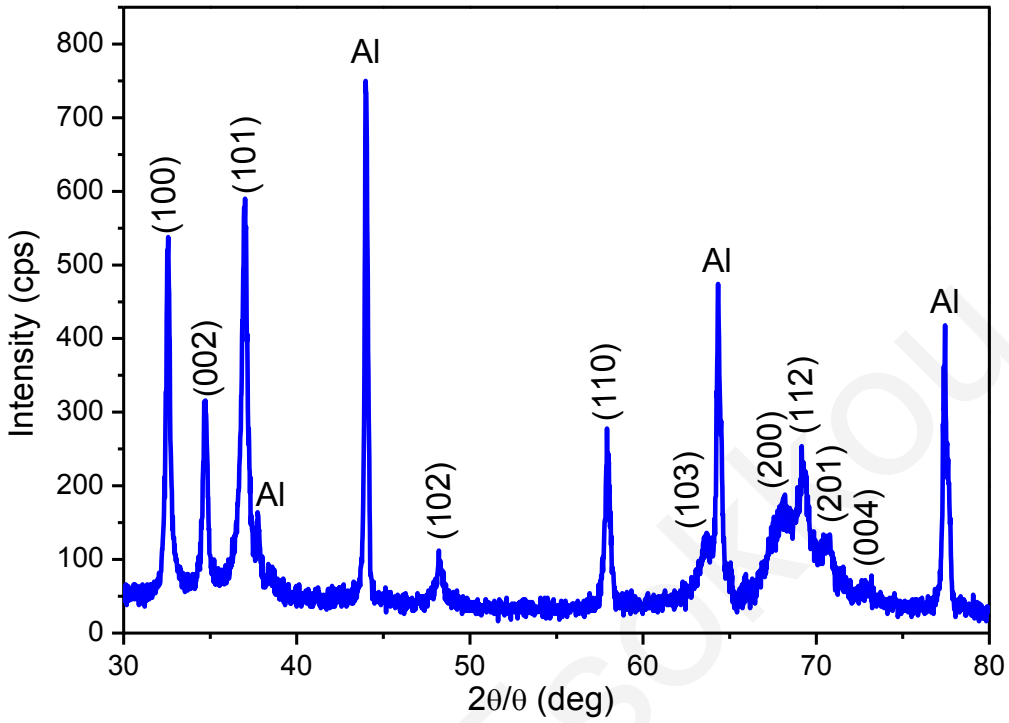

Figure 4.3. XRD pattern of GaN NWs on sapphire. The peaks shown are attributed to crystallographic planes of GaN NWs, except those that originate from the sample holder and are identified in the pattern.

4.2 Carrier Dynamics in GaN Nanowires

In bulk GaN, point and structural defects have a crucial role in the optical properties and carriers relaxation. For example, photoluminescence spectrum exhibits usually a broad yellow band, which suppresses the band edge emission in the UV region. The origin of the yellow luminescence has been extensively investigated by several groups and is believed that it originates from shallow donor or conduction band states to deep acceptor states.[151–155] Given the potential impact that GaN NWs may have in optoelectronic applications, it is of great importance to understand not only the fundamental behaviour of photogenerated carriers upon excitation and their subsequent relaxation, but also the dominant relaxation mechanisms in this nanostructured material.

Previous studies on the optical properties of GaN NWs have focused on steady-state photoluminescence (PL) measurements in most cases taken at low temperatures.[22,156,157] From room temperature PL measurements reported by Chen *et al.* for Fe-catalyzed GaN NWs, band edge emission as well as yellow emission were observed. Cai *et al.* observed only UV band emission for straight GaN NWs, while yellow luminescence was dominant for corrugated GaN NWs, as referred previously.[158]

While the dynamic carrier behaviour has been extensively investigated for bulk GaN,[159–161] carrier dynamics in GaN NWs and, in particular, the role of defect-related states within the band gap on carrier relaxation have not been investigated. Specifically only time resolved PL measurements that investigate the radiative relaxation mechanisms in GaN NWs with picosecond resolution have been reported.[162,163] In this work, transient absorption measurements were performed in GaN NWs using a non-degenerate pump-probe technique with above and below band gap excitation. Femtosecond laser pulse excitation provides the required temporal resolution for investigating carrier dynamics on an ultrafast time scale and so time resolved absorption spectroscopy provides an important insight into the relaxation of the photogenerated carriers into energy states located above and below the conduction band edge.

4.2.1 Non-Degenerate Absorption Change Measurements for Above Band Gap Excitation

Non-degenerate time resolved absorption change measurements were performed in GaN NWs using ultrashort pulses from an amplifier laser system. Since GaN is a wide band gap semiconductor with a direct band gap at approximately E_g = 3.4 eV (λ = 365 nm) at room temperature, the pump pulses are generated from the OPA providing tenability over the excitation wavelength. Following UV excitation pulses, carriers are directly excited from the valence band states into the Γ-valley conduction band states. A white light supercontinuum in the UV region was utilized to investigate conduction band states and shallow donor states, while a white light supercontinuum in the visible region was used to monitor defect states

located at energies within the band gap. These two optical setups for white light continuum generation utilized to optically investigate the GaN NWs, are described in detail in Chapter 3. In all measurements, time evolution of transmission and reflection changes were taken simultaneously to allow the estimation of the differential absorption by using the equation 3.1.

4.2.1.1 Probing Wavelength Dependent Measurements

Initially, above band gap UV pulses were used to excite the valence band electrons into the conduction band states. Measurements were performed for a variety of probing wavelengths between UV and IR region. The different probing wavelengths provide information for energy relaxation of the photogenerated carriers at different energy states of the NW system.

Fig. 4.4 shows the time evolution of absorption change for excitation pulses at 320 nm (E_{photon} = 3.87 eV) and different probing wavelengths ranging in the region between 340-980 nm (corresponding to photon energies: 3.64 – 1.26 eV) for times up to 50 ps for clarification purposes. In the inset of the Fig. 4.4, the measurements for time delays up to 500 ps are shown. The absorbed pump fluence for these data was estimated to be ~ 0.5 mJ/cm^2. For comparison purposes, the normalized absorption change data are shown in Fig. 4.5 for probing wavelengths between 370-980 nm. Also, seen as an inset in Fig. 4.5, is the state filling minimum signal, which is plotted as a function of probing wavelength. No signal from the sapphire substrate contributes to the overall signal due to its large band gap (E_g = 9.1 eV) and its high crystallinity.

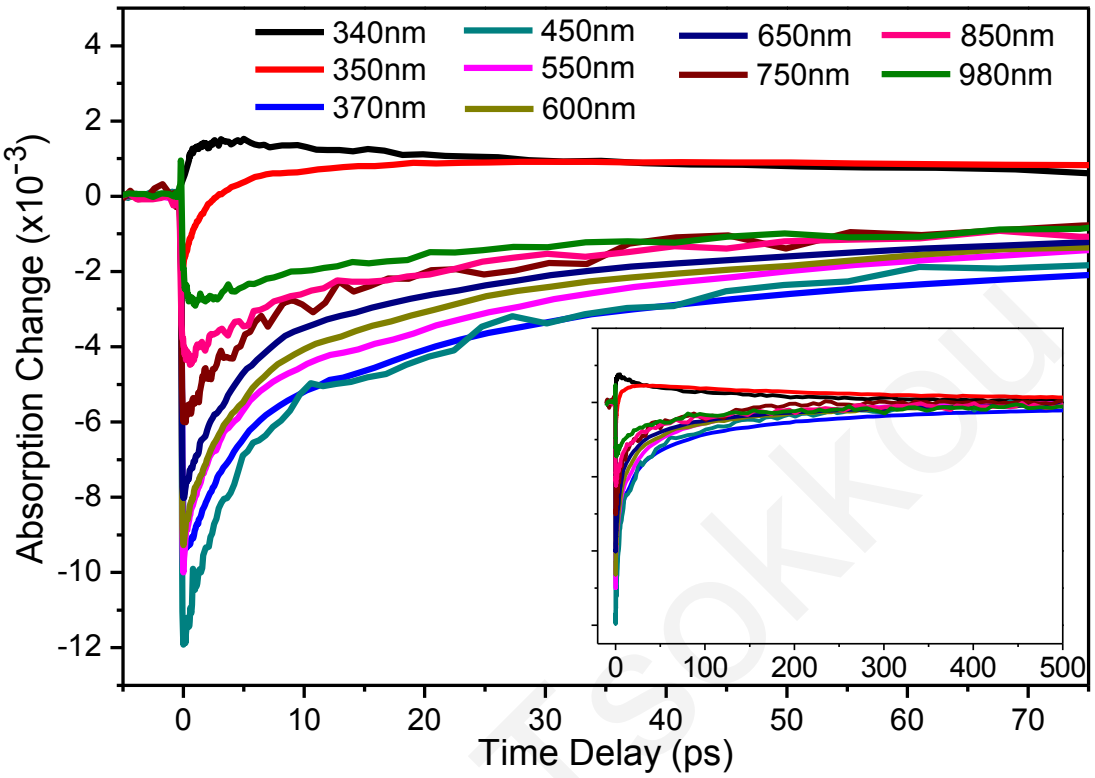

Figure 4.4. Nondegenerate, time resolved, transient absorption measurements of the GaN NWs using ultrafast excitation pulses at 320 nm and probing pulses in the range 340–980 nm. In the inset of the figure, the results for times up to 500 ps are shown.

Clearly evident from the data in Fig. 4.4 is the different temporal behavior of the induced absorption for probing wavelengths corresponding to photon energy above and below the band edge of the GaN NWs. The measured signal appears to be negative over the entire range of wavelengths with energy below the band gap. What appears to be common in all the curves is a fast initial response reaching a minimum or maximum depending on the probing wavelength, which is then followed by a slower recovery toward equilibrium. It is well known that above band gap excitation of a semiconductor material will result in the generation of carriers that will occupy the available energy states near the excitation region. As a consequence of this occupation of states, a negative change in absorption is expected, known as state filling. However, in addition to state filling, free carriers may undergo secondary excitation by the probe laser pulse resulting in what is known as "free-carrier absorption".

This is a positive contribution to the induced absorption and it usually competes with state filling, which is negative.

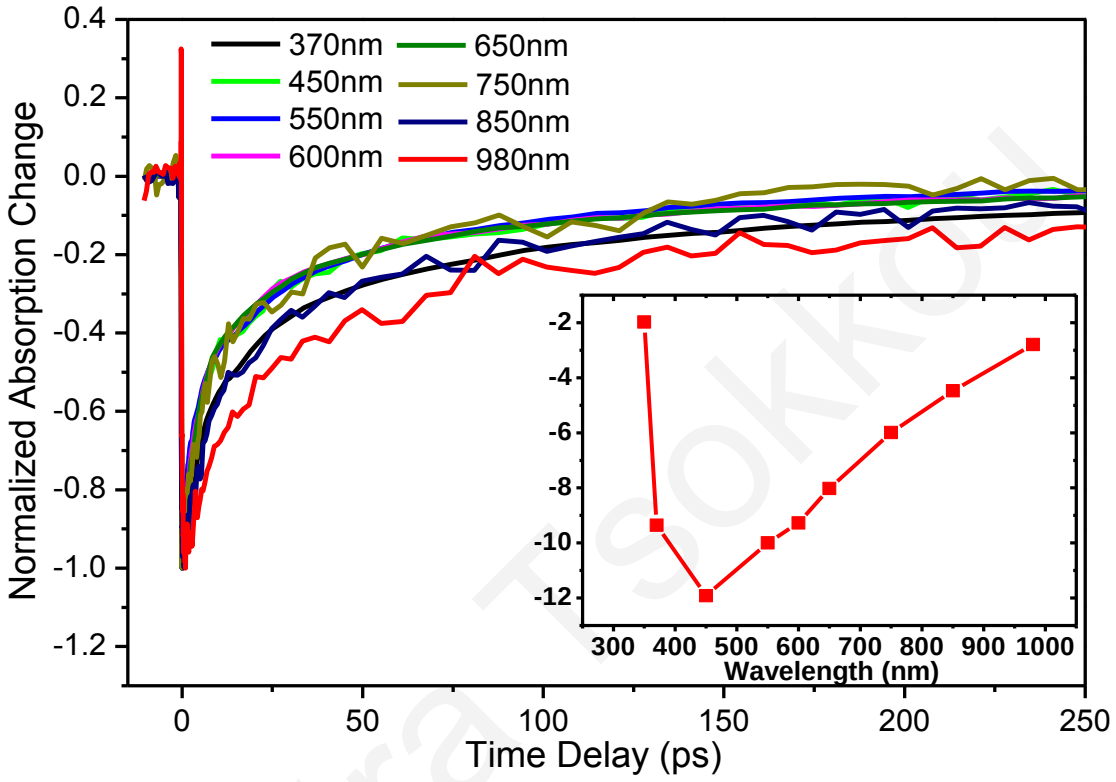

Figure 4.5. Time evolution of normalized differential absorption change for probing pulses in the range between 370-980 nm. In the inset of the figure, state filling minimum is shown vs probing wavelength for above band gap excitation at 320 nm.

It is interesting to point out that in the CVD-grown GaN NWs when probing at 340 nm, which is above the band edge, we notice a positive signal suggesting that free-carrier absorption is the dominant contribution. Although this is not expected, since state filling should be present for these states, we believe that as a consequence of strong coupling between the photogenerated carriers and energetically higher states with an energy difference corresponding to the probing wavelength, free-carrier absorption prevails.

A more complex behavior is observed when probing at 350 nm. State filling is initially observed, but with increasing delay time the signal becomes positive before it returns to equilibrium. Furthermore, strong state filling effects are observed for all probing wavelengths

between 370 and 980 nm. This result suggests that defect-related states are located within the entire band gap of the GaN NWs. This is clearly seen in the inset of Fig. 4.5 where state filling minimum versus wavelength is shown and which to a first approximation reflects the density of states at the probing wavelength.

The temporal evolution of the absorption change for different probing wavelengths can be categorized into the two different groups as evident from the normalized absorption plots in the Fig. 4.5. It appears that signal in energy states between 450-750 nm show approximately the same temporal evolution.

Different time evolution is observed for the larger probing wavelengths between 850 - 980 nm. The observed differences in relaxation times obtained when probing at 850 nm and 980 nm, we believe are associated with the simultaneous contributions of free carrier absorption and state filling effects. This is more pronounced for 980 nm, evident from the small positive signal observed for delay times near $t = 0$ ps.

Further, to be able to calculate the carrier relaxation times from the different states we have to assure that no many body effects, such as Auger recombination take place. Therefore, more measurements are needed to extract further conclusions and will be discussed in the following sections.

4.2.1.2 Pump-Fluence Dependent Measurements for Conduction Band States – Detection of U valley

The unusual behavior observed in the experimental data shown in the previous section at the probing wavelengths 340 nm and 350 nm has to be further investigated. Therefore, intensity measurements have been carried out for pump UV pulses at 320 nm and the probing wavelength of 350 nm (E_{photon} = 3.54 eV), as seen in Fig. 4.6. Measurements were performed for pump fluences between 110-975 μJ/cm^2.

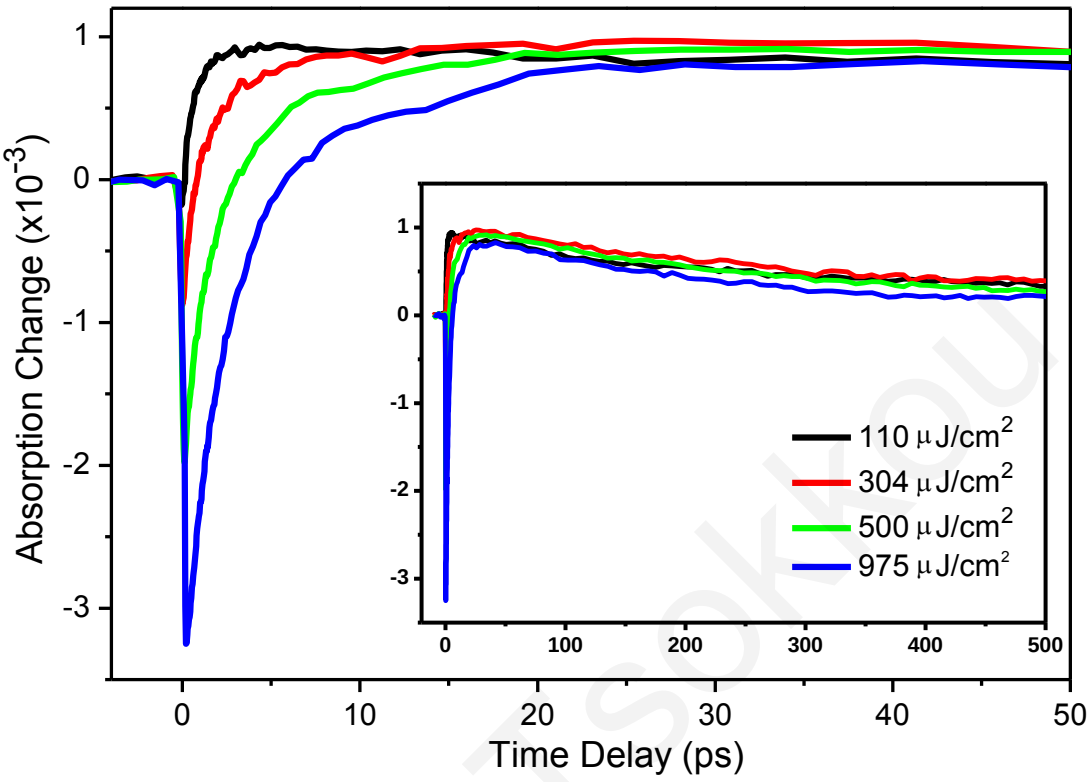

Figure 4.6. Nondegenerate, time resolved, transient absorption measurements of the GaN NWs using ultrafast excitation pulses at 320 nm and probing pulses at 350 nm for different pump fluences between 110-975 μJ/cm^2.

Clearly evident is the initial negative state filling, which is intensity dependent. As pump fluence increases state filling becomes more significant and larger times are needed for the signal to change sign. This observed state filling is associated with the occupation of states located near the band edge, so we need to consider the possibility that the observed positive signal in the temporal profiles of the measurements could be due to band gap renormalization, as has already been reported in degenerated pump-probe measurements for bulk GaN.[164]

The band gap renormalization describes the change in the energy band diagram, which may become evident when a large number of carriers are photoexcited into the conduction band states. Band gap renormalization is an intensity dependent effect originating by the coulombic interaction of free carriers generated into the conduction band states. As a result of a high density of carriers, shrinkage of the band gap occurs. Therefore when probing close to the band edge, for times close to t = 0 ps the band gap varies and probe beam detects energy

states with different densities of states, which influence the observed temporal evolution of the signal. Nevertheless, in our non-degenerate transient absorption measurements, band gap renormalization would be expected to be observed first as a positive signal, since states with larger densities of states are detected and band filling is weak. For larger times, state filling would be observed as the carriers reach the probing state.

Furthermore, the maximum positive signal and its temporal behavior do not exhibit any dependence on the incident fluence and thus on the photogenerated carrier density, as seen in the inset of Fig. 4.6. In view of the above, it is believed that the positive signal in Fig. 4.6 is not associated with band gap renormalization, but rather with free-carrier absorption. In what follows we will explain in more detail the observed free-carrier absorption at 350 nm. It is important to point out that the different temporal behavior observed for state filling and free-carrier absorption suggests that these contributions are related to different energy states. In this case, state filling signal appears to increase linearly with increasing pump fluence. This observation is consistent with the fact that higher pump fluences lead to larger occupation of states in the conduction band by the photogenerated carriers. It is worthy to mention that with increasing pump fluence, state filling appears to take longer, suggesting that Auger recombination is negligible for states in the conduction band located around 3.5 eV, even for the highest fluences (~1 mJ/cm^2) used in this work.

For longer delay times, free-carrier absorption appears to dominate. Furthermore, the relaxation of this positive signal appears to be almost identical for all pump fluences, as can be clearly seen in the inset of the Fig. 4.6. This suggests that the two competitive effects are not influenced in the same way by the increment in pump energy, despite that both effects are carrier density dependent. The observations above suggest that the saturation of free-carrier absorption occurs even for the lowest pump energy used in these experiments. We should also note that in the measurements of Fig. 4.4, no free-carrier absorption is observed for probing wavelengths larger than 350 nm, setting a minimum limit for the energy difference between the coupled states where free-carrier transitions take place. Given the above observations, it is believed that free-carrier transitions take place between a defect-related state located inside the band gap, which becomes fully occupied by carriers, and the indirect satellite valley of the conduction band. The possibility that free-carrier transitions may occur between states in the conduction band is ruled out given the intensity dependent measurements of Fig. 4.6. In such

case, as pump fluence increases is expected that due to the larger number of carriers generated into the conduction states, higher maximum absorption signal would be observed.

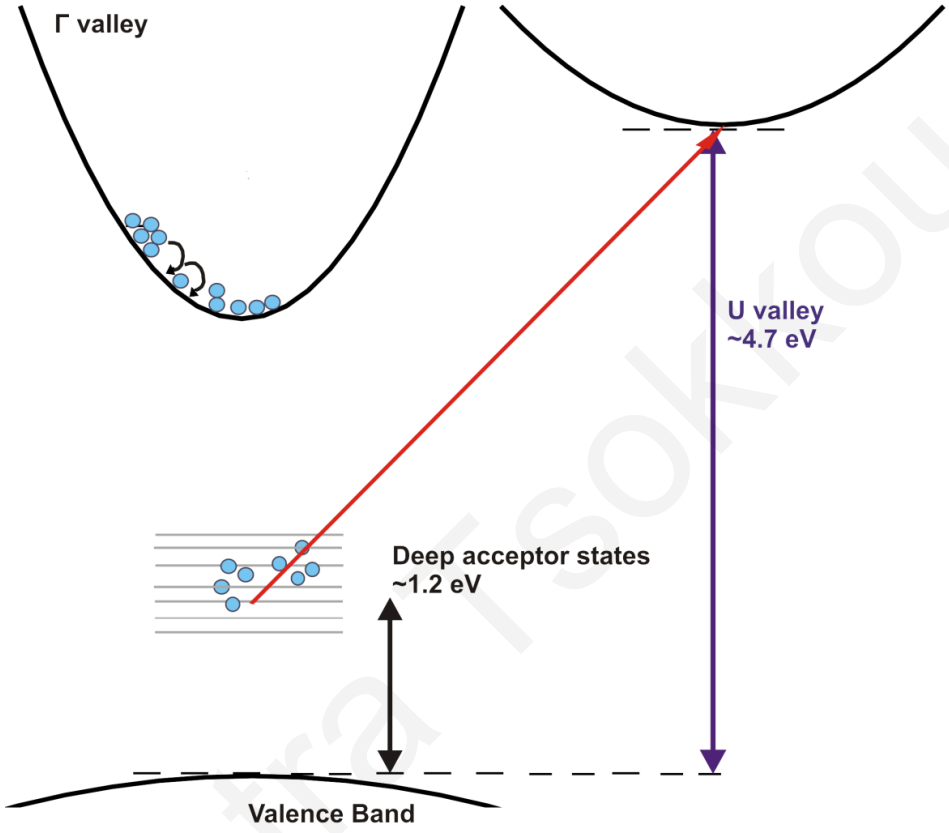

Figure 4.7. A simplified band diagram of GaN NWs, where the energetic positions of deep acceptor states and the *U* valley are shown.

In interpreting our experimental results we took into consideration a theoretical model for the distribution of defect states in GaN proposed by Shalish *et al.*.[154] According to this model, deep acceptor states correlated with the yellow luminescence observed for bulk GaN are attributed to Ga vacancies, which are centered at ~ 1.2 eV from the top of the valence band. Taking into consideration the minimum energy difference between the energy states for the observation of free-carrier absorption (~ 3.54 eV), we conclude that the energy difference between the indirect valley and valence band is ~ 4.7 eV. This transition is seen in a simplified band diagram shown in the Fig. 4.7, where the energy levels of the deep acceptor states and the *U* valley are shown.

Our experimental results is in very good agreement with the minimum energy of the *U*-valley (~ 4.73 eV) for the bulk wurtzite GaN reported by Sun *et al.*.[160] In this study, non-degenerate transmission change experiments were performed using below band gap IR excitation pulses and UV probe pulses on Si-doped bulk GaN. In this way, the relaxation of conduction band electrons is resolved, while carriers from the valence band are not disturbed. It is expected that the response of the signal will change, when the pump energy is higher than the intervalley threshold and an additional contribution to the signal from the intervalley scattered electrons is evident, that allows the determination of the energy for the *U* valley. It should be pointed out that no changes in the energy states are expected due to quantum confinement effects, since the diameter of the wires is much larger than the exciton Bohr radius for this material (~ 11 nm).[165]

4.2.1.3 Pump-Fluence Dependent Measurements for Shallow Donor States

To further improve our understanding on the carrier dynamics in the GaN NWs intensity measurements have also been carried out using 320 nm pump pulses and probe pulses at 370 nm, thus probing energy states placed just below the direct band edge. The intensity measurements of absorption change are normalized for comparison purposes and are shown in Fig. 4.8. The observed state filling is attributed to the occupation of shallow donor energy states due to nitrogen vacancies and oxygen impurities by the photogenerated carriers.[155]

Clearly evident from the normalized data is that carrier relaxation becomes faster with increasing pump fluence indicating that is strongly affected by the non-radiative Auger recombination. Given that Auger recombination was negligible for the carriers within the conduction band energy states (Fig. 4.6), we conclude that the observed Auger effects must arise from interactions of carriers within the defect-related states.

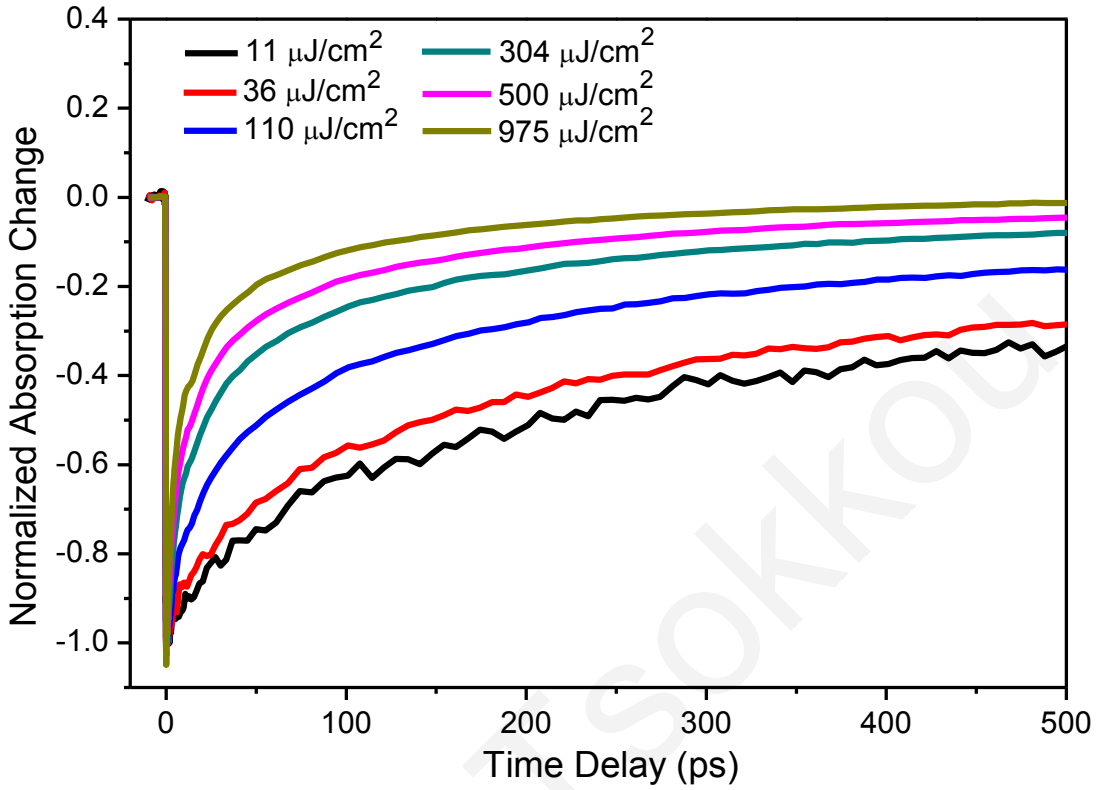

Figure 4.8. Normalized transient absorption change in the GaN NWs using ultrafast excitation pulses at 320 nm and a probing wavelength at 370 nm for different pump fluences.

Relaxation times can be found for the lowest pump energy of 11 μJ/cm^2, where Auger recombination is expected to be negligible. Therefore, the experimental data are fitted using multiple exponential decays, as the one shown in the equation 3.4. Best fitting was obtained using a biexponential decay $(N(t) = N_1 \exp(-t/t_1) + N_2 \exp(-t/t_2))$ corresponding to two relaxation mechanisms that contribute to the signal. The first mechanism with a time constant ≈ 50 ps (30 %) is attributed to relaxation of carriers from shallow donor states that originate from native defects, or due to the surface of the NWs and relaxing to the midgap states. The second mechanism with a time constant of ≈ 655 ps (70 %) is believed to be associated with carriers relaxing to the deep acceptor states inside the band gap. Here we should point out that the latter mechanism may be responsible for the observed yellow luminescence (~ 2.30 eV) in GaN.[166] However, we cannot rule out the possibility that carriers may relax to lower shallow acceptor states or recombine.

4.2.2 Non-Degenerate Absorption Change Measurements With Excitation Below Band Gap

In this section, we investigate the excitation of carriers to energy states within the band gap. Second harmonic generation of ultrafast amplified pulses at 800 nm was used to excite carriers from the valence band to bang gap states. Probing of these photogenerated carriers has been accomplished utilizing white light continuum in the visible part of the spectrum. Transient differential absorption measurements reveal the carrier dynamics through the defect states in GaN NWs following below band gap excitation at 400 nm.

4.2.2.1 Probing Wavelength Dependent Measurements

In a defect free semiconductor material, following ultrafast excitation at moderate fluence where nonlinear effects such as photon absorption are negligible, below band gap excitation will result in negligible generation of carriers and therefore no change in absorption. However, as a result of the existence of point and structural defects energetically located within the gap, absorption of photons from the excitation pulse, will result in the generation of non-equilibrium carriers in these defect states.

Thus to investigate the carrier dynamics within the defect-related states that are energetically located inside the band gap, non-degenerate time resolved absorption measurements have been performed using excitation at 400 nm (E_{photon} = 3.1 eV). The differential absorption measurements for probing wavelengths between 500–980 nm are shown in Fig. 4.9. The estimated absorbed pump fluence in these measurements was approximately ~ 10 μJ/cm^2.

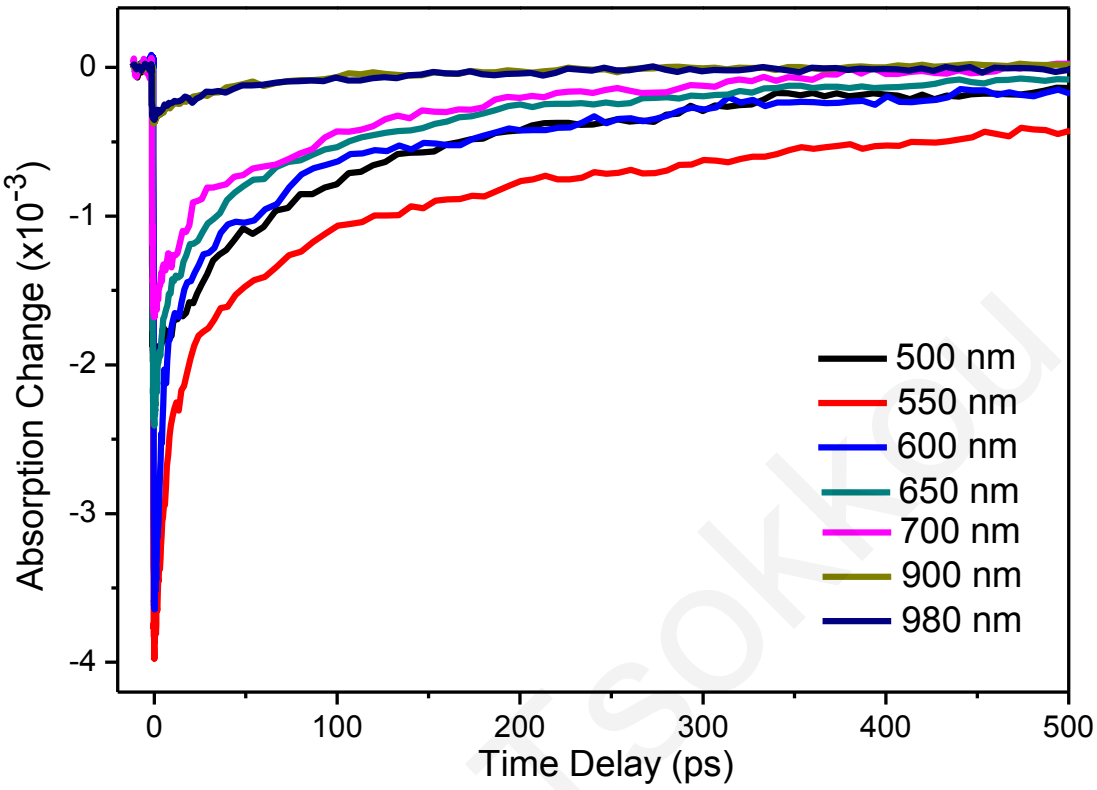

Figure 4.9. Nondegenerate transient absorption measurements of the GaN NWs using ultrafast excitation pulses at 400 nm and probing pulses in the range 500–980 nm.

The induced absorption change when probing below the band edge reveals a large density of defect states. Here, we should also point out that no signal was detected when the excitation wavelength was set to 650 nm (E_{photon} = 1.9 eV), even for pump energies ten times higher than the energy used at 400 nm, setting an upper bound to the density of defect states in this region. Clearly evident from Fig. 4.9 is the dominant state filling, which prevails over free-carrier absorption for all probing wavelengths in the region between 500 and 980 nm. This behavior is in agreement with the previous results obtained for above band gap excitation.

Since Auger recombination seems to be evident when probing the shallow donor states, it is necessary for intensity measurements to be carried out before extract any conclusions about the relaxation mechanisms and times.

4.2.2.2 Pump-Fluence Dependent Measurements for Midgap States

In this section, we investigate the intensity effect for excitation pulses at 400 nm and probing wavelength at 550 nm. The absorption pump fluences in these experiments range between 1 and 21 μJ/cm^2. These measurements were repeated at λ_{probe} = 500 nm with similar results.

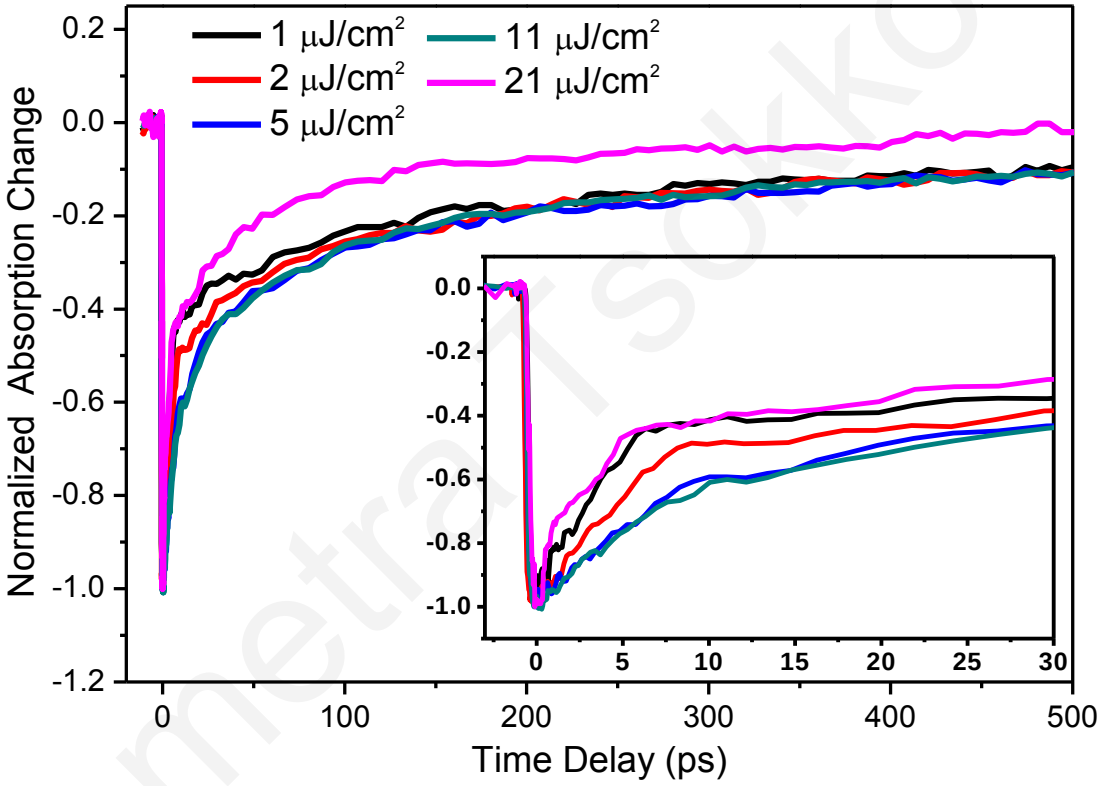

Figure 4.10. Nondegenerate transient absorption measurements of the GaN NWs using ultrafast excitation pulses at 400 nm and probing pulses at 550 nm for different pump absorbed fluences.

Normalized intensity differential absorption measurements are shown in Fig. 4.10 for comparison purposes. Multi-exponential curves were used to fit the experimental data and best fits were obtained for double exponential decay curves. The fast relaxation component as seen in the inset of Fig. 4.10 becomes slightly slower, i.e., increased from 6.5 to 12 ps (60 %), as the pump fluence increased from 1 to 11 μJ/cm^2. This is due to the larger number of

carriers that occupy the defect-related states, and as a result these carriers need longer times to leave the probing region. It is believed that the fast relaxation time is the required time for probed carriers to relax to energetically close states. The slow relaxation component is estimated to be ~ 350 ps (40 %) and is probably associated with nonradiative transitions to the lower acceptor states. For fluence higher than 11 μJ/cm^2, a change in the temporal behavior of the induced absorption is observed. It appears that carrier relaxation becomes faster at 21 μJ/cm^2, indicating that Auger recombination maybe present for the midgap states, when a threshold in carrier density is exceeded.

4.2.3 Band Diagram of GaN Nanowires

To help the reader obtain a clear picture of the dynamics in GaN NWs, we have included a schematic band diagram model (Fig. 4.11) showing the different defect states and the relaxation mechanisms obtained from the interpretation of our experimental data. The excitation of the sample with an UV laser pulse is indicated with a purple arrow that results in the generation of free carriers into the conduction states. The main relaxation mechanisms within the band gap are identified with capital letters "*A*–*D*". The transitions discussed above, between deep acceptor states (~ 1.2 eV) and states within the *U*-valley (~ 4.7 eV) observed when the probing energy is larger than 3.5 eV are also shown with a red arrow.

As discussed previously, our results indicate the existence of energy states throughout the band diagram. Further, for the shallow donor states, carriers relax to lower states via two different mechanisms. From the fast relaxation time (~ 50 ps) the carriers relax to lower midgap states as identified by mechanism *A*. Although the majority of carriers leave these states via a much slower relaxation process into deep acceptor states (~ 655 ps), i.e. mechanism *B*, or even recombine. Additionally, carriers from the midgap states relax into lower states via a fast relaxation time associated with mechanism *C* to lower midgap states, or via a slower relaxation time (~ 350 ps) to deep acceptor states, which is identified as mechanism *D*.

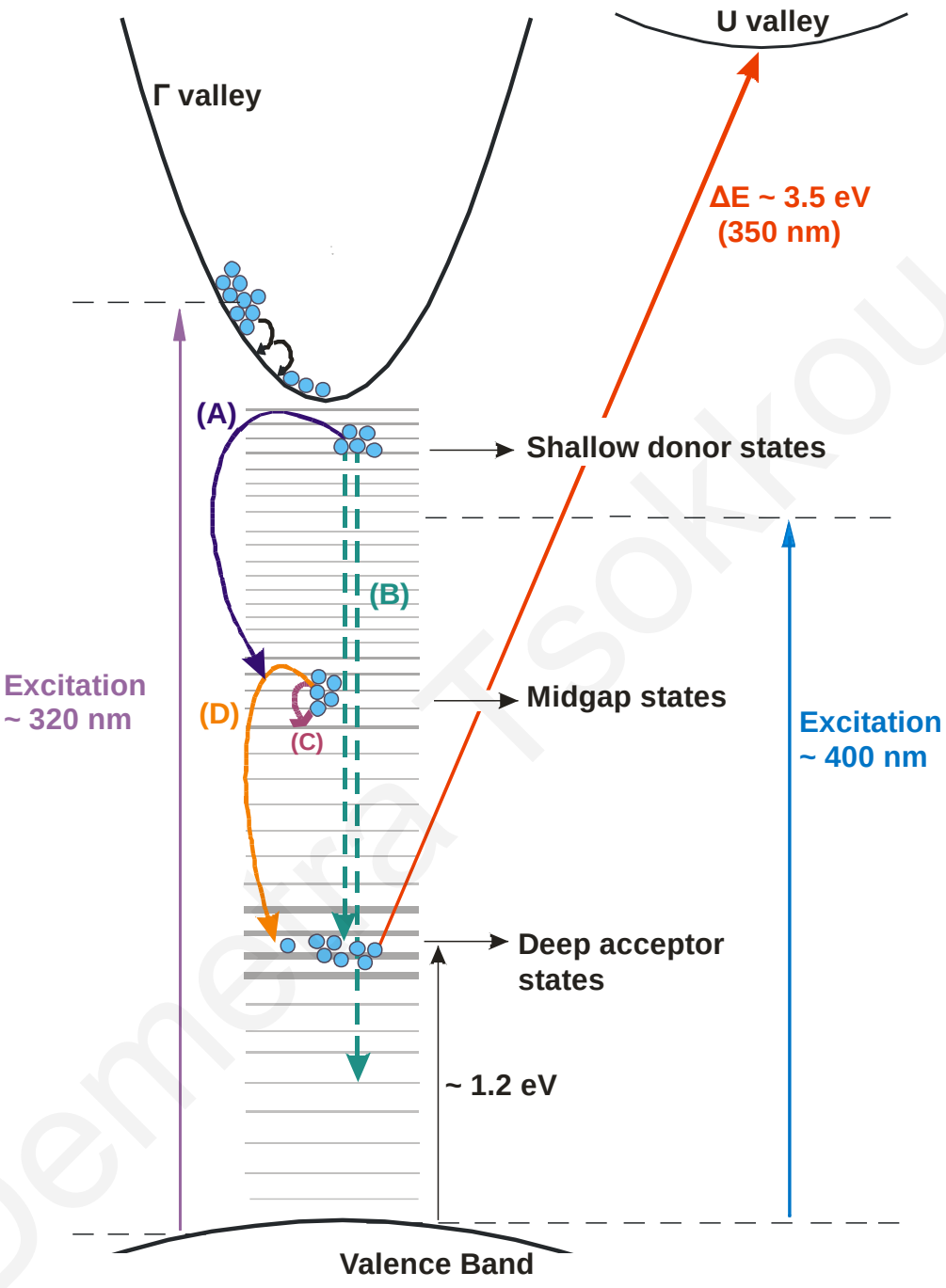

Figure 4.11. Schematic energy band diagram of GaN NWs. The excitation at 320 nm generating carriers within the conduction band is depicted as a vertical arrow. Relaxation mechanisms within the band gap are identified as A–D. Free-carrier absorption from the deep acceptor states to the *U*-valley (ΔE = 3.5 eV) is also shown in the diagram.

4.3 Conclusions

In chapter 4, the growth process followed for the synthesis of GaN NWs via APCVD is presented. GaN NWs have grown by APCVD, via direct nitridation of Ga with NH_3 at 950 °C. It has been shown that the presence of hydrogen flow during the synthesis experiment is essential for the growth of GaN NWs. Further, the characteristics of these NWs were examined via SEM methods. GaN NWs have a diameter of ≈ 100 nm and diameter up to few microns. Additionally, their wurtzite structure was determined via XRD methods.

Furthermore, we presented our detailed studies of the time evolution of photoexcited carriers when using above band gap excitation (UV pump pulses) and different probing wavelengths from the UV to the IR region of the spectrum.

The relaxation dynamics of the photogenerated carriers suggest three distinct regions of energy states below the band edge identified as *shallow donor states*, *midgap states*, and *deep acceptor states.* The effects on carrier relaxation of defect-related states inherit in APCVD grown GaN NWs have been studied in detail. Transient absorption measurements reveal a large number of defect states located below the band edge. These states are placed throughout the entire band gap, and their presences were confirmed via state filling effects observed for all probing wavelengths below the band edge. A simplified band gap model, which incorporates the three distinct regions of states namely, shallow donor, midgap and deep acceptor states, has been utilized to explain the carrier dynamics following femtosecond pulse excitation.

Furthermore, it appears that Auger recombination is not a contributing factor in the carrier relaxation of carriers located within the conduction band even for the highest fluence used in this work. On the contrary, Auger recombination has been observed when probing the shallow donor states just below the band edge for fluences as low as 36 $\mu J/cm^2$. Measurements at the lowest fluence reveal a biexponential relaxation related to the donor states with the fast component corresponding to the relaxation carriers into the midgap states and the slow component of 0.65 ns associated with the relaxation into the deep acceptor states. Differential absorption measurements when probing above the band gap reveal free-carrier absorption contribution corresponding to coupling between the deep acceptor states

located at 1.2 eV from the valence band and the indirect *U*-valley. The observed threshold limit of 3.5 eV to the coupling between these states suggests that the *U*-valley is located approximately 4.7 eV from the valence band in the GaN NWs.

Chapter 5

Carrier Dynamics in In_2O_3 Nanowires

The study of carrier dynamics in In_2O_3 NWs is the main focus in this chapter. The chapter begins with an overview of the synthesis of In_2O_3 NWs. The optimum experimental conditions for the synthesis of the In_2O_3 NWs using APCVD are described. The characteristics of these NWs determined by SEM, XRD and steady state transmission spectroscopy methods are presented.

Following the successful optimization of In_2O_3 NWs, time resolved absorption spectroscopy experiments in these NWs have been investigated in detail. Ultrafast laser pulses with photon energy larger than the band gap energy have been used to generate non-equilibrium carrier density in the conduction band of the NW system. The evolution of the photogenerated carriers has been investigated using transient differential absorption spectroscopy with probing photon energies having a wavelength range between UV and IR region of the spectrum. These experiments reveal the presence of shallow donor and midgap states within the band gap of this NW system. From the differential reflection signal long-lived periodic oscillations were evident due to the generation and propagation of coherent longitudinal acoustic phonons in these In_2O_3 NWs. Pump fluence dependent measurements for the different kind of states revealed that Auger recombination contributes in the carrier evolution for high pump fluences. Furthermore, the use of multiexponential decay curves to fit the experimental data provided information on the carrier relaxation processes. A schematic band diagram for the In_2O_3 NWs that also includes the relaxation mechanisms detected in our experiments, is presented.

5.1 Synthesis of In_2O_3 Nanowires

In what follows, a short overview of synthesis methods approached by many groups for the growth of In_2O_3 NWs is given. The synthesis method and the optimum conditions of In_2O_3 NWs used in this work are presented. Characterization using SEM, XRD and steady state transmission are presented for the optimized grown NWs.

5.1.1 Overview for In_2O_3 Nanowires

Similarly, as for GaN NWs a lot of effort has been given in the past decade for determining the synthesis conditions of In_2O_3 NWs. In_2O_3 NWs have been synthesized by a variety of methods. Many studies can be found in the literature that report different experimental conditions for In_2O_3 NWs growth via CVD. They have also been synthesized by other methods such as laser ablation[167] and electrodeposition.[168]

Different synthesis methods fall into two categories depending on whether a catalyst is used during NWs growth. Several groups have reported that the vapor-solid mechanism is responsible for the NW growth. In this mechanism, structural defects, such as screw dislocations serve as the nucleation sites for the NW growth. In this process, the evaporation of the source material occurs at high temperatures, while the NWs are collected at a lower temperature. This is in agreement with Wu *et al.* where they used carbothermal reduction of In_2O_3 powder at temperatures above $\geq$ 980 ^oC to synthesize In_2O_3 NWs.[169,170] A different approach has been reported by Cai *et al*. where they utilized In spheres and water. At 850 ^oC a gas reaction between the evaporated source material and vapor water occurs and In_2O_3 NWs grow via vapor-solid process.[171]

Metal In has also been used as a source material. In_2O_3 NWs have been synthesized by direct oxidation of In at high temperatures (1200-1300 ^oC) using a continuum flow of a mixture of O_2 and Ar.[172,173] Although in this case, it is reported that the responsible mechanism for the NW growth is the self-catalysis mechanism, in other words In has the role of a catalyst.

The metal that had been used mostly as a catalyst for the synthesis of In_2O_3 NWs via VLS mechanism is Au. Liang *et al.* were the first to report the synthesis of In_2O_3 NWs by heating an InP substrate coated with a thin Au layer at 1080 ^oC under Ar/O_2 atmosphere.[174] Few years later from Liang's study, Kar *et al.* have reported the synthesis of In_2O_3 NWs by thermal evaporation of In metal when using continuum O_2 flow at 1000 ^oC.[175] Similar process has been also used by Yan *et al.*, although O_2 flow was introduced into the system only before the entire experiment process.[176] Alternately, a different method has been followed by Wang's group that has grown In_2O_3 NWs at a lower temperature. They used In thin films that were coated with a few nm of Au onto a Si substrate. In a two-step process, the films were first annealed at 130 ^oC for 20 min in Ar atmosphere and then the temperature elevated at 400 ^oC for 10 min. In_2O_3 NWs have been obtained when they used films of few hundreds of nm. Next, they reported NWs with improved characteristics such as higher yield, when In films that contain an amount of oxygen were used.[177] Another way to achieve growth of In_2O_3 NWs via VLS mechanism is through direct hydrogen reduction of In_2O_3, as suggested by Zhang *et al.*. They have synthesized In_2O_3 NWs at 700-750 ^oC, while Ag nanoparticles were used as a catalyst.[178,179]

5.1.2 Optimum Growth Conditions

Following a careful analysis of previous reports by other groups on synthesis of In_2O_3 NWs via APCVD, a sequence of experiments were performed to investigate the affect that different experimental conditions have on the morphology of the resultant products onto the substrate. In this section, the optimum conditions for the growth of In_2O_3 NWs using APCVD are discussed in detail. The different steps of the recipe for the In_2O_3 NW synthesis are shown in table 5.1.

High purity In powder (Aldrich, Mesh -100, 99.99%) was used and about ≈ 0.2 g was weighed and loaded into a quartz boat. In_2O_3 NWs were grown on n^+ Si (111) substrates that were coated with 0.5 nm of Au, which was deposited on Si (111) via sputtering at a slow rate using an Ar plasma under a pressure < 10^{-4} mbar. After loading the In powder and Au/Si

(111) samples into the quartz boat, it was inserted into the reactor and positioned directly above the thermocouple. Initially, oxygen was admitted into the reactor at a flow of 50 sccm for 10 min at room temperature. Following this, the O_2 flow was terminated and Ar was introduced at 500 sccm for 10 min after which the temperature was increased up to 700 °C, using a ramp rate of 30 °C/min. During growth the temperature and flow of Ar were maintained constant at 700 °C and 100 sccm, respectively, for 90 min. Finally, upon cooling down the flow of Ar was maintained at 100 sccm and the sample was removed from the reactor only after cooling down to room temperature. Upon visual inspection, the surface of the sample had a light-blue color, while the In powder, which melts at 157 °C always formed a gray-like, spherical drop with metallic appearance. For the purpose of ultrafast spectroscopy, In_2O_3 NWs were grown directly on quartz which was also coated with ≈ 0.5 nm of Au. SEM images and XRD pattern did not show any significant differences as compared to the case that when Si was used as a substrate.

Step	Name	Gas flow (sccm)	Temperature (^oC)	Duration (min)
1	System Purge (a)	50 O_2	25	10
	(b)	500 Ar	25	10
2	Rise of Temperature	100 Ar	25→700	22
3	Growth Process	100 Ar	700	90
4	System Cooling	100 Ar	700→23	60

Table 5.1. Growth parameters of In_2O_3 NWs using APCVD technique.

No NWs were obtained on plain Si (111), suggesting that the In_2O_3 NWs grow via the VLS mechanism as has been also reported by other groups.[175,179,180] Although Au-In alloy starts to occur at temperatures above 450 ^oC, no deposition occurred for temperatures lower than T_G = 700 ^oC due to the formation of an oxide shell around the molten indium upstream, which reduces the vapor pressure of indium inside the reactor, even though O_2 was always admitted at the very beginning of the process and room temperature. This is also consistent

with the fact that no In_2O_3 NWs were obtained for T < 900 °C under a flow of O_2 during growth, which leads to the formation of an even thicker oxide shell surrounding the molten In upstream. For T > 900 °C, the expanding In melt is known to break open the oxide shell, releasing In which then reacts directly with O_2 and leads to the formation of a large density of octahedral In_2O_3 nanocrystals with an average diameter of 500 nm.[181] Consequently, oxidation of In under a flow of O_2 during growth does not lead to the formation of In_2O_3 NWs and so it is essential that the O_2 level is maintained low which is consistent with the use of 5% H_2 in the growth of In_2O_3 NWs by Yan *et al*..[176]

5.1.3 Characterization of In_2O_3 Nanowires

Typical SEM images of the In_2O_3 NWs, grown at 700 °C directly on the Au-coated quartz substrate, are shown in Figs. 5.1 (a) and 5.1 (b). A high density of In_2O_3 NWs is clearly apparent and the NWs have an average diameter of ≈ 100 $\pm$ 20 nm and lengths up to few micrometers, as can be seen from Fig. 5.1 (a).

Fig. 5.1 (b) reveals the large density and uniformity of the NWs on the substrate. It should be also pointed out that the diameter of the NWs is not uniform along their length and they are tapered at their edges. This effect is attributed to the fact that source materials are not only absorbed by the Au nanoparticles, but are also incorporated onto the side plane of the NWs, which leads to the radial growth of the In_2O_3 NWs. Similar observations have been observed by other groups in the case of In_2O_3 NWs.[176,177] However, we cannot exclude the possibility that the size of the catalyst droplet reduces during growth process due to incorporation of Au atoms into the NW, that changes progressively the size of In_2O_3 NWs.[182]

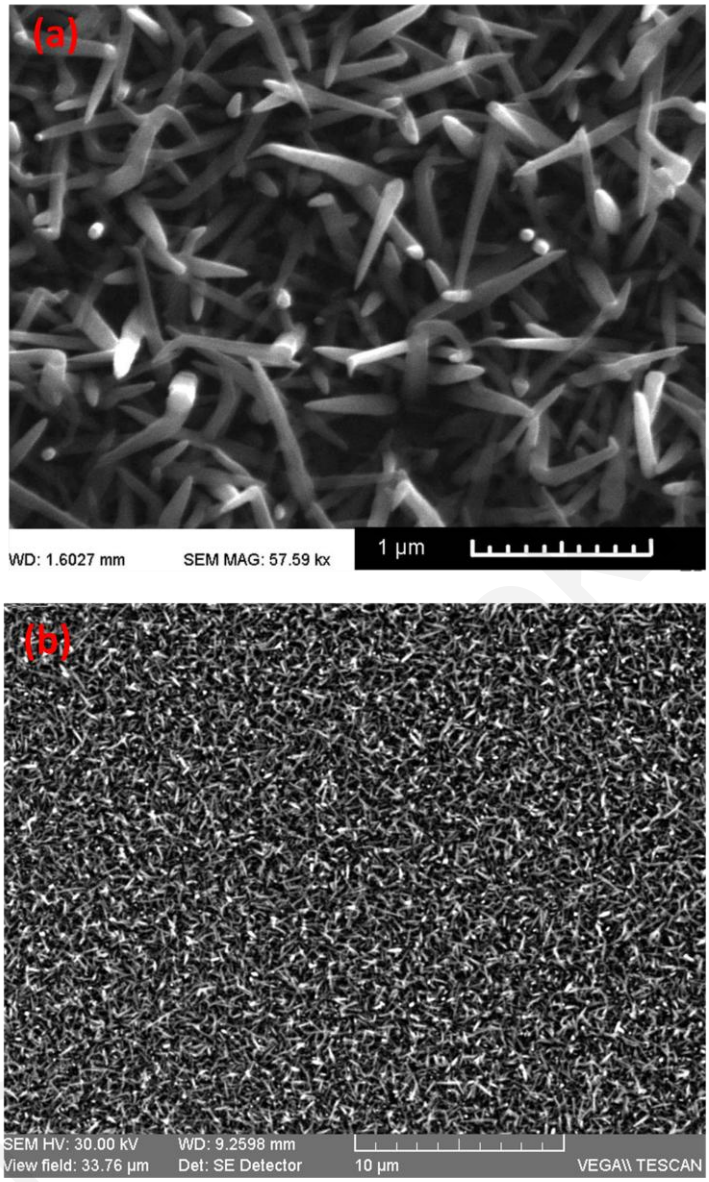

Figure 5.1. SEM images of the In_2O_3 NWs grown at 700 °C on 0.5 nm Au/quartz substrate.

In order to examine the crystal structure of the material, XRD measurements were performed and the results are shown in the Fig. 5.2. After identifying the peaks caused by the silicon substrate and the aluminum sample holder, the In_2O_3 NWs grown at T_G = 700 °C on silicon are characterized by intense reflection peaks corresponding to the (2 1 1), (2 2 2), (4 1 1), (4 0 0), (4 4 0), and (6 2 2) crystallographic planes of In_2O_3 having the cubic bixbyite structure, also called C type rare earth oxide structure with a lattice constant a =10.11 Å.[179]

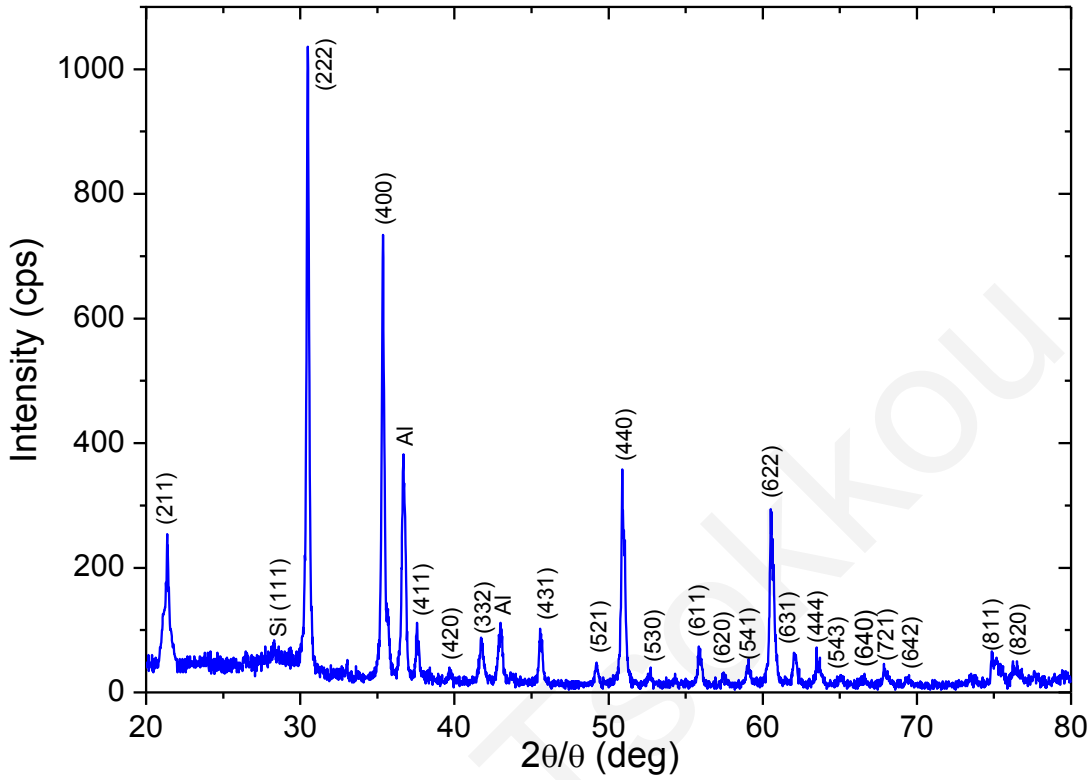

Figure 5.2. X-ray diffraction pattern of the In_2O_3 NWs grown on quartz. The peaks shown are attributed to crystallographic planes of In_2O_3 NWs, except those that originate from the sample holder and Si (111) and are identified in the pattern.

Steady state transmission measurements were carried out following the growth of the In_2O_3 NWs on quartz at wavelengths between 250-800 nm. The experimental data are shown in Fig. 5.3, indicating that transmission signal is high for wavelengths above 400 nm. A small reduction of transmission signal in the region between 500-600 nm is attributed to the presence of surface plasmon resonance due to Au nanoparticles and that will be further discussed in the Appendix A. The absorption coefficient of In_2O_3 NWs can be extracted using the equation 2.1 as seen in the inset of the Fig. 5.3.

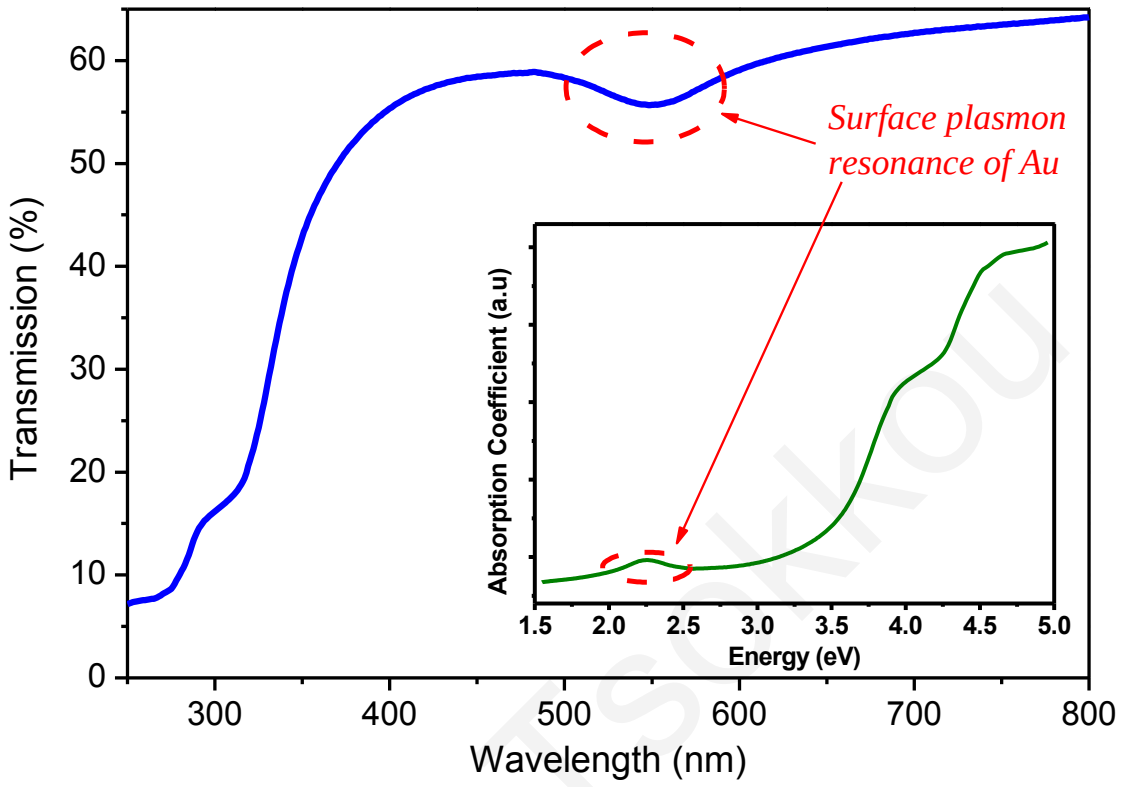

Figure 5.3. Optical transmission spectrum of In_2O_3 NWs on quartz. The inset shows the absorption coefficient of In_2O_3 NWs versus the photon energy.

The energy of the band gap of a direct semiconductor can be determined from the absorption spectrum. Absorption coefficient in a direct band gap semiconductor is directly related to the band gap following the equation 2.2. The band gap can be estimated by extrapolating the graph between the square of absorption versus photon energy. Fig. 5.4 is a plot of the absorption coefficient squared versus the photon energy providing an estimate of the energy gap of the In_2O_3 NWs, which is found to be equal to E_g = 3.5 eV (λ = 354 nm). This result is in good agreement with the literature reported values.[183] Modification of the band structure caused by quantum confinement effects are not expected to be significant in this case, due to the large diameter of the NWs used in this study in comparison with the exciton Bohr radius, which is equal to 2.4 nm in the case of In_2O_3.[184]

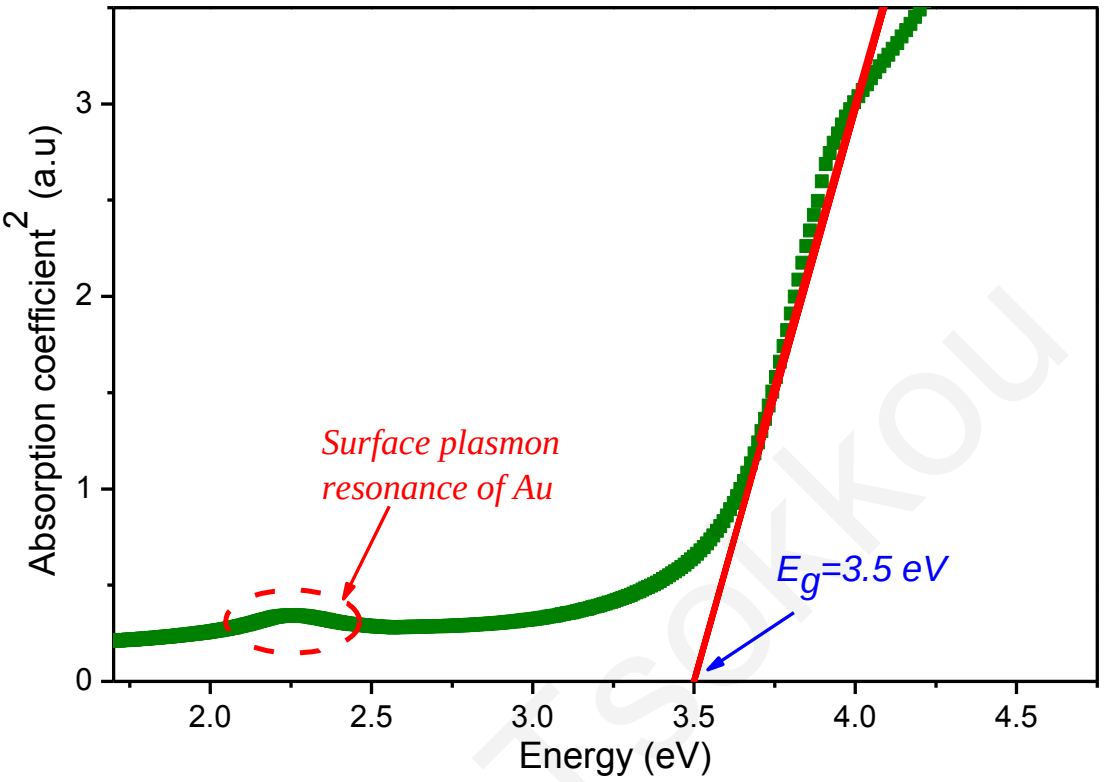

Figure 5.4. Square of absorption coefficient vs the photon energy, which provides an estimation for the bandgap of the In_2O_3 NWs.

5.2 Carrier Dynamics in In_2O_3 Nanowires for Above Band Gap Excitation

Previous investigations of photoluminescence in nonintentionally doped In_2O_3 NWs have revealed peaks with energies below the band gap, which are associated with oxygen defect states, such as vacancies and antisites.[172,173,175,184] However, there has been no detailed investigation using ultrafast time resolved absorption spectroscopy which can provide a more detailed understanding on the energy levels of the electronic states in In_2O_3 NWs and other important physical properties. To study carrier dynamics in the In_2O_3 NWs, time resolved absorption measurements were performed using an amplified laser system to generate ultrashort pulses whereas an OPA was utilized to convert the pump wavelength into the UV region of the spectrum. UV excitation pulses with photon energy larger than 3.5 eV (λ = 350

nm), are necessary to generate carriers into the conduction band of In_2O_3 NWs. White light continuum from UV to IR region was also necessary to probe states above and below the band gap, when using non-degenerate time resolved absorption spectroscopy. Differential transmission and reflection signals were used to calculate the evolution of the absorption change signal using the equation (3.1).

5.2.1 Probing Wavelength Dependent Measurements

Time resolved absorption change measurements using optical excitation at 320 nm (E_{photon} = 3.87 eV) and different probing wavelengths between 340-980 nm, corresponding to energies from 1.27 eV up to 3.17 eV were carried out and shown in Fig. 5.5. The estimated absorbed pump fluence was approximately 575 μJ/cm^2. In the investigated spectrum region, no contribution of the quartz substrate is expected, due to its large band gap (E_g = 8.4 eV).

Looking at the experimental data, we notice a positive or negative change in the absorption depending on the probing wavelength. Generally, an initial fast increase, or decrease, is observed in the absorption that is followed by a much longer recovery. A negative change in absorption is measured for probing wavelengths below 410 nm and within the spectral region of 520–550 nm. The observed negative change in the absorption is attributed to state filling, which is due to the occupation of energy states by photogenerated carriers. On the other hand, a positive change is recorded between 430–500 nm and 600–980 nm. This positive change in the photo-induced absorption is a result of carrier re-excitation to higher energy states by the probing pulses. As mentioned previously, in most cases both effects are present, while the sign is determined by the dominant effect and the temporal evolution reflects carrier relaxation out of the probing states. We should point out that the recovery of absorption is quite different between the two regions; specifically in the visible probing region, the recovery is much faster than the respective recovery in the UV probing region. The different temporal evolution of the signal in the two regions is indicative that different kinds of states are detected.

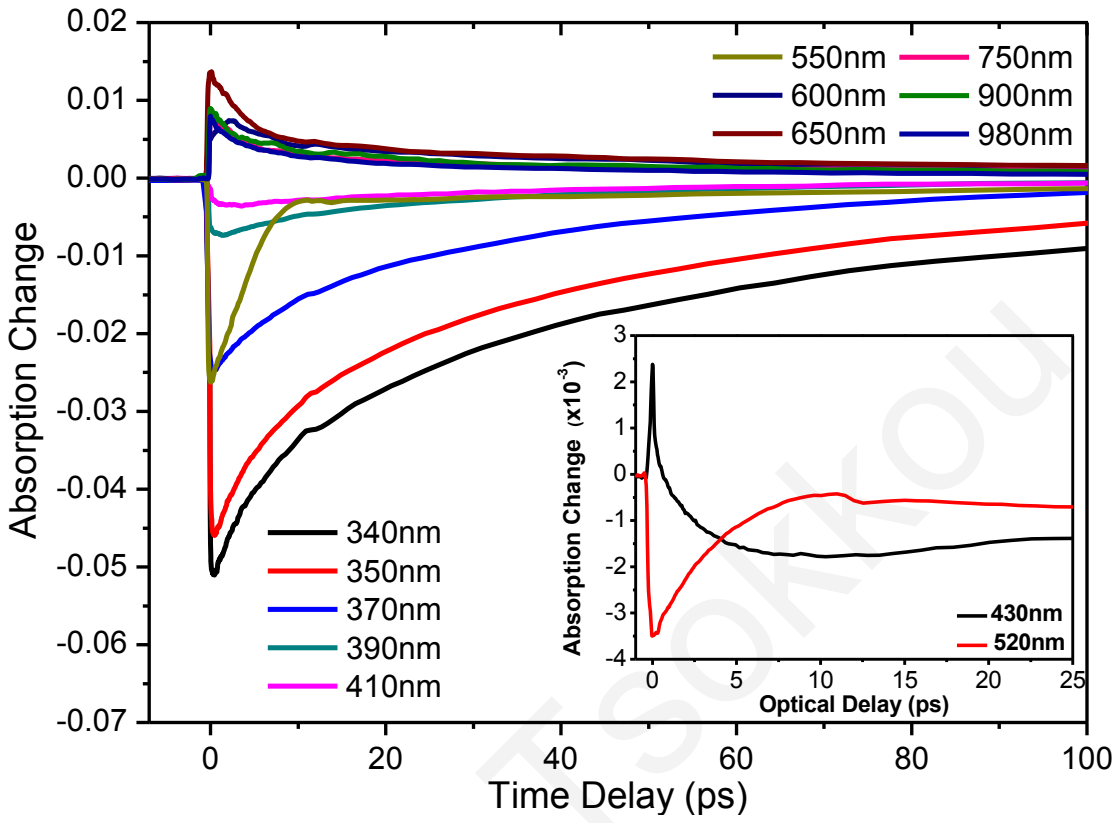

Figure 5.5. Non-degenerate, time-resolved, transient absorption measurements of the In_2O_3 NWs using ultrafast excitation pulses at 320 nm and probing pulses in the range of 340–980 nm.

Above band gap excitation (λ = 320 nm) will result in the generation of electrons in the conduction band. These photo-generated carriers will initially occupy the conduction states resulting in state filling. This effect is expected to be the dominant effect for probing wavelengths corresponding to energies larger than the band gap. Therefore, strong state filling is observed for probing wavelengths smaller than 350 nm. The same behaviour with similar relaxation times is also observed for probing wavelengths corresponding to energies just below the band edge in the region between 370 - 410 nm, as it will be evident below. These observations are attributed to additional energy states that are located below the conduction band edge and are associated with oxygen defects in the In_2O_3 NWs. This is in agreement with previous reports, which suggest that oxygen vacancies are formed due to incomplete oxidation during growth and act as donors resulting in additional states below the conduction band edge.[172,173,175,184] In addition, indium interstitials, as detected in the case of In_2O_3

octahedrons, may also be a contributing factor to the presence of energy states within the band gap.[185]

As probing wavelength increases in the region between 350-410 nm, the negative maximum signal at t = 0 ps becomes smaller, since free carrier absorption effects are also present. This is more evident at 430 nm, when a more complicated behaviour is observed. Initially, free carrier absorption is observed for times near the zero optical delay, while state filling becomes evident for longer times, as shown in the inset of Fig. 5.5. This behaviour is attributed to free carrier absorption from energy states near the excitation region to higher energy states and results in a positive change in absorption. However, as carriers relax into the probing states below the band edge, state filling effects become evident and clearly dominate for longer times.

It is clearly evident from the non-degenerate transient absorption measurements for In_2O_3 NWs that free carrier absorption is the dominant effect following ultrafast pulse excitation when probing in the IR spectral region. A delay in reaching maximum signal is noted when probing at 600 nm. This is a result of the simultaneous existence of state filling effect, due to the plasmon resonance from Au nanoparticles and free carrier absorption from the In_2O_3 NWs. Here we should point out that a different behaviour is observed in the narrow probing region of 520–550 nm, where strong state filling is apparent. In order to confirm this, we repeated the experiment using a sample of a 0.5 nm Au thin film on quartz using similar experimental conditions that are further discussed in Appendix A. The surface plasmon resonance of the Au is responsible for the observed signal. No signal from Au nanoparticles was obtained in different regions.

Apart from this minor difference at 600 nm, it appears that the carrier relaxation is similar at all longer probing wavelengths suggesting that the same kind of states is probed. We believe that these probed states are not states in the conduction band or states located just below the conduction band edge due to the different temporal behaviours between the three regions at the same pump fluence. This conclusion is further supported by intensity measurements that are discussed in detail below, supporting that the probed states are midgap states.

5.2.2 Observation of Acoustic Phonons in In_2O_3 Nanowires

A closer look at the transient reflection measurements for probing wavelengths greater than 390 nm depicts an interesting oscillatory behaviour, as shown in Figs. 5.6 and 5.7. Similar observations were obtained in the transmission change measurements.

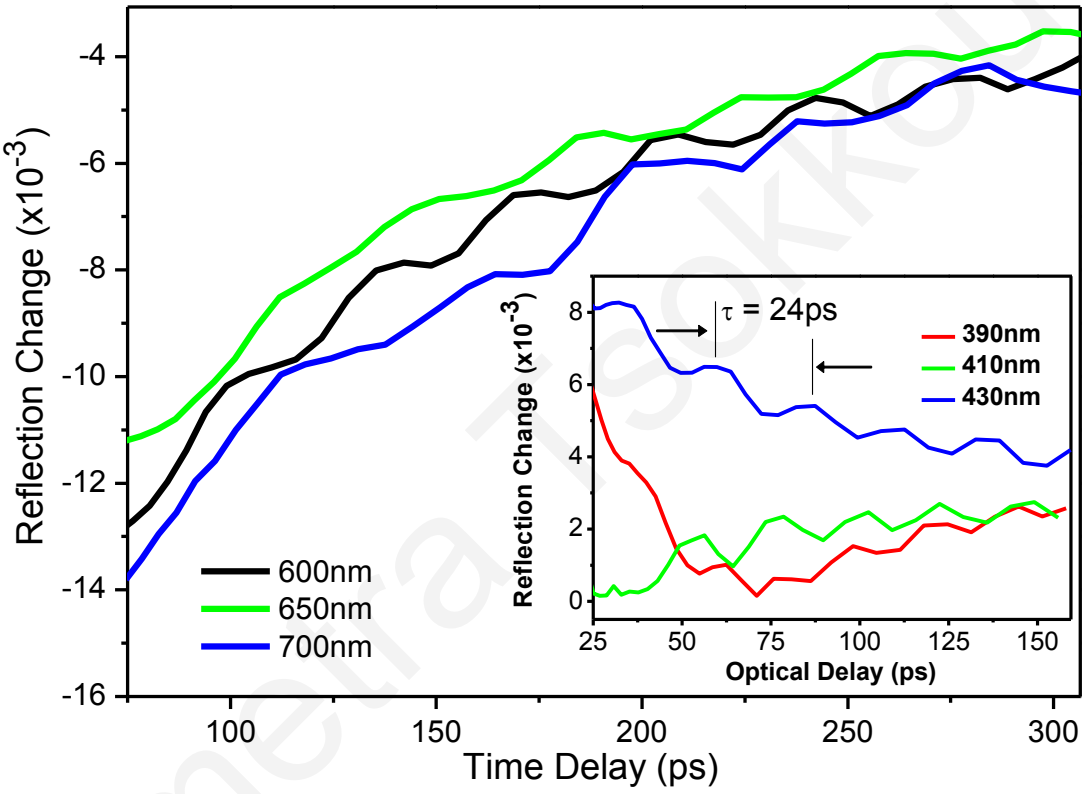

Figure 5.6. Reflection change is shown for times greater than few tens of ps using ultrafast excitation pulses at 320 nm and probing wavelengths between 600–700 nm and 390–430 nm, shown in the inset of the figure.

Long-lived oscillations are superimposed on the differential reflectivity signal following a few tens of picoseconds from the initial excitation. Measuring the period of oscillations for each probing wavelength is observed that remains constant within the 300 ps time window exhibited. On the contrary period of oscillations depends on the probing wavelength. A plot of the period of oscillations versus the probing wavelength shown in the inset of Fig. 5.8, suggests a linear dependence. We believe that the observed oscillations are

associated with coherent longitudinal acoustic phonons generated at the Au nanoparticles and, then lunged into the In_2O_3 NWs.[186,187]

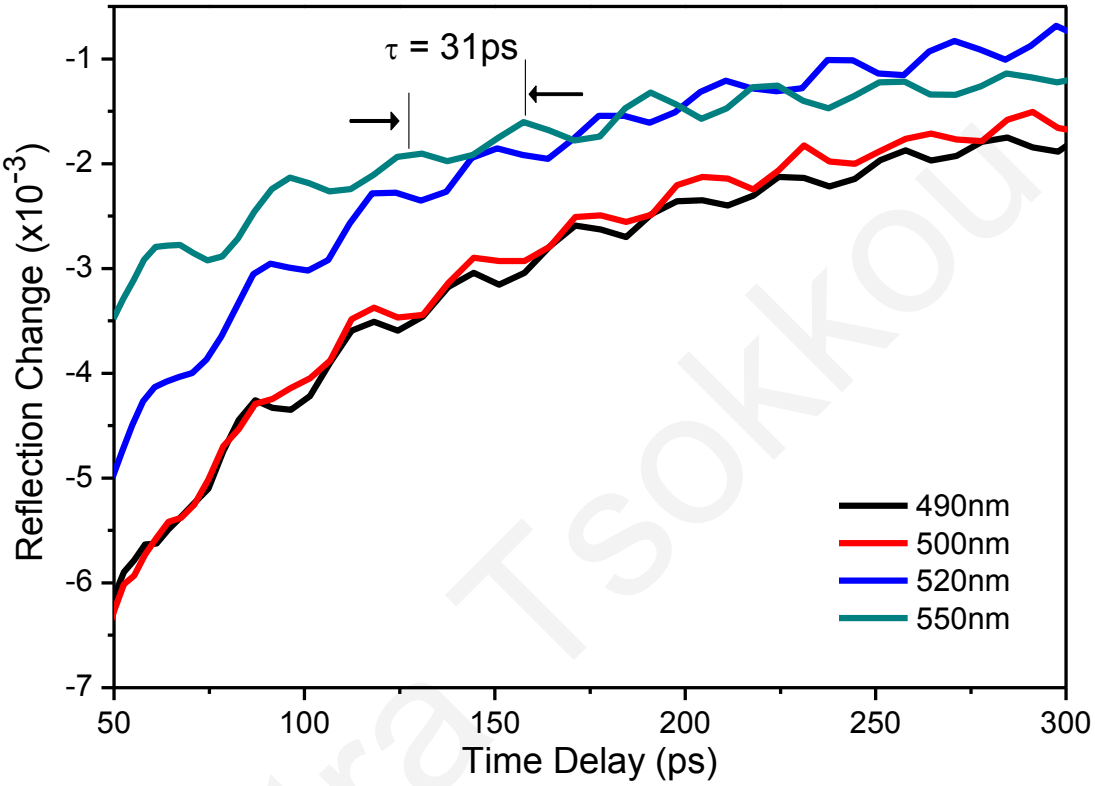

Figure 5.7. Reflection change is shown for times greater than 50 ps using ultrafast excitation pulses at 320 nm and probing wavelengths between 490–550 nm.

Various mechanisms have been proposed for the generation of the coherent longitudinal acoustic phonons including deformation potential leading to electronic stress[188] and heat-induced thermal stress.[189] The linearity of oscillation period is indicative that coherent longitudinal acoustic phonons are the origin of the oscillating response. This behaviour was firstly explained by Thomsen *et al.*[189] and recently extended by Wu *et al.*.[190] In Thomsen model, after excitation of the sample by a femtosecond laser pulse, electron-electron and electron-phonon thermalization may also result in an increment of the electron and lattice temperatures at the surface that further induce a transient thermal stress on a subpicosecond time scale. Wu's model takes also into consideration that electron excitation can lead to a distortion of the lattice equilibrium. By weakening the interatomic bonds, the lattice constant

increases and induces an electronic stress to the lattice. Electronic/thermal stress generates a longitudinal acoustic phonon pulse, which propagates onto the sample at a speed of the material sound velocity and modifies the local dielectric constants, creates a discontinuity, which eventually changes the refractive index and consequently the optical properties of the material. In more simplified words, since the surface layer is heated, the lattice expands very quickly, while the layers below are compressed, creating a strain wave.

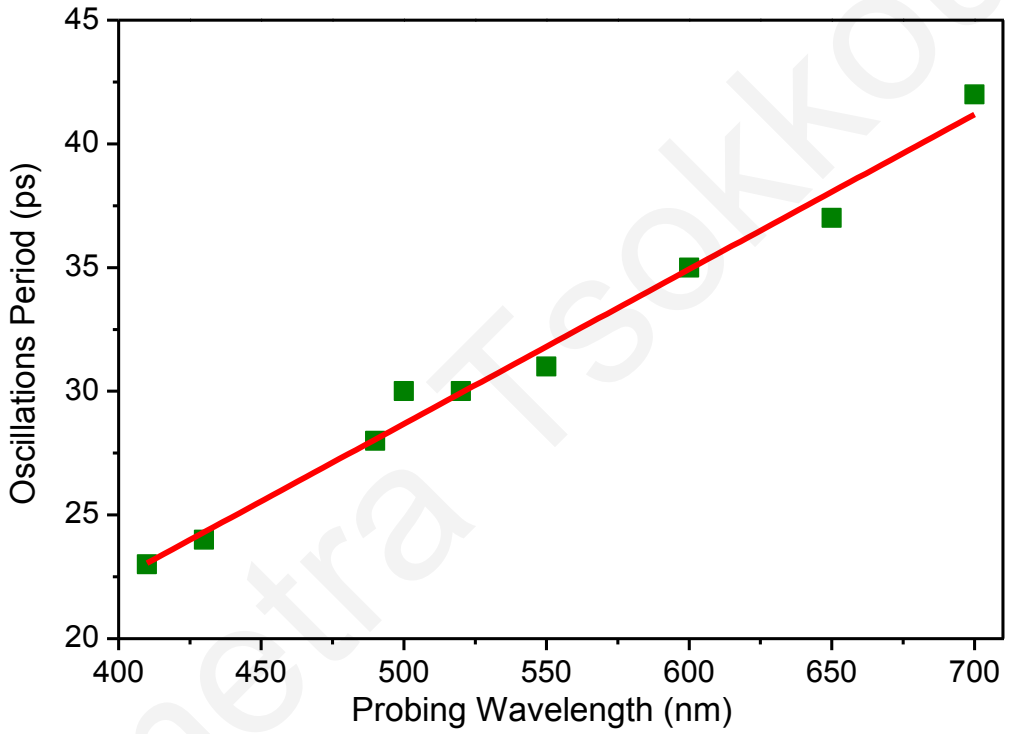

Figure 5.8. The period of oscillations is presented as a function of probing wavelength.

In our case, we believe that the observed oscillations are associated with coherent acoustic phonons generated at the Au nanoparticles and lunged into the In_2O_3 NWs. This wave modifies the local dielectric constants and creates a discontinuity. When the time delayed probe pulse incidents onto the sample, part of the light is reflected from the spatial discontinuity of the dielectric constant and the rest of the transmitted light reaches the Au interface where it gets reflected. Therefore as these acoustic phonons travel along the axis of the NWs, the Au surface and the strain wave surface act as an interferometer giving the oscillations observed in the reflectivity, and also transmission signal, as a function of time

delay between the pump and probe beams. Oscillations arise from the fact that the distance between the two surfaces is constantly changing with time, causing a periodic phase difference between the two reflected beams. A linear fit of the period of oscillation versus the probing wavelength was performed based on the equation (5.1),

$$\tau = \frac{\lambda}{2n\upsilon_s \cos\theta} \tag{5.1}$$

where λ is the probing wavelength, n is the refraction index, which is equal to n = 1.98 at 500 nm in the case of In_2O_3,[191] v_s is the sound velocity in the material, and θ is the angle between probe pulse and the normal to the sample. This linear fit gave an estimate of the sound velocity in indium oxide to be approximately $v_s = (4.1 \pm 0.5) \times 10^5$ *cm/s*.

5.2.3 Pump-Fluence Dependent Measurements for Conduction Band, Donor and Midgap States

To further improve our understanding of the carrier relaxation mechanisms in In_2O_3 NWs, transient absorption measurements were performed at several excitation fluences for different probing wavelengths. The normalized transient absorption measurements at probing wavelength of 350 nm, which corresponds to states above the band gap for different pump fluences between 3-635 μJ/cm^2 are shown in Fig. 5.9.

Additionally, the dependence of the absorption change signal on the pump beam intensity for probing wavelengths of 370 nm and 980 nm, corresponding at states below the band gap have also been studied and are shown in Figs. 5.10 and 5.11, respectively. In all investigated cases, carrier relaxation becomes faster as the carrier concentration increases, suggesting that Auger recombination is a contributing factor in the dynamics at the fluences used in this work. Since the recovery of the absorption signal becomes faster with increasing pump fluence, the possibility of saturation effect is ruled out.

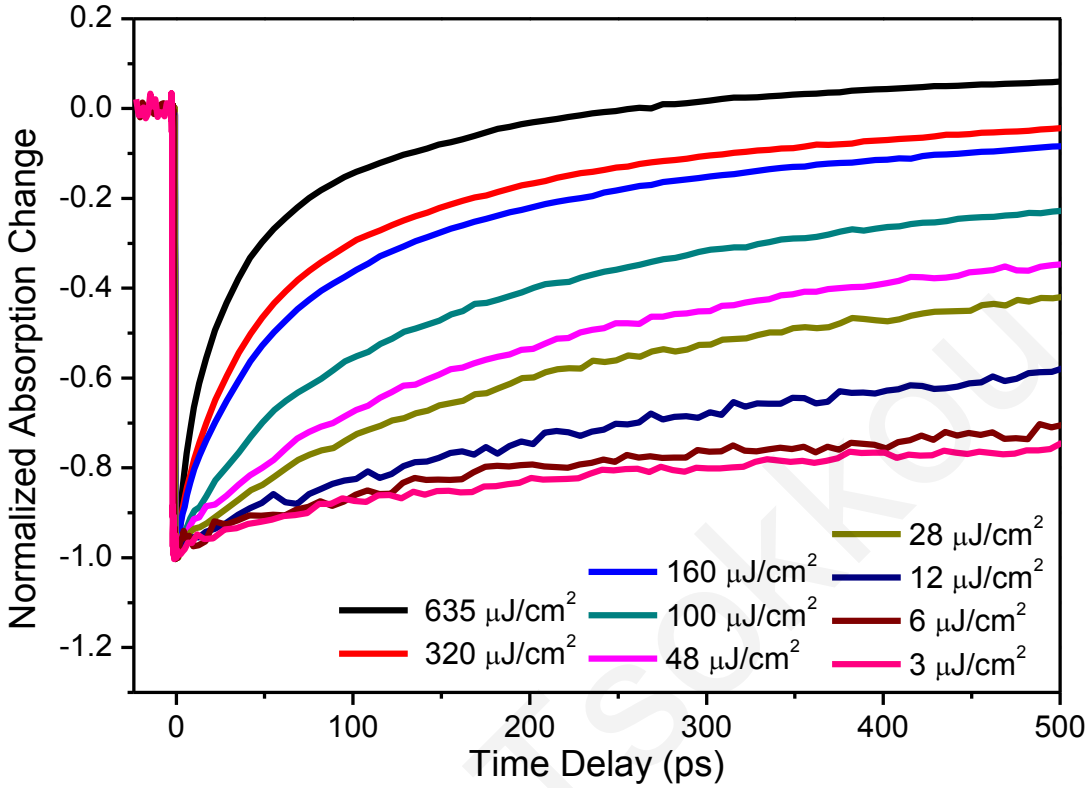

Figure 5.9. Time resolved transient normalized absorption measurements of the In_2O_3 NWs on quartz using ultrafast UV excitation pulses at 320 nm and probing pulses at 350 nm for different absorbed fluences.

For the smaller probing wavelengths (λ = 350 nm), Auger recombination appears to also have a significant role in the relaxation of the carriers. This effect diminishes with decreasing intensity and considered negligible for energies smaller than 3 μJ/cm^2. At higher intensities, relaxation times cannot be calculated due to the simultaneously presence of Auger effects and relaxation of carriers in lower energy states. When Auger effects are absent, the temporal profile of the induced absorption change is a direct measure of the relaxation of the photo-generated carrier out of the probing energy states. Using the normalized experimental data obtained at the lowest used pump intensity, a single exponential recovery $(\Delta A(t) = A_0 \exp(-t/t_1))$ is observed with a time constant of t_1 = 1.5 ns.

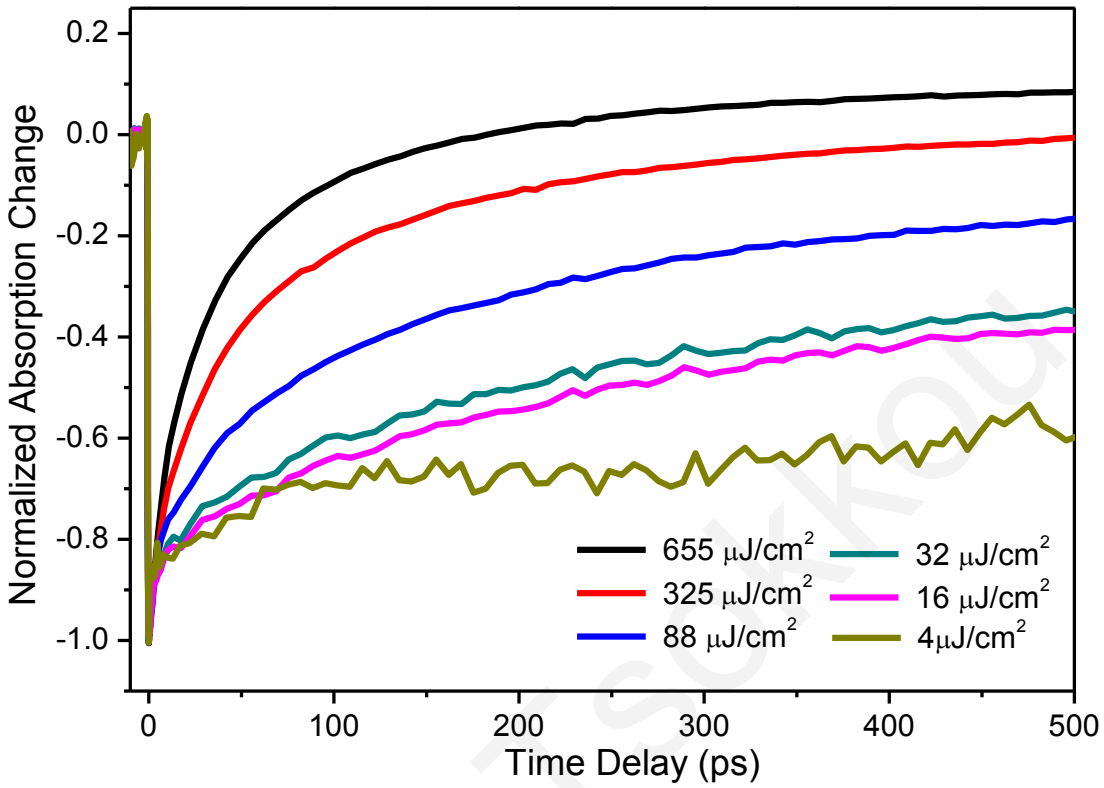

Figure 5.10. Time resolved transient normalized absorption measurements of the In_2O_3 NWs on quartz using ultrafast UV excitation pulses at 320 nm and probing pulses at 370 nm for different absorbed fluences.

When probing states just below the band gap (λ = 370 nm), strong influence of Auger recombination effects are also evident similar to the case of 350 nm (Fig. 5.10). Nevertheless, at early times a faster component appears at the absorption change signal even for low pump fluences, which is not present at 350 nm. Estimating relaxation times for the lowest measured pump fluences, best fitting was achieved when using bi-exponential time dependence, $(\Delta A(t) = a_1 \exp(-t/t_1) + a_2 \exp(-t/t_2))$, where a_i represents the percentage of carriers which participates in each mechanism. A fast relaxation time of 15 ps (a_1 = 20%) was detected, which is attributed to carrier relaxation from donor states to lower donor states or even midgap states via non-radiative processes. Additionally, a much slower time of 1.5 ns (a_2 = 80%) is detected corresponding to recombination of carriers. Here we should point out that intensity measurements taken at probing wavelengths of 390 nm depict similar temporal behaviour as that at 370 nm.

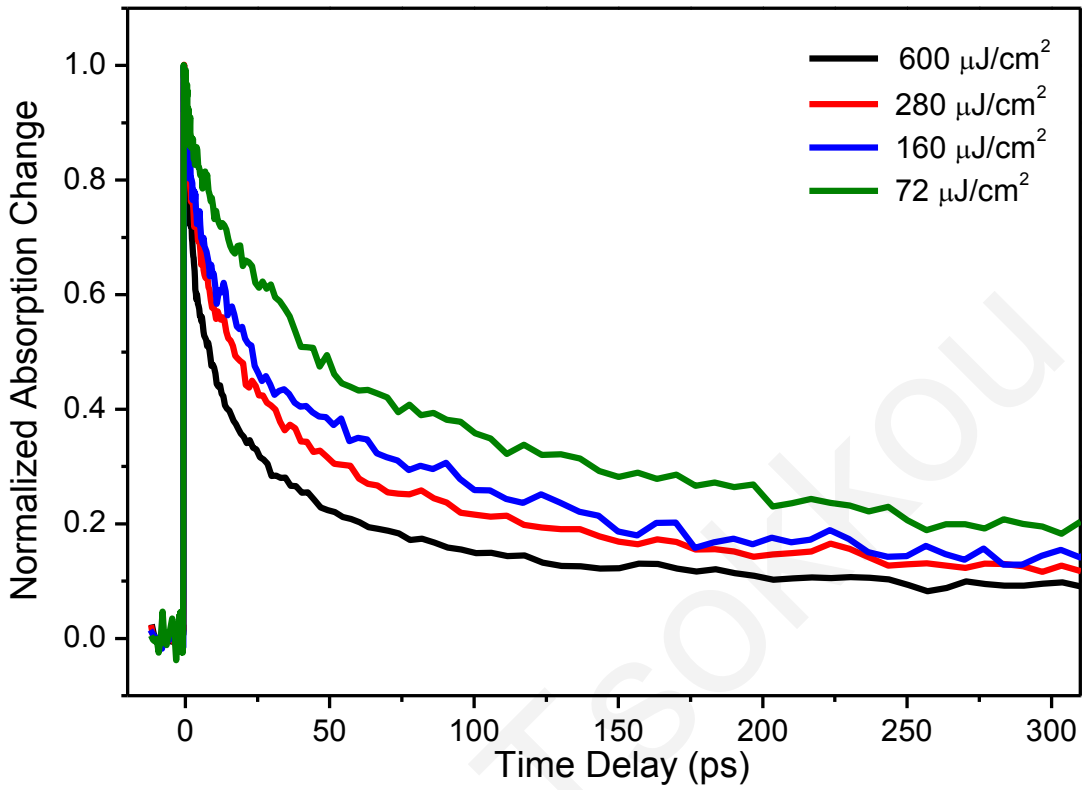

Figure 5.11. Time resolved transient normalized absorption measurements of the In_2O_3 NWs on quartz using ultrafast UV excitation pulses at 320 nm and probing pulses at 980 nm for different absorbed fluences.

The data in Fig. 5.11 clearly show that free carrier absorption is the main contributing factor for a probing wavelength equal to 980 nm. Furthermore, the temporal behaviour is different from that seen when probing above or just below the band gap. This suggests that we are actually probing within the band gap and most likely the midgap states. This is further supported by the fact that Auger recombination is less pronounced at the same fluence than when probing at 350 nm, which is attributed to the distribution of the photogenerated carriers in the large number of states below the band edge. Measurements at the lowest fluence shown in Fig. 5.11 depict a fast relaxation time constant of 26 ps (a_1 = 40%) which is attributed to transitions between surface/defect states. In addition, a slow relaxation time is also present which is of the order of hundreds of picoseconds (~300 ps, a_2 = 60%) attributed to non-radiative recombination.

	a_1	t_1 (ps)	a_2	t_2 (ps)
Conduction band states	1	1500	---	----
Band-tail states	0.2	15	0.8	1500
Midgap states	0.4	26	0.6	300

Table 5.2. Fitting parameters from the experimental data from different kind of states when using the lowest pump fluence.

The fitting parameters extracted from the experimental data are summarized in the Table 5.2. The relaxation times for *i* mechanism as well the percentage of carriers that leave the detected states through *i* mechanism are shown. We have attempted to also perform non-degenerate measurements using pump wavelength at 400 nm (E_{photon} = 3.1 eV) corresponding to states located below the band gap but no signal was obtained. This result indicates that a small number of defect states are located at the region below 3.1 eV, which is also consisted with the fact that no state filling is observed for wavelengths larger than 430 nm (E_{photon} = 2.9 eV).

5.2.4 Band diagram of In_2O_3 Nanowires

To clarify carrier dynamics obtained from time resolved absorption spectroscopy experiments, a diagram of the band structure of In_2O_3 NWs and carrier evolution toward equilibrium is shown in the Fig. 5.12. As it has been found from steady state transmission spectroscopy experiments, the energy band gap of In_2O_3 NWs is 3.5 eV.

Under UV ultrashort excitation at 320 nm (E_{photon} = 3.87 eV), carriers are generated into the conduction band states that successively relax into lower energy states. Intensity measurements performed at 350 nm probing wavelength reveals that carriers from the conduction band states recombine at times 1.5 ns, probably via nonradiative mechanism, since no photoluminescence has been observed for In_2O_3 from the edge of the conduction band.

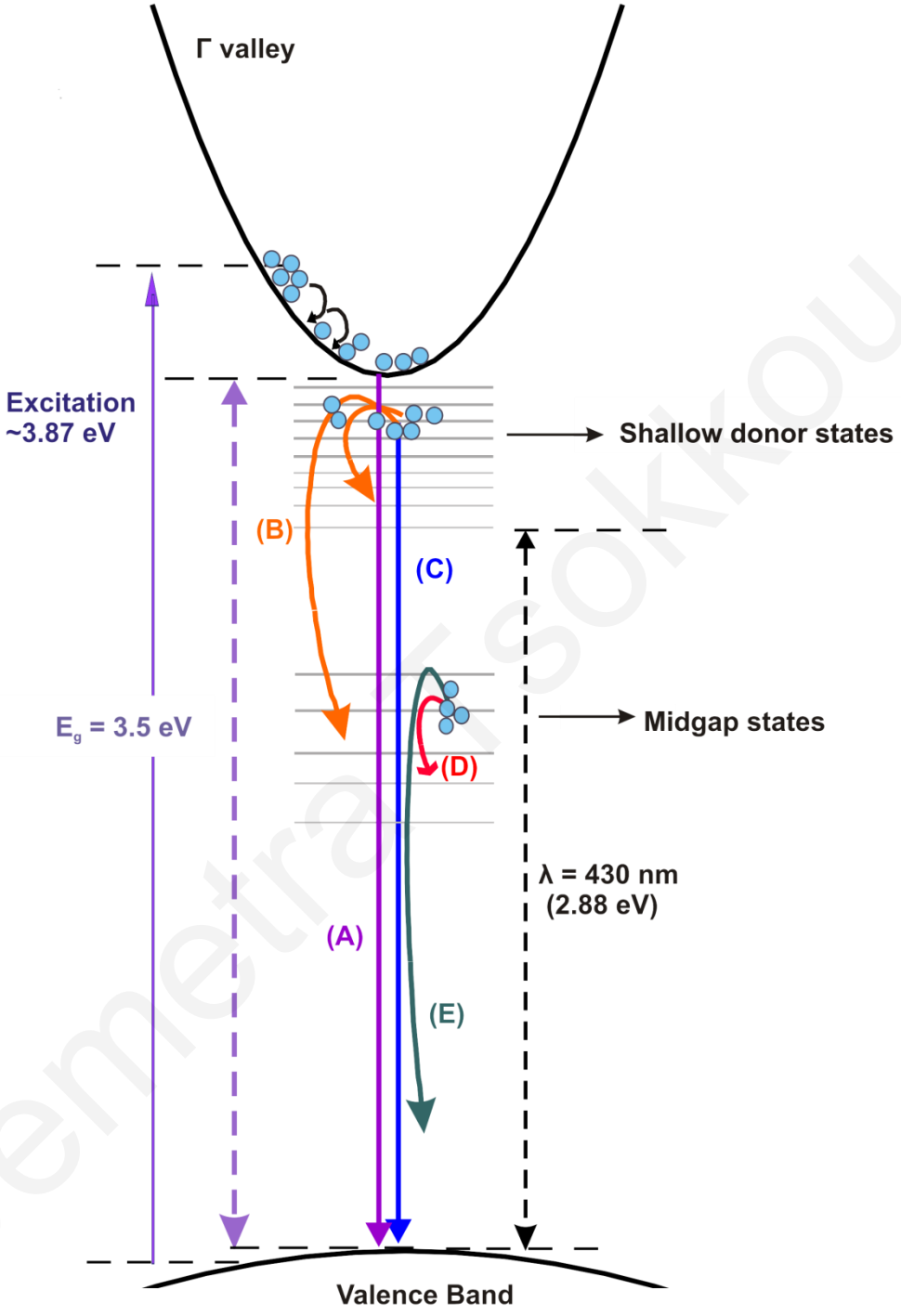

Figure 5.12. A schematic band diagram of In_2O_3 NWs determined by the analysis of time resolved non-degenerate absorption and steady state transmission measurements.

This mechanism is indicated as Mechanism *A* in the band diagram. Furthermore, carriers from the shallow donor states (band-tail states), relax via two mechanisms. A fast relaxation time at 15 ps is attributed to non-radiative recombination of carriers into lower states, such as donor states or even midgap states, mentioned as Mechanism *B*. Additionally, carriers in these states recombine with states in the valence band with similar times as the relaxation of carriers in the conduction band states – Mechanism *C*. Furthermore, midgap states are located in the region below 2.9 eV, are also detected. From midgap states, carriers move to lower midgap states with times 26 ps, associated with mechanism C. Carriers in these states are shown to recombine probably non-radiatively with times of ~ 300 ps – Mechanism *D*.

5.3 Conclusions

In summary, In_2O_3 NWs are grown via APCVD and thermal evaporation of In at 700 ^oC in Ar atmosphere. In this process, it was found that introduction of a small amount of O_2 into the system promotes NWs growth. NWs with an average diameter of 100 $\pm$ 20 nm and length up to few micrometers are obtained. VLS mechanism is responsible for the In_2O_3 NWs growth and Au is an appropriate choice of a catalyst. Steady state transmission measurements provided an estimate of the energy gap of these NWs to be 3.5 eV.

Ultrafast carrier dynamics in In_2O_3 NWs following excitation above the direct band gap was investigated in detail. Transient absorption measurements revealed that state filling is the dominant effect for states above the conduction band edge, as well as for states residing below the conduction band edge demonstrating the importance of shallow traps -associated with defect states- in the relaxation of photogenerated carriers.

Furthermore, time resolved intensity measurements revealed the important role that Auger recombination plays in the relaxation of ultrafast photogenerated carriers and provided the maximum fluence (3 $\mu J/cm^2$) where Auger recombination may be considered negligible. Transient measurements in this low-fluence regime for carriers above the band gap revealed single exponential recovery of the order of 1.5 ns associated with recombination of the photogenerated carriers. Similar behavior has also been observed for the photogenerated

carriers distributed within the shallow traps just below the band edge. Furthermore, measurements at longer probing wavelengths provided an estimate of the nonradiative relaxation of carriers (~ 300 ps) which are distributed among the midgap states.

Furthermore, time-resolved measurements revealed an oscillatory behavior in the reflection signal for probing wavelengths longer than 390 nm. This behavior is attributed to acoustic phonons which provided an estimate of the sound velocity in In_2O_3 NWs to be $v_s = (4.1 \pm 0.5) \times 10^5$ cm/s.

Chapter 6

Carrier Dynamics and Transport Properties in SnO_2 Nanowires

In this Chapter, the experimental results for SnO_2 NWs are presented. Initially, a brief overview on the work that has been carried in the past on the SnO_2 NWs synthesis is given. Then, the optimum growth conditions of these SnO_2 NWs via APCVD, as well as low pressure CVD are described. The characterization of SnO_2 NWs has been done using SEM, XRD, steady state absorption spectroscopy and PL spectroscopy measurements.

The main focus in this Chapter is ultrafast characterization of SnO_2 NWs that has been performed using the time resolved absorption spectroscopy, as well as TDTS and TRTS experiments. Carrier dynamics have been investigated utilizing both techniques taking advantage of their complementary information. The results reveal the important role of shallow donor and deep defect states in the relaxation of photogenerated carriers. Transient absorption and THz intensity measurements reveal that Auger recombination plays an important role here. Based on ultrafast carrier dynamic characterization, a schematic of a band diagram representation for SnO_2 NWs is presented. Furthermore, TDTS has been used to derive the complex optical constants and intrinsic conductivity spectrums in SnO_2 NWs in the THz region. Moreover, TRTS were performed using different pump fluences to calculate the complex photoconductivity spectrum using UV excitation pulses. The conductivity data are explained using the Drude-Smith model and conclusions about the transport properties of carriers in SnO_2 NWs are extracted.

6.1 Synthesis of SnO_2 Nanowires

In this section, a brief overview for the growth of SnO_2 NWs is given. Then, the optimum conditions of the SnO_2 NWs synthesis via APCVD and low pressure CVD techniques are discussed. In addition, the characteristics of SnO_2 NWs determined via SEM, XRD, steady state transmission and PL measurements are presented and discussed. For TRTS measurements, a smaller fraction of SnO_2 NWs had to be transferred onto a quartz substrate by drop casting after being harvested from the parent substrate by sonication.

6.1.1 Overview of SnO_2 Nanowires

1-D SnO_2 nanostructures, and especially NWs, have been synthesized by a variety of techniques, including CVD,[192–197] laser ablation of pure tin in an oxidizing Ar/O_2 atmosphere,[75] oxidation of electrodeposited Sn wires[198] and solvothermal synthesis.[199] High quality SnO_2 NWs have been obtained using electrodeposition, where NWs have grown in porous alumina membrane in an oxidizing atmosphere.[200] A drawback of this process is that it involves long growth times.

Different methods have been reported on the synthesis of SnO_2 NWs via CVD technique. Several studies report the growth of SnO_2 NWs via carbothermal reduction of SnO_2 powder.[192–194] Different kinds of carbon have been utilized including activated carbon, graphite and carbon nanotubes. Synthesis has also been achieved via oxidation of Sn vapor under continuum flow of oxygen at elevated temperatures (800-100 ^oC) at low pressure (10^{-2} Torr)[195] or thermal evaporation of Sn at 900 ^oC at atmospheric pressure.[196,197]

In most cases, the synthesis of SnO_2 NWs is achieved in the presence of Au catalyst nanoparticles via the VLS mechanism, however, self catalysis VLS mechanism has also been reported in the case of SnO_2 NWs by Li *et al.* via direct evaporation of SnO nanoparticles at 1550 ^oC.[201]

6.1.2 Optimum Growth Conditions

In our case, SnO_2 NWs were initially grown using APCVD. The growth conditions are given in detail below and are also summarized in the Table 6.1. Pure Sn powder was used as a source material and Au as a catalyst.

Firstly, 0.2 g of Sn powder (Aldrich, Mesh 100, < 150 μm 99.5 %) was weight. Then, the source material was placed into a quartz boat next to a Si (001) or quartz substrate, which is coated with 0.5 nm thin film of Au. To purge the system, Ar was introduced for 10 min under a flow of 500 sccm. Then, the temperature increased up to 800 ^{o}C using a ramp rate of 30 ^{o}C/min under 100 sccm Ar flow. During the growth process, the temperature of the reactor and Ar flow were maintained at 800 ^{o}C and 100 sccm, respectively for 60 min. For these NWs, no oxygen had to be introduced into the system during the growth process, as has been observed in the case of In_2O_3 NWs. In the last step of the experiment, the sample was cooled down under a 100 sccm Ar for 45 min, while the sample was removed from the reactor after cooling down to room temperature.

Step	Name	Gas flow (sccm)	Temperature (^{o}C)	Duration (min)
1	**System Purge**	500 Ar	25	10
2	**Rise of Temperature**	100 Ar	25→800	26
3	**Growth Process**	100 Ar	800	60
4	**System Cooling**	100 Ar	800→25	45

Table 6.1. Growth parameters of SnO_2 NWs using APCVD technique.

SnO_2 NWs were also observed at temperatures as low as 700 ^{o}C, but at a lower yield. Optimum temperature to obtain high yield of SnO_2 NWs and a uniform coverage of the substrate is 800 ^{o}C. Our observations are in agreement with the optimum conditions reported by Johnson *et al.*[196] and Mazeina *et al.*[197] that have synthesized SnO_2 NWs without any use of oxygen during the growth process at 900 ^{o}C. In addition, no growth was observed in the

absence of Au catalyst from the substrate, suggesting that VLS mechanism is responsible for the SnO_2 NWs growth, in agreement with other reports with similar experimental conditions.[196,197]

Step	Name	Gas flow (sccm)	Temperature (°C)	Duration (min)
1	**System Purge**	500 Ar	25	10
2	**Rise of Temperature**	100 Ar	25→800	26
3	**Growth Process**	600 Ar 10 O_2	800	60
4	**System Cooling**	100 Ar	800→25	45

Table 6.2. Growth parameters of SnO_2 NWs grown using LPCVD technique.

SnO_2 NWs have also been grown using a slightly different process namely low pressure CVD (LPCVD). Prior to growth, the tube was evacuated to a pressure of $1x10^{-3}$ mbar. SnO_2 NWs were grown on 1 nm Au/Si (001) via thermal oxidation of Sn powder at 800 °C under a flow of 600 sccm Ar:10 sccm O_2 for 1 hr. The growth conditions are summarized in Table 6.2. These growth conditions are similar to that used by Yang *et al.*.[195] When low pressure is used, the residual oxygen from the system is eliminated. This results in the increment of the In vapour pressure during the step that the temperature of the reactor rises.

6.1.3 Characterization of SnO_2 Nanowires

Steady state transmission, PL, SEM and XRD where utilized to characterize the NWs. SEM images of the investigated samples are shown in Fig. 6.1. From the images, we estimate the SnO_2 NWs have diameters of 50-100 nm and lengths up to micrometer scale.

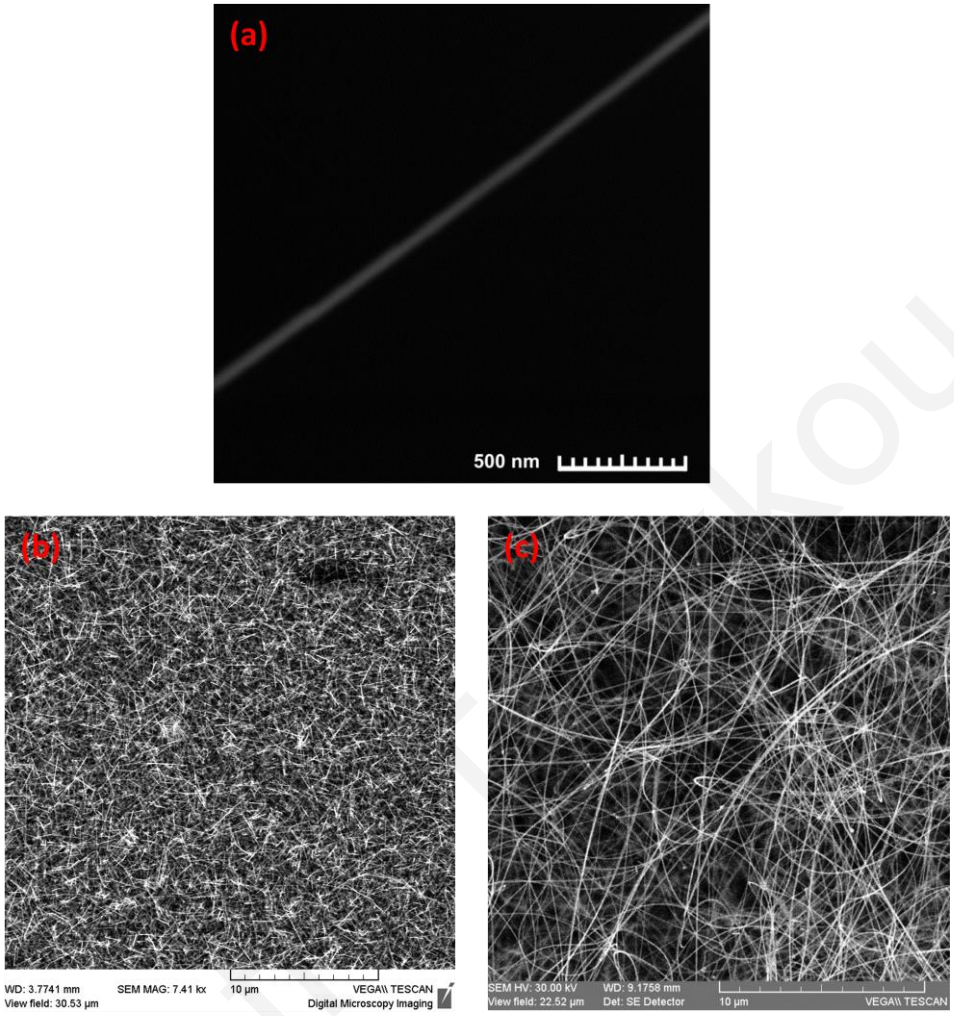

Figure 6.1. Typical SEM images of SnO_2 NWs; (a), (b) SEM images of APCVD-grown SnO_2 NWs on Si substrate; and (c) SEM image of LPCVD-grown SnO_2 NWs on Si substrate.

Furthermore, the diameter of the SnO_2 NWs was found to be uniform along their length. The high density of the NWs and the uniform deposition on the substrate are evident in the SEM image (Fig. 6.1 (b)). It is also revealed that the APCVD-grown SnO_2 NWs have lengths up to few micrometers ($\leq$ 5 µm).

A SEM image of the SnO_2 NWs grown via LPCVD is shown in the Fig. 6.1 (c). The main difference observed between the SnO_2 NWs synthesized via LPCVD is their longer length exceeding the 10 µm. Similar results have been obtained for SnO_2 NWs grown on quartz substrate.

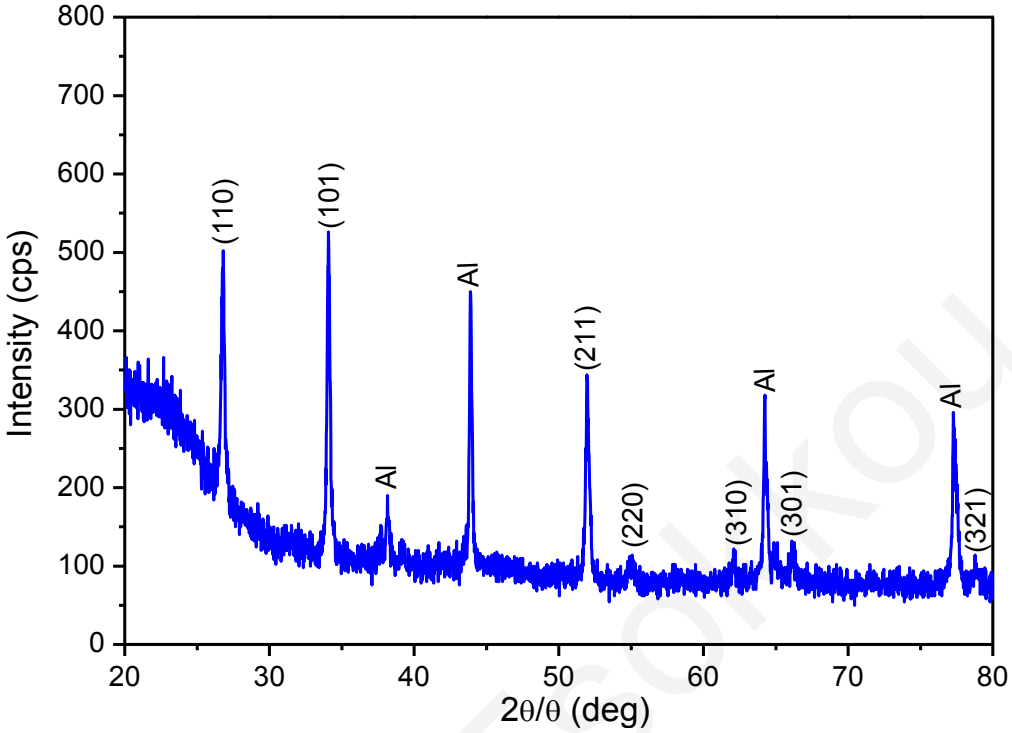

Figure 6.2. XRD spectrum of the SnO_2 NWs grown at 800 ^oC on 0.5 nm Au/quartz. The peaks shown are attributed to crystallographic planes of SnO_2 NWs, except those that originate from the sample holder and are identified in the pattern.

In order to examine the crystal structure of the grown material, XRD measurements were performed on the as-synthesized samples. Fig. 6.2 shows the diffractogram of a sample grown on quartz substrate. The SnO_2 NWs grown at the optimum temperature i.e. T_G = 800°C on quartz are characterized by the (1 1 0), (1 0 1), (2 1 1), (2 2 0), (3 1 0), (3 0 1), (3 2 1) peaks in X-ray diffraction spectra. After subtracting the peaks caused by the aluminum sample holder, the remaining diffraction peaks can be indexed to the tetragonal rutile structure of SnO_2, with lattice constants of a = 4.734 Å and c = 3.185 Å.[202]

In Fig. 6.3 the absorption coefficient spectrum of SnO_2 NWs on quartz substrate is shown as a function of photon energy in the region between 1.5 and 5 eV. The absorption spectrum has been calculated from the measured transmitted signal, as in the case of In_2O_3 NWs. In the inset of the Fig. 6.3, the square of absorption spectrum is given, which is used for the estimation of the energy band gap of the SnO_2 NWs. In this case, by extrapolating the

linear region of square of absorption coefficient (α^2) versus photon energy plots to $\alpha^2 = 0$, the band gap of the direct semiconductor SnO_2 NWs is found to be 3.77 eV.

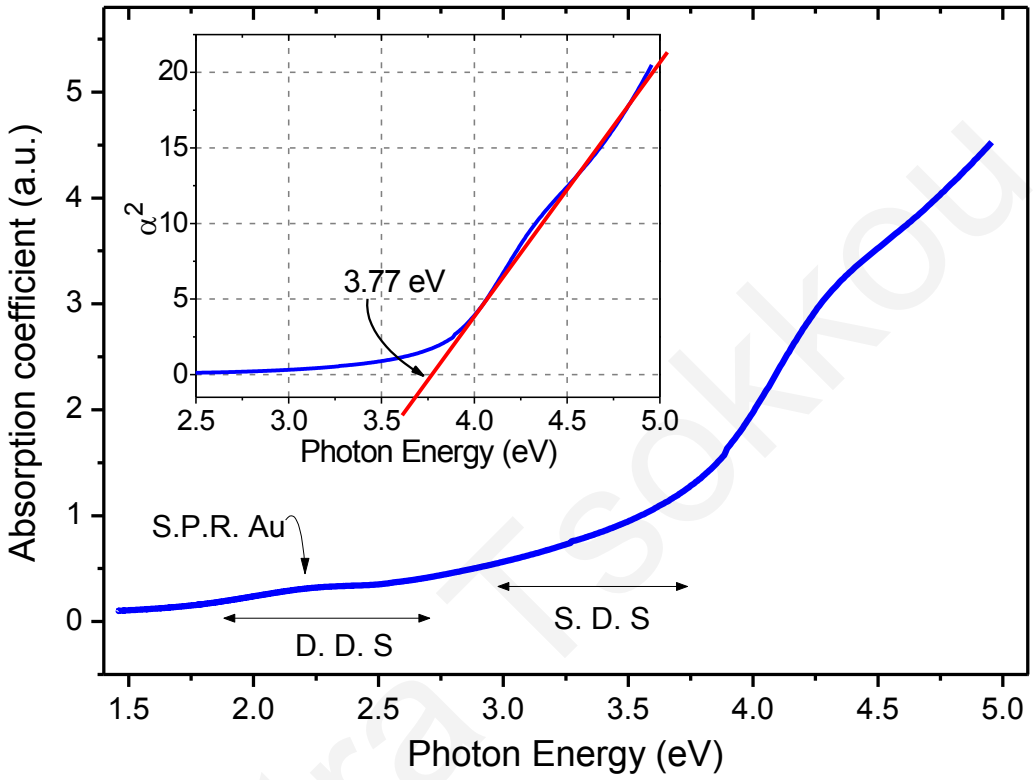

Figure 6.3. Steady state transmission measurements carried out on SnO_2 NWs using a UV/VIS/IR spectrometer. The upper corner inset shows a plot of the square of the absorption vs. incident photon energy, providing us with an estimate of the bandgap energy 3.77 eV. There are two broad absorption bands below the bandgap; D.D.S – deep defect states and S.D.S. – shallow donor states.

An interesting behavior is the two broad absorption bands that are evident for energies below the band gap of SnO_2 NWs in the region between 1.8 - 3.7 eV. These states are usually attributed to defects generated into the SnO_2 NWs during the growth process. The first band is located just below the band gap of the SnO_2 NWs due to shallow defect states. The second band is observed at lower energies due to deep defect states. The role of these states in carrier relaxation will be studied using time resolved absorption measurements, which are extensively discussed in the following sections. An absorption peak in the region between 2.1-2.5 eV, is attributed to the surface plasmon resonance of Au nanoparticles.

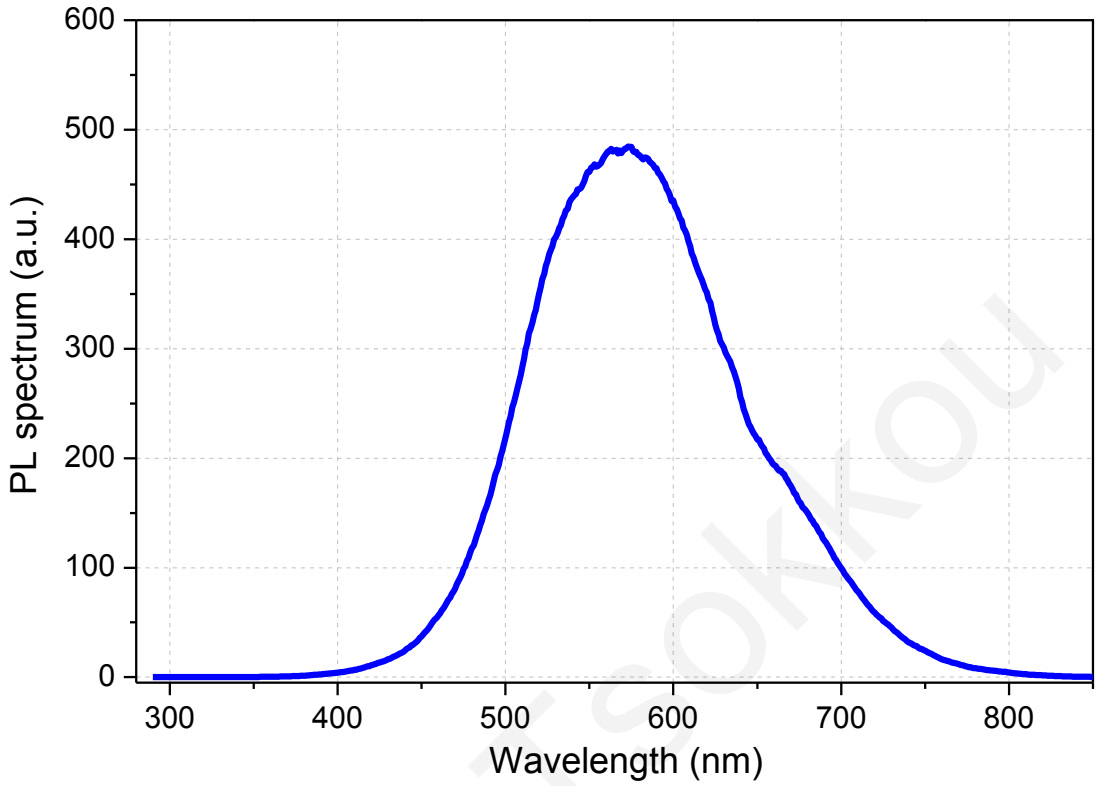

Figure 6.4 PL spectrum of as-grown SnO_2 NWs at room temperature using excitation at 266 nm.

Furthermore, PL measurements were performed at room temperature to give information for the radiative recombination mechanisms that take place in the SnO_2 NWs. The excitation source, was an ultrafast Ti:Sapphire amplifier centered at 800 nm, with time duration of 75 fs and a repetition rate of 250 kHz. In order to photoexcite carriers into the conduction band states the fundamental wavelength was converted into the UV region via nonlinear mixing. Specifically, third harmonic frequency mixing of the 800 nm ultrafast pulses resulted into 266 nm. The energy per pulse incident on the sample was 0.08 pJ over a spot of 2 mm in diameter.

The PL spectrum of the as-grown SnO_2 NWs on Si substrate is shown in the Fig. 6.4. A broad peak centered at ~ 573 nm (~ 2.2 eV) is detected, which is attributed mainly to oxygen defect states located within the band gap. Our results are consistent with several other works on these NWs.[197,201,203–206] From these studies, no band edge emission UV luminescence has been observed for SnO_2 NWs.

6.1.4 Nanowire Transfer

Following SnO_2 NWs synthesis, part of the NWs had to be transferred onto a different substrate for the fabrication of lower density SnO_2 NWs samples. The most straightforward process is achieved via sonicating the NW sample in a solvent. In our case, isopropyl alcohol (IPA) is an appropriate choice.

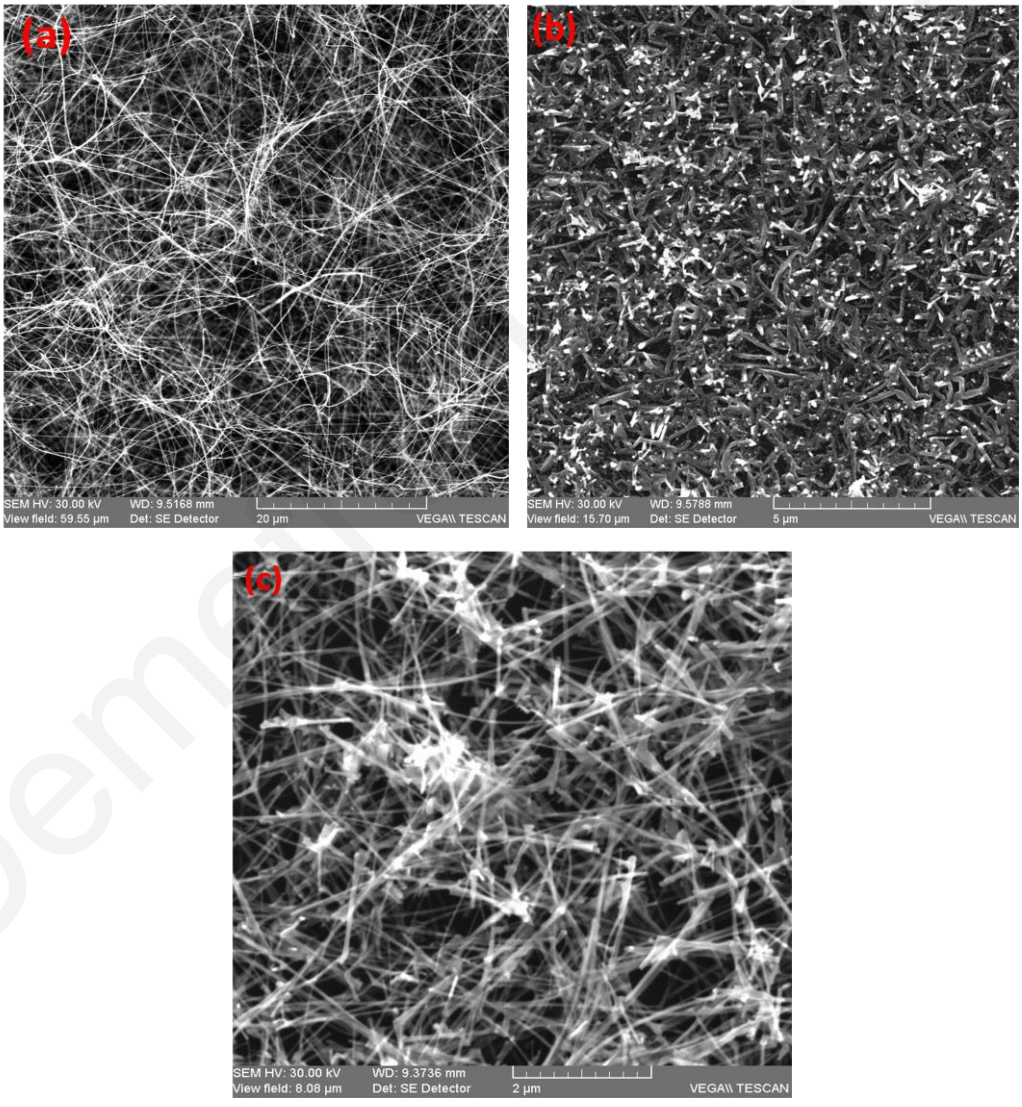

Figure 6.5. SEM images of (a) as-grown SnO_2 NWs before any processing of the sample, (b) the same sample after 5 min of sonication using IPA as a solvent and (c) a sample of transferred SnO_2 NWs.

The process of transferring the NWs is as follows: initially, the as-grown SnO_2 NWs sample is submerged into a small amount of IPA solvent (usually ~1 ml), where the NWs are suspended via sonication. For this process, a Cole-Parmer 8892 ultrasonic cleaner is used and the sample is sonicated for few minutes (≈ 5 min). Then by using a pipette, few drops of the liquid are transferred from the solution onto a new silicon or quartz substrate.

Fig. 6.5 shows SEM images of (a) as-grown SnO_2 NWs and (b) the same sample after 5 min of sonication in IPA. These SEM images confirm that a large fraction of NWs is transferred into the solution. A SEM image of the transferred SnO_2 NWs onto a different substrate is shown in the Fig 6.5 (c). The only difference observed between as-grown and transferred SnO_2 NWs is that few NWs break into shorter fragments. Longer times of sonication intensify this effect and more NWs with shorter length are observed.

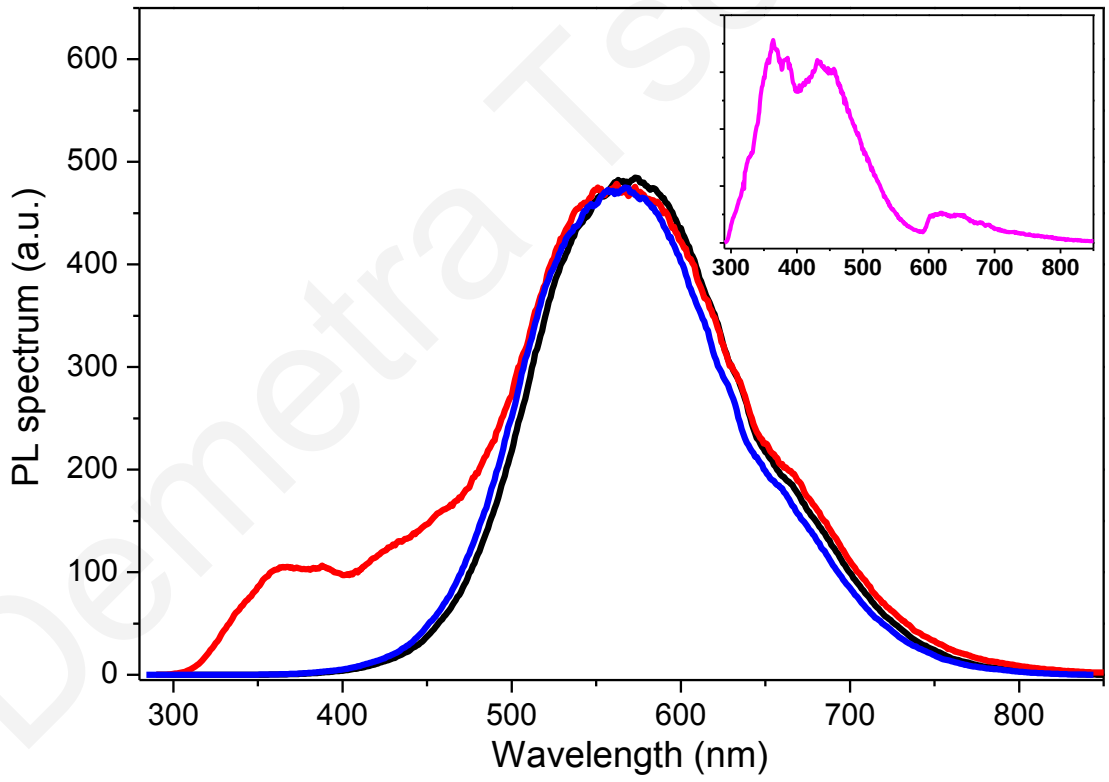

Figure 6.6 PL spectrum of (a) as-grown SnO_2 NWs (black line), (b) transferred SnO_2 NWs using IPA as a solvent (red line) and (c) previous sample after heated at 100 ^oC for 2 hours (blue line). Additionally, in the inset of the figure, PL spectrum of IPA is included. All different samples were excited with ultrashort pulses at 266 nm.

To verify that no changes have been induced on the surface of the NWs due to the transport of SnO_2 NWs onto a different substrate, PL measurements were taken at room temperature. PL measurements performed on as-grown SnO_2 NWs (black line) and transferred SnO_2 NWs when IPA is used as a solvent (red line) when using excitation at 266 nm, are seen in the Fig. 6.6. In both cases, SnO_2 NWs were transferred on Si substrate. For clarity, in the inset of the Fig. 6.6 the PL spectrum of pure IPA is presented.

For the as-grown SnO_2 NWs, a broad band between 400-800 nm is seen. In addition with the peak related to the SnO_2 NWs, an extra broad peak is evident in the PL spectrum of the transferred SnO_2 NWs, which is located in the region between 290-500 nm. This peak is related to the remaining amount of IPA onto the substrate, as it is clearly evident from the PL spectrum of the IPA solvent shown in the inset of the Fig. 6.6. However, it is clear that no significant change is caused to the PL peak originating from the SnO_2 NWs. To eliminate the contribution of the solvent, the substrates were placed onto a hot-plate at an elevated temperature larger than the solvent boiling point (82.5 ^{o}C) to evaporate the solvent prior to further investigation. Therefore, the transferred SnO_2 NWs were heated at 120 ^{o}C for 2 hours. Afterwards, PL measurements were repeated as seen with a blue line in the Fig. 6.6 and it is obvious that the contribution of the additional peak is eliminated.

6.2 Carrier Dynamics in SnO_2 Nanowires

Until now, the optical properties of SnO_2 NWs have only been investigated using conventional steady state techniques. However, no ultrafast characterization has been performed on this NW system. In the following sections, we present an investigation of the carrier dynamics in photoexcited SnO_2 NWs using different ultrafast spectroscopic techniques. First, degenerate and non-degenerate absorption change measurements using time resolved absorption spectroscopy are presented and discussed. Following this, the experimental results of carrier dynamics using time resolved THz transmission spectroscopy are given and discussed. Similarly to the case of GaN and In_2O_3 NWs, a schematic

representation of a band diagram of the SnO_2 NWs based on our experimental results is proposed.

6.2.1 Carrier Dynamics in SnO_2 Nanowires Using Time Resolved Absorption Spectroscopy for Above Band Gap Excitation

Time resolved absorption spectroscopy was performed using an ultrafast amplifier system. The ultrashort pump pulses wavelength was converted via the OPA to 310 nm (E = 4.00 eV). This excitation will generate carriers into the conduction band states of SnO_2 NWs. Both white light generation setups were used to extend the available probing wavelengths in the spectral region between UV and IR. Measurements of reflection and transmission change have been carried out for each case to calculate the absorption change using the equation (3.1).

6.2.1.1 Probing Wavelength Dependent Measurements

The experimental results of differential absorption in SnO_2 NWs using excitation pulses at 310 nm (E_{photon} = 4.00 eV) and probing wavelengths between 310-750 nm, corresponding to energies from 4.00 eV to 1.65 eV, are shown in the Fig. 6.7. Measurements are shown for time delays up to 500 ps. The pump fluence used for all measurements was constant at 500 $\mu J/cm^2$.

Excitation of SnO_2 NWs with ultrashort laser pulses with photon energy larger than the band gap energy, results in the generation of electron–hole pairs into the conduction band states. At short times, carriers undergo several stages of energy relaxation and spatial redistribution and conduction states below the initial excitation states are occupied with carriers, similarly with energy states below the band gap.

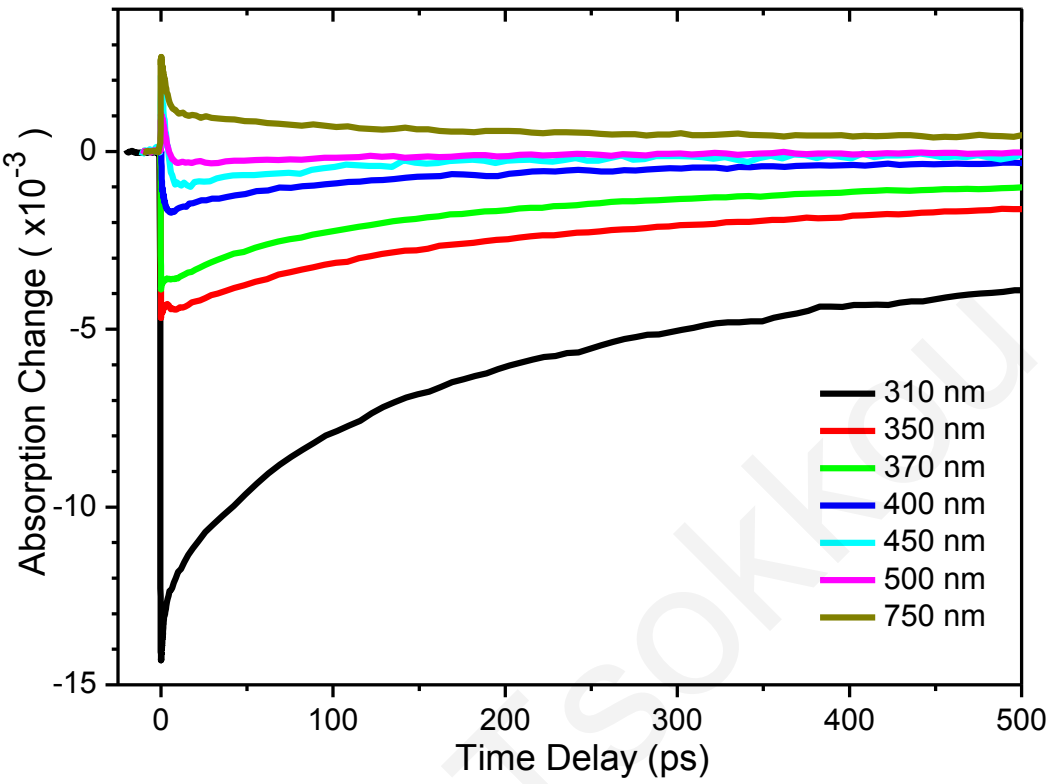

Figure 6.7. Non-degenerate, time-resolved, transient absorption measurements of the SnO_2 NWs using ultrafast excitation pulses at 310 nm and probing pulses in the range of 310–750 nm.

Fig. 6.7 depicts the temporal behavior over a series of probe wavelengths corresponding to probing states with energies above and below the band gap of the SnO_2 NWs. It is clearly evident that the behavior of the absorption change is different for the various probing wavelengths used, due to detection of different kind of energy states. What is common in the different absorption change measurements is the sharp increase or decrease of the induced absorption at times close to zero that is followed by a long recovery toward equilibrium. For probing wavelengths into the UV region (λ = 310-370 nm), strong negative signal is detected, which its maximum becomes progressively less negative as the probing wavelength increases. For probing wavelengths between 450-500 nm, a small contribution of a positive signal is also detected at times near zero, but very quickly the signal changes sign and becomes negative. Additionally, the overall absorption change becomes positive for probing wavelength at 750 nm.

Negative or positive absorption change observed at different probing regions is attributed to the different effects detected in each case, namely state filling or free carrier absorption. The change of sign referred above for probing wavelengths between 450- 500 nm, is a consequence of the presence of both effects, while the sign is determined by the dominant effect in different time delays. These observations suggest that while the state filling effect is the dominant effect at probing wavelengths close to the excitation region, the free carrier absorption effects are also present for probing wavelengths larger than 350 nm, and these effects become stronger as the wavelength increase. The presence of the free carrier absorption effects are also supported by the "dip" observed at probing wavelengths between 350-370 nm at time delays near zero.

Additionally, the observation of negative signal for probing wavelengths smaller than 500 nm is indicative of the existence of defect states at the corresponding energies. This is further supported by steady state transmission measurements in these SnO_2 NWs. These defects states are the shallow donor states located just below the band gap.

Measurements for probing wavelengths in the region between 520-600 nm are not shown here, since the observed signal is attributed to the surface plasmon resonance of the Au nanoparticles required for the growth of SnO_2 NWs, similar to the results obtained for In_2O_3 NWs.

6.2.1.2 Pump-Fluence Dependent Measurements for Conduction Band and Shallow Donor States

To further investigate the relaxation dynamics in the SnO_2 NWs from the conduction band states, we have performed degenerated time-resolved differential absorption measurements at 310 nm for different pump fluences. Fig. 6.8 shows the degenerate transient normalized differential absorption for excitation fluences covering a range between 50 to 500 $\mu J/cm^2$ and time delays up to 500 ps.

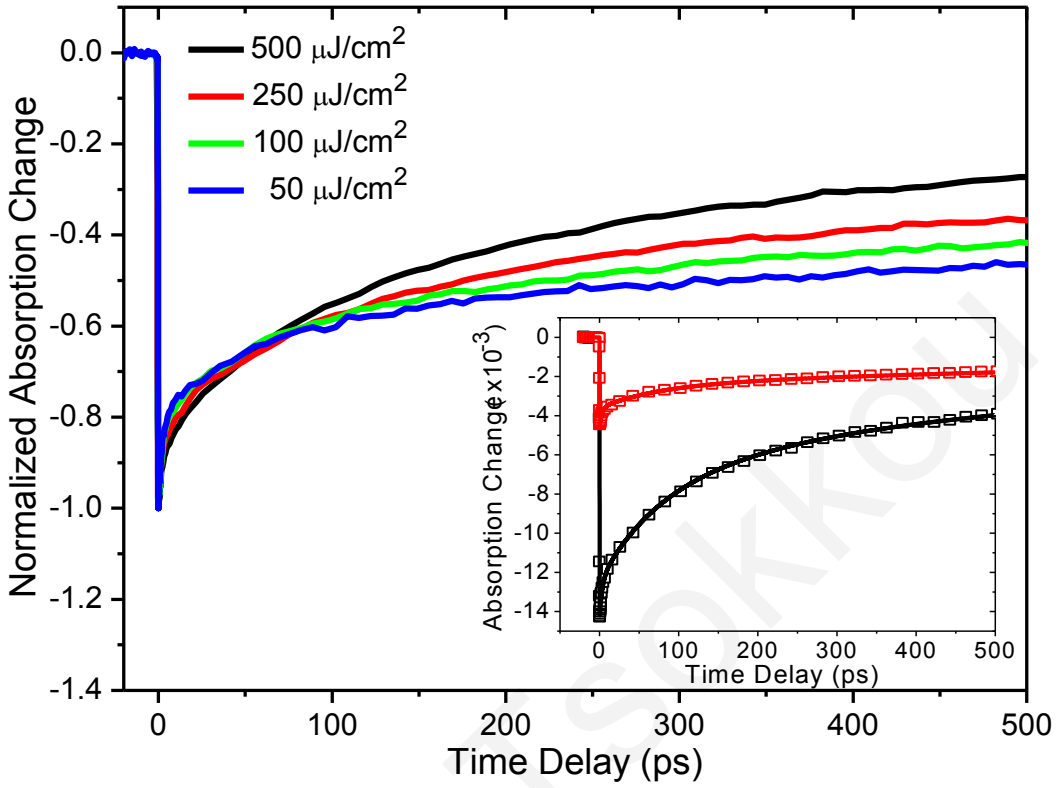

Figure 6.8. Time resolved transient normalized absorption measurements of the SnO_2 NWs on quartz substrate using ultrafast both pumping and probing pulses at 310 nm for different pump fluences between 50-500 μJ/cm^2. In the inset, the experimental data of absorption change are shown (points) in addition to the best fits (solid lines) obtained using a simple model that includes multiexponential decays and Auger recombination.

In degenerate pump-probe experiments where the probing and excitation beams have the same wavelength, one expects to see a negative change in absorption. This is consisted with the results obtained from our experiments. Since the excitation wavelength corresponds to energies above the band gap, conduction band states are populated with carriers and strong negative signal due to state filling effects is observed. The temporal evolution of the normalized absorption change indicates that the decays are carrier density dependent for the range of fluences used in this study. Specifically, it is evident that the signal recovery becomes faster on the long time scale as the pump fluence increases. This suggests that Auger recombination maybe a contributing factor to the carrier dynamics in SnO_2 NWs.

Given that Auger recombination is considered negligible at the lowest pump fluence (= 50 μJ/cm^2) one may use simple multi-exponential fit to the experimental data. A three exponential decay function is necessary to sufficiently fit the data. The first component corresponds to a fast relaxation time of t_1 = 2.4 ps (18%), which we believe is attributed to carriers moving out from the conduction band states into shallow donor states. The two slower relaxation components obtained from the fit were t_2 = 68 ps (22%) and t_3 = 2.3 ns (60%). Taking into account that no luminescence is observed for SnO_2 NWs from the band edge near 3.77 eV and the fact that the lowest band to band transitions are symmetry forbidden,[207] the slow relaxation time cannot be assigned to recombination of carriers from the conduction band edge. Therefore, we believe that the slow relaxation time is associated with the time needed for the carriers to recombine from the shallow donor and deep defect states. Due to the large number of photogenerated carriers in these experiments, saturation of the defect states seems to occur. As a consequence, the carriers cannot leave the conduction states and remain there for large times until they can relax to the lower defect states. Therefore, the long relaxation times of carriers from the defect states are being effectively seen when probing above the band gap. We believe that the second time constant (t_2 = 68 ps) is associated with relaxation of carriers from the conduction band states to the deep defect states. Moreover, due to saturation of defect states, this relaxation time might be the required time for carriers from the shallow donor defect states to relax into the deep defect states.

Following the estimation of relaxation times in SnO_2 NWs from the results for the lowest pump fluence, it was possible to obtain fits at higher pump fluences. Moreover, to verify validity that the faster times are a consequence of the Auger effects presence, a simple model was used that incorporates the three exponential mechanisms along with the Auger recombination. As seen in the inset of the Fig. 6.8, where the experimental data (points) and the fits from the model (solid lines) at the highest and the lowest used pump fluence are shown, relative good fits were obtained using an Auger coefficient of $(7.5 \pm 2.5) \times 10^{-31}$ cm^6/s.

Furthermore, pump fluence dependent non-degenerate measurements were performed upon photoexcitation of SnO_2 NWs at 310 nm and probing pulses at 350 nm. This probing wavelength corresponds to photon energy 3.54 eV, which is lower than the band gap energy of SnO_2 NWs. The experimental data of the time resolved normalized absorption change for

different pump fluences in the region between 50-500 μJ/cm^2 and for times up to 500 ps, are shown in the Fig. 6.9.

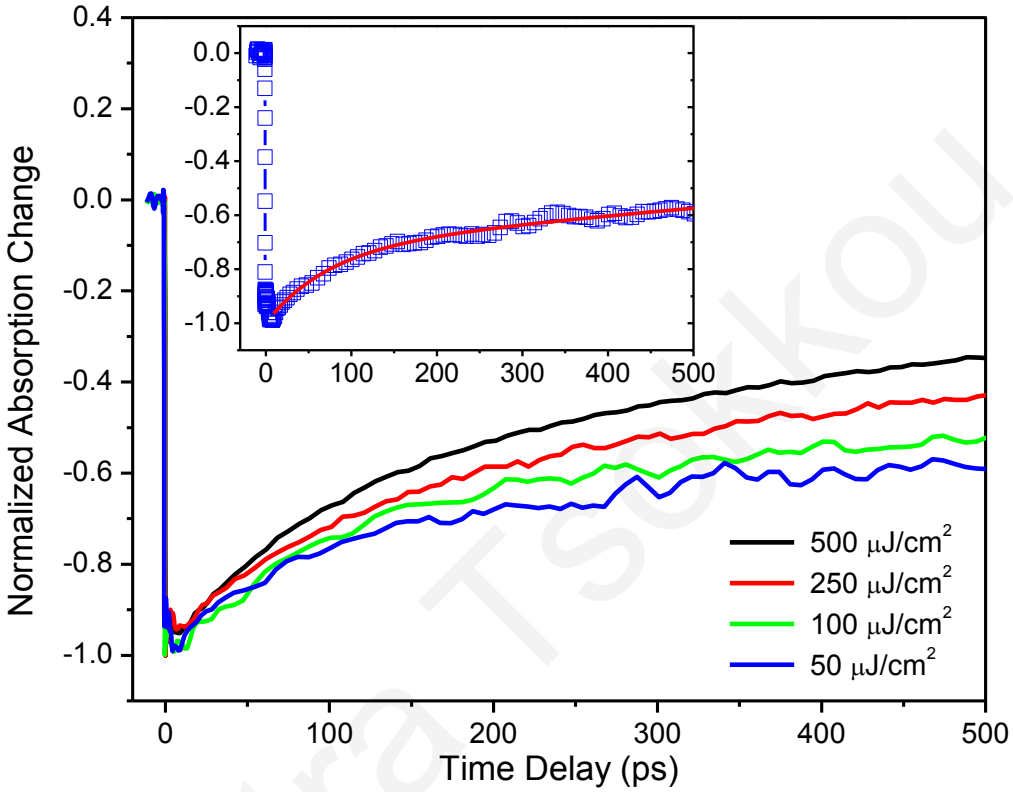

Figure 6.9. Time resolved transient normalized absorption measurements of the SnO_2 NWs on quartz substrate using ultrafast using excitation pulses at 310 nm and probing pulses at 350 nm for different pump fluences between 50-500 μJ/cm^2. In the inset, the normalized absorption change data along with the fit obtained from double exponential decay are shown.

The observation of the negative signal, attributing to state filling effects is indicative that shallow donor states exist below the band gap of the SnO_2 NWs. From the experimental data is evident that Auger recombination also influences the evolution of the signal. Similarly to the process followed for the results from degenerate measurements, using the data for the lowest pump fluence, where Auger effects are considered negligible, carrier relaxation times were derived. Double exponential decay curves are needed to fit sufficiently the experimental data, shown in the inset of the Fig. 6.9. Therefore, two relaxation times are obtained, a fast time of 72 ps (27%) and a slow one of 2.08 ns (73%). We believe that the fast relaxation time

is associated with carriers moving from these shallow donor states to the lower deep defect states. This result supports also our suggestion that saturation of defect states exist, since this fast relaxation time is similar with the second relaxation time t_2 detected from the measurements for the conduction band states. The slow relaxation time is attributed to recombination of carriers from the shallow donor states. These measurements have also been carried out for other probing wavelengths corresponding to shallow donor states and similar results were obtained.

6.2.2 Carrier Dynamics in SnO_2 Nanowires Using Time Resolved THz Transmission Spectroscopy

TRTS is an alternative method that can be used to obtain information about the temporal behavior of carriers after photoexcitation of the SnO_2 NWs. The experimental setup used for these experiments is described in section 2.2.1 which uses the output pulses from the *Tsunami* mode-locked oscillator and the *Spitfire* regenerative amplifier.

From TRTS measurements, the carrier dynamics of the SnO_2 NWs were studied, when monitoring the transmitted THz pulse peak amplitude and scanning the delay between the optical excitation and the THz pulses. Due to its low photon energy (~ meV) the secondary excitations of the photoexcited carriers by the absorption of the THz pulse are attributed to intraband transitions. UV ultrashort pulses at 266 nm were used to generate carriers in conduction band states. Measurements were taken for different pump fluences corresponding to different excitation carrier densities between 5×10^{18} cm^{-3} and 5.6×10^{19} cm^{-3}. Fig. 6.10 shows the negative THz pulse transmission change for different carrier densities within a time window of 400 ps.

As observed in the case of time resolved absorption spectroscopy measurements, for all cases a sharp decrease in the transmission change signal is initially observed that is followed by a much slower recovery back to equilibrium value. By comparing the normalized pump fluence-dependent transmission traces shown in the inset of the Fig. 6.10, it is obvious that carrier relaxation becomes progressively faster as the photogenerated carrier density

increases. Such behaviour is expected when Auger recombination contributes to the carrier relaxation.

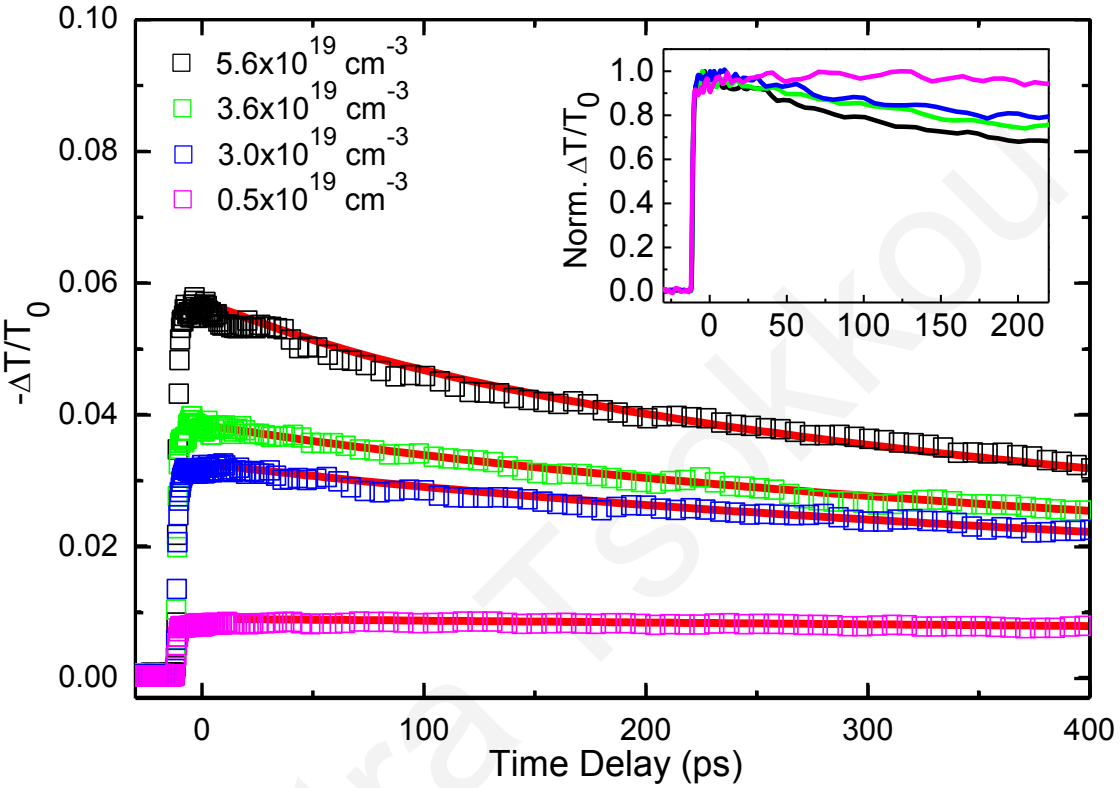

Figure 6.10. Time evolution of the maximum THz electric field amplitude change excited at 266 nm using different pump fluences to inject a different number of carriers in SnO_2 NWs for carrier densities between 0.5-5.6 10^{19} carriers/cm^3, as labeled in the figure. For comparison purposes in the inset, the normalized transmission change signal is presented.

To verify the validity of this assertion, a differential rate equation model is used to explain the evolution of photogenerated carriers back to equilibrium. In this model, described by equation 6.1, the recombination time is described by the first term of the differential equation whereas Auger recombination is described by the second term.[116]

$$\frac{dN}{dt} = -\frac{N(t)}{\tau} - \gamma\, N^3(t) \qquad (6.1)$$

where *N(t)* corresponds to carrier density, τ is the recombination time and γ the Auger coefficient of SnO_2. This differential equation has an exact solution. The recombination time τ of the system was determined at the lowest pump fluence, where the Auger recombination is considered to be negligible. Best fits were obtained when using a single exponential decay with a recombination time of τ = 2.5 ns. This time is probably attributed to transitions from defect states, deep defect states or even from shallow donor states as has been detected from time resolved absorption spectroscopy, steady state transmission and PL measurements. By using the carrier density and the estimated recombination time, we find that the suggested model fits well the experimental data for all pump fluences used here, as seen by the solid lines in Fig. 6.10, supporting our interpretation that Auger recombination is responsible for the faster relaxation times. The Auger coefficient γ in SnO_2 NWs, which is the fitting parameter in this process, is determined to be equal to $\gamma = (7.2 \pm 2.0) \times 10^{-31}$ cm^6/s, which is in agreement with values reported from the time resolved absorption measurements in SnO_2 NWs.

6.2.3 Band Diagram of SnO_2 Nanowires

A schematic representation of a band diagram for the SnO_2 NWs based on our experimental results from the steady state and time resolved measurements, is shown in the Fig. 6.11. Steady state transmission measurements, suggest a direct gap at 3.77 eV for SnO_2 NWs.

Upon UV photoexcitation with photon energies larger than the energy gap, the conduction band states are populated by carriers. The existence of defect states, the shallow donor states and the deep donor states has been detected, located below the conduction band.

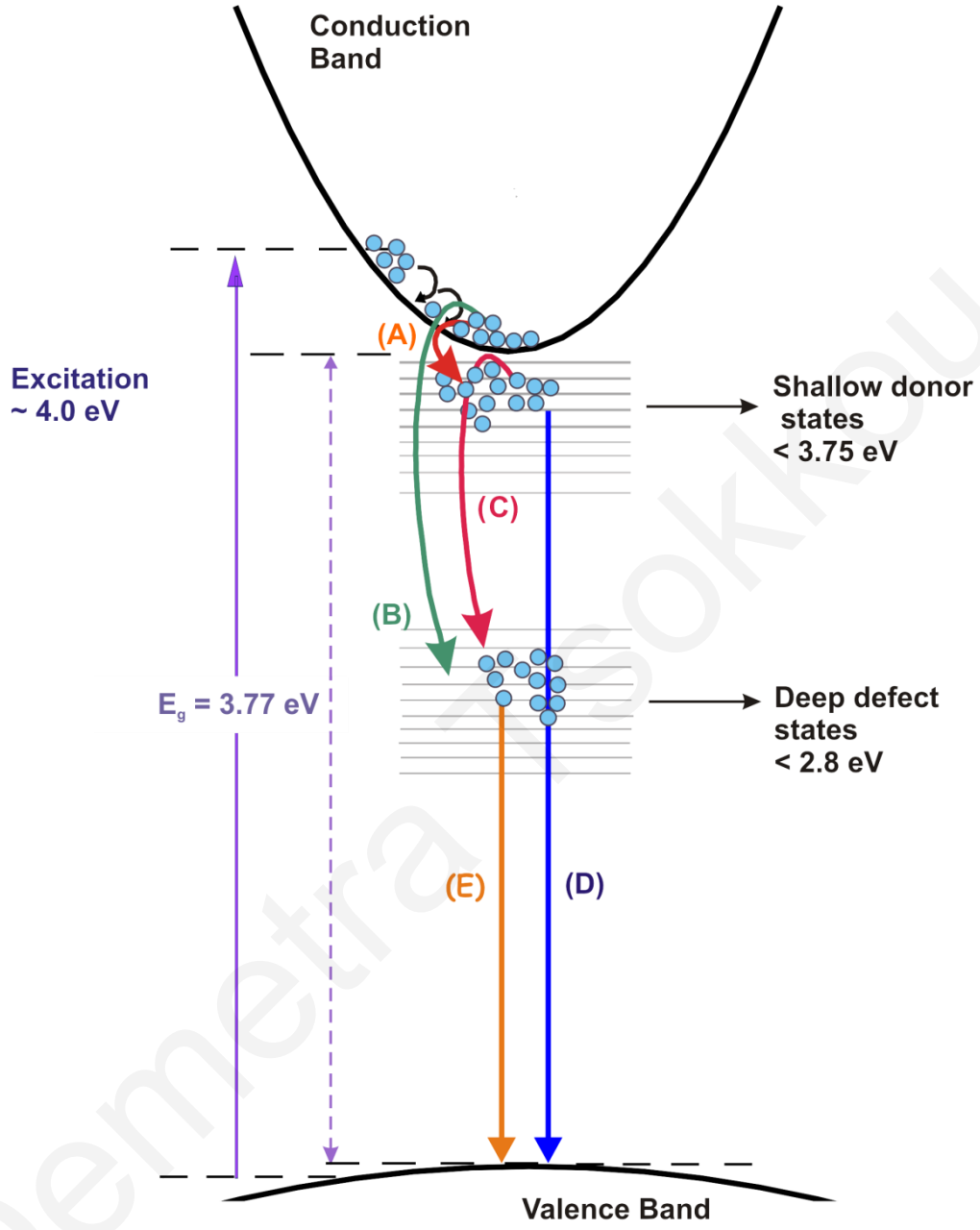

Figure 6.11. A schematic band diagram of SnO_2 NWs, as it has determined by the analysis of time resolved absorption change, time resolved THz transmission change, steady state transmission and PL measurements.

Intensity dependent absorption measurements show that carriers relax from conduction band states to the shallow donor states with a fast relaxation time constant of 2.4 ps, which is

depicted with Mechanism *A* in the Fig. 6.11. In addition, carriers from the conduction band states might relax to deep defect states with a slower relaxation time constant of 68 ps – Mechanism *B*. However, since saturation of states occurs, this recombination time might be attributed to the transitions from shallow donor states to the deep defect states, which is also supported by the intensity measurements for shallow donor states. This transition is indicated as Mechanism *C*. Moreover, carriers recombine from shallow donor states and deep defect states via a slow relaxation time, mentioned as Mechanism *D* and Mechanism *E*, respectively.

6.3 Investigation of Optical Properties in SnO_2 Nanowires in THz Region

TDTS measurements were performed to determine the optical properties and the intrinsic conductivity of SnO_2 NWs in the THz region. In these measurements, transmission of the THz electric field through the SnO_2 NWs and quartz substrate, and only through the reference quartz substrate, were taken in order to estimate their optical properties and intrinsic conductivity.

6.3.1 Complex Refractive Index of Quartz Substrate in THz Region

In this section, TDTS measurements were performed to determine the optical properties of the quartz substrate. In order to calculate the refractive index and absorption coefficient of the quartz substrate, the complex frequency spectrum for THz electric field through an empty sample holder -reference signal- and the modified THz signal after propagating through a quartz substrate have to be measured. The data analysis used to determine the complex refractive index described in the section 3.2.2, is used.

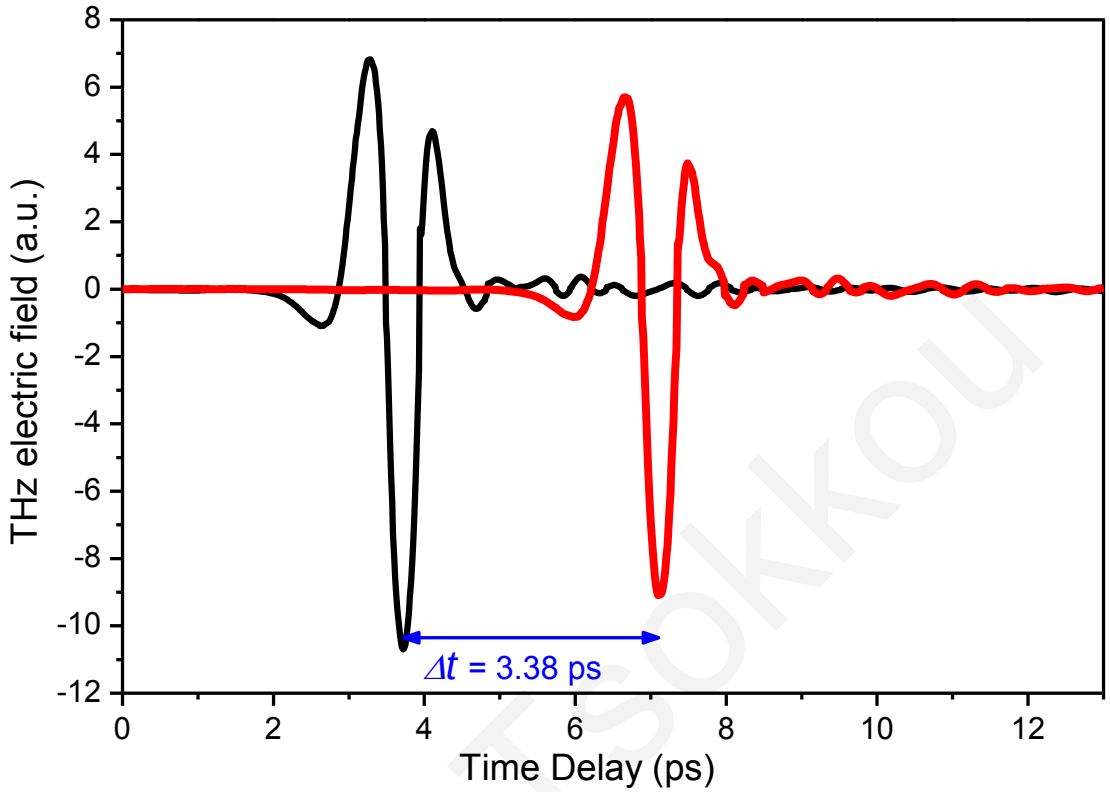

Figure 6.12. Temporal profile of the THz electric field propagating through an empty sample holder – the reference signal - (black line) and quartz substrate (red line) measured with TDTS.

The time domain data of the reference THz electric field (black line) and that through the quartz substrate (red line) were measured and are shown in Fig. 6.12. The time domain data are taken for times up to 13 ps. The thickness of the quartz substrate (d = 1 mm) is large enough to ensure a large time difference between the main part of the pulse and the first reflected pulse. Therefore, no contribution of the first echo is observed in the THz electric field for the measured time window.

The temporal delay between the reference pulse and the pulse through the quartz results from the different refractive index that the pulse experiences as it propagates along the quartz substrate, while the weaker maximum signal is due to attenuation of the THz pulse of its absorption from the quartz. The temporal delay between the maxima reference THz electric field and that obtained when propagating through the quartz substrate (Δt = 3.38 ps) can be used to make a rough estimation of the real refractive index of quartz. Knowing the

sample thickness and using the relation, $n = 1 + \frac{\Delta t\ c}{d}$, the refractive index of quartz is estimated to be n = 2.01.

The phase and amplitude spectra of the THz electric fields for reference signal and THz signal through quartz substrate corresponding to the temporal signals shown in Fig. 6.12, are plotted in Figs. 6.13 (a) and 6.13 (b), respectively. The difference observed in the phase between the two signals is a result of the different refractive index, while the weaker amplitude of the amplitude after propagates through quartz is due to absorption of THz radiation from the quartz. Then, to derive information about the optical properties of the quartz, the equations 3.10a and 3.10b were used.

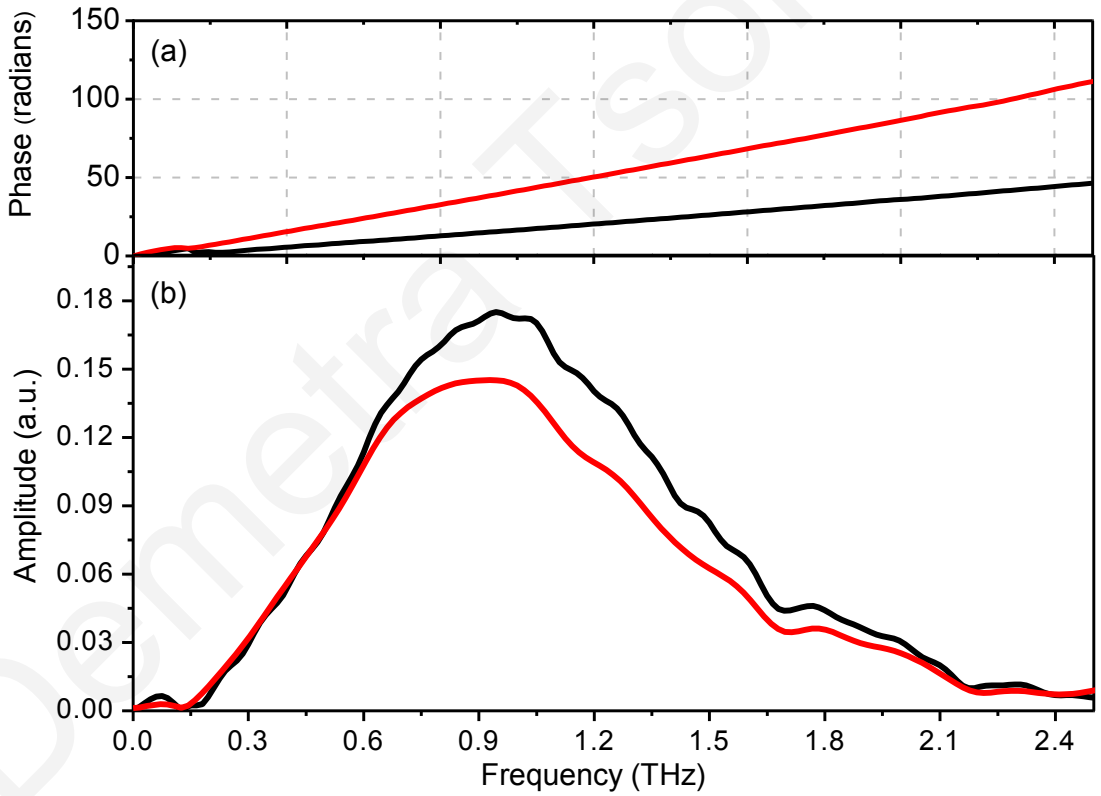

Figure 6.13. Frequency domain (a) phase and (b) amplitude of both reference (black line) and 1 mm quartz substrate (red line).

The frequency dependence of the refractive index and absorption coefficient of quartz substrate were obtained in the region between 0.25 and 2.1 THz and are shown in Figs. 6.14

(a) and 6.14 (b), respectively. It can be observed that the refractive index does not show any significant frequency dependence and has a nearly constant value ranging between 2.01-2.02. Absorption coefficient *a(ω)* is very small in the THz region and takes values below 5 cm^{-1} in the probed region that indicates weak absorption of the THz radiation by the quartz, as expected. Optical properties calculated here are in agreement with values reported elsewhere for the quartz substrate.[208]

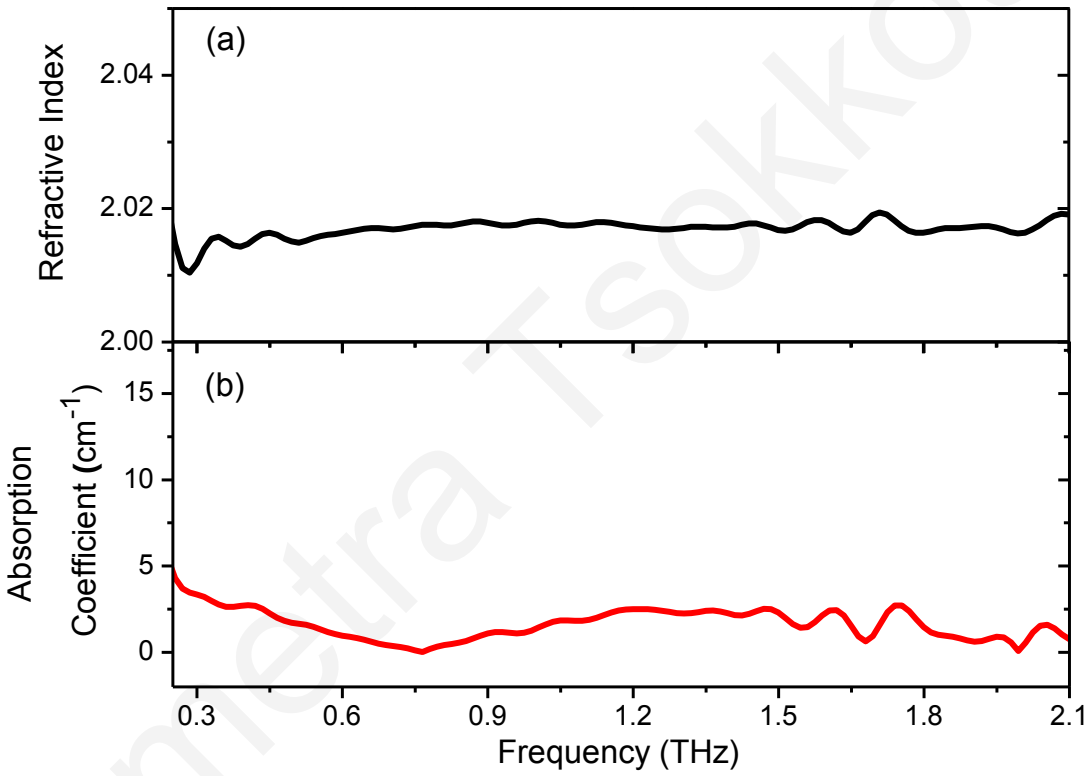

Figure 6.14. (a) Refractive index and (b) absorption coefficient of quartz substrate in the THz region between 0.25-2.1 THz.

6.3.2 Complex Refractive Index and Intrinsic Conductivity in SnO_2 Nanowires in THz Region

In the following pages, the TDTS measurements that were performed for the calculation of optical and transport properties for SnO_2 NWs on quartz substrate, are presented and discussed. To obtain quantitative information from non-excited SnO_2 NWs, a thick sample is necessary to cause detectable changes in the THz waveform. Therefore, the growth process during the SnO_2 NWs synthesis lasted for 3 hours, so that more material is deposited onto the substrate. The thickness of this sample was estimated, as the weight of the deposited material was measured and assuming that the NWs form a uniform film onto the substrate. In our case it was found that the thickness is approximately $d \approx 21$ μm.

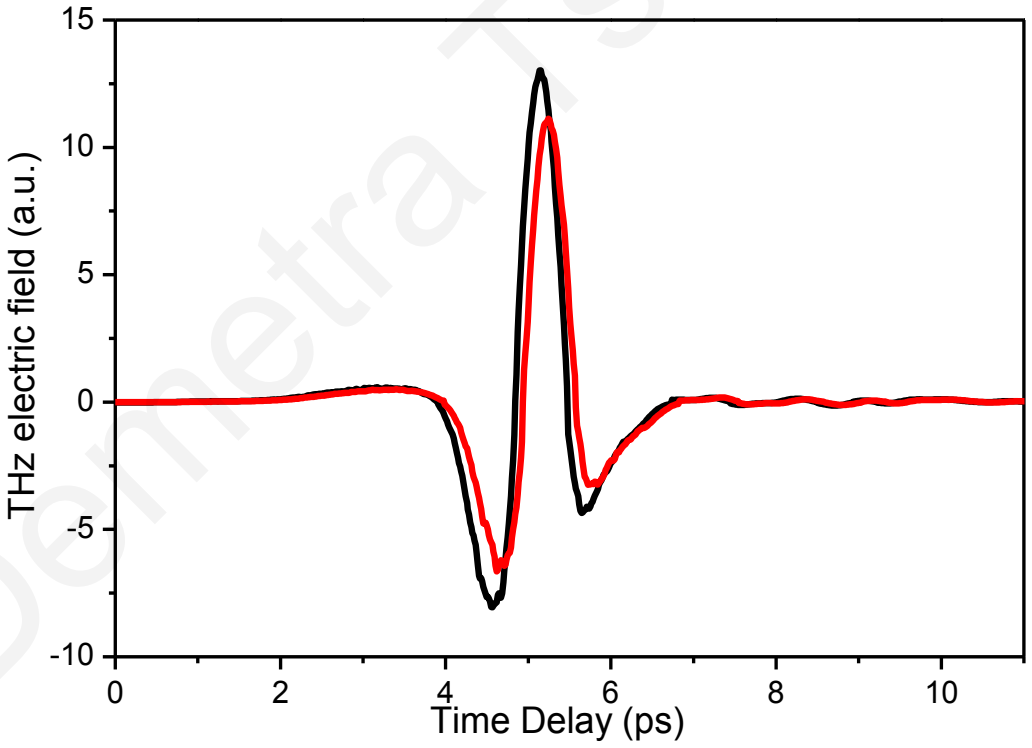

Figure 6.15. Temporal profile of THz pulse electric field transmitted through SnO_2 NWs on quartz substrate (red line) and only through quartz substrate (black line).

Then, the measurements of the temporal THz electric field transmitted through the non-excited as-grown SnO_2 NWs sample on quartz substrate and only through quartz, which is the reference signal in this case, were taken. These measurements for quartz substrate and the unexcited sample are shown in Fig. 6.15 with black and red solid lines, respectively.

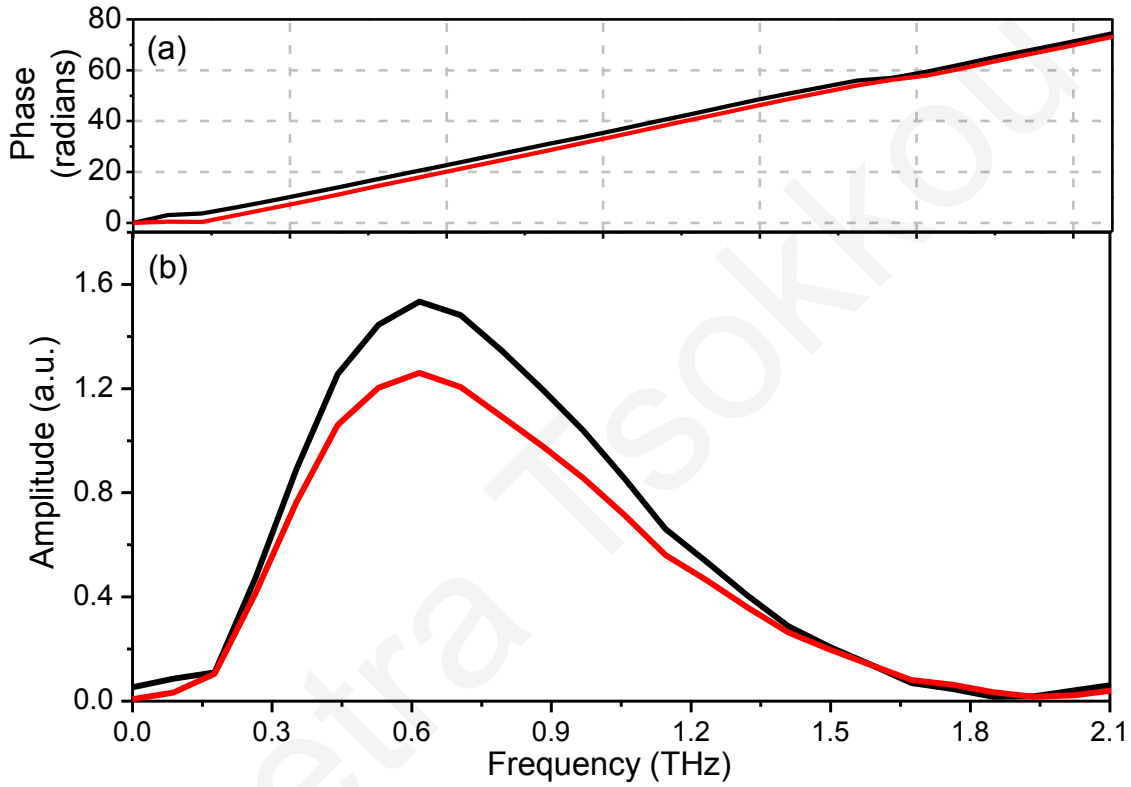

Figure 6.16. (a) Phase and (b) amplitude of SnO_2 NWs on quartz substrate (red line) and only quartz substrate (black) obtained when performing discrete Fourier transform in the temporal signals shown in the Fig. 6.15.

The Fourier transformed data are used to yield the refractive index and absorption coefficient of the SnO_2 NWs. The Fourier transformed amplitude, as well as the phase of SnO_2 NWs on quartz substrate (red line) and only that of quartz substrate, are shown in the Figs. 6.15 (a) and 6.15 (b). Since the wavelength of THz pulses is much larger than the dimensions of the NWs, we can approach the NWs system as a thin film on the substrate. Initially, the properties of the SnO_2 NWs were extracted using the analysis followed in the

case of thin films that it is described in section 3.2.3. The refractive index of quartz in THz region calculated previously is used.

The same calculations were repeated to obtain the refractive index and the absorption coefficient in SnO_2 NWs using an effective medium approximation to account the fact that the THz pulse propagates not only through SnO_2 NWs, but through a mixture of SnO_2 NWs and air. In this model, the sample is consisted by SnO_2 NWs that cover the substrate with a filling factor f_s, considering the approximation, $\varepsilon_{eff}(\omega) = f_s \varepsilon_{eff}(\omega) + (1 - f_s)\varepsilon_m(\omega)$, where $\varepsilon_{eff(m)}(\omega)$ is the dielectric constant of composite (air). Using this model the contribution of the NWs on the frequency dependent dielectric constant $\varepsilon_{NW}(\omega)$ is calculated. This method has been used previously for carbon nanotubes[209] and InN nanorods.[210] No differences in the refractive index and absorption coefficient spectrums were obtained when this approach was utilized.

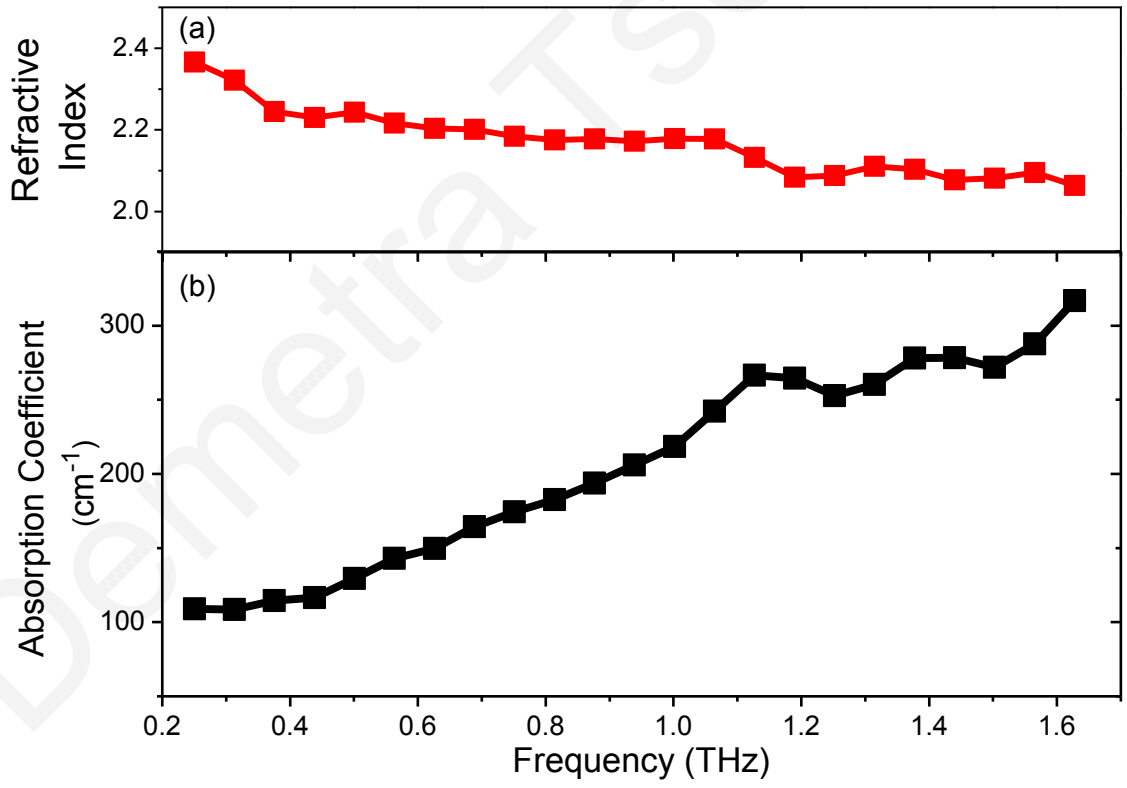

Figure 6.17. (a) Refractive index and (b) absorption coefficient of SnO_2 NWs in the region between 0.25-1.6 THz.

The refractive index (red squares) and absorption coefficient (black squares) calculated in the region of 0.25-1.6 THz are shown in the inset of Fig. 6.17. The refractive index changes monotonically from ≈ 2.4 to ≈ 2.1, which is larger than the refractive index of bulk SnO_2 in the visible region, i.e. $n \approx 2$.[211] On the other hand, the absorption coefficient is monotonically increasing in the probed region from 110 cm^{-1} at 0.25 THz up to 300 cm^{-1} at 1.6 THz.

Optical properties, such as refractive index and absorption coefficient, and complex conductivity are related to each other, as it is described in section 3.2.3. The real (black squares) and imaginary (red circles) parts of the frequency dependent intrinsic conductivity determined from the analysis of the data, are shown in Fig. 6.18.

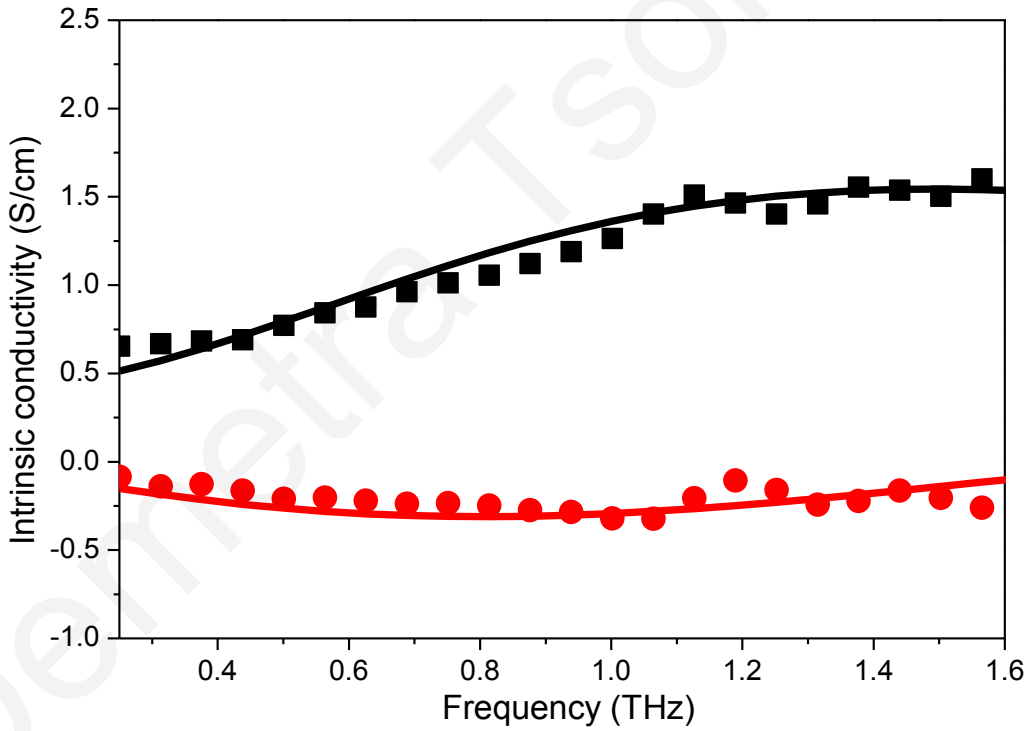

Figure 6.18. Real (black squares) and imaginary (red circles) parts of the intrinsic conductivity in SnO_2 NWs are depicted with dots. Solid lines present the results obtained with Drude-Smith model.

It is clearly evident that the signal for frequency-dependent complex conductivity strongly deviates from the usual Drude like behaviour observed in the case of bulk semiconducting materials. The real part of the conductivity increases monotonically, while the

imaginary part of the conductivity is negative. Similar behaviour has also been observed for Si nanocrystals,[212] InN nanorods[210] and ZnO NWs[113] and is attributed to the localization of carriers in the nanostructures. Such behavior can be described by the Drude –Smith model. The equation 3.18 described in section 3.2.1 is fitted to the experimental data of the intrinsic conductivity. In this equation, we used the bulk SnO_2 effective electron mass $m^* = 0.275\ m_0$, where m_0 is the bare electron mass ($m_0 = 9.1093897 \times 10^{-31}$ kg).[213] In practice, only the first term of the summation of equation 3.18 is taken into account.

In an attempt to give a physical meaning to the persistence of velocity Monte Carlo simulations have been performed by Němec *et al.* to calculate the conductivity spectrum in the THz region.[214] For simplicity, their calculations were performed for the case for semiconducting nanoparticles. It is found that the carriers become localized when the nanostructure dimensions are comparable to the mean free path of the carriers and that similar observations with that given by the Drude-Smith model can be expected. Additionally, the persistence of velocity c_1 is related to the probability that the carriers backscatter at the surface of the nanostructure. They have also concluded that the degree of localization also depends on the probability that upon scattering with the particle boundary a charge carrier is reflected back into the particle.

Clearly, the Drude-Smith model fits well the experimental data shown in the Fig. 6.18 as denoted by red and black solid lines for real and imaginary part of conductivity, respectively. The intrinsic carrier concentration in the SnO_2 NWs is determined to be $n = (3.3 \pm 0.4) \times 10^{16}\ cm^{-3}$, whereas the scattering time τ equals (75 $\pm$ 7) fs. Furthermore, the persistence of velocity is determined to be c_1 = - 0.85 $\pm$ 0.02. Given that the persistence of velocity is less than -0.5 this indicates suppression of long carrier transport in these NWs due to the spatial localization of carriers. The estimated value of c_1 and scattering time correspond to a macroscopic *dc* mobility of $\mu = \mu_m(1 + c_1) \approx (72 \pm 10)$ cm^2/Vs, where μ_m is the respective bulk mobility.

6.4 Investigation of Transport Properties in Photoexcited SnO_2 Nanowires

To further improve our understanding on the transport properties of the carriers in these SnO_2 NWs, measurements were performed after photoexcitation of the sample. These measurements are further analyzed to extract the photoconductivity of the SnO_2 NWs. Measurements were performed as a function of excitation intensity to investigate the dependence of the photoconductivity on the induced carrier density. To determine the frequency dependence of the photoconductivity spectrum with TRTS, the difference temporal shape of the THz transmission electric field through the optically excited sample has to be measured at a fixed time delay between the pump and the THz pulses. In these measurements, the reference measurement is the static THz electric field measured for the SnO_2 NWs in its equilibrium state, in the absence of any excitation.

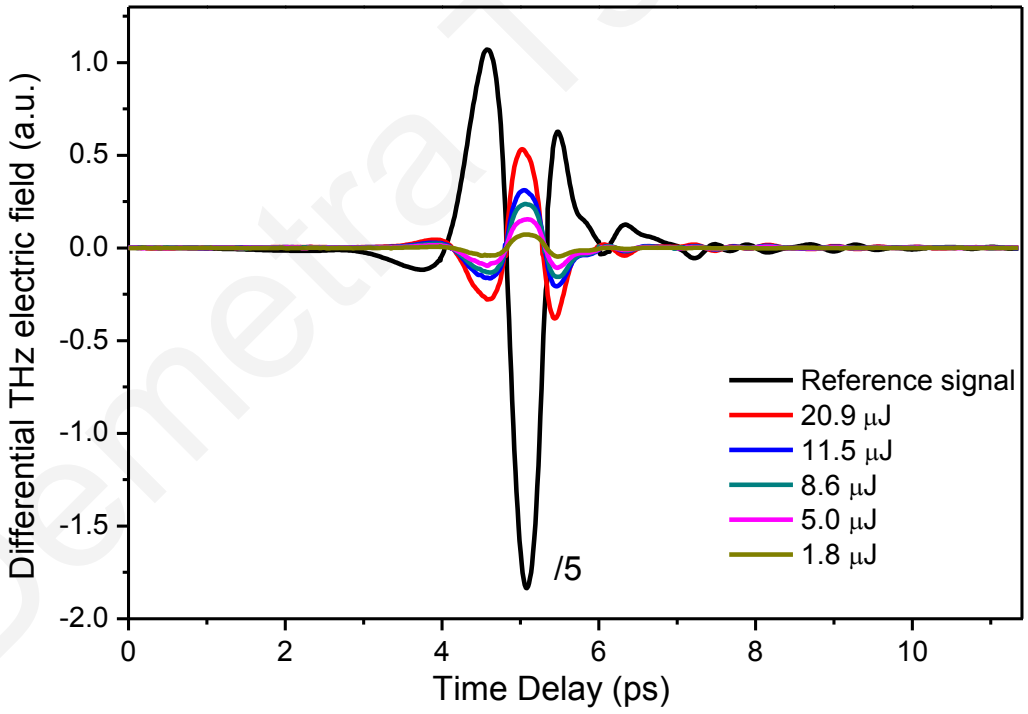

Figure 6.19. Reference THz signal (black lines) taken for the unexcited SnO_2 NWs/quartz substrate and the differential THz electric field propagated through the photoexcited SnO_2 NWs/quartz substrate, when using different pump energies in the region between 20.9-1.8 μJ/pulse corresponding to carrier densities between (0.5-5.5) × 10^{19} carriers/cm^3.

The temporal profile of the differential change of the THz transmitted electric field as it propagates through the optically excited SnO_2 NWs sample was measured upon exciting the sample with different pump fluences. In our measurements, we utilized UV pulses of 100 fs at 266 nm with various pump energies in the range between 20.9-1.8 μJ/pulse that corresponds to carrier densities between (0.5 -5.5) × 10^{19} carriers/cm^3. Measurements were carried out with the probe beam delayed at $t_{pump\text{-}probe}$ = 5 ps following the excitation pulse, where the THz signal has reached a maximum plateau, and before significant recombination of carriers could occur. The experimental data of the differential THz electric fields are shown in the Fig. 6.19 for a time window of ≈ 11 ps. The reference THz electric field for the unexcited SnO_2 NWs on quartz substrate -reference signal- is also included in the Fig. 6.19, depicted with a black line.

One can observe that the differential THz electric field measured in all cases for SnO_2 NWs has an opposite sign from the THz electric field of unexcited SnO_2 NWs. The differential THz electric field is defined as the difference between the THz waveform from the photoexcited sample and the reference THz waveform. In the case of the photoexcited sample, the pump pulse induces free carriers into the conduction band states that eventually increase the sample absorption in the THz region, resulting in smaller amplitude in the transmitted THz waveform. In principle in this kind of experiments one can measure the direct shape of both the photoexcited SnO_2 NWs and reference THz pulses. Because the difference in signal intensity between photoexcited and non-photoexcited samples is at least one order of magnitude smaller than the signal itself, this difference method allows much more accurate determination of the photoconductivity.

To obtain the photoconductivity of the material, the complex frequency spectrum for both temporal unexcited and photoexcited signal has to be obtained by performing a discrete fourier transform at the time domain data. In the case of NWs, a different model than the one used for thin films has to be applied, to incorporate the fact that the THz pulse propagates through a mixture of NWs/air, in order to obtain reliable values for the measured photoconductivity. Therefore, it is important to account for the filling factor of the NWs f_s on the substrate and the procedure described in the section 3.3.1 has to be applied to extract the photoconductivity. Following careful examination of different SEM images for the transferred SnO_2 NWs the filling factor was estimated to be approximately 0.25. For the calculation of

photoconductivity, the ratio E_{NW}/E_{air} is needed, which is defined by using the Fresnel transmission coefficient in THz region and the high frequency dielectric constant which in the case of SnO_2 is equal to $\varepsilon_\infty = 3.9$.[215]

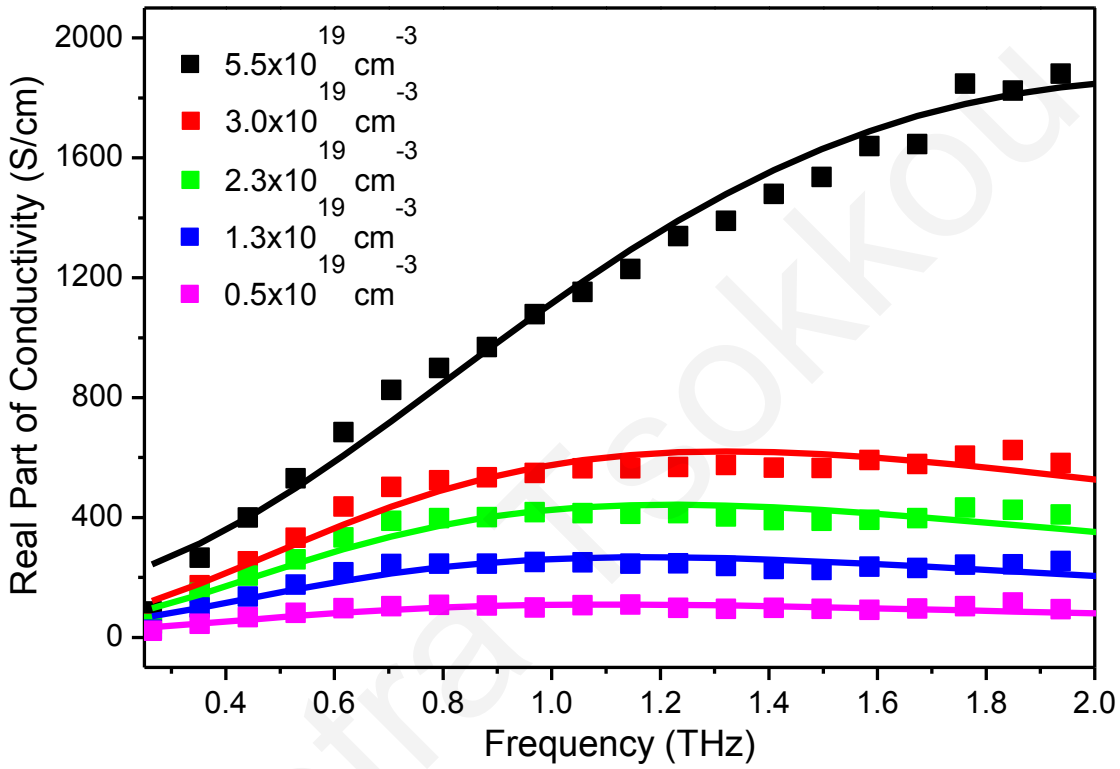

Figure 6.20. Real part of conductivity spectrum of SnO_2 NWs (dot lines) at different photogenerated carrier densities between (0.5-5.5) × 10^{19} carriers/cm^3, at $t_{pump\text{-}probe}$ = 5 ps after photoexcitation. Solid lines displayed corresponds to the best fits results given by the Drude-Smith model.

The real and imaginary parts of the photoconductivity for different pump fluences are shown in Figs. 6.20 and 6.21, respectively in the frequency range between 0.25-2.0 THz. The frequency dependence of the real part of the photoconductivity is similar to that obtained for non-excited SnO_2 NWs, as seen in Fig. 6.20. On the other hand, the imaginary part of the photoconductivity shown in Fig. 6.21 is more complex. It appears to be negative at low frequencies and becomes positive at larger frequencies.

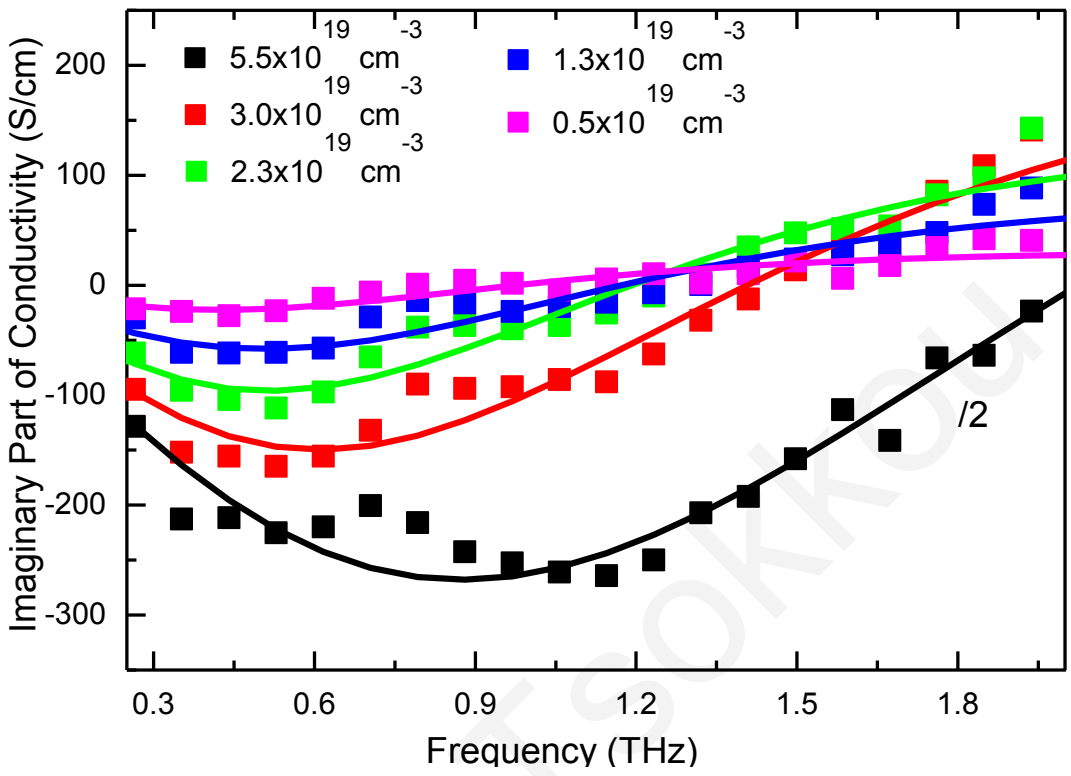

Figure 6.21. Imaginary part of conductivity spectrum of SnO_2 NWs (dot lines) at different photogenerated carrier densities between (0.5-5.5) × 10^{19} carriers/cm^3, at $t_{pump\text{-}probe}$ = 5 ps after photoexcitation. Solid lines displayed corresponds to the best fits results given by the Drude-Smith model.

At first glance such behaviour can be explained by either the *Drude–Smith model* or by the surface plasmon resonance model[216] as has been proposed for GaAs NWs[112] and nanoporous TiO_2.[217] The characteristic feature of surface plasmon resonance exhibited in the visible region for metals, is expected to be observed in THz region for the semiconducting materials. As discussed by Pitarke *et al.* for the case of cylindrical structures,[216] the plasmon frequency ω_s in NWs which is the characteristic frequency that zero frequency crossing point in the imaginary part, is related to the bulk plasmon frequency by $\omega_s = \sqrt{2}\omega_p$, where $\omega_P = \left(\frac{Ne^2}{\varepsilon_0 \varepsilon_\infty m^*}\right)^{1/2}$, where N is the carrier density, and ε_∞ the high-frequency dielectric response of the NWs. This is valid when the THz electric field polarization is normal to the

NW surface. As it can be observed the plasmon frequency is carrier density dependent. For the SnO_2 NWs and carrier densities considered here, a careful estimate of the SnO_2 NWs plasmon frequency indicate that it is out of the frequency range measured here (>14 THz, when $N_0 = 0.5\times10^{19}$ carriers/cm^3) thus eliminating the plasmon resonance model.

Moreover *the Drude-Smith model* can sufficiently describe the experimental data, as shown by the solid lines in the Figs. 6.20 and 6.21 corresponding to the best fits. Table 6.3 displays the extracted best fitting parameters using the Drude-Smith conductivity for carrier density N, scattering time τ and persistence of velocity c_1 for the different pump energies utilized in this work.

N_0 x 10^{19} (carriers/cm^3)	N x 10^{19} (carriers/cm^3)	τ (fs)	c_1
5.5	4.5 ± 0.2	70 ± 4	-0.94 ± 0.01
3.0	0.9 ± 0.1	110 ± 5	-0.93 ± 0.01
2.3	0.5 ± 0.1	119 ± 4	-0.91 ± 0.01
1.3	0.40 ± 0.08	120 ± 6	-0.90 ± 0.01
0.5	0.15 ± 0.05	130 ± 6	-0.90 ± 0.01

Table 6.3. Parameters of carrier density N, scattering time τ and persistence of velocity c, extracted by fitting experimental data of Figs. 6.20 and 6.21 to *Drude-Smith* conductivity model are shown.

From the Table 6.3, it appears that a larger fraction of the initial photogenerated carriers contribute to the photoconductivity with increasing pump fluence. This is to be expected given that at $t_{pump\text{-}probe}$ = 5 ps after photoexcitation, most of the photogenerated carriers in the SnO_2 NWs, lose their excess energy and relax to the bottom of the conduction band or move at the shallow states - defect or surface states. For such high pump fluences, we expect that defect states are saturated by photoexcited carriers in SnO_2 NWs, as has been previously observed by time resolved absorption spectroscopy measurements. In addition to the fact that no band to band recombination of carriers is expected, a large number of the

initial carriers that are generated, remain in conduction band states. These free charge carriers are likely to contribute to the photoconductivity. Therefore, in the case of the highest pump fluence it seems that the majority of photoinduced carriers contribute to the conductivity signal and the estimated carrier density ($\approx 4.5\times10^{19}$ carriers/cm^3) is close to the initial absorbed carrier density ($\approx 5.5\times10^{19}$ carriers/cm^3). The difference is most likely due to the fact that some of the carriers become immobile as they are trapped into the defect/interface states. Accordingly, as the pump fluence decreases the number of initial carriers contributing to the photoconductivity becomes lower, since more carriers are trapped into the defect/interface states.

Furthermore, the persistence of velocity in this sample is strongly negative even for the lowest pump fluence used. This behavior suggests a strong localization of carriers in the SnO_2 NWs, since transport of carriers between different SnO_2 NWs is inhibited. There are several ways that carriers may transport into adjacent NWs, such as diffusion through pathways between connected NWs, tunneling or hopping.[218] As a consequence of the low volume filling factor of the SnO_2 NWs on the substrate used here, few interconnections between adjacent SnO_2 NWs exist. In addition, the SnO_2 NWs are placed onto the insulating SiO_2 and are surrounded by air, potential barriers at the surface of the NWs are high, so that tunneling or hopping of carriers into different NWs is mainly prohibited. Furthermore, the persistence of velocity becomes slightly more negative as the carrier density increases. We speculate that for such high carrier densities, a large number of carriers remain in the conduction band and since a limited number of pathways exist for carriers to move into a different SnO_2 NW, carriers become localized. As expected, the scattering time appears to be also carrier density dependent and becomes larger as the carrier density increases.

Results obtained from TDTS measurements cannot be directly compared to the results from the TRTS technique, since samples with different filling factor were used. In the case of the TDTS measurements, properties of SnO_2 NWs with a larger filling factor were investigated in contrast to those transferred. We believe that this is the reason for the slightly smaller negative value of persistence of velocity.

6.5 Conclusions

SnO_2 NWs are grown via APCVD using thermal evaporation of Sn at 800 ^oC in Ar atmosphere. In addition, SnO_2 NWs were obtained via direct oxidation of Sn at 800 ^oC using APCVD. NWs with a diameter of 50-100 nm and length up to micrometer scale were obtained. VLS mechanism is responsible for the SnO_2 NWs growth and Au is an appropriate choice of a catalyst.

In conclusion, we have investigated the ultrafast dynamic behavior of SnO_2 NWs using above band gap excitation UV femtosecond pulses. Transmission measurements of the NWs provide us with an estimate of the band gap at 3.77 eV and reveal broad absorption bands below the band edge. Furthermore, the results from the PL measurements also support the crucial role that the defect states play in SnO_2 NWs. In addition, these absorption bands appear to influence the relaxation of the photogenerated carriers in the NWs. Transient differential absorption measurements reveal the different pathways and time constants associated with the relaxation of the photogenerated carriers. Measurements suggest that the photogenerated carriers take a few picoseconds to move into the shallow traps states whereas it takes ~ 68 ps to move from the shallow to the deep trap states. Furthermore, recombination of electrons from these traps states with holes in the valence band takes ~ 2 ns. Auger recombination has a contribution to the carrier dynamics at the highest fluence used in this study (~500 $\mu J/cm^2$), however at fluence of 50 $\mu J/cm^2$ Auger recombination appears to be negligible. Transient absorption intensity measurements provided us with an estimate of the Auger coefficient for the SnO_2 NWs to be approximately $(7.5 \pm 2.5) \times 10^{-31}$ cm^6/s.

Further investigation of carrier dynamics in SnO_2 NWs has been achieved using TRTS. Intensity dependent measurements of the transmission have been performed and the time dependence of the photogenerated carriers has been modelled by a rate equation, which includes Auger recombination. The Auger coefficient was determined to be $\gamma = (7.2 \pm 2.0) \times 10^{-31}$ cm^6/s, which is in agreement with the results obtained from time resolved absorption spectroscopy measurements. Moreover, a recombination time of 2.5 ns has been detected, which we believe that it is attributed to the time that carriers need to recombine from shallow donor states or deep defect states.

THz spectroscopy has also been applied to investigate the photo-induced and intrinsic conductivity in SnO_2 NWs using the *Drude-Smith* model. We demonstrate that the intrinsic conductivity and photo-conductivity is affected by carrier localization in the SnO_2 NWs, which is a result of the diameter and low density of SnO_2 NWs on the substrate. From photoconductivity measurements and carrier densities between $(0.5\text{-}5.5) \times 10^{19}$ cm^{-3}, we find that the scattering time decreases from 140 to 70 fs. The refractive index of the NWs was found to vary from 2.4 to 2.1 with increasing THz frequency, while the mobility of SnO_2 NWs was determined to be (72 ± 10) cm^2/Vs.

Chapter 7

Conclusions

Semiconducting NWs are considered one of the best controlled nanoscale building blocks and have become an intensively studied topic in semiconductor technology. In the last two decades, the development of the manufacturing methods enabled the fabrication of structures in nanometer scale, which resulted in an extensive study of their growth conditions. Nowadays, NWs are grown with well controlled characteristics including chemical composition, diameter and length.

In a simple semiconductor following optical excitation, the photogenerated carriers will lose their kinetic energy through optical phonon emission. These carriers will relax to the bottom (top) of the conduction (valence) band and eventually recombine. However, due to the spatial confinement in nanostructures, the presence of boundaries, surface and defect states, it results in more complicated relaxation mechanisms. Energy relaxation and the role of defects/surface states in semiconducting NWs are of particular importance. Most of these mechanisms occur on a picosecond or femtosecond time scale. At the same time, the discovery and use of ultrafast pulses over the past three decades has revolutionized our understanding of carrier dynamics in semiconducting materials, initially in bulk form and more recently in nanostructures.

The main objective of this thesis is to provide a detailed understanding of the carrier dynamics in GaN, In_2O_3 and SnO_2 NWs. In this research work, femtosecond transient absorption spectroscopy and THz transmission spectroscopy have been utilized to study carrier dynamics in the above semiconducting NWs. Our interest in GaN, In_2O_3 and SnO_2

NWs arise from their potential for a plethora of future applications in the areas of electronic, optoelectronic and sensing devices. Experiments of time resolved absorption spectroscopy have been performed as a function of various parameters, including photon energies of excitation and probing pulses corresponding to above and below the band gap and different fluences of excitation. The carrier dynamics and the band structure details in these NWs revealed by our time resolved measurements have been described in detail. Furthermore, to study the fundamental properties of SnO_2 NWs, an experimental setup for time resolved THz spectroscopy has been designed and constructed providing subpicosecond temporal resolution. Recombination mechanisms, optical constants, intrinsic conductivity, as well as photoconductivity have been investigated using this method. These properties have remained poorly understood in this class of materials despite of their technological importance, mainly due to the difficulties in measurements.

The initial objective of this work was the synthesis of GaN, In_2O_3 and SnO_2 NWs and the determination of their characteristics. The different species of the semiconducting NWs have been prepared via APCVD method. Various techniques including SEM, XRD and steady state transmission spectroscopy have been applied to investigate the morphology, the crystal structure and the optical properties for the optimization of these NWs.

The GaN NWs have been grown via direct nitridation of metal Ga at 950 ^oC in the presence of a small amount of hydrogen flow. Straight GaN NWs with a uniform diameter of 100 nm along their length and lengths up to few microns were observed.

The synthesis of In_2O_3 NWs has been accomplished via thermal evaporation of In powder at 700 ^oC in the absence of continuum flow of oxygen. However, a small amount of oxygen had to be introduced into the system at the beginning of the experiment to obtain In_2O_3 NWs with sufficient length. From the characterization of In_2O_3 NWs, it was revealed that tapered NWs with a diameter of (100 $\pm$ 20) nm were obtained and length up to few microns. Also, the band gap of this direct band semiconductor has been estimated and found to be equal to 3.5 eV.

Finally, SnO_2 NWs have been grown via thermal evaporation of Sn powder at 800 ^oC in Ar atmosphere. These NWs have a uniform diameter between 50-100 nm and length of few microns. Moreover, SnO_2 NWs have also been synthesized via LPCVD at 800 ^oC under a flow of 600 sccms Ar:10 sccm O_2 at $1x10^{-3}$ mbar. The different lengths between the APCVD-

grown SnO_2 NWs and LPCVD-grown SnO_2 NWs are the only difference obtained. LPCVD-grown SnO_2 NWs have lengths larger than 10 microns. The energy band gap in SnO_2 NWs has been found to be 3.77 eV.

The main objective of this thesis is the in-depth investigation of the carrier dynamics of the NWs using femtosecond time resolved absorption spectroscopy. Non-degenerate time resolved differential absorption measurements were performed for GaN NWs using above and below band gap excitation. The use of a variety of probing wavelengths in the range between UV and IR region enable the detection of different kind of states in these GaN NWs. Strong state filling detected for all probing wavelengths in the spectral range between 370 nm and 980 nm (1.26 - 3.35 eV) corresponding to energies below the energy gap of GaN, indicates the existence of high density of defect states for these energy levels. Detection of *U* valley has been observed for photoexcitation of GaN NWs above the band gap and probing wavelength smaller than 350 nm. From our analysis is shown that for these experimental conditions, strong coupling between the deep acceptor states at ~ 1.2 eV and *U* valley takes place and the energy difference of the *U* valley and the valence band was determined to be 4.7 eV. From the pump fluence dependent measurements at probing wavelengths of 370 nm and 550 nm is shown that Auger recombination is present when probing shallow donor states and midgap states. On the other hand, Auger effects are not present when probing the conduction band states even for the highest pump fluence used here (~ 1 mJ/cm^2). From shallow donor states, carriers relax to lower midgap states with a time constant of ~ 50 ps, while the majority of carriers that populate these states relax to shallow acceptor states or even recombine with a slower relaxation time of 655 ps. Measurements for the midgap states show that the carriers relax to lower midgap states with a time between 6.5-12 ps, as the pump fluence increases from 1-11 $\mu J/cm^2$, or to deep acceptor states via a slower relaxation time of ~ 350 ps.

Similar measurements have been performed in the case of In_2O_3 NWs. Above band gap excitation revealed complex relaxation paths from the conduction band states to shallow donor sates and midgap defect states. State filling effects observed for probing wavelengths smaller than 430 nm show that defect states exist at these energy levels. Moreover, differential absorption obtained for these probing wavelengths have similar temporal evolution and therefore we conclude that the same kind of states are detected, named the shallow donor states. From the differential reflection data, long lived oscillations are evident

for times up to 300 ps, as a result of the generation and propagation of coherent acoustic phonons in In_2O_3 NWs. The presence of coherent longitudinal acoustic phonons is supported by the linear dependence of the oscillation period on the probing wavelength. Also, the sound velocity in In_2O_3 NWs was found to be equal to $v_s = (4.1 \pm 0.5) \times 10^5$ cm/s. Moreover, the pump fluence dependent measurements were performed for the different kind of states detected. From the experimental data is obvious that Auger recombination is present in all cases. Carriers move out the conduction band states at times of ~ 1.5 ns. Furthermore, a similar slow relaxation time has been observed for shallow donor states from where they probably recombine. In addition, a fast relaxation time ~ 15 ps has been observed associated with carriers from shallow donor states relaxing to lower donor states or even midgap states. Different relaxation times have been obtained for carriers detected in the midgap states. The carriers from these states relax to lower states with a time constant of 26 ps or recombine nonradiative with a time of several hundreds of picoseconds (~ 300 ps). No signal was observed when using excitation pulses below the band gap, evident that a much lower density of defects exist in In_2O_3 NWs in comparison to GaN NWs. A schematic of a band diagram for In_2O_3 NWs following carrier dynamic measurements has been proposed.

Carrier dynamics of SnO_2 NWs have been investigated using time resolved absorption spectroscopy and TRTS. From these measurements, the influence of the defect states on carrier dynamics is shown. Two distinct regions of states have been observed the shallow donor states and the deep defect states. These results are also supported from steady state transmission and PL measurements. Saturation of defect states is observed. As a consequence the relaxation of carriers obtained from degenerate absorption change measurements reflects the required time for carriers to move out from the defect states. Carriers from the shallow defect states relax to the lower deep level states with a time constant of 68 ps, which is very close to the relaxation time detected from the non-degenerate measurements directly for these states. Furthermore, it is noted that carriers recombine from shallow donor states with time 2.08 ps. A slow relaxation time ~ 2.3 ns, was also observed from degenerate measurements, which are attributed to recombination of carriers either from shallow donor states or even deep level states. These times are in agreement with the recombination time obtained from TRTS measurements. Auger recombination appears to be a contributing factor in the dynamics of this system. The Auger coefficient in SnO_2 NWs was estimated using a simple

model and fitting the experimental data. The coefficient is determined to be equal to $\gamma = (7.5 \pm 2.5) \times 10^{-31}$ cm^6/s when time resolved absorption measurements were used whereas $\gamma = (7.2 \pm 2.0) \times 10^{-31}$ cm^6/s from the TRTS measurements.

Furthermore, TDTS and TRTS were utilized to investigate the complex refractive index, intrinsic conductivity and photoconductivity in SnO_2 NWs. The refractive index of SnO_2 NWs in the region between 0.2-1.6 THz was found to decrease from 2.4 to 2.1, while the absorption coefficient increases from 100 cm^{-1} to 350 cm^{-1}. Intrinsic conductivity, but also photoconductivity spectrums of SnO_2 NWs reveal suppression of long transport of carriers attributed to spatial confinement of carriers. The experimental data are interpreted via a modified Drude model proposed by Smith that incorporates the localization of carriers into the nanostructures.[131] The important characteristic constants, including scattering time and carrier density that contribute to photoconductivity have been obtained. From intrinsic conductivity spectrum the carrier density in SnO_2 NWs is determined to be $n = (3.3 \pm 0.4) \times 10^{16}$ cm^{-3}, the scattering time τ equals (75 $\pm$ 7) fs and the persistence of velocity $c_1 = -0.85 \pm 0.02$, indicating suppression of long carrier transport in these NWs. Also, the macroscopic *dc* mobility has been calculated to be equal $\mu \approx (72 \pm 10)$ cm^2/Vs. Moreover, the analysis of the photoconductivity measurements based on the Drude-Smith model revealed that the scattering time decreases from 140 to 70 fs as the carrier density increases from 0.5×10^{19} cm^{-3} to 5.5×10^{19} cm^{-3}. Evident from the analysis is a strong localization of carriers.

Although, a great deal of research has already been done out on semiconducting NWs using ultrafast techniques, many questions remained unanswered. For example, it is necessary to understand how the modifications in NW diameter or doping influence the electronic properties and relaxation mechanisms in NWs. In addition, it would be interesting to examine the cases where radically heterostructred core-shell NWs are synthesized and investigate the passivation of surface states in these NWs and the way that relaxation processes and time constants change. For example, it has been found that passivation of surface states by the shell, can lead to longer relaxation times.

To conclude, the carrier dynamics of GaN, In_2O_3 and SnO_2 NWs were investigated using ultrafast characterization methods. These measurements provided a detailed understanding of various effects and relaxation mechanisms of photogenerated carriers. In

addition, the role of defects in these NWs and the manner that they influence their electronic and optical properties is resolved. It is also shown that Auger recombination plays a significant role in the carrier dynamics for high pump fluences in these quasi-1-D nanostructures. Moreover, we have shown that important results for the electronic and also transport properties can be extracted for the NWs from the TRTS experiments and that spatial localization of carriers in NWs affects strongly the conductivity spectrums obtained from these measurements.

Appendix A

Surface Plasmon Resonances of Au Nanoparticles

From time resolved absorption measurements, a different behaviour is observed in the narrow probing region of 520–550 nm, where strong state filling is apparent. The surface plasmon resonance of the Au nanoparticles is responsible for the observed signal. This behavior has been observred for In_2O_3 NWs and SnO_2 NWs. In order to confirm this, we repeated the experiment using a sample of a 0.5 nm Au thin film on quartz using similar experimental conditions -pump wavelength, probe wavelength and pump fluence- to observe the carrier evolution in the region between 520 and 600 nm, as shown in Fig. A.1. The intensity of the pump beam was about 490 $\mu J/cm^2$. Measurements were taken for times up to 600 ps, but since significant changes are observed for small times, data for times up to 70 ps are shown here. No signal was detected in other spectral regions due to Au.

The presence of the surface plasmon resonance in this region is also supported by the steady state transmission measurements, shown in the Fig. 5.3. This effect induces an extra reduction in the transmission signal, and subsequently an increment in the absorption coefficient, as observed in the region between 520 and 600 nm. In time resolved absorption change signal, the fast negative rise of the signal is followed by a slower decay towards equilibrium in all probing wavelengths. The maximum state filling signal is observed at 550 nm in agreement with the maximum signal of the absorption coefficient in steady state transmission measurements and coincides with the minimum at the steady state transmission spectrum of In_2O_3 NWs due to the formation of Au nanoparticles.

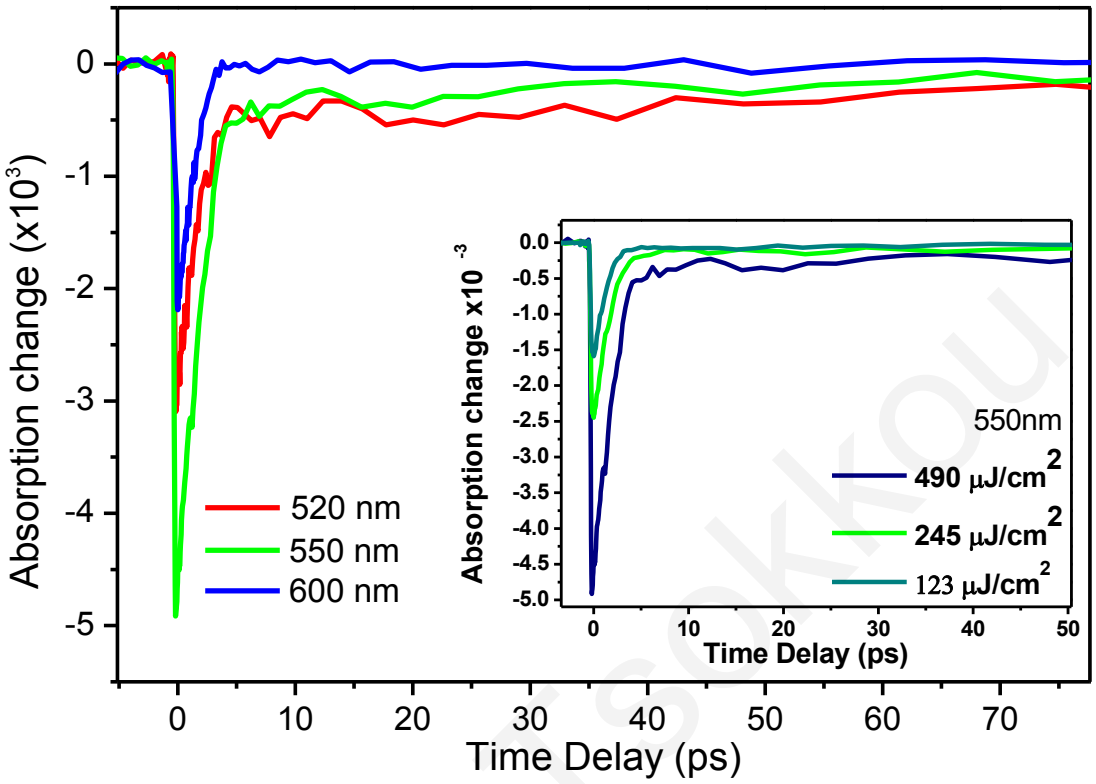

Figure A.1. Non-degenerate, time-resolved, transient absorption measurements of the Au nanoparticles as resulted by a 0.5 nm Au thin film using ultrafast excitation pulses at 320 nm and probing pulses in the range of 520-600 nm. In the inset of the figure, intensity measurements are shown for probing wavelength at 550 nm, where maximum signal was observed.

The appearance of surface plasmon resonance is a characteristic feature exhibited in the visible spectral region by metal nanostructures, such as nanoparticles or even in a planar surface between a metal-dielectric interface, due to the coupled oscillations of the electron density interacting with the applied electromagnetic field.[216] Qualitatively, in the case of metal nanoparticles, which are much smaller than the wavelength of the incident electromagnetic field; the electrons inside the particle feel a uniform electric field, which shifts the conduction electrons collectively onto the surface of the nanoparticles. Then, the interaction of electrons with the lattice ions leads to a restoring force leading to oscillations of the electron density. If the frequency of the probe beam is an eigenfrequency of this oscillation leads to a strong modification of the absorption coefficient, which is detectable in our time resolved absorption measurements. The resonance frequency depends on the

polarizability of the medium around the nanoparticles and the particle size. It is worth to mention that the signal due to surface plasmons is so strong that the contribution of carriers generated in the NWs into the total signal is not apparent.

After excitation of the Au thin films with UV pump pulses both interband and intraband absorption processes take place in Au and electrons are excited to higher energy states. In Au the lonesome electron of the external shell participates in intraband transitions associated with transitions between different s-p states changing the distribution of electrons near the Fermi level. Furthermore, interband processes can take place that involve electron transitions between d-band states and s-p states, since the threshold of interband transitions in Au requires energy above 2.4 eV.[219] As the pump pulse excites the sample, a number of electrons from their initial states will be excited into states above the Fermi level, changing the electron distribution into the metal. The excited electrons do not oscillate at the same frequency as the unexcited electrons. Therefore, the number of carriers into the initial – unexcited- states, that are responsible for the plasmon resonance band in the steady state transmission signal, is reduced. As a consequence, absorption from the carriers in the unexcited states is reduced and absorption change signal after ultrafast excitation ($\Delta A = A - A_0$) appears to be negative.

Afterwards, carriers relax towards equilibrium via several non-radiative processes, which lead to the temporal evolution of the observed signal. Initially, a non-Fermi distribution of electrons is formed which are thermalized among themselves via electron-electron interactions[220] and then lose their excess energy via electron-phonon interactions resulting in an equilibrium of electrons and lattice temperature.[221] Because of the large electron population, electron-electron scattering takes place on a time scale shorter than the laser pulse duration, which is usually on the order of 10 fs and is not detectable in these measurements.[130] To provide more information, intensity measurements were also performed for probing wavelength at 550 nm of the 0.5 nm Au thin film on quartz substrate, as seen in the inset of the Fig. A.1. By normalizing the experimental data and then fitting the results with multi-exponential curves, it is concluded that one relaxation mechanism is present and that relaxation time increases ranging between 1.4-2.3 ps, as pump fluence increases. Relaxation time is attributed to the required time for thermalization of carriers through electron-phonon coupling. As the intensity of the beam increases, a larger number of carriers is excited and

therefore they need more time to return back to equilibrium. For the highest pump beam intensity used (= 490 μJ/cm^2), a contribution of a much slower component is apparent and the relaxation is found to be biexponential. A slower relaxation time of about ~ 100 ps is detected. This behaviour was even more profound in the measurements obtained for In_2O_3 NWs were the pump intensity used was even larger, as can be observed in Fig. 5.10. The reason is that as the electrons cool, the lattice is heated and the observed slow time is the lifetime of lattice phonons. Our results are in agreement with time resolved absorption measurements reported by *Ahmadi et al*, for Au nanoparticles with a radius of approximately 15 nm, were a maximum plasmon surface resonance was obtained at 530 nm.[222]

Appendix B

Publications

Carrier dynamics and conductivity of SnO_2 nanowires investigated by time-resolved terahertz spectroscopy

Demetra Tsokkou,[1] Andreas Othonos,[1,a)] and Matthew Zervos[2]
[1]*Department of Physics, Research Center of Ultrafast Science, University of Cyprus, P.O. Box 20537, Nicosia 1678, Cyprus*
[2]*Department of Mechanical Engineering, Nanostructured Materials and Devices Laboratory, University of Cyprus, P.O. Box 20537, Nicosia 1678, Cyprus*

(Received 6 February 2012; accepted 7 March 2012; published online 26 March 2012)

THz spectroscopy has been applied to investigate the photo-induced and intrinsic conductivity in SnO_2 nanowires using the Drude-Smith model. The refractive index of the nanowires was found to decrease from 2.4 to 2.1 with increasing THz frequency and the dc mobility of the non-excited nanowires was determined to be 72 ± 10 cm^2/Vs. Measurements reveal that scattering times are carrier density dependent, while a strong suppression of long transport is evident. Intensity-dependent measurements provided an estimate of the Auger coefficient found to be $\gamma = (7.2 \pm 2.0) \times 10^{-31}$ cm^6/s.
 [http://dx.doi.org/10.1063/1.3698097]

Tin oxide (SnO_2) is considered an important n-type wide-bandgap semiconductor which has received a great deal of attention over the past few years mainly due to its high transparency in the visible part of the spectrum and sensitivity to certain gasses which make it technologically important for the fabrication of optoelectronic devices[1–3] and sensors.[4] Furthermore, in recent years, the field of semiconducting metal oxides has benefited a great deal from the development of one-dimensional nanostructures such as nanowires (NWs) and nanorods (NRs) due to their interesting properties arising from their small size and high surface-to-volume ratio.[5] In view of this there has been growing interest in the synthesis of SnO_2 NWs, the study of their fundamental electronic and optoelectronic properties and finally device applications.[6–8] Time domain THz spectroscopy (TDTS) and time resolved THz spectroscopy (TRTS) have been recently used to provide insight into the physical properties of semiconductor nanostructured materials, such as nanoparticles[9,10] and nanowires.[11,12] A significant advantage of these techniques is the ability to distinguish between free or localized carriers, excitons, and surface plasmon resonances, since they have different signatures in the photoconductivity spectrum.[13] Another advantage is that the transport parameters such as mobility can be measured without the need of fabricating contacts thereby providing rapid feedback for optimisation and the use of NWs for applications in transistors and transparent conductive electrodes.[14,15]

In this work, we have utilized TDTS to investigate the optical properties and intrinsic conductivity of SnO_2 NWs in the THz region. Furthermore, TRTS measurements were used to probe the carrier dynamics and transport properties on ps timescale. Time resolved measurements revealed that Auger recombination is negligible for carrier densities smaller than 5×10^{18} carriers/cm^3. Furthermore, carrier density studies have determined a recombination time of 2.5 ns and an Auger coefficient of $\gamma = (7.2 \pm 2.0) \times 10^{-31}$ cm^6/s. The conductivity measurements reveal localization of carriers and strong suppression of long transport. From the intrinsic conductivity data, we have estimated a mobility of (72 ± 10) cm^2/Vs. Moreover an analysis of the photoconductivity measurements based on the Drude-Smith model revealed that the scattering time decreases from 140 to 70 fs as the carrier density increases from 0.5×10^{19} cm^{-3} to 5.5×10^{19} cm^{-3}.

A *Spectra Physics Tsunami* Ti:Sapphire oscillator and a *Spitfire* regenerative amplifier were used to generate output pulses of 100 fs at 800 nm, with a repetition rate at 1 kHz and energy of 1.1 mJ/pulse. These, pulses are introduced into a conventional TRTS experimental apparatus.[13] UV was used to excite carriers into the conduction band states since SnO_2 is a wide bandgap semiconductor. This was achieved via third harmonic frequency mixing, providing pump pulses at 266 nm and energy up to 70 μJ/pulse. The generation of THz pulses was accomplished by nonlinear optical rectification in a 0.5 mm $\langle 110 \rangle$ ZnTe nonlinear crystal, and detection was achieved via free-electrooptic sampling technique using a second 0.5 mm $\langle 110 \rangle$ ZnTe crystal.

SnO_2 NWs were grown on 1 nm Au/Si(001) using a low pressure chemical vapour deposition reactor at 800 °C under a flow of 600 sccms Ar: 10 sccms O_2 at 1×10^{-3} mbar for 1 h, described in detail elsewhere.[8] The SnO_2 NWs have diameters of 50-100 nm and lengths up to ≥ 10 μm. For the measurements the SnO_2 NWs were transferred on quartz substrate by drop casting after being harvested from the parent substrate by sonication.

Initially, the carrier dynamics of the SnO_2 NWs were measured by photoexciting at 266 nm and sampling the change in the peak of the THz transmission signal as a function of temporal delay between pump and probe pulses. Figure 1 shows the negative change in THz pulse transmission within a time window of 400 ps for different excitation carrier densities between 5×10^{18} cm^{-3} and 5.6×10^{19} cm^{-3}.

By comparing the normalized pump fluence-dependent transmission traces shown in the inset of the Fig. 1, it is obvious that carrier relaxation becomes progressively faster as the photogenerated carrier density increases. Such behaviour is expected when Auger recombination effects contribute to the carrier relaxation. To verify the validity of this

a)Electronic mail: othonos@ucy.ac.cy.

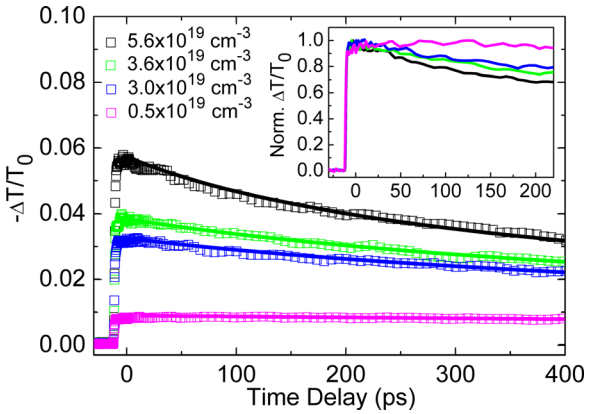

FIG. 1. Time resolved change in the THz transmission (dotted lines) using different pump fluences corresponding to carrier densities between $(0.5–5.6) \times 10^{19}\,\mathrm{cm}^{-3}$. For comparison purposes, the inset shows the normalized change in the transmission signal.

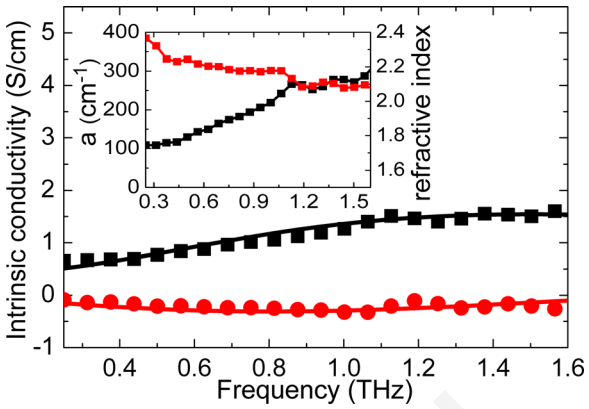

FIG. 2. Real (black squares) and imaginary (red circles) parts of the intrinsic conductivity in SnO_2 NWs for the region 0.25–1.6 THz. Solid lines have been obtained using the Drude–Smith model. The inset shows the frequency dependence of the refractive index (red squares) and absorption coefficient (black squares).

assertion, a differential rate equation model is used to explain the evolution of photogenerated carriers back to equilibrium. In this model, the recombination time is described by the first term of the differential equation whereas Auger recombination is described by the second term[16]

$$\frac{dN(t)}{dt} = -\frac{N(t)}{\tau} - \gamma \mathrm{N}^3(t), \tag{1}$$

where $N(t)$ corresponds to carrier density, τ is the recombination time and γ the Auger coefficient of SnO_2. The recombination time τ of the system was determined at the lowest carrier density where Auger recombination is considered negligible. Best fits were obtained when using a single exponential decay with a recombination time of $\tau = 2.5$ ns. The Auger coefficient γ in this NW system, was determined to be equal to $\gamma = (7.2 \pm 2.0) \times 10^{-31}\,\mathrm{cm}^6/\mathrm{s}$, which is in agreement with values reported in the same NWs elsewhere.[8]

TDTS measurements were utilized to determine the optical properties and the intrinsic conductivity of SnO_2 NWs in the THz region. Initially, measurements of the temporal THz electric field transmitted through SnO_2 NWs grown on Au/quartz without optical excitation, but also through plain quartz substrate were determined. The refractive index of the quartz substrate, was determined to be nearly constant ≈ 2.0 over the spectral region between 0.25-2 THz, while the absorption coefficient was considered negligible ($\leq 5\,\mathrm{cm}^{-1}$), in agreement with values reported elsewhere.[17] The properties of the SnO_2 NWs were extracted using the analysis followed for thin films.[18] No differences in the results were determined when an effective medium approximation (EMA) analysis was utilized.[19] The inset of Fig. 2 shows the refractive index (red squares) and absorption coefficient (black squares) calculated in the region of 0.25–1.6 THz. Clearly evident is a larger index of refraction than the refractive index of bulk SnO_2 in the visible region, $n \approx 2$,[20] which decreases monotonically from ≈ 2.4 to ≈ 2.1 with increasing THz frequency.

On the other hand, the absorption coefficient is monotonically increasing in the probed region from $110\,\mathrm{cm}^{-1}$ at 0.25 THz up to $300\,\mathrm{cm}^{-1}$ at 1.6 THz. Furthermore, Fig. 2 displays the real (black squares) and imaginary (red circles) parts of the frequency dependent intrinsic conductivity determined from the analysis of the data. Here we should point out that the real part of the conductivity increases monotonically, while the imaginary part of the conductivity appears to be negative. Similar behaviour has also been observed in Si nanocrystals,[10] InN nanorods,[21] and ZnO NWs,[11] which is described by the Drude–Smith model[22] and is attributed to the localization of carriers. This model, as described by Eq. (2), includes additional terms to modify the classical Drude system and incorporates the effect of incomplete randomization of carrier momentum after collisions

$$\sigma(\omega) = \frac{\mathrm{N}e^2\tau}{m^*(1 - i\omega\tau)}\left[1 + \sum_{j=1}^{\infty}\frac{c_j}{(1 - i\omega\tau)^j}\right], \tag{2}$$

where e is the electron charge, m^* the effective electron mass, τ the *scattering time*, and c_j the *persistence of velocity* after a number of j collisions. In the above equation we utilized the effective electron mass $m^* = 0.275\,m_0$ (m_0 the bare electron mass) for bulk SnO_2.[23] In practice, only the first term of the summation of Eq. (2) is taken into account. In an attempt to give a physical meaning to the *persistence of velocity* Monte Carlo simulations have been performed for the case of free charge carriers localized in semiconducting nanoparticles.[24] It was found that when the nanostructure dimensions are comparable to the mean free path, similar observations with that given by the Drude–Smith model can be expected, where the *persistence of velocity* c_1 is related to the possibility that carriers backscatter at the surface of the nanostructure. Clearly, the Drude–Smith model fits very well the experimental data shown in Fig. 2 as denoted by red and black lines for real and imaginary part of conductivity. The intrinsic carrier concentration in the SnO_2 NWs was determined to be $n = (3.3 \pm 0.4) \times 10^{16}\,\mathrm{cm}^{-3}$ whereas the scattering time τ (75 ± 7) fs. Furthermore, the persistence of velocity was estimated to be $c_1 = -0.85 \pm 0.02$. Given that the *persistence of velocity* is less than -0.5 this indicates suppression of long carrier transport due to the spatial localization of carriers. The estimated value of c_1 and scattering

time correspond to a macroscopic dc mobility of $\mu = \mu_m(1 + c_1) \approx (72 \pm 10)$ cm^2/Vs, where μ_m is the respective bulk mobility.

To further improve our understanding on the transport properties of the carriers in photoexcited SnO_2 NWs, photoconductivity measurements were performed. Here it is important to note that it is necessary to account for the filling factor of the NWs f_s on the substrate in order to obtain reliable values for the measured photoconductivity. Following careful examination of different SEM images the filling factor was estimated to be approximately 0.25. We should point out that a similar procedure has been previously applied for GaAs NWs (Ref. 12) in extracting the photoconductivity. In our measurements we utilized ultraviolet pulses at 266 nm at various pump energies in the range between 20.9–1.8 μJ/pulse. Measurements were carried out with the probe beam delayed at ~5 ps following the excitation pulse, where the THz signal has reached a maximum plateau, and before significant recombination of carriers could occur. We notice that the frequency dependence of the real part of the photoconductivity is similar to that obtained for the non-excited SnO_2 NWs, as seen in Fig. 3(a). On the other hand the imaginary part of the photoconductivity shown in Fig. 3(b) is more complex. It appears to be negative at low frequencies and becomes positive at larger frequencies. At first glance such behaviour can be explained by either the Drude–Smith model or by the surface plasmon resonance model[25] as has been proposed for GaAs NWs.[12] However, a careful estimate of the SnO_2 NWs plasmon frequency for the carrier densities considered in this work indicate that it is out of the frequency range measured here (>14 THz, when $N_0 = 0.5 \times 10^{19}$ carriers/cm^3) thus eliminating the plasmon resonance model. Moreover, the Drude–Smith model can sufficiently describe the experimental data as shown by the solid lines in the Figs.

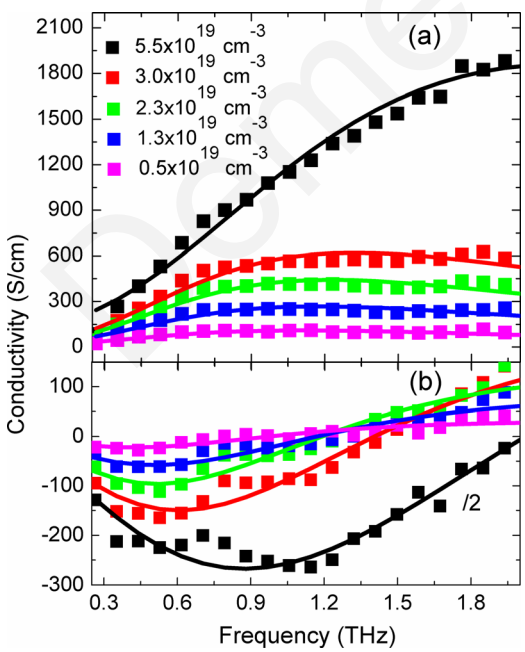

FIG. 3. (a) Real and (b) imaginary parts of conductivity spectrum of SnO_2 NWs (dot lines) at different pump energies corresponding to carrier densities $N_0 = (5.6–0.5) \times 10^{19}$ cm^{-3}, 5 ps after photoexcitation. Solid lines correspond to best fits using the Drude-Smith model.

3(a) and 3(b) corresponding to the best fits. Table I display the extracted best fitting parameters using the Drude-Smith conductivity for carrier density N, scattering time τ and *persistence of velocity* c_1 for the different pump energies utilized in this work.

From the Table I it appears that a larger fraction of the photo-generated carriers contribute to the photoconductivity with increasing pump fluence. This is to be expected given that, 5 ps after photoexcitation, most of the photogenerated carriers in the SnO_2 NWs lose their excess energy and relax to the bottom of the conduction band or move into shallow defect states or surface states. For such high pump fluences, we expect that these states are saturated by the photoexcited carriers in SnO_2 NWs as has been previously observed.[8] In addition to the fact that no band to band recombination of carriers is expected, since no band edge photoluminescence has been observed from these SnO_2 NWs, a large number of the initial carriers that are generated remain in conduction band states. These free charge carriers are likely to contribute to the photoconductivity. Therefore, in the case of the highest pump fluence it seems that the majority of photoinduced carriers contribute to the conductivity signal and the estimated carrier density ($\approx 4.5 \times 10^{19}$ carriers/cm^3) is close to the initial phogenerated carrier density ($\approx 5.5 \times 10^{19}$ carriers/cm^3). The difference is most likely due to the fact that some of the carriers become immobile as they are trapped into the defect/interface states. Accordingly, as the pump fluence decreases the number of initial carriers contributing to the photoconductivity becomes lower, since more carriers are trapped into defect/interface states. Furthermore, the *persistence of velocity* in this sample is strongly negative even for the lowest pump fluences used. This behavior suggests a strong localization of carriers in the SnO_2 NWs, since transport of carriers between different SnO_2 NWs is inhibited. There are several ways that carriers may transport into adjacent NWs, such as diffusion through pathways between connected NWs, tunneling or hopping.[26] As a consequence of the low volume filling factor of the SnO_2 NWs on the quartz substrate few interconnections between adjacent SnO_2 NWs exist. In addition the SnO_2 NWs are placed onto insulating SiO_2 and are surrounded by air so the potential barriers at the surface of the NWs are high, thereby preventing tunneling or hopping of carriers into different NWs. Moreover, the *persistence of velocity* becomes slightly more negative as the carrier density increases. We speculate that for such high carrier densities, a large number of carriers remain in the conduction band and a limited number of pathways exist for

TABLE I. Parameters of carrier density N, scattering time τ, and persistence of velocity c_1, extracted by fitting experimental data of Fig. 3 to Drude-Smith conductivity model.

$N_0 \times 10^{19}$ (carriers/cm^3)	$N \times 10^{19}$ (carriers/cm^3)	τ (fs)	C_1
5.5	4.5 ± 0.2	70 ± 4	-0.94 ± 0.01
3.0	0.9 ± 0.1	110 ± 5	-0.93 ± 0.01
2.3	0.5 ± 0.1	119 ± 4	-0.91 ± 0.01
1.3	0.40 ± 0.08	120 ± 6	-0.90 ± 0.01
0.5	0.15 ± 0.05	130 ± 6	-0.90 ± 0.01

carriers to move into a different SnO_2 NW, so carriers become localized. As expected the scattering time appears to be also carrier density dependent and becomes larger as the carrier density increases.

Results obtained from TDTS measurements cannot be directly compared to the results from the TRTS technique, since samples with different filling factor were used. In the case of the TDTS measurements, properties of SnO_2 NWs with a larger filling factor were investigated in contrast to those transferred. We believe that this is the reason for the slightly smaller negative value of persistence of velocity.

In summary, intensity dependent carrier dynamics have been measured and the time dependence of the photogenerated carriers modelled by including Auger recombination in a rate equation. This gave an Auger coefficient $\gamma = (7.2 \pm 2.0) \times 10^{-31}\,cm^6/s$ and a recombination time of 2.5 ns. We demonstrate that the intrinsic conductivity and photo-conductivity is affected by carrier localization in the SnO_2 NWs, which is a result of the diameter and low density of SnO_2 NWs on the substrate. For carrier densities between $0.5–5.5 \times 10^{19}\,cm^{-3}$, we find that the scattering time decreases from 140 to 70 fs. The refractive index varies between 2.4-2.1 in the probed region, while the mobility of SnO_2 NWs was found to be $(72 \pm 10)\,cm^2/Vs$.

[1]J. Maier and W. Gopel, J. Solid State Chem. **72**, 293 (1988).
[2]S. A. Pianaro, P. R. Bueno, E. Longo, and J. A. Varela, J. Mater. Sci. Lett. **14**, 692 (1995).
[3]N. Amin, T. Isaka, A. Yamada, and M. Konagai, Sol. Energy Mater. Sol. Cells **67**, 195 (2001).
[4]N. Yamazoe, Sens. Actuators B **5**, 7 (1991).
[5]Z. W. Pan, Z. R. Dai, and Z. L.Wang, Science **291**, 1947 (2001).
[6]Z. Liu, D. Zhang, S. Han, C. Li, T. Tang, W. Jin, X. Liu, B. Lei, and C. Zhou, Adv. Mater. **15**, 1754 (2003).
[7]M. J. Zheng, G. H. Li, X. Y. Zhang, S. Y. Huang, Y. Lei, and L. D. Zhang, Chem. Mater. **13**, 3859 (2001).
[8]A. Othonos, M. Zervos, and D. Tsokkou, Nanoscale Res. Lett. **4**, 828 (2009).
[9]M. C. Beard, G. M. Turner, J. E. Murhpy, O. I. Micic, M. C. Hanna, A. J. Nozik, and C. A. Schmuttenmaer, Nano Lett. **3**, 1695 (2003).
[10]D. G. Cooke, A. N. MacDonald, A. Hryciw, J. Wang, Q. Li, A. Meldrum, and F. A. Hegmann, Phys. Rev. B **73**, 193311 (2006).
[11]J. B. Baxter and C. A. Schmuttenmaer, J. Phys. Chem. **110**, 25229 (2006).
[12]P. Parkinson, J. Lloyd-Hughes, Q. Gao, H. H. Tan, C. Jagadish, M. B. Johnston, and L. M. Herz, Nano Lett. **7**, 2162 (2007).
[13]R. Ulbricht, E. Hendry, J. Shan, T. F. Heinz, and M. Bonn, Rev. Mod. Phys. **83**, 543 (2011).
[14]Q. Wan, E. Dattoli, and W. Lu, Small **4**, 451 (2008).
[15]Y.-D. Ko, J.-G. Kang, J.-G. Park, S. Lee, and D.-W. Kim, Nanotechnology **20**, 455701 (2009).
[16]M. Ghanassi, M. C. Schanne-Klein, F. Hache, A. I. Ekimov, D. Ricard, and C. Flytzanis, Appl. Phys. Lett. **62**, 78 (1993).
[17]D. Grischkowsky, S. Keiding, M. V. Exter, and C. Fattinger, J. Opt. Soc. Am. B **7**, 2006 (1990).
[18]T.-R. Tsai, S.-J. Chen, C.-F. Chang, S.-H. Hsu, T.-Y. Lin, and C.-C. Chi, Opt. Express **14**, 4898 (2006).
[19]F. J. García-Vital, J. M. Pitarke, and J. B. Pendry, Phys. Rev. Lett. **78**, 4289 (1997).
[20]E. Shanthi, V. Dutta, A. Banerjee, and K. L. Chopra, J. Appl. Phys. **51**, 6243 (1980).
[21]H. Ahn, Y.-P. Ku, Y.-C. Wang, C.-H. Chuang, S. Gwo, and C.-L. Pan, Appl. Phys. Lett. **91**, 163105 (2007).
[22]N. V. Smith, Phys. Rev. B **64**, 155106 (2001).
[23]K. J. Button, C. G. Fonstad, and W. Dreybrodt, Phys. Rev. B **4**, 4539 (1971).
[24]H. Němec, P. Kužel, and V. Sundström, Phys. Rev. B **79**, 115309 (2009).
[25]J. M. Pitarke, V. M. Silkin, E. V. Chulkov, and P. M. Echenique, Rep. Prog. Phys. **70**, 1 (2007).
[26]L. V. Titova, T. L. Cocker, D. G. Cooke, X. Wang, A. Meldrum, and F. A. Hegmann, Phys. Rev. B **83**, 085403 (2011).

Defect states of chemical vapor deposition grown GaN nanowires: Effects and mechanisms in the relaxation of carriers

Demetra Tsokkou,[1] Andreas Othonos,[1,a)] and Matthew Zervos[2]
[1]*Department of Physics, Research Center of Ultrafast Science, University of Cyprus, P.O. Box 20537, 1678 Nicosia, Cyprus*
[2]*Department of Mechanical and Manufacturing Engineering, Nanostructured Materials and Devices Laboratory, Materials Science Group, University of Cyprus, P.O. Box 20537, 1678 Nicosia, Cyprus*

(Received 4 June 2009; accepted 31 July 2009; published online 9 September 2009)

Carrier relaxation in GaN nanowires, grown by atmospheric pressure chemical vapor deposition, via direct nitridation of Ga with NH_3 at 950 °C has been investigated in detail. Differential absorption measurements reveal a large number of defect states located within the band gap. The relaxation dynamics of the photogenerated carriers suggest three distinct regions of energy states below the band edge identified as *shallow donor states*, *midgap states*, and *deep acceptor states*. Measurements suggest that Auger recombination is not a contributing factor in carrier relaxation even at the highest fluence ($\sim$1 mJ/cm^2) used in this work for carriers located within the conduction band. On the contrary, Auger recombination has been observed when probing the shallow donor states for fluences above 40 μJ/cm^2. Measurements at the lowest fluence reveal a biexponential relaxation for the donor states with the fast component ($\sim$50 ps) corresponding to the relaxation of carriers into the midgap states and the slow component of 0.65 ns associated with the relaxation into the deep acceptor states. Measurements reveal free-carrier absorption contribution from the deep acceptor states to the *U*-valley with an observed threshold limit of 3.5 eV suggesting the *U*-valley is located approximately 4.7 eV from the valence band. © *2009 American Institute of Physics*. [doi:10.1063/1.3212989]

I. INTRODUCTION

Group III-nitride (III-N) compound semiconductors, and especially GaN, InN, AlN, and their ternary or quaternary alloys, have proven to be useful for electronic and optoelectronic devices and have been investigated extensively over the past decade.[1–5] GaN epitaxial layers are an interesting material for optoelectronic devices emitting in the blue and ultraviolet (UV) regions and have already been utilized not only in commercial light emitting diodes and lasers[6–8] but also for the fabrication of UV photodetectors[9] due to the direct band gap, which is equal to 3.4 eV at room temperature (RT). Additionally, GaN has been used in high temperature, power electronic devices[10] such as field effect transistors.[11,12] On the other hand, III-N nanostructures, and especially nanowires (NWs), are interesting, since the lattice mismatch between GaN and the substrate on which they are grown is not so much of a severe constraint as in the case of homo- or heteroepitaxial growth of GaN. As a consequence, improved control on the formation of defects is feasible, which will potentially lead to nanodevices with enhanced performance and the possibility of direct integration with mainstream Si devices. In view of this, a great deal of work has been done in determining the growth conditions and investigating the structural, optical, and electrical properties of GaN NWs.[13] GaN NWs have already been grown not only by different methods, such as chemical vapor deposition (CVD),[13] metal organic CVD,[14] and molecular beam epitaxy,[15] but also via the arc discharge method,[16] pyrolysis,[17] and pulsed laser ablation.[18]

Given the potential impact that GaN may have in optoelectronic applications, it is of great importance to understand not only the fundamental behavior of photogenerated carriers upon excitation and their subsequent relaxation, but also the dominant relaxation mechanisms in this nanostructured material. Previous studies on the optical properties of GaN NWs have focused on steady-state photoluminescence (PL) measurements.[13,19,20] While the dynamic carrier behavior has been extensively investigated for bulk GaN,[21–23] carrier dynamics in GaN NWs and, in particular, the role of defect-related states within the band gap on carrier relaxation have not been investigated. Specifically only time resolved PL measurements have been reported.[24,25] In this work, transient absorption measurements were performed in GaN NWs using a nondegenerate pump-probe technique with above and below band gap excitation. Femtosecond laser pulse excitation provides the required temporal resolution for investigating carrier dynamics on an ultrafast time scale and so time resolved absorption spectroscopy provides an important insight into relaxation of the photogenerated carriers into energy states located above and below the conduction band (CB) edge.

II. EXPERIMENTAL PROCEDURE

GaN NWs were grown, initially, on *n* type Si (111) and then on sapphire (Al_2O_3) via atmospheric pressure CVD and direct nitridation of metal Ga with NH_3. Initially a thin film

a)Electronic mail: othonos@ucy.ac.cy.

of Au with thickness of ≈0.5 nm was deposited on Si(111) or Al_2O_3 via sputtering at a slow rate <5 Å/s using an Ar ion plasma. Before the deposition of Au film, substrates were cleaned in HF, rinsed in ionized water, and dried with nitrogen. The Au-coated substrate was placed in an alumina boat and then ≈0.3 g of pure metal Ga (Aldrich 99.99%) was carefully placed in the boat <5 mm upstream from the sample. The boat was then loaded at the center of a 25 mm quartz tube directly above the thermocouple used to measure the heater temperature. Initially, the tube was flushed with 500 SCCM (SCCM denotes cubic centimeter per minute at STP) of Ar and 500 SCCM of N_2 containing 5% H_2, for 10 min in order to eliminate residual oxygen and moisture contained in the reactor. Afterwards, the temperature of the furnace was increased to 950 °C with a ramp rate of 15 °C/min, under a steady flow of 100 SCCM of N_2:5%H_2. Subsequently, the temperature was maintained at 950 °C for 1 h and NH_3 was allowed to flow at 25 SCCM using a reduced flow of 75 SCCM of N_2:5%H_2. At the end of the growth period the reactor was allowed to cool down to RT in flows of 25 SCCM of NH_3 and 75 SCCM of N_2:5%H_2. Upon removal from the reactor the Si or Al_2O_3 substrates were covered with a white-blue colored layer. The morphology of the GaN NWs was investigated by using a TESCAN scanning electron microscope (SEM), and the crystal structure and phase purity of the NWs were determined by x-ray diffraction (XRD) using a SHIMADZU XRD-6000 diffractometer and Al holders.

Transient absorption measurements were performed using two different ultrafast amplifier laser systems in a typical supercontinuum pump-probe configuration.[26] The first system contains a self mode-locked Ti:sapphire generating 35 fs, 5 nJ pulses at ~800 nm with a repetition rate of 100 MHz. A regenerative amplifier is used to intensify the pulses approximately 10^6 times at a repetition rate of 5 kHz. An optical parametric amplifier was utilized to generate excitation pulses in the UV region of the spectrum for above band gap excitation of the GaN NWs. A small part of the fundamental energy was used to generate a supercontinuum white light in the visible/near infrared region of the spectrum for transient nondegenerate absorption measurements. Additionally, a second harmonic crystal was used in a different setup to double the frequency of the fundamental light for the generation of white light continuum in the UV region. Moreover, a second ultrafast amplifier system uses a similar apparatus to produce excitation pulses at 400 nm with time duration of 100 fs and a repetition rate of 1 kHz.

III. RESULTS AND DISCUSSION

So far GaN NWs have been grown by the direct nitridation of metal Ga with NH_3,[13,27–29] at temperatures above 900 °C due to the reduced vapor pressure of Ga at lower temperatures. In order to enhance the vapor pressure of Ga at lower growth temperatures Chang and Wu[30] used Ga acetylacetonate as a precursor, and, more recently, Yu *et al.*[31] used a mixture of Ga and CaF_2.[31] Different metals have been used as a catalyst for the synthesis of GaN NWs, such as transitions metals Ni,[27,28,31] Fe,[13] In,[13] and Co.[13] However, controversial results have been reported when Au is used as a catalyst, since Cai *et al.*[27] reported the synthesis of GaN NWs with this catalyst, while Zhang and Zhang[28] mentioned that no wires were formed. A typical SEM image of the high density GaN NWs grown on 0.5 nm Au/Al_2O_3 is shown in Fig. 1. Straight wires with uniform diameters of ≈100 nm and lengths up to a few microns are observed. Figure 2 shows the XRD pattern of the GaN NWs grown on sapphire where the peaks correspond to the (100), (002), (101), (110), and (112) crystallographic planes of the hexagonal wurtzite structure of GaN with lattice constants a=0.318 nm and c=0.518 nm.[29] In agreement with previous investigations on GaN NWs,[13,27–29] high growth temperatures ≥900 °C are necessary for the growth of GaN NWs by direct nitridation of metal Ga with NH_3. NWs were also obtained at 900 °C, but their density was higher at 950 °C. We also found that the addition of H_2 to the gas flow, during the temperature ramp and growth step, is crucial to prevent the oxidation of

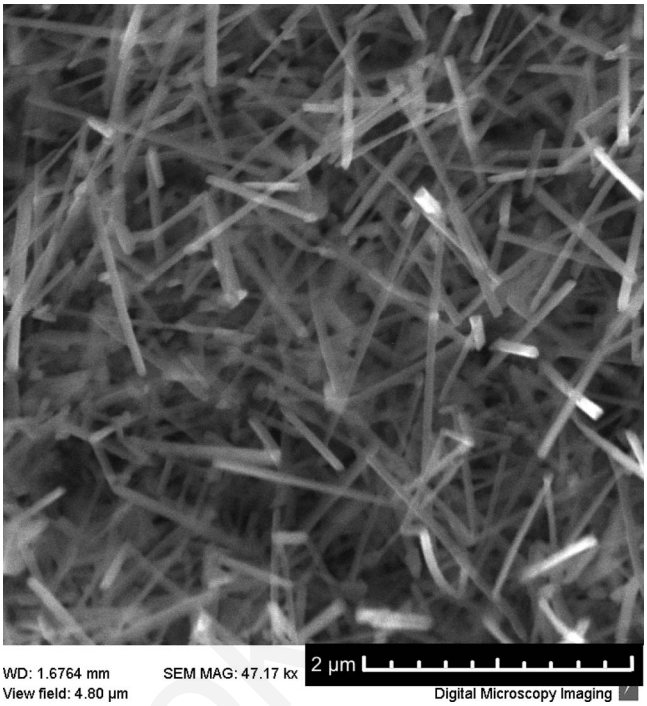

FIG. 1. SEM image of the GaN NWs on Au/Al_2O_3.

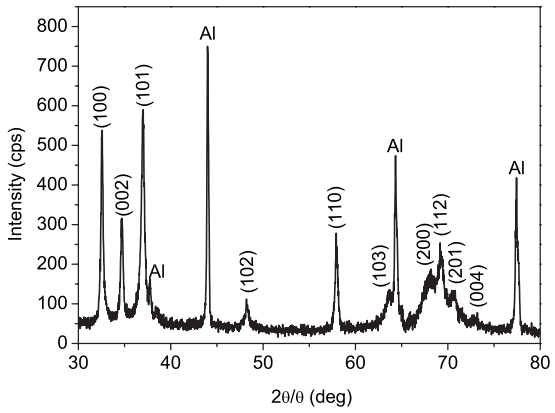

FIG. 2. XRD pattern of GaN NWs on sapphire.

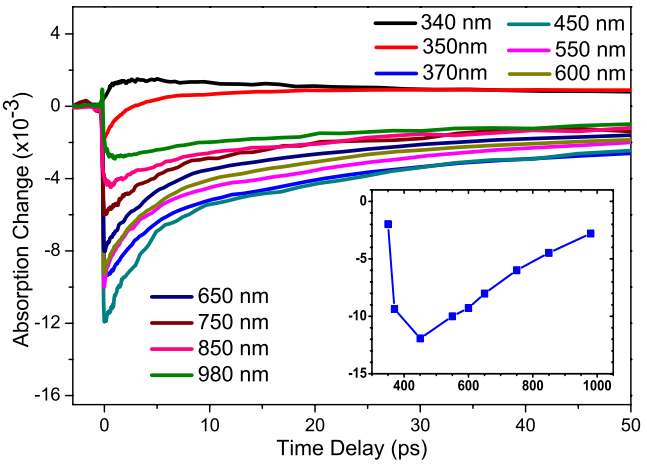

FIG. 3. (Color online) Nondegenerate, time resolved, transient absorption measurements of the GaN NWs using ultrafast excitation pulses at 320 nm and probing pulses in the range 340–980 nm. In the inset state filling minimum is shown vs probing wavelength.

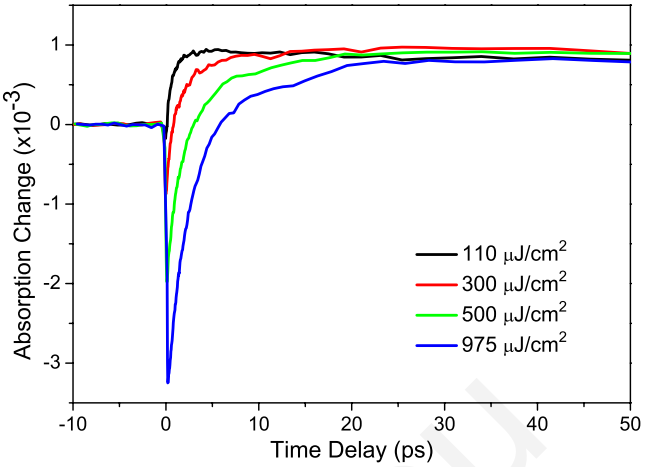

FIG. 4. (Color online) Nondegenerate, time resolved, transient absorption measurements of the GaN NWs using ultrafast excitation pulses at 320 nm and probing pulses at 350 nm for different pump fluences.

Ga from residual O_2 in the reactor. In addition when NH_3 was included during the temperature ramp it leads to the nitridation of the Ga upstream, which in turn reduced the vapor pressure at the growth temperature. No GaN NWs were obtained on silicon or sapphire alone confirming that the GaN NWs grow by the vapor-liquid-solid mechanism. In contrast with a previous study[28] Au is a proper choice for the growth of GaN NWs.

Figure 3 shows transient absorption nondegenerate measurements using UV femtosecond pulse excitation and, in particular, the time evolution of absorption change for excitation pulses at 320 nm (3.87 eV) and different probing wavelengths ranging between the UV and near IR region of the spectrum. Measurements were carried out for delays up to 500 ps, although only 50 ps are shown in Fig. 3 for clarification purposes. The absorbed pump fluence for these data was estimated to be ~ 0.5 mJ/cm^2. Also seen as an inset in Fig. 3 is the state filling minimum signal, which is plotted as a function of probing wavelength. Clearly evident from the data in Fig. 3 is the different temporal behavior of the induced absorption for probing wavelengths corresponding to photon energy above and below the band edge of the GaN NWs. What appears to be common in all the curves is a fast initial response reaching a minimum or maximum depending on the probing wavelength, which is then followed by a slower recovery toward equilibrium. It is well known that above band gap excitation of a semiconductor material will result in the generation of carriers that will occupy the available energy states near the excitation region. As a consequence of this occupation of states, a negative change in absorption is expected, known as state filling. However, in addition to state filling, free carriers may undergo secondary excitation by the probe laser pulse resulting in what is known as "free-carrier absorption." This is a positive contribution to the induced absorption and it usually competes with state filling, which is negative. Normally state filling is the dominant contribution when probing above the band edge, whereas free-carrier absorption is the dominant process when probing below the band edge. It is interesting to point out that in the CVD grown GaN NWs when probing at 340 nm, which is above the band edge, we notice a positive signal suggesting that free-carrier absorption is the dominant contribution. Although this is not expected, we believe that as a consequence of strong coupling between the photogenerated carriers and energetically higher states with an energy difference corresponding to the probing wavelength, free-carrier absorption prevails.

A more complex behavior is observed when probing at 350 nm. State filling is initially observed, but with increasing delay time the signal becomes positive before it returns to equilibrium. Furthermore, strong state filling effects are observed for all probing wavelengths between 370 and 980 nm. This result suggests that defect-related states are located within the entire band gap of the GaN NWs. This is clearly seen in the inset of Fig. 3 where state filling minimum versus wavelength is shown and which to a first approximation reflects the density of states at the probing wavelength.

To further investigate the transient behavior of the GaN NWs, intensity measurements have been carried out at the probing wavelength of 350 nm, as seen in Fig. 4. Clearly evident is the initial negative state filling, which is intensity dependent. This observed state filling is associated with the occupation of states located near the band edge, so we need to consider the possibility that the observed positive signal in the temporal profiles of the measurements could be due to band gap renormalization, as has already been reported in degenerated pump-probe measurements for bulk GaN.[32] Nevertheless, in nondegenerate transient absorption measurements, band gap renormalization would be expected to be observed first, followed by state filling when the carriers reach the probing state. Furthermore, the maximum positive signal and its temporal behavior do not exhibit any dependence on the incident fluence and thus on the photogenerated carrier density. In view of the above, it is believed that the positive signal in Fig. 4 is not associated with band gap renormalization, but rather with free-carrier absorption.

In what follows we will explain in more detail the observed free-carrier absorption at 350 nm. It is important to point out that the different temporal behavior observed for

state filling and free-carrier absorption suggests that these contributions are related to different energy states. The state filling signal appears to increase linearly with increasing pump fluence. This observation is consistent with the fact that higher pump fluences lead to larger occupation of states in the CB by the photogenerated carriers. It is worthy to mention that with increasing pump fluence, state filling appears to take longer, suggesting that Auger recombination is negligible for states in the CB located around 3.5 eV, even for the highest fluences (~ 1 mJ/cm^2) used in this work. For longer delay times free-carrier absorption appears to dominate. Furthermore, the relaxation of this signal appears to be almost identical for all pump fluences as seen in the inset of Fig. 4. This suggests that the two competitive effects are not influenced in the same way by the increment in pump energy, despite that both effects are carrier density dependent. The observations above suggest that the saturation of free-carrier absorption occurs even for the lowest pump energy used in these experiments. We should also note that in the measurements of Fig. 3, no free-carrier absorption is observed for probing wavelengths larger than 350 nm (3.5 eV), setting a minimum limit for the energy difference between the coupled states where free-carrier transitions take place. Given the above observations, it is believed that free-carrier transitions take place between a defect-related state located inside the band gap and the indirect satellite valley of the CB. The possibility that free-carrier transitions may occur between states in the CB is ruled out given the intensity dependent measurements of Fig. 4. In interpreting our experimental results we took into consideration a theoretical model for the distribution of defect states in GaN proposed by Shalish *et al.*[33] According to this model, deep acceptor states correlated with the yellow luminescence are attributed to Ga vacancies, which are centered at ~ 1.2 eV from the top of the valence band. Taking into consideration the minimum energy difference between the energy states for the observation of free-carrier absorption (~ 3.54 eV), we conclude that the energy difference between the indirect valley and valence band is ~ 4.7 eV. This result is in very good agreement with the minimum energy of the *U*-valley (~ 4.73 eV) for the bulk wurtzite GaN reported by Sun *et al.*[21] No changes in the energy states are expected due to quantum confinement effects, since the diameter of the wires is much larger than the exciton Bohr radius for this material.[34]

To help the reader obtain a clear picture of the dynamics in GaN NWs we have included a schematic band diagram model (Fig. 5) showing the various defect states and relaxation mechanisms utilized in our interpretation. The main relaxation mechanisms within the band gap are identified as "A–D." The transitions discussed above, between deep acceptor states (~ 1.2 eV) and states within the *U*-valley (~ 4.7 eV), and observed when the probing energy is larger than 3.5 eV are also shown with an arrow.

To further improve our understanding of the carrier dynamics in the GaN NWs intensity measurements have also been carried out at 370 nm thus probing energy states placed just below the direct band edge. The intensity measurements are normalized for comparison purposes and are shown in Fig. 6. The observed state filling is attributed to the occupation of shallow donor energy states due to nitrogen vacancies and oxygen impurities[35] by the photogenerated carriers. Clearly evident from the normalized data is that carrier relaxation becomes faster with increasing pump fluence indicating that Auger recombination is present. Given that Auger recombination was negligible for the carriers within the CB energy states (Fig. 4), we conclude that the observed Auger effects must arise from interactions of carriers within the defect-related states. Relaxation times for the lowest pump energy of 11 μJ/cm^2, where Auger recombination is expected to be negligible, have been estimated using multiple exponential decays. Best fitting was obtained using a biexponential decay corresponding to two relaxation mechanisms. The first mechanism with a time constant ≈ 50 ps

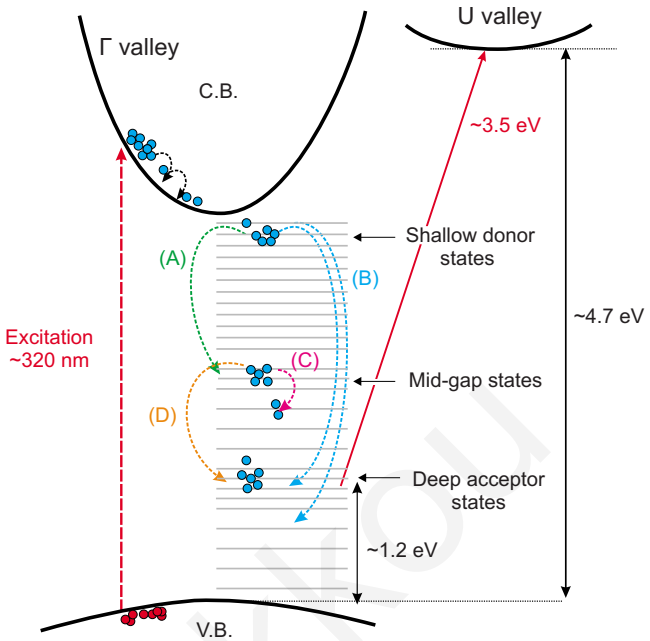

FIG. 5. (Color online) Schematic energy band diagram of GaN NWs. The excitation at 320 nm generating carriers within the CB is depicted as a vertical dashed arrow. Relaxation mechanisms within the band gap are identified as A–D (dot arrows). Free-carrier absorption from the deep acceptor states to the *U*-valley ($\Delta E \sim 3.5$ eV) is also shown in the diagram.

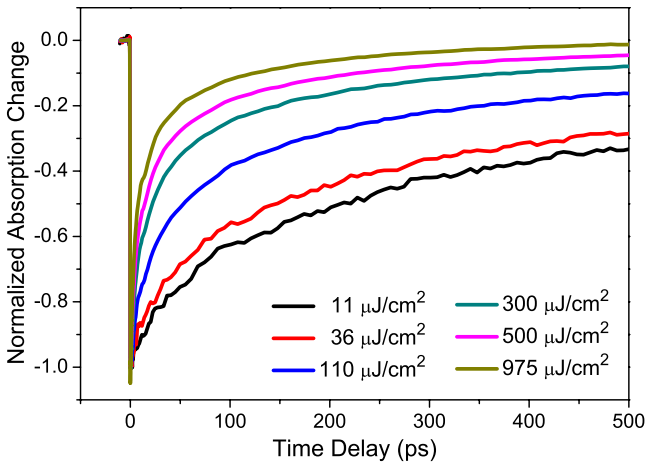

FIG. 6. (Color online) Normalized transient absorption change in the GaN NWs using ultrafast excitation pulses at 320 nm and a probing wavelength at 370 nm for different pump fluences.

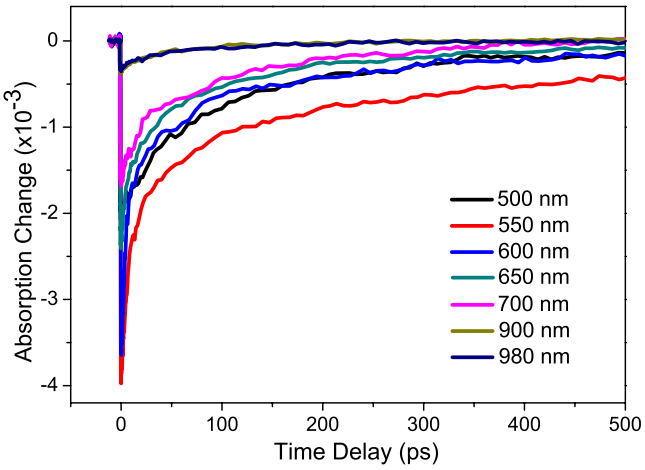

FIG. 7. (Color online) Nondegenerate transient absorption measurements of the GaN NWs using ultrafast excitation pulses at 400 nm and probing pulses in the range 340–980 nm.

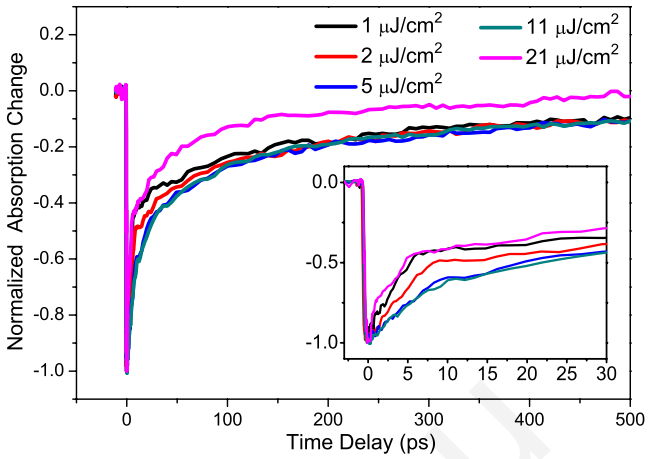

FIG. 8. (Color online) Nondegenerate transient absorption measurements of the GaN NWs using ultrafast excitation pulses at 400 nm and probing pulses at 550 nm for different pump fluences.

(30%) is attributed to carriers originating from native defects, or due to the surface of the NWs and relaxing to the midgap states. This mechanism is identified as mechanism A in Fig. 5. The second mechanism with a time constant of ≈655 ps (70%) is believed to be associated with carriers relaxing to the deep acceptor states inside the band gap i.e., mechanism B. Here we should point out that the latter mechanism may be responsible for the observed yellow luminescence (~2.30 eV) in GaN.[36] However, we cannot rule out the possibility that carriers may relax to lower shallow acceptor states or recombine.

To further investigate carrier dynamics within the defect-related states that are energetically located inside the band gap, nondegenerate time resolved absorption measurements have been performed using excitation at 400 nm (3.1 eV). The temporal measurements are shown in Fig. 7. The estimated absorbed pump fluence in these measurements is ~10 $\mu J/cm^2$. The induced absorption change when probing below the band edge reveals a large density of defect states. Here we should also point out that no signal was detected when the excitation wavelength was set to 650 nm (≡1.9 eV), even for pump energies ten times higher than the energy used at 400 nm, confirming that a much lower density of states exists in this region. Clearly evident from Fig. 7 is the dominant state filling, which prevails over free-carrier absorption for all probing wavelengths in the region between 500 and 980 nm. This behavior is in agreement with the previous results obtained for above band gap excitation. A comparison of the dynamics above and below band gap excitation reveals similar time constants when the absorption fluence was kept approximately constant.

Finally, intensity measurements were performed for excitation pulses at 400 nm, probing wavelength at 550 nm and for absorption fluences ranging between 1 and 21 $\mu J/cm^2$. Figure 8 shows the normalized intensity measurements for comparison purposes. The fast relaxation component as seen in the inset of Fig. 8 becomes slightly slower, i.e., increased from 6.5 to 12 ps (60%), as the fluence increased from 1 to 11 $\mu J/cm^2$. This is due to the larger number of carriers that occupy the defect-related states, and as a result these carriers need longer times to leave the probing region. It is believed that the fast relaxation time is associated with mechanism C in Fig. 5, which is the required time for probed carriers to relax to energetically close states. The slow relaxation component is estimated to be ~350 ps (40%) and is probably associated with nonradiative transitions to the lower acceptor states, which is identified as mechanism D in Fig. 5. For fluence higher than 11 $\mu J/cm^2$, a change in the temporal behavior of the induced absorption is observed. It appears that carrier relaxation becomes faster at 22 $\mu J/cm^2$, indicating that Auger recombination is present for the midgap states when a threshold in carrier density is exceeded.

IV. CONCLUSIONS

The effects on carrier relaxation of defect-related states inherit in CVD grown GaN NWs have been studied in detail. Transient absorption measurements reveal a large number of defect states located below the band edge. These states are placed throughout the entire band gap, and their presences were confirmed via state filling effects observed for all probing wavelengths below the band edge. A simplified band gap model, which incorporates three distinct regions of states, namely, shallow donor, midgap, and deep acceptor states located below the band edge, has been utilized to explain the carrier dynamics following femtosecond pulse excitation. Furthermore, it appears that Auger recombination is not a contributing factor in the carrier relaxation of carriers located within the CB even for the highest fluence used in this work. On the contrary, Auger recombination has been observed when probing the shallow donor states just below the band edge for fluences as low as 36 $\mu J/cm^2$. Measurements at the lowest fluence reveal a biexponential relaxation related to the donor states with the fast component corresponding to the relaxation carriers into the midgap states and the slow component of 0.65 ns associated with the relaxation into the deep acceptor states. Differential absorption measurements when probing above the band gap reveal free-carrier absorption contribution corresponding to coupling between the deep acceptor states located at 1.2 eV from the valence band and the indirect *U*-valley. The observed threshold limit of 3.5 eV to

the coupling between these states suggests that the *U*-valley is located approximately 4.7 eV from the valence band in the GaN NWs.

ACKNOWLEDGMENTS

The work in this article was supported by the Research Promotion Foundation of Cyprus under Grants EPYNE/0506/02, EPYAN/0506/04, BE0308/03 for fundamental research in the area of nanotechnology and nanomaterials.

[1]S. C. Jain, M. Willander, J. Narayan, and R. Van Overstraeten, Appl. Phys. Lett. **87**, 965 (2000).
[2]H. Hirayama, J. Appl. Phys. **97**, 091101 (2005).
[3]O. Ambacher, J. Phys. D **31**, 2653 (1998).
[4]A. G. Bhuiyan, A. Hashimoto, and A. Yamamoto, J. Appl. Phys. **94**, 2779 (2003).
[5]B. Monemar, J. Mater. Sci.: Mater. Electron. **10**, 227 (1999).
[6]S. Nakamura, M. Senoh, S.-I. Nagahama, N. Iwasa, T. Yamada, T. Matsushita, H. Kiyoku, Y. Sugimoto, T. Kozaki, H. Umemoto, M. Sano, and K. Chocho, Appl. Phys. Lett. **72**, 211 (1998).
[7]F. A. Ponce and D. P. Bour, Nature Mater. **386**, 351 (1997).
[8]J. W. Orton and C. T. Foxon, Rep. Prog. Phys. **61**, 1 (1998).
[9]H. Morkoc, A. Di Carlo, and R. Cingolani, Solid-State Electron. **46**, 157 (2002).
[10]M. S. Shur, Solid-State Electron. **42**, 2131 (1998).
[11]S. Yoshida and H. Ishii, Phys. Status Solidi A **188**, 243 (2001).
[12]S. C. Binari, K. Doverspike, G. Kelner, H. B. Dietrich, and A. E. Wickenden, Solid-State Electron. **41**, 177 (1997).
[13]C.-C. Chen, C.-C. Yeh, C.-H. Chen, M.-Y. Yu, H.-L. Liu, J.-J. Wu, K.-H. Chen, L.-C. Chen, J.-Y. Peng, and Y.-F. Chen, J. Am. Chem. Soc. **123**, 2791 (2001).
[14]T. Kuykendall, P. J. Pauzauskie, S. Lee, Y. F. Zhang, J. Goldberger, and P. D. Yang, Nano Lett. **3**, 1063 (2003).
[15]K. A. Bertness, A. Roshko, L. M. Mansfield, T. E. Harvey, and N. A. Sanford, J. Cryst. Growth **300**, 94 (2007).
[16]W. Han, P. Redlich, F. Ernst, and M. Ruhle, Appl. Phys. Lett. **76**, 652 (2000).
[17]W.-Q. Han and A. Zettl, Appl. Phys. Lett. **80**, 303 (2002).
[18]D. K. T. Ng, L. S. Tan, and M. H. Hong, Curr. Appl. Phys. **6**, 403 (2006).
[19]B. Ha, S. H. Seo, J. H. Cho, C. S. Yoon, J. Yoo, G. C. Yi, C. Y. Park, and C. J. Lee, J. Phys. Chem. **109**, 11095 (2005).
[20]J. Yoo, Y.-J. Hong, S. J. An, G.-C. Yi, B. Chon, T. Joo, J.-W. Kim, and J.-S. Lee, Appl. Phys. Lett. **89**, 043124 (2006).
[21]C.-K. Sun, Y.-L. Huang, S. Keller, U. K. Mishra, and S. P. DenBaars, Phys. Rev. B **59**, 13535 (1999).
[22]O. Aoudé, P. Disseix, J. Leymarie, and A. Vasson, M. Leroux, E. Aujol, B. Beaumout, A. Trassoudaine, and Y. André, Phys. Rev. B **77**, 045206 (2008).
[23]E. D. O' Sullivan, S. Hess, R. A. Taylor, N. J. Cain, V. Roberts, J. S. Roberts, and J. F. Ryan, Physica B **272**, 402 (1999).
[24]B. Chon, S. R. Ryu, Y.-J. Hong, J. Yoo, G.-C. Yi, T. Joo, and Y. M. Jung, J. Mol. Struct. **883–884**, 209 (2008).
[25]J. Renard, B. Amstatt, C. Bougerol, E. Bellet-Amalric, B. Daudin, and B. Gayral, J. Appl. Phys. **104**, 103528 (2008).
[26]A. Othonos, J. Appl. Phys. **83**, 1789 (1998).
[27]X. M. Cai, A. B. Djurisic, and M. H. Xie, Thin Solid Films **515**, 984 (2006).
[28]J. Zhang and L. Zhang, J. Vac. Sci. Technol. B **21**, 2415 (2003).
[29]C. C. Tang, S. S. Fan, H. Y. Dang, P. Li, and Y. M. Liu, Appl. Phys. Lett. **77**, 1961 (2000).
[30]K.-W. Chang and J.-J. Wu, J. Phys. Chem. B **106**, 7796 (2002).
[31]L. Yu, Y. Ma, and Z. Hu, J. Cryst. Growth **310**, 5237 (2008).
[32]C.-K. Sun, J.-C. Liang, X.-Y. Yu, S. Keller, U. K. Mishra, and S. P. DenBaars, Appl. Phys. Lett. **78**, 2724 (2001).
[33]I. Shalish, L. Kronik, G. Segal, Y. Rosenwaks, Y. Shapira, U. Tisch, and J. Salzman, Phys. Rev. B **59**, 9748 (1999).
[34]Y. Xie, Y. Qian, and W. Wang, Science **272**, 1926 (1996).
[35]C. B. Soh, S. J. Chua, H. F. Lim, D. Z. Chi, S. Tripathy, and W. Liu, J. Appl. Phys. **96**, 1341 (2004).
[36]M. A. Reshchikov and H. Morkoc, J. Appl. Phys. **97**, 061301 (2005).

Ultrafast time-resolved spectroscopy of In_2O_3 nanowires

Demetra Tsokkou,[1] Andreas Othonos,[1,a)] and Matthew Zervos[2]
[1]*Department of Physics, Research Center of Ultrafast Science, University of Cyprus, P.O. Box 20537, Nicosia 1678, Cyprus*
[2]*Department of Mechanical Engineering, Nanostructured Materials and Devices Laboratory, University of Cyprus, P.O. Box 20537, Nicosia 1678, Cyprus*

(Received 27 August 2009; accepted 13 September 2009; published online 21 October 2009)

Ultrafast carrier dynamics in In_2O_3 nanowires with an average diameter of $\approx 100 \pm 20$ nm grown by the vapor-liquid-solid method have been investigated in detail using differential absorption spectroscopy with femtosecond resolution. Measurements revealed that state filling is important for states above the band gap and states just below the band edge, thus demonstrating the critical role that shallow traps play in the relaxation of the photogenerated carriers. Furthermore, time-resolved intensity measurements revealed the importance of Auger recombination in the relaxation of carriers in the In_2O_3 nanowires and provided the maximum fluence (~ 3 $\mu J/cm^2$) where this recombination mechanism may be considered negligible. Transient measurements in this low-fluence regime for carriers above the band gap revealed single exponential recovery (~ 1.5 ns) associated with recombination of the photogenerated carriers. Similar behavior has been observed for the photogenerated carriers distributed within the shallow traps just below the band edge. Furthermore, measurements at longer probing wavelengths provided an estimate of the nonradiative relaxation of carriers (~ 300 ps), which are distributed among the midgap states. Finally, long-lived oscillations in the transient reflection were detected, which corresponds to the presence of longitudinal acoustic phonons in the In_2O_3 nanowires. © *2009 American Institute of Physics*. [doi:10.1063/1.3245339]

I. INTRODUCTION

Indium oxide (In_2O_3) is an important, *n*-type semiconductor oxide,[1] due to its large band gap, i.e., $E_G = 3.5-3.75$ eV and has been utilized for applications in electronic and optoelectronic devices, such as window heaters, flat planet displays, solar cells, and organic light emitting diodes.[2–4] In addition, In_2O_3 nanowires (NWs) are suitable candidates for gas sensors and the detection of toxic gases such as NO_2, NO, and NH_3 (Refs. 5–7) due to the enhanced surface-to-volume ratio but also as field effect transistors.[8] Furthermore In_2O_3 NWs grown by the vapor-liquid-solid (VLS) mechanism can be readily integrated with mainstream Si devices since the issue of lattice mismatch is not so critical; i.e., NWs can be grown with relative ease by the VLS mechanism on a large variety of substrates. Consequently, in addition to quantum confinement, their electronic and optoelectronic properties are expected to be also dependent on the surfaces states and properties. Previous investigations of photoluminescence in nonintentionally doped In_2O_3 NWs have revealed peaks with energies below the band gap,[9–12] which are associated with oxygen defect states, such as vacancies and antisites. However, there has been no detailed investigation using ultrafast time-resolved spectroscopy which can provide a more detailed understanding of the nature of the electronic states in In_2O_3 NWs and other important physical properties. Consequently, we have undertaken a detailed investigation of the carrier dynamics and relaxation mechanisms in In_2O_3 NWs that were grown by chemical vapor deposition (CVD). We find that the relaxation times of carriers excited into the conduction band (CB) are similar to those in shallow, defect related states, which are energetically situated just below the CB edge. In contrast, we find that midgap states have a different temporal behavior, while long-lived oscillations in the reflection were also detected due to longitudinal phonons. These findings are discussed in detail in addition to extracting relaxation times and the velocity of sound in In_2O_3 NWs.

II. EXPERIMENTAL PROCEDURE

Indium oxide NWs were prepared using an atmospheric pressure CVD reactor consisting of four mass flow controllers (MFCs) and a horizontal quartz tube furnace, capable of reaching a maximum temperature of 1100 °C. High purity indium powder (Aldrich, Mesh −100, 99.99%) was used and about ≈0.2 g was weighed and loaded into a quartz boat. In_2O_3 NWs were grown on n^+ Si(111) substrates that were coated with 0.5 nm of Au which was deposited on Si(111) via sputtering at a slow rate using an Ar plasma under a pressure $<10^{-4}$ mbar. After loading the In powder and Au/Si(111) samples into the quartz boat, it was inserted into the reactor and positioned directly above the thermocouple used to measure the heater temperature.

Initially, oxygen was admitted into the reactor at a flow of 50 SCCM (SCCM denotes cubic centimeter per minute at STP) for 10 min at room temperature (RT). Following this the O_2 flow was terminated and argon (Ar) was introduced at 500 SCCM for 10 min after which the temperature was increased up to 700 °C, using a ramp rate of 30 °C/min. During growth the temperature and flow of Ar were maintained constant at 700 °C and 100 SCCM, respectively, for 90 min.

a)Electronic mail: othonos@ucy.ac.cy.

Finally, upon cooling down the flow of Ar was maintained at 100 SCCM and the sample was removed from the reactor only after cooling down to RT. Upon visual inspection, the surface of the sample had a light-blue color, while the In powder, which melts at 157 °C always formed a graylike, spherical drop. For the purpose of ultrafast spectroscopy, In_2O_3 NWs were grown directly on quartz which was also coated with ≈0.5 nm of Au.

The morphology of the In_2O_3 NWs was examined with a Tescan scanning electron microscope (SEM) while the crystal structure and the phase purity of the NWs were investigated using a Shimadzu, XRD-6000, x-ray diffractometer and Cu $K\alpha$ source. A scan of θ-2θ in the range between 20° and 80° was performed for the In_2O_3 NWs that were grown on Si(111) and quartz. Following this the optical transmission spectrum was obtained by a standard UV/visible spectrometer (Perkin Elmer Lambda 950). Furthermore, transient nondegenerate absorption spectroscopy was performed using a typical supercontinuum pump-probe configuration.[13] The initial femtosecond laser source used in the experiment was a self-mode-locked Ti:sapphire oscillator generating 45 fs, 5 nJ pulses at 790 nm with a repetition rate of 100 MHz. These pulses were amplified $\sim 10^6$ times in a typical regenerative amplifier system producing 45 fs pulses at a repetition rate of 5 kHz. Part of the output energy was then directed into an optical parametric amplifier generating femtosecond pulses in the UV spectral region. A small part of the fundamental energy was also used to generate a supercontinuum white light by focusing on a thin sapphire plate. Two such setups were utilized in order to broaden the range of selected probing wavelengths. The first setup is used to generate the continuum white light in the region between 400 and 1000 nm, while the second one produces wavelengths in ultraviolet region between 300 and 400 nm, by using an additional second harmonic crystal. The desired probing wavelength was selected by using a band-pass filter and transmission and reflection changes were detected by Si detectors.

III. RESULTS AND DISCUSSION

Indium oxide NWs have been grown by a variety of methods including CVD via carbothermal reduction of In_2O_3 and active carbon at 980 °C,[14] direct oxidation of In under high temperatures (≥1000 °C) [10,15,16] and thermal evaporation of In, in the presence of H_2O vapor at 850 °C and a flow of 50 SCCM Ar.[17] Moreover, Zhang *et al.*[18] synthesized In_2O_3 NWs by using hydrogen and Ag as a catalyst. In addition, In_2O_3 NWs have been grown by annealing of Au/In films at 400 °C.[19,20] A typical SEM image of the In_2O_3 NWs, grown at 700 °C directly on the Au coated quartz substrate, is shown in Fig. 1. A high density of In_2O_3 NWs is clearly apparent and the NWs have an average diameter of $\approx 100 \pm 20$ nm and lengths up to few micrometers, as can be seen from Fig. 1. It should be pointed out that the diameter of the NWs is not uniform along their length and they are tapered at their edges.

The In_2O_3 NWs grown at T_G=700 °C on silicon and quartz are characterized by intense reflection peaks corresponding to the (2 1 1), (2 2 2), (4 1 1), (4 0 0), (4 4 0), and

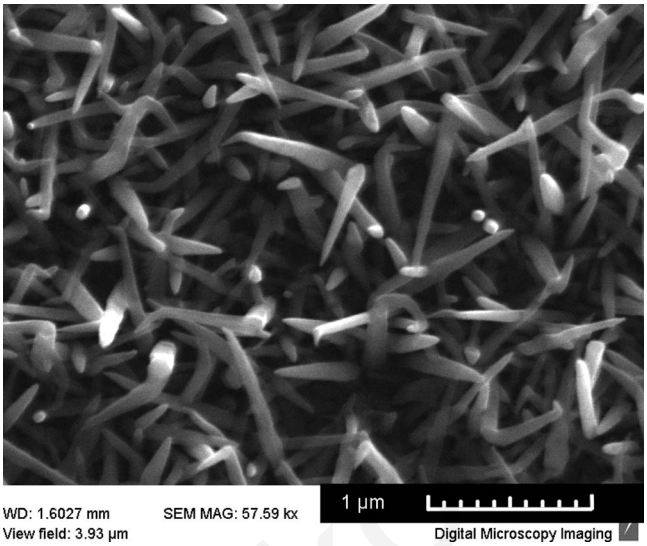

FIG. 1. SEM images of the In_2O_3 NWs grown at 700 °C on 0.5 nm Au/quartz.

(6 2 2) crystallographic planes of In_2O_3 having the cubic bixbyite structure, also called C type rare earth oxide structure with a lattice constant a=10.11 Å.[18] No NWs were obtained on plain Si (111), suggesting that the In_2O_3 NWs grow by the VLS mechanism as has been also reported by other groups.[10,18,20] In addition, no deposition occurred for temperatures lower than T_G=700 °C due to the formation of an oxide shell around the molten indium upstream, which reduces the vapor pressure of indium inside the reactor, even though O_2 was always admitted at the very beginning of the process and RT. This is also consistent with the fact that no In_2O_3 NWs were obtained for $T \leq 900$ °C under a flow of O_2 during growth, which leads to the formation of an even thicker oxide shell surrounding the molten In upstream (Fig. 2). For $T > 900$ °C, the expanding In melt is known to break open the oxide shell, releasing In which then reacts directly with O_2 and leads to the formation of a large density of octahedral In_2O_3 nanocrystals with an average diameter of 500 nm, as described in detail elsewhere.[21] Consequently, oxidation of In under a flow of O_2 during growth does not lead to the formation of In_2O_3 NWs and so it is essential that the O_2 level is maintained low which is consistent with the use of 5% H_2 in the growth of In_2O_3 NWs by Zhang *et al.*[18]

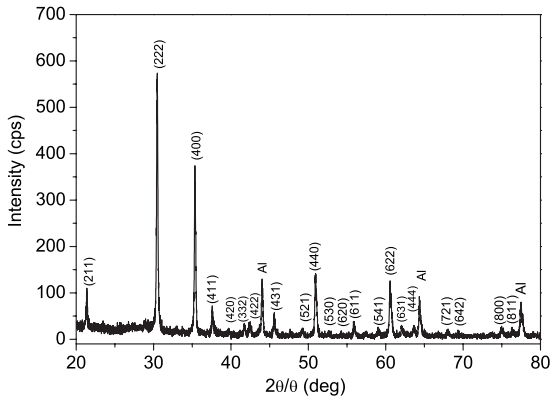

FIG. 2. X-ray diffraction pattern of the In_2O_3 NWs grown on quartz.

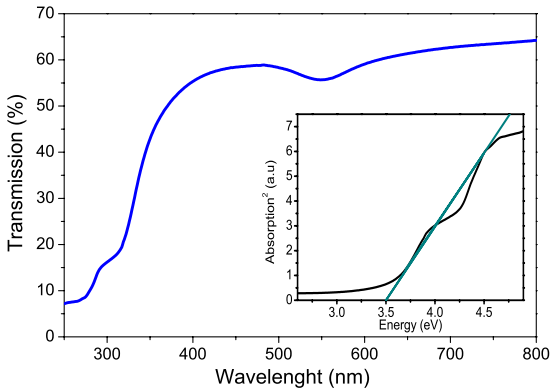

FIG. 3. (Color online) Optical transmission spectrum of In_2O_3 NWs on quartz. The inset shows the square of the absorption vs the energy providing an estimate for the bandgap of the In_2O_3 NWs.

Steady state transmission measurements were carried out following the growth of the In_2O_3 NWs and are shown in Fig. 3. The inset of Fig. 3 is a plot of the absorption squared versus the photon energy providing an estimate of the energy gap of the In_2O_3 NWs, which is $\approx$3.5 eV ($\equiv$354 nm). Following this, time-resolved absorption measurements using optical excitation at 320 nm and different probing wavelengths were carried out and shown in Fig. 4. The estimated absorbed pump fluence was approximately 575 $\mu J/cm^2$. Looking at the experimental data, we notice a positive or negative change in the absorption depending on the probing wavelength. Generally, an initial fast increase, or decrease, is observed in the absorption that is followed by a much longer recovery. A negative change in absorption is observed for probing wavelengths below 410 nm and within the spectral region of 520–550 nm. We should point out that the recovery of absorption is quite different between the two regions; specifically in the visible probing region, the recovery is much faster than the respective recovery in the UV probing region. On the other hand, a positive change is recorded between 430–500 and 600–980 nm. This positive change in the photoinduced absorption is a result of carrier re-excitation to higher energy states by the probing pulses and is dependent

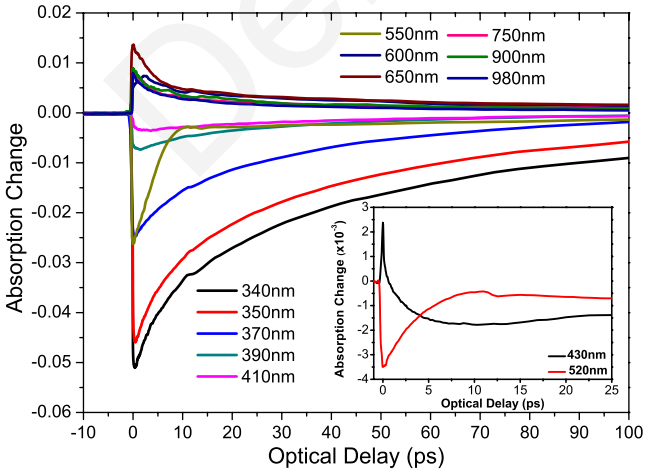

FIG. 4. (Color online) Nondegenerate, time-resolved, transient absorption measurements of the In_2O_3 NWs using ultrafast excitation pulses at 320 nm and probing pulses in the range of 340–980 nm.

on the number of carriers present in the probing energy states and the coupling efficiency between the initial and final states. The observed negative change in the absorption is attributed to state filling, which is due to the occupation of energy states by photogenerated carriers. In most cases both effects are present, while the sign is determined by the dominant effect and the temporal evolution reflects carrier relaxation out of the probing states.

Above band gap excitation ($\lambda > 320$ nm) will result in the generation of electrons (holes) in the conduction (valence) band. These photogenerated carriers will occupy states, resulting in state filling. This is the dominant effect for probing wavelengths corresponding to energies larger than the band gap. The same behavior with similar relaxation times is also observed for probing wavelengths corresponding to energies just below the band edge. These are attributed to additional energy states that are located below the CB edge and are associated with oxygen defects in the In_2O_3 NWs. This is in agreement with previous reports,[9–12] which suggest that oxygen vacancies are formed due to incomplete oxidation during growth and act as donors resulting in additional states below the CB edge. In addition, indium interstitials, as in the case of In_2O_3 octahedrons,[22] may also be a contributing factor to the presence of energy states within the band gap. A more complicated behavior is observed at 430 nm. Initially, free carrier absorption is observed for times near the zero optical delay, while state filling becomes evident for longer times, as shown in the inset of Fig. 4. This behavior is attributed to free carrier absorption from energy states near the excitation region to higher energy states and results in a positive change in absorption. However, as carriers relax into the probing states below the band edge, state filling effects become evident and clearly dominate for longer times.

Here we should point out that a different behavior is observed in the narrow probing region of 520–550 nm, where state filling is apparent, due to the surface plasmon resonance of the Au which is required for the formation of In_2O_3 NWs. This plasmon resonance is due to the electron interaction with the electromagnetic field, associated with intraband and interband transitions of conduction electrons between 5*d* and 6*s* orbitals.[23–25] In order to confirm this, we repeated the experiment using only 0.5 nm Au on quartz observing the same behavior, in the region between 520 and 600 nm. No signal was detected in other regions. The presence of the surface plasmon resonance in this region is also supported by the steady state transmission measurements. This effect induces an extra reduction in the transmission signal as observed in the region between 520 and 600 nm, as shown in Fig. 3.

It is clearly evident from the transient absorption measurements that free carrier absorption is the dominant effect following ultrafast pulse excitation when probing in the IR spectral region. A delay in reaching maximum signal is noted when probing at 600 nm. This is a result of the simultaneous existence of state filling effect, due to the plasmon resonance and free carrier absorption from the In_2O_3 NWs. Apart from this minor difference at 600 nm, it appears that the carrier relaxation is the same at all longer probing wavelengths, sug-

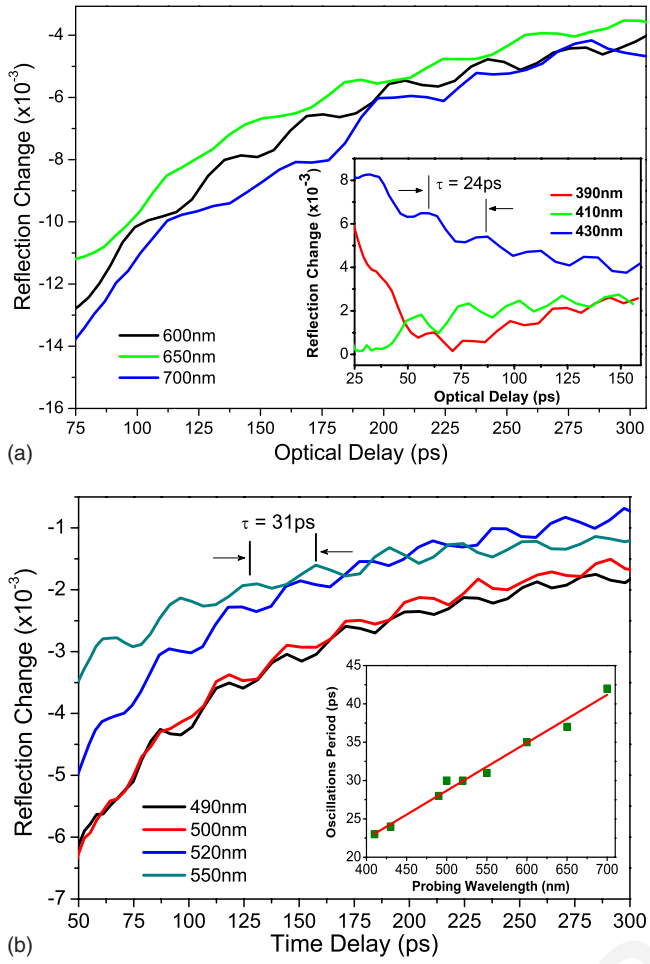

FIG. 5. (Color online) Reflection change is shown for times greater than 50 ps and probing wavelengths between (a) 600–700 and 390–430 nm, in the inset of Fig. 5(a), and (b) 490–550 nm. The period of oscillations is presented in the inset of Fig. 5(b) as a function of probing wavelength.

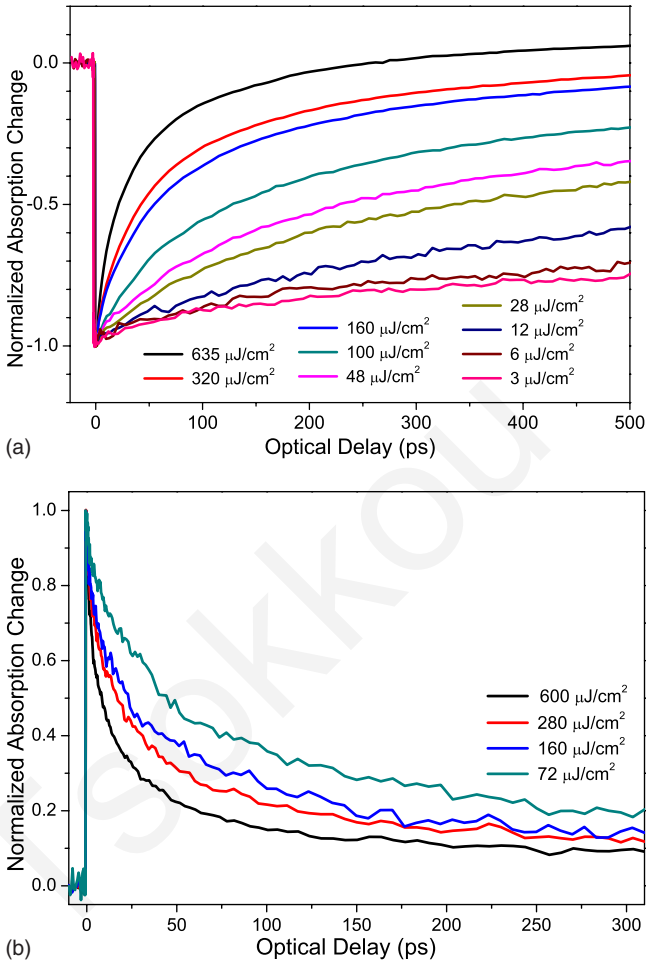

FIG. 6. (Color online) Time resolved transient normalized absorption measurements of the In_2O_3 NWs on quartz using ultrafast UV excitation pumping pulses at 320 nm and probing pulses at (a) 350 nm and (b) 980 nm for different absorbed fluences.

gesting that the same kind of states are probed. We believe that these probed states are not states in the CB or states located just below the CB edge due to the different temporal behaviors between the two regions, at the specified pump fluence. This conclusion is further supported by intensity measurements that are discussed in detail below, supporting that the probed states are midgap states.

A closer look at the transient absorption measurements for probing wavelengths greater than 390 nm depicts an interesting oscillatory behavior, as shown in Figs. 5(a) and 5(b). Long-lived oscillations are observed in the differential reflectivity following a few tens of picoseconds from the initial excitation. A plot of the period of oscillations versus the probing wavelength, shown in the inset of Fig. 5(b), suggests a linear dependence.

We believe that the observed oscillations are associated with coherent acoustic phonons[26,27] generated at the Au nanoparticles and lunged into the In_2O_3 NWs. This wave modifies the local dielectric constants and creates a discontinuity. When the probe pulse is incident onto the sample, part of the light is reflected from the discontinuity of the dielectric constant and the rest of the transmitted light reaches the Au interface where it gets reflected. Therefore as these acoustic phonons travel along the axis of the NWs, the Au surface and the strain wave surface act as an interferometer. Oscillations arise from the fact that the distance between the two surfaces is constantly changing with time, causing a periodic phase difference between the two reflected beams. A linear fit of the period of oscillation versus the probing wavelength was performed based on the equation given by Thomsen *et al.*:[28]

$$\tau = \lambda/(2nv_s \cos\theta), \quad (1)$$

where λ is the probing wavelength, n is the refraction index, which is equal to $n=1.98$ at 500 nm in the case of In_2O_3,[29] v_s is the sound velocity in the material, and θ is the angle between probe pulse and the normal to the sample. This fit gave an estimate of the sound velocity in indium oxide to be approximately $v_s=(4.1\pm0.5)\times10^5$ cm/s.

To further improve our understanding of the carrier relaxation mechanism in this material, transient absorption measurements were performed at different excitation fluences. Normalized transient absorption measurements at probing wavelengths of 350 and 980 nm are shown in Figs. 6(a) and 6(b), respectively. In both cases, carrier relaxation becomes faster as the carrier concentration increases, suggesting that Auger recombination is a contributing factor in the dynamics at the fluence used in this work. For the smaller

probing wavelengths (350 nm), Auger recombination appears to play a significant role in the relaxation of the carriers. This effect diminishes with decreasing intensity and considered negligible for energies smaller than 3 $\mu J/cm^2$. At such low intensities, a single exponential recovery is observed with a time constant of 1.5 ns. Here we should point out that intensity measurements at probing wavelengths of 370 and 390 nm depict similar temporal behavior. The data in Fig. 6(b) clearly show that free carrier absorption is the main contributing factor for a probing wavelength equal to 980 nm. Furthermore, the temporal behavior is different from that seen when probing above the band gap. This suggests that we are actually probing within the band gap and most likely the midgap states. This is further supported by the fact that Auger recombination is less pronounced [see Fig. 6(b)] at the same fluence than when probing at 350 nm which is attributed to the distribution of the photogenerated carriers in the large number of states below the band edge. Measurements at the lowest fluence shown in Fig. 6(b) depict a fast relaxation time constant of 26 ps which is attributed to transitions between surface/defect states. In addition, a slow relaxation time is also present which is of the order of hundreds of picoseconds (≈300 ps) attributed to nonradiative recombination.

IV. CONCLUSIONS

Ultrafast carrier dynamics in In_2O_3 NWs following the excitation above the direct band gap was investigated in detail. Steady state transmission measurements provided an estimate of the energy gap of these NWs to be 3.5 eV. Transient absorption measurements revealed that state filling is the dominant effect for states above the CB edge, as well as for states residing below the CB edge demonstrating the importance of shallow traps (associated with defect states) in the relaxation of photogenerated carriers. Furthermore, time-resolved intensity measurements revealed the important role that Auger recombination plays in the relaxation of ultrafast photogenerated carriers and provided the maximum fluence (3 $\mu J/cm^2$) where Auger recombination may be considered negligible. Transient measurements in this low-fluence regime for carriers above the band gap revealed single exponential recovery of the order of ~1.5 ns associated with recombination of the photogenerated carriers. Similar behavior has also been observed for the photogenerated carriers distributed within the shallow traps just below the band edge. Furthermore, measurements at longer probing wavelengths provided an estimate of the nonradiative relaxation of carriers (~300 ps) which are distributed among the midgap states. Furthermore, time-resolved measurements revealed an oscillatory behavior in the reflection signal for probing wavelengths longer than 390 nm. This behavior is attributed to acoustic phonons which provided an estimate of the sound velocity in In_2O_3 NWs to be $v_s=(4.1\pm0.5)\times10^5$ cm/s.

ACKNOWLEDGMENTS

The work in this article was supported by the Research Promotion Foundation of Cyprus under Grant Nos. EPYNE/0504/06, EPYNE/0506/02, EPYAN/0506/04, and BE0308/03 for fundamental research in the area of nanotechnology and nanomaterials.

[1] O. N. Mryasov and A. J. Freeman, Phys. Rev. B **64**, 233111 (2001).
[2] C. G. Granqvist, Appl. Phys. A: Mater. Sci. Process. **57**, 19 (1993).
[3] H. Kobayashi, T. Ishiba, Y. Nakato, and H. Mori, J. Appl. Phys. **78**, 3931 (1995).
[4] J. S. Kim, R. H. Friend, and F. Cacialli, Appl. Phys. Lett. **74**, 3084 (1999).
[5] C. S. Rout, K. Ganesh, A. Govindaraj, and C. N. R. Rao, Appl. Phys. A: Mater. Sci. Process. **85**, 241 (2006).
[6] D. Zhang, C. Li, X. Liu, S. Han, T. Tang, and C. Zhou, Appl. Phys. Lett. **83**, 1845 (2003).
[7] D. Zhang, Z. Liu, C. Li, T. Tang, X. Liu, S. Han, B. Lei, and C. Zhou, Nano Lett. **4**, 1919 (2004).
[8] D. Zhang, C. Li, S. Han, X. Liu, T. Tang, W. Jin, and C. Zhou, Appl. Phys. Lett. **82**, 112 (2003).
[9] F. Zeng, X. Zhang, J. Wang, L. Wang, and L. Zhang, Nanotechnology **15**, 596 (2004).
[10] S. Kar and S. Chaudhuri, Chem. Phys. Lett. **422**, 424 (2006).
[11] M. Mazzera, M. Zha, D. Calestani, A. Zappettini, L. Lazzarini, G. Salviati, and L. Zanotti, Nanotechnology **18**, 355707 (2007).
[12] D. Calestani, M. Zha, A. Zappettini, L. Lazzarini, and L. Zanotti, Chem. Phys. Lett. **445**, 251 (2007).
[13] A. Othonos, J. Appl. Phys. **83**, 1789 (1998).
[14] X. C. Wu, J. M. Hong, Z. J. Han, and Y. R. Tao, Chem. Phys. Lett. **373**, 28 (2003).
[15] X. S. Peng, G. W. Meng, J. Zhang, X. F. Wang, Y. W. Wang, C. Z. Wang, and L. D. Zhang, J. Mater. Chem. **12**, 1602 (2002).
[16] X. S. Peng, Y. W. Wang, J. Zhang, X. F. Wang, L. X. Zhao, G. W. Meng, and L. D. Zhang, Appl. Phys. A: Mater. Sci. Process. **74**, 437 (2002).
[17] L. Dai, X. L. Chen, J. K. Jian, M. He, T. Zhou, and B. Q. Hu, Appl. Phys. A: Mater. Sci. Process. **75**, 687 (2002).
[18] J. Zhang, X. Qing, F. Jiang, and Z. Dai, Chem. Phys. Lett. **371**, 311 (2003).
[19] S. Q. Li, X. Y. Liang, C. Wang, X. Q. Fu, and T. H. Wang, Appl. Phys. Lett. **88**, 163111 (2006).
[20] Y. X. Liang, S. Q. Loi, L. Nie, Y. G. Wang, and T. H. Wang, Appl. Phys. Lett. **88**, 193119 (2006).
[21] M. Zervos, D. Tsokkou, M. Pervolaraki, and A. Othonos, Nanoscale Res. Lett. **4**, 491 (2009).
[22] M. Kumar, V. N. Singh, F. Singh, K. V. Lakshmi, B. R. Mehta, and J. P. Singh, Appl. Phys. Lett. **92**, 171907 (2008).
[23] A. Devizis, V. Vaicikauskas, and V. Gulbinas, Appl. Opt. **45**, 2535 (2006).
[24] S. Link, C. Burda, Z. L. Wang, and M. A. El-Sayed, J. Chem. Phys. **111**, 1255 (1999).
[25] T. S. Ahmadi, S. L. Logunov, and M. A. El-Sayed, J. Phys. Chem. **100**, 8053 (1996).
[26] M. Wraback, H. Shen, V. Sampath, C. J. Collins, G. A. Garrett, and W. L. Sarney, Phys. Status Solidi A **202**, 790 (2005).
[27] S. Wu, P. Geiser, J. Jun, J. Karpinski, J. R. Park, and R. Sobolewski, Appl. Phys. Lett. **88**, 041917 (2006).
[28] C. Thomsen, H. T. Grahn, H. J. Maris, and J. Tauc, Phys. Rev. B **34**, 4129 (1986).
[29] B. R. Krishna, T. K. Subramanian, B. S. Nadia, and S. Ruthann, Opt. Mater. (Amsterdam, Neth.) **15**, 217 (2000).

Nanoscale Res Lett (2009) 4:828–833
DOI 10.1007/s11671-009-9323-9

NANO EXPRESS

Tin Oxide Nanowires: The Influence of Trap States on Ultrafast Carrier Relaxation

Andreas Othonos · Matthew Zervos · Demetra Tsokkou

Received: 31 January 2009 / Accepted: 14 April 2009 / Published online: 30 April 2009

Abstract We have studied the optical properties and carrier dynamics in SnO_2 nanowires (NWs) with an average radius of 50 nm that were grown via the vapor–liquid solid method. Transient differential absorption measurements have been employed to investigate the ultrafast relaxation dynamics of photogenerated carriers in the SnO_2 NWs. Steady state transmission measurements revealed that the band gap of these NWs is 3.77 eV and contains two broad absorption bands. The first is located below the band edge (shallow traps) and the second near the center of the band gap (deep traps). Both of these absorption bands seem to play a crucial role in the relaxation of the photogenerated carriers. Time resolved measurements suggest that the photogenerated carriers take a few picoseconds to move into the shallow trap states whereas they take $\sim$70 ps to move from the shallow to the deep trap states. Furthermore the recombination process of electrons in these trap states with holes in the valence band takes $\sim$2 ns. Auger recombination appears to be important at the highest fluence used in this study (500 $\mu J/cm^2$); however, it has negligible effect for fluences below 50 $\mu J/cm^2$. The Auger coefficient for the SnO_2 NWs was estimated to be $7.5 \pm 2.5 \times 10^{-31}$ cm^6/s.

A. Othonos (✉) · D. Tsokkou
Department of Physics, Research Centre of Ultrafast Science, University of Cyprus, P.O. Box 20537, 1678 Nicosia, Cyprus
e-mail: othonos@ucy.ac.cy

M. Zervos
Department of Mechanical and Manufacturing Engineering, Materials Science Group, Nanostructured Materials and Devices Laboratory, University of Cyprus, P.O. Box 20537, 1678 Nicosia, Cyprus

Keywords SnO_2 nanowires · Chemical vapour deposition · Carrier dynamics · Differential absorption spectroscopy

Introduction

Tin oxide (SnO_2) is considered an important wide-bandgap *n*-type semiconductor which has received a great deal of attention over the past few years due to its high transparency in the visible part of the spectrum and sensitivity to certain gases which make it technologically important for optoelectronic devices [1–6] and sensors [7]. In addition Sn is readily available and cheaper compared to indium (In) which is used for the growth of indium oxide (In_2O_3). Furthermore, in recent years, the field of semiconducting metal oxides has benefited a great deal from the development of one-dimensional nanostructures such as nanowires (NWs) and nanorods (NRs) due to their interesting properties arising from their small size [8, 9] and high surface-to-volume ratio. In view of this, there has been growing interest in the synthesis of SnO_2 NWs, the study of their fundamental electronic and optoelectronic properties, and finally device applications [10–13].

Despite the potential applications of SnO_2 NWs there has been no detailed study of the fundamental, ultrafast carrier relaxation mechanisms of the photogenerated carriers in this nanostructured material. Consequently, here we investigate the carrier dynamics in SnO_2 NWs and obtain a detailed understanding of the various relaxation mechanisms and the influence of trap states using transient white light absorption spectroscopy [14–16] with femtosecond resolution. We find that the band gap of the SnO_2 NWs is 3.77 eV and contains two broad absorption bands, the first of which is located below the band edge and is related to

shallow trap states while the second is near the center of the band gap due to deep trap states. Detailed transient measurements revealed their energetic position, carrier relaxation times, and the importance of Auger recombination.

Experimental Procedure

The SnO_2 NWs were grown using an atmospheric pressure chemical vapour deposition (APCVD) reactor which consists of four mass flow controllers (MFC's) and a horizontal quartz tube furnace, capable of reaching a maximum temperature of 1100 °C. Initially, approximately 0.2 g of fine Sn powder (Aldrich, <150 μm, 99.5%) was weighed and loaded into a quartz boat together with a square piece of Si(111) which was coated with 0.5 nm of Au. The Au layer was deposited via sputtering at a slow rate <5 Å/s using an Ar plasma under a pressure $<10^{-4}$ mBar. The sample was positioned a few mm downstream from the Sn and subsequently the boat was loaded into the reactor and positioned directly above the thermocouple used to measure the heater temperature at the centre of tube. After loading the boat at room temperature (RT), Ar (99.999%) was introduced at a flow rate of 500 standard cubic centimetres per minute (sccm) for 5 min in order to purge the tube.

Following this the temperature was ramped to 800 °C in an Ar flow of 100 sccm at a rate of 30 °C/min. Upon reaching T_G, the flow of Ar was maintained at 100 sccm for a further 90 min after which the tube was allowed to cool down over at least an hour in an inert gas flow of Ar, 100 sccm. The sample was removed only when the temperature was lower than 100 °C. For the optical measurements, NWs were grown directly onto square pieces of quartz that were coated with 0.5 nm of Au and had an area of $\approx 6 \times 6$ mm^2. The morphology of the SnO_2 NWs was examined with a TESCAN scanning electron microscope (SEM) while the crystal structure and the phase purity of the NWs were investigated using a SHIMADZU, XRD-6000, X-ray diffractometer, and Cu Ka source. A scan of θ–2θ in the range between 20° and 80° was performed for the SnO_2 NWs that were grown on Si(111) and quartz.

In this study, we investigate the ultrafast dynamic behavior of carriers in SnO_2 NWs following femtosecond pulse excitation through the temporal behavior of differential absorption [14–16]. The experimental study was carried out using an ultrafast amplifier system operating at 5 kHz. A self mode-locked Ti: Sapphire oscillator centered at 796 nm and generating 45 fs pulses was the source of short pulses. Approximately 1 mJ of amplified energy was used to pump an Optical Parametric Amplifier (OPA) providing ultrafast pulses in the UV range of the spectrum. The rest of the energy from the amplifier was used to generate 400 nm from a BBO crystal via second harmonic generation and white light super continuum. The UV femtosecond pulses from the OPA were used to excite the nanowires given that the expected band gap of this material is around 3.7 eV. A small part of the fundamental 796 nm pulses were used to generate VIS-IR super continuum light by focusing the beam on a 1 mm thick sapphire plate. Similarly a super continuum light in the UV region of the spectrum was also generated using 400 nm pulses. The white light probe beam was used in a pump-probe non-collinear geometry, with the pump beam been generated from the OPA. To minimize the broadening of the laser pulse, optical elements such as focusing mirrors were utilized in the setup. The reflected and transmission probe beams were separately directed onto their respective detectors after passing through a band pass filter and thus selecting the probe wavelength from the broad band white light. The differential reflected and transmission signals were measured using lock-in amplifiers with reference to the optical chopper frequency of the pump beam. The temporal variation in the photo-induced absorption was extracted using the transient reflection and transmission measurements, thus providing a means of monitoring the carrier dynamics within the probing region [14].

Results and Discussion

Tin oxide NWs have been grown so far by a variety of methods including thermal evaporation [17, 18], chemical vapour deposition [19], and the VLS method using carbothermal reduction of stannous oxide SnO at 880 °C for 90 min [20]. On the other hand, stannic oxide, SnO_2 NWs have been grown by direct oxidation of Sn at 900 °C under a flow of 10 sccm O_2 [21]. Similarly, Yang et al. obtained SnO_2 NWs at 900 °C under a flow of 50 sccm O_2 [22] while Wan et al. [23] obtained Sb doped SnO_2 NWs by heating up the mixture at 20 °C/min up to 900 °C under a flow of 500 sccm Ar with a trace of O_2. A typical scanning electron microscope (SEM) image of the SnO_2 NWs grown on quartz is shown in Fig. 1 where it is apparent that a large coverage has been obtained. The SnO_2 NWs have an average diameter of 50 nm and lengths ≥5 μms. Furthermore the diameter of the SnO_2 NWs was found to be uniform along their length. The growth of the SnO_2 NWs occurs via the formation of Au nanoparticles (NPs) from the thin layer of Au and the VLS mechanism. No NWs were obtained on Si(111) or quartz alone. In addition we have found that direct oxidation using a flow of O_2 during growth hinders the formation of SnO_2 NWs due to the oxidation of the Sn upstream, which melts at 232 °C and which in turn reduces the vapour pressure, especially at low temperatures i.e., $T \leq 800$ °C. While we obtained SnO_2 NWs at temperatures as low as 700 °C we find that the

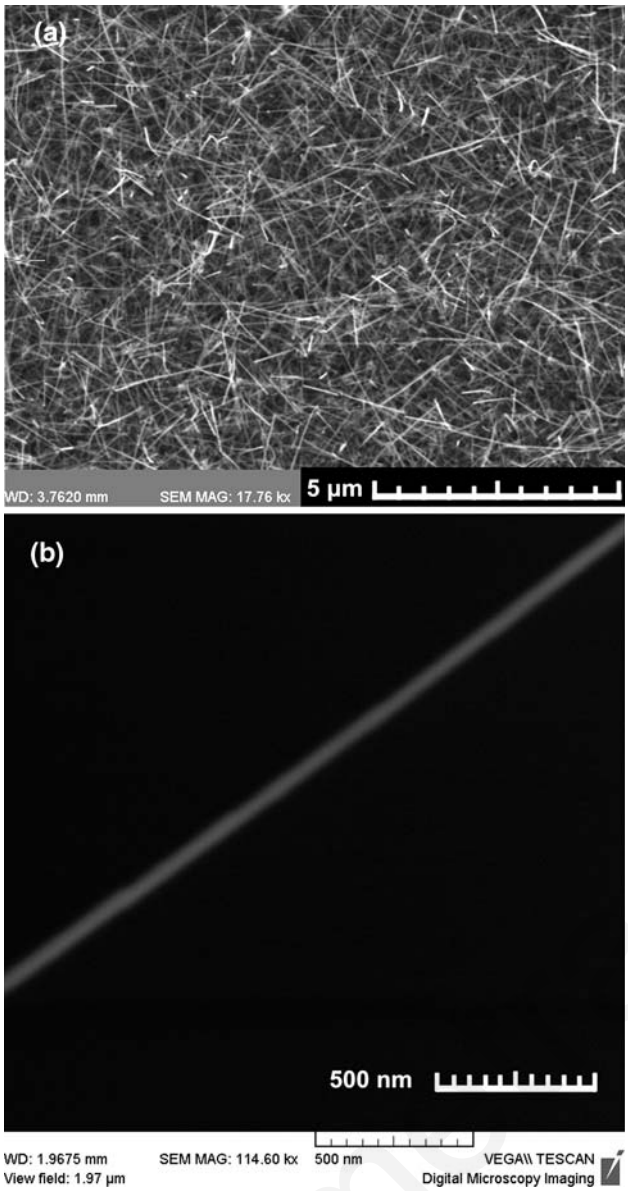

Fig. 1 SEM images of SnO_2 NWs grown at 800 °C with an average diameter of 50 nm

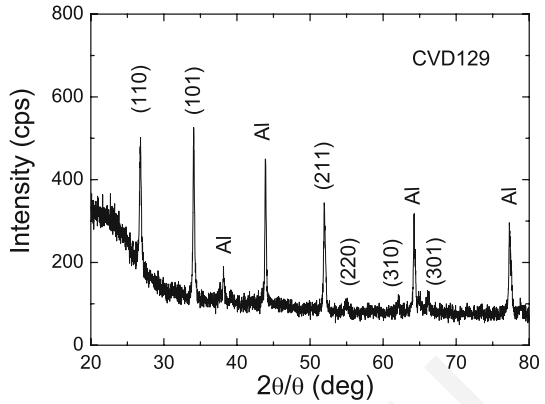

Fig. 2 XRD spectrum of the SnO_2 NWs grown at 800 °C on 0.5 nm Au/quartz

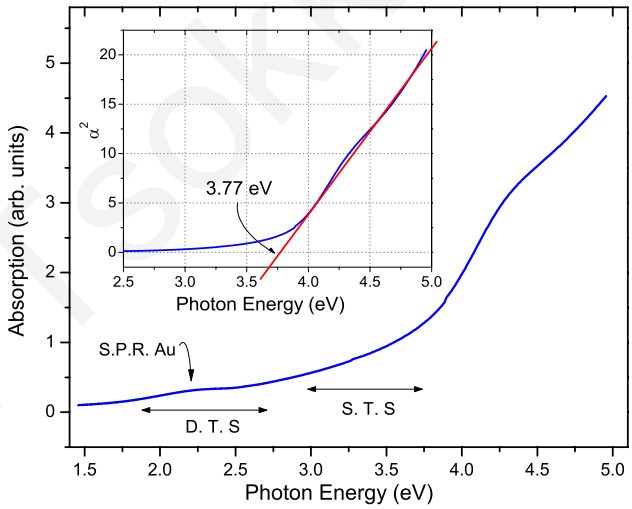

Fig. 3 Steady state transmission measurements carried out on SnO_2 NWs using a UV-IR spectrometer. The upper corner inset shows a plot of the square of the absorption versus incident photon energy, providing us with an estimate of the bandgap energy 3.77 eV. There are two broad absorption bands below the bandgap referred to as D.T.S—deep trap states and S.T.S.—shallow trap states

optimum temperature for a high yield and uniform coverage is 800 °C. The optimum growth conditions are therefore close to those described by Wan et al. [23] who use only a trace of oxygen under a larger flow of Ar i.e., 500 sccm as opposed to 100 sccm used here. In our case the formation of SnO_2 NWs is due to the oxygen admitted into the APCVD reactor at RT prior to the temperature ramp. The SnO_2 NWs grown at the optimum temperature i.e., $T_G = 800$ °C on quartz are characterized by the (1 1 0), (1 0 1), (2 1 1), (2 2 0), (3 1 0), and (3 0 1) peaks in the X-ray diffraction spectrum shown in Fig. 2. Diffraction peaks can be indexed to the tetragonal rutile structure of SnO_2 [22, 24]. We should point out that the Al peaks appearing in the XRD spectrum of Fig. 2 are due to the sample holder.

Following the growth of SnO_2 NWs, we performed steady state transmission measurements on the NWs grown on quartz. Figure 3 shows the optical absorption of the SnO_2 NWs covering a spectral range from the UV near to the IR. Given that SnO_2 is a direct gap semiconductor, a plot of the square of the absorption versus the incident photon energy provides a measure of the bandgap which was determined to be approximately 3.77 eV (see inset of Fig. 3). Here we should point out that there appears to be a broad absorption band around 4.2 eV which we believe to be due to lower lying valance bands [25]. In addition to

determining the energy bandgap, the absorption spectrum depicts several features within the energy gap of these NWs. There appears to be a broad absorption band below the band edge covering a range from 3.7 eV to 1.8 eV which may be divided into two regions [26, 27]. The first broad absorption band which starts just below the conduction-band edge of the NWs is associated with impurity traps and these are therefore commonly referred to as shallow trap states (S.T.S.). The second band is referred to as the deep trap states (D.T.S.) band generated by defects or/and surface imperfections. Both of these absorption bands seem to play a crucial role in the relaxation of photoexcited carriers on a femtosecond timescale. Furthermore, there appears to be a weak absorption band centred around 2.2 eV (see Fig. 3) which corresponds to the well known Surface Plasmon Resonance (S·P.R.) of Au nanoparticles that are required as catalysts for the formation of the SnO_2 NWs on quartz.

Figure 4 shows typical time resolved differential absorption measurements for the SnO_2 NWs excited at fluence of approximately 0.5 mJ/cm^2 with UV ultrafast pulses at 4.00 eV (310 nm) and probed at different photon probing energies ranging from UV to near IR. The *x*-axis on this graph corresponds to the optical delay between the pump and the probe pulse whereas the *y*-axis indicates the induced absorption. The behaviour appears to be complex and varies over the probing spectral range. For some of the probing wavelengths there is a sharp drop in the absorption reaching a minimum value and then followed by a slower recovery toward equilibrium that takes hundreds of pico-seconds, whereas in other cases there is a positive change in the absorption with again a recovery towards equilibrium.

These observed changes in absorption are associated with excitation of the SnO_2 NWs by photons whose energy is larger than the bandgap energy which results in the generation of non-equilibrium carriers. These non-equilibrium carriers will distribute themselves along energy states that are normally unoccupied under equilibrium conditions. The occupation of states (referred to as state filling) following an ultrafast laser pulse will appear as a reduction in the absorption at the probing energy states. Clearly the observed recovery of this negative absorption change will be a direct measure of the time required by the photogenerated carriers to move out of the occupied states. Furthermore, a positive change in the induced absorption is also observed in the transient absorption measurements. This phenomenon is mainly due to secondary excitation of the photo-generated carriers by the probing photons from their initial states to higher energy states. This "free-carrier absorption" depends on the number of carriers present at the initial states and the coupling coefficient between the two energy bands. The temporal profile of this positive induced absorption is again a direct measure of the presence of the photo-generated carrier at the probing energy states.

We will begin the analysis of the data from the degenerate induced absorption measurements where the excitation and probing photon energies were 4.00 eV. It is important to point out that the observed sharp drop reaching a minimum (state filling) is pulse width limited, which is expected since we are probing the same energy states that we are exciting. To obtain a better understanding of the dynamics for the degenerate pump-probe data, we have performed intensity measurements as seen in Fig. 5.

The normalized induced absorption measurements seen in Fig. 5 clearly indicate that with increasing fluence there is a faster recovery on the long time scale. This suggests that

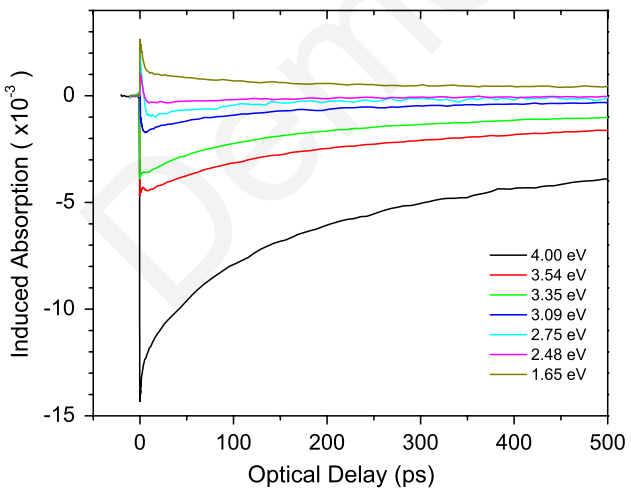

Fig. 4 Time-resolved differential absorption of SnO_2 nanowires excited with 4.00 eV photons (310 nm) at fluence of 500 μJ/cm^2 and probe at different photon energies ranging from UV to near IR

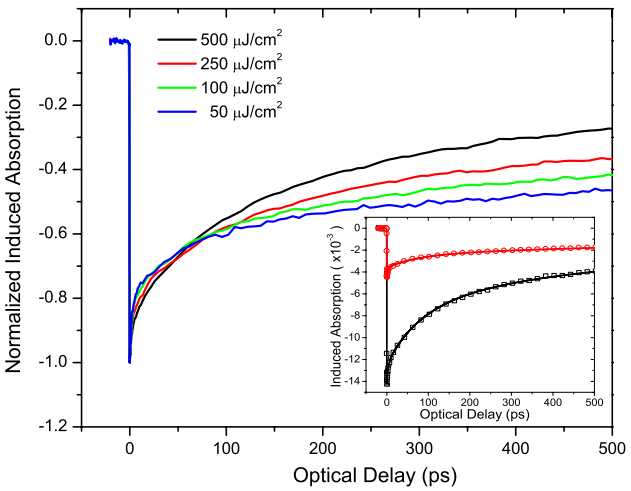

Fig. 5 Time-resolved normalized differential absorption intensity measurements of SnO_2 NWs excited with 4.0 eV and probe at 4.0 eV. The different curves correspond to different incident absorption fluence of the NWs. The inset shows the fits (*solid lines*) to the actual differential absorption data (*points*) using a simple model which includes multi-exponential decays and Auger recombination

Auger recombination is a contributing factor at the fluence used in this study. With decreasing fluence, Auger recombination becomes less important, and for the NWs used in this study at fluence less than 50 μJ/cm^2, this contribution may be considered negligible. A simple multi-exponential fit to the experimental result at 50 μJ/cm^2 shows that a minimum requirement of three exponential function is necessary for a good fit to the data. The time constants obtained from this fit were 2.4 ps (18%), 68 ps (22%), and 2.3 ns (60%). A more detailed analysis of the experimental data was performed using a simple differential equation model which incorporated the above three exponential decay mechanisms along with Auger recombination. Making use of the time constants obtained for the lowest fluence utilized in these experiments, where Auger recombination was negligible, it was possible to obtain fits to the differential absorption data at higher fluences. Relative good fits to the experimental data (see inset Fig. 5) were obtained using an Auger coefficient of $7.5 \pm 2.5 \times 10^{-31}$ cm^6/s.

A schematic diagram of the various proposed relaxation paths is shown in Fig. 6, to help the reader obtain a clear picture of the dynamics. The first time constant (2.4 ps) listed above, corresponds to mechanism 1, (see Fig. 6) whereas the second time constant is associated with mechanism 2 or 3 through carrier saturation in the shallow trap states. Given that no direct recombination was observed from the conduction to the valence band which is corroborated by the absence of photoluminescence near 3.75 eV, we

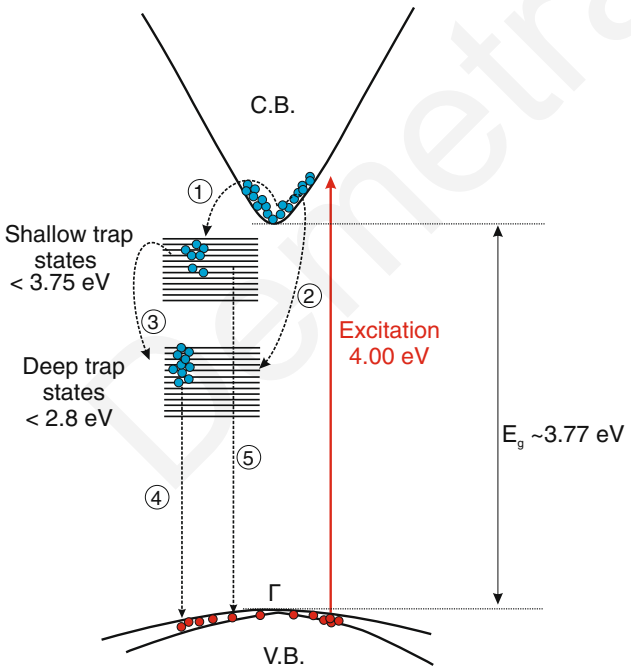

Fig. 6 A schematic diagram of the energy band gap diagram of SnO_2 NWs with the various relaxation mechanisms following carrier photoexcitation by an ultrafast pulse

believe that the long time constant is associated with the carriers moving through the shallow and deep trap states. Saturation of these states from the large number of carriers will result in the decay of paths 4 and/or 5 being effectively seen when probing above the band gap.

We should also point out that the fast decay component, which is associated with mechanism 1 of the photo-generated carriers when they are moving into the shallow traps states, appears to become slower with increasing fluence (Fig. 5). This is most likely due to saturation of available shallow trap states. Furthermore, in the above proposed model, the holes generated near the Γ point will also relax to the top of the valence band. However, the expected relaxation within the valence band is much faster than the multi-picosecond relaxation mechanisms shown in Fig. 6. This is expected given the small excess kinetic energy received by the holes during excitation.

Considering next the time-resolved absorption measurements (Fig. 4) for probing photon energies below the band gap energy (shallow traps) from 3.54 eV (350 nm) to 3.3 eV (380 nm), we notice that although the maximum state filling occurs very close to $t = 0$ (within the pulse width), there appears to be a small drop and then a small rise after a few picoseconds. This behavior is due to a small free-carrier contribution which reduces the state filling contribution thus artificially making this feature ("dip") appear near the tip of the maximum signal. This is clearly obvious when looking at the differential absorption in Fig. 4 with decreasing probing photon energy. The free-carrier "dip" increases with increasing probing wavelength and eventually becomes the main contributing factor at the longer probing wavelengths.

Furthermore, intensity measurements carried out over a range of 500–50 μJ/cm^2 at the probing photon energy of 3.54 eV (350 nm) indicate that Auger recombination has a noticeable effect only at the maximum fluence, however, at fluence as low as ~50 μJ/cm^2, this effect becomes negligible. A multi-exponential fit to the data shows a minimum requirement of two exponential function for a good fit with time constants of 72 ps (27%) and 2.08 ns (73%). Most likely the fast time constant is associated with carriers moving into the deep traps (path 3 in Fig. 6) whereas the long decay is associated with recombination of the carriers (path 5 in Fig. 6). Here we should point out that differential absorption intensity measurements have also been carried at other probing photon energies within the top shallow trap states with similar results.

Considering the differential absorption measurements in Fig. 4 for the longer probing wavelengths, we notice an increase in free-carrier contribution. This contribution becomes dominant for probing photon energies below 1.65 eV (750 nm), where no trap states can be reached from the valence band thus excluding state filling. The initial fast recovery component which is of the order of a

few picoseconds seen in these measurements is attributed to free-carrier contributions within the trap states.

Finally we should point out that due to the presence of Au nanoparticles (NPs) which are required as a catalysts in the formation of the SnO_2 NWs, transient absorption measurements in the probing region 2.4–2.1 eV depict the well known surface plasmon resonance of Au [28–30]. Time resolved measurements outside the above probing spectral region show no evidence of differential absorption signal from Au. Furthermore, measurements with excitation photons having energy below the band gap of SnO_2 show signal only at the probing region of the surface plasmon resonance. Identical results were obtained when transient absorption measurements were carried out on just the quartz substrate coated with the 0.5 nm film of the Au catalyst. It appears that the Au NPs required for the formation of the NWs have no effect on probing the carrier dynamics in SnO_2 NWs despite the strong plasmon resonance.

In conclusion, we have investigated the ultrafast dynamic behavior of SnO_2 nanowires using above band gap excitation UV femtosecond pulses. Transmission measurements of the NWs provided us with an estimate of the band gap at 3.75 eV and reveal broad absorption bands below the band edge. These absorption bands appear to play an important role in the relaxation of the photogenerated carriers in the NWs. Transient differential absorption measurements reveal the different pathways and time constants associated with the relaxation of the photogenerated carriers. Measurements suggest that the photogenerated carriers take a few picoseconds to move into the shallow traps states whereas it takes $\sim$70 ps to move from the shallow to the deep trap states. Furthermore, recombination of electrons from these traps states with holes in the valence band takes $\sim$2 ns. Auger recombination has a contribution to the carrier dynamics at the highest fluence used in this study ($\sim$500 μJ/cm^2), however at fluence of 50 μJ/cm^2 Auger recombination appears to be negligible. Transient absorption intensity measurements provided us with an estimate of the Auger coefficient for the SnO_2 NWs to be approximately $7.5 \pm 2.5 \times 10^{-31}$ cm^6/s.

Acknowledgments The study in this article was partially supported by the research programs; EPYNE/0504/06, ERYAN/0506/04, and ERYNE/0506/02 funded by the Cyprus Research Promotion Foundation in Cyprus.

References

1. Z.M. Jarzebski, J.P. Marton, J. Electrochem. Soc. **123**, 1990 (1976)
2. J. Maier, W. Gopel, J. Solid State Chem. **72**, 293 (1988). doi:10.1016/0022-4596(88)90032-1
3. K.P. Kumar, A.D. Domodaran, J. Mater. Sci. **24**, 220 (1989). doi:10.1007/BF00660957
4. S.A. Pianaro, P.R. Bueno, E. Longo, J.A. Varela, J. Mater. Sci. Lett. **14**, 692 (1995). doi:10.1007/BF00253373
5. P.I. Rovira, R.W. Collins, J. Appl. Phys. **85**, 2015 (1999). doi:10.1063/1.369496
6. N. Amin, T. Isaka, A. Yamada, M. Konagai, Sol. Energy Mater. Sol. Cells **67**, 195 (2001). doi:10.1016/S0927-0248(00)00281-6
7. N. Yamazoe, Sens. Actuators B Chem. **5**, 7 (1991). doi:10.1016/0925-4005(91)80213-4
8. Z.W. Pan, Z.R. Dai, Z.L. Wang, Science **291**, 1947 (2001). doi:10.1126/science.1058120
9. J. Zhang, J. Liu, J.L. Huang, P. Kim, C.M. Lieber, Science **274**, 757 (1996). doi:10.1126/science.274.5288.757
10. Z.R. Dai, J.L. Gole, J.D. Stout, Z.L. Wang, J. Phys. Chem. B **106**, 1274 (2002). doi:10.1021/jp013214r
11. Z. Liu, D. Zhang, S. Han, C. Li, T. Tang, W. Jin, X. Liu, B. Lei, C. Zhou, Adv. Mater. **15**, 1754 (2003). doi:10.1002/adma.200305439
12. X.C. Jiang, Y.L. Wang, T. Herricks, Y.N. Xia, J. Mater. Chem. **14**, 695 (2004). doi:10.1039/b313938g
13. M.J. Zheng, G.H. Li, X.Y. Zhang, S.Y. Huang, Y. Lei, L.D. Zhang, Chem. Mater. **13**, 3859 (2001). doi:10.1021/cm010084q
14. A. Othonos, J. Appl. Phys. **83**, 1789 (1998). doi:10.1063/1.367411
15. A. Othonos, E. Lioudakis, U. Philipose, H.E. Ruda, Appl. Phys. Lett. **91**, 241113 (2007). doi:10.1063/1.2825290
16. A. Othonos, M. Zervos, M. Pervolaraki, Nanoscale Res. Lett. **4**, 122 (2009). doi:10.1007/s11671-008-9211-8
17. M.S. Arnold, P. Avouris, Z.W. Pan, Z.L. Wang, J. Phys. Chem. B **107**, 659 (2003). doi:10.1021/jp0271054
18. X.Y. Xue, Y.J. Chen, Y.G. Liu, S.L. Shi, Y.G. Wang, T.H. Wang, Appl. Phys. Lett. **88**, 201907 (2006). doi:10.1063/1.2203941
19. S. Mathur, S. Barth, H. Shen, J.-C. Pyun, U. Werner, Small **1**, 713 (2005)
20. A. Kar, J. Yang, M. Dutta, M.A. Stroscio, J. Kumari, M. Meyyappan, Nanotechnology **20**, 065704 (2009). doi:10.1088/0957-4484/20/6/065704
21. Y.J. Ma, F. Zhou, L. Lu, Z. Zhang, Solid State Commun. **130**, 313 (2004). doi:10.1016/j.ssc.2004.02.013
22. M.-R. Yang, S.-Y. Chu, R.-C. Chang, Sens. Actuators B **122**, 269 (2007). doi:10.1016/j.snb.2006.05.034
23. Q. Wan, E.N. Dattoli, W. Lu, Appl. Phys. Lett. **90**, 222107 (2007). doi:10.1063/1.2743746
24. M. Chen, X. Xia, Z. Wang, Microelectron. Eng. **85**, 1379 (2008). doi:10.1016/j.mee.2008.01.027
25. F.J. Arlinghaus, J. Phys. Chem. Solids **35**, 931 (1974). doi:10.1016/S0022-3697(74)80102-2
26. R. Liu, Y. Chen, F. Wang, L. Cao, A. Pan, G. Yang, T. Wang, B. Zou, Physica E **39**, 223 (2007). doi:10.1016/j.physe.2007.04.009
27. D. Maestre, A. Cremades, J. Piqueras, J. Appl. Phys. **95**, 3027 (2004). doi:10.1063/1.1647267
28. A. Devizis, V. Vaicikauskas, V. Gulbinas, Appl. Opt. **45**, 11 (2006). doi:10.1364/AO.45.002535
29. S. Link, C. Burda, Z.L. Wang, M.A. El-Sayed, J. Chem. Phys. **111**, 3 (1999). doi:10.1063/1.479310
30. T.S. Ahmadi, S.L. Logunov, M.A. El-Sayed, J. Phys. Chem. **100**, 20 (1996). doi:10.1021/jp960484e

Bibliography

[1] R. Feynman, Engineering. Sci. **23**, 22 (1960).

[2] Y. Xia, P. Yang, Y. Sun, Y. Wu, B. Mayers, B. Gates, Y. Yin, F. Kim, and H. Yan, Advanced Materials **15**, 353-389 (2003).

[3] G. Hodes, Advanced Materials **19**, 639-655 (2007).

[4] P.M. Fauchet, Materials Today **8**, 26–33 (2005).

[5] A.P. Alivisatos, Science **271**, 933 (1996).

[6] T. Vossmeyer, L. Katsikas, M. Giersig, I.G. Popovic, K. Diesner, A. Chemseddine, A. Eychmüller, and H. Weller, The Journal of Physical Chemistry **98**, 7665–7673 (1994).

[7] A.A. Seraphin, S.-T. Ngiam, and K.D. Kolenbrander, Journal of Applied Physics **80**, 6429 (1996).

[8] A. Kolmakov and M. Moskovits, Annual Review of Materials Research **34**, 151-180 (2004).

[9] K.J. Choi and H.W. Jang, Sensors **10**, 4083-4099 (2010).

[10] Z.W. Pan, Z.R. Dai, and Z.L. Wang, Science (New York, N.Y.) **291**, 1947-9 (2001).

[11] L. Qin, J. Xu, X. Dong, Q. Pan, Z. Cheng, Q. Xiang, and F. Li, Nanotechnology **19**, 185705 (2008).

[12] X.C. Jiang, S.X. Xiong, Z.A. Tian, and C.Y. Chen, The Journal Of **115**, 1800-1810 (2011).

[13] Z. Guo, X. Chen, W.-H. Xu, J. Li, G.-M. Yang, M.-Q. Li, J.-H. Liu, and X.-J. Huang, Materials Today **14**, 42-49 (2011).

[14] L.J. Lauhon, M.S. Gudiksen, and C.M. Lieber, Philosophical Transactions. Series A, Mathematical, Physical, and Engineering Sciences **362**, 1247-60 (2004).

[15] J.D. Holmes, Science **287**, 1471-1473 (2000).

[16] S. Kodambaka, J. Tersoff, M.C. Reuter, and F.M. Ross, Science (New York, N.Y.) **316**, 729-32 (2007).

[17] M.H. Huang, Y. Wu, H. Feick, N. Tran, E. Weber, and P. Yang, Advanced Materials **13**, 113–116 (2001).

[18] K.C. Kam, F.L. Deepak, A.K. Cheetham, and C.N.R. Rao, Chemical Physics Letters **397**, 329-334 (2004).

[19] Z.R. Dai, J.L. Gole, J.D. Stout, and Z.L. Wang, The Journal of Physical Chemistry B **106**, 1274–1279 (2002).

[20] Y.C. Choi, W.S. Kim, Y.S. Park, S.M. Lee, D.J. Bae, Y.H. Lee, G.S. Park, W.B. Choi, N.S. Lee, and J.M. Kim, Advanced Materials **12**, 746–750 (2000).

[21] Q. Wu, Z. Hu, X. Wang, Y. Hu, Y. Tian, and Y. Chen, Diamond and Related Materials **13**, 38-41 (2004).

[22] C.C. Chen, C.C. Yeh, C.H. Chen, M.Y. Yu, H.L. Liu, J.J. Wu, K.H. Chen, L.C. Chen, J.Y. Peng, and Y.F. Chen, Journal of the American Chemical Society **123**, 2791-8 (2001).

[23] S. Vaddiraju, A. Mohite, A. Chin, M. Meyyappan, G. Sumanasekera, B.W. Alphenaar, and M.K. Sunkara, Nano Letters **5**, 1625-31 (2005).

[24] M. Zervos and A. Othonos, Nanoscale Research Letters **4**, 1103-1109 (2009).

[25] S.A. Dayeh, C. Soci, X.-Y. Bao, and D. Wang, Nano Today **4**, 347-358 (2009).

[26] J. Hu, Y. Bando, J. Zhan, C. Zhi, and D. Golberg, Nano Letters **6**, 1136-40 (2006).

[27] R.S. Wagner and W.C. Ellis, Applied Physics Letters **4**, 89-90 (1964).

[28] A.I. Persson, M.W. Larsson, S. Stenström, B.J. Ohlsson, L. Samuelson, and L.R. Wallenberg, Nature Materials **3**, 677-81 (2004).

[29] K.A. Dick, K. Deppert, T. Mårtensson, B. Mandl, L. Samuelson, and W. Seifert, Nano Letters **5**, 761-4 (2005).

[30] K. Kolasinski, Current Opinion in Solid State and Materials Science **10**, 182-191 (2006).

[31] V. Dubrovskii, N. Sibirev, G. Cirlin, J. Harmand, and V. Ustinov, Physical Review E **73**, 1-10 (2006).

[32] N. Wang, Y. Cai, and R.Q. Zhang, Materials Science and Engineering: R: Reports **60**, 1-51 (2008).

[33] P.R. Bandaru and P. Pichanusakorn, Semiconductor Science and Technology **25**, 024003 (2010).

[34] E. Sutter, B. Ozturk, and P. Sutter, Nanotechnology **19**, 435607 (2008).

[35] U. Philipose, T. Xu, S. Yang, P. Sun, H.E. Ruda, Y.Q. Wang, and K.L. Kavanagh, Journal of Applied Physics **100**, 084316 (2006).

[36] S.D. Hersee, X. Sun, and X. Wang, Nano Letters **6**, 1808–1811 (2006).

[37] H.-M. Wu and J.-Y. Liang, Ferroelectrics **383**, 95-101 (2009).

[38] P. Yang, H. Yan, S. Mao, R. Russo, J. Johnson, R. Saykally, N. Morris, J. Pham, R. He, and H.-J. Choi, Advanced Functional Materials **12**, 323 (2002).

[39] M.C. Johnson, S. Aloni, D.E. McCready, and E.D. Bourret-Courchesne, Crystal Growth & Design **6**, 1936–1941 (2006).

[40] M. Gudiksen and C.M. Lieber, Journal of the American Chemical Society **122**, 8801–8802 (2000).

[41] M.S. Gudiksen, J. Wang, and C.M. Lieber, The Journal of Physical Chemistry B **105**, 4062–4064 (2001).

[42] J. Hu, T.W. Odom, and C.M. Lieber, Accounts of Chemical Research **32**, 435-445 (1999).

[43] M. Plante, J. Garrett, S. Ghosh, P. Kruse, H. Schriemer, T. Hall, and R. Lapierre, Applied Surface Science **253**, 2348-2354 (2006).

[44] X. Duan, Advanced Materials 298-302 (2000).

[45] P. Nguyen, H.T. Ng, and M. Meyyappan, Advanced Materials **17**, 1773-1777 (2005).

[46] S.C. Jain, M. Willander, J. Narayan, and R.V. Overstraeten, Journal of Applied Physics **87**, 965 (2000).

[47] A.G. Bhuiyan, A. Hashimoto, and A. Yamamoto, Journal of Applied Physics **94**, 2779 (2003).

[48] B. Monemar, Journal of Materials Science: Materials in Electronics **10**, 227–254 (1999).

[49] H. Hirayama, Journal of Applied Physics **97**, 091101 (2005).

[50] O. Ambacher, Journal of Physics D: Applied Physics **31**, 2653-2710 (1998).

[51] S. Nakamura, M. Senoh, S.-ichi Nagahama, N. Iwasa, T. Yamada, T. Matsushita, H. Kiyoku, Y. Sugimoto, T. Kozaki, H. Umemoto, M. Sano, and K. Chocho, Applied Physics Letters **72**, 2014 (1998).

[52] F.A. Ponce and D.P. Bour, Nature **386**, 351–359 (1997).

[53] J.W. Orton and C.T. Foxon, Reports on Progress in Physics **61**, 1 (1998).

[54] H. Morkoc, A. Di Carlo, and R. Cingolani, Solid-State Electronics **46**, 157–202 (2002).

[55] M. Shur, Solid-State Electronics **42**, 2131-2138 (1998).

[56] S. Yoshida and H. Ishii, Physica Status Solidi (a) **188**, 243-246 (2001).

[57] S.C. Binari, K. Doverspike, G. Kelner, H. Dietrich, and A. Wickenden, Solid-State Electronics **41**, 177–180 (1997).

[58] H. Kobayashi, T. Ishida, Y. Nakato, and H. Mori, Journal of Applied Physics **78**, 3931 (1995).

[59] J.S. Kim, R.H. Friend, and F. Cacialli, Applied Physics Letters **74**, 3084 (1999).

[60] D. Zhang, C. Li, S. Han, X. Liu, T. Tang, W. Jin, and C. Zhou, Applied Physics Letters **82**, 112 (2003).

[61] J. Maier, Journal of Solid State Chemistry **302**, 293-302 (1988).

[62] K.P. Kumar and A.D. Domodaran, Journal of Materials Science **24**, 220 (1989).

[63] S.A. Pianaro, P.R. Bueno, E. Longo, and J.A. Varela, Journal of Materials Science Letters **14**, 692–694 (1995).

[64] P.I. Rovira and R.W. Collins, Journal of Applied Physics **85**, 2015 (1999).

[65] N. Amin, T. Isaka, and A. Yamada, Solar Energy Materials and Solar **67**, 195-201 (2001).

[66] J. Zhang, J. Liu, L.J. Huang, K. P, and C.M. Lieber, Science **274**, 757 (1996).

[67] C.S. Rout, K. Ganesh, A. Govindaraj, and C.N.R. Rao, Applied Physics A **85**, 241-246 (2006).

[68] D. Zhang, C. Li, X. Liu, S. Han, T. Tang, and C. Zhou, Applied Physics Letters **83**, 1845 (2003).

[69] D. Zhang, Z. Liu, C. Li, T. Tang, X. Liu, and S. Han, Nano Letters **4**, 1919-1924 (2004).

[70] S. Shimizu and M. Egashira, MRS Bull **24**, 18 (1999).

[71] K. Schierbaum, U. Weimar, W. Göpel, and R. Kowalkowski, Sensors and Actuators B: Chemical **3**, 205–214 (1991).

[72] S.G. Ansari, S.R. Sainkar, R.N. Karekar, R.C. Aiyer, and S.K. Kulkarni, Test **295**, 271-276 (1997).

[73] Y. Cheng, P. Xiong, L. Fields, J.P. Zheng, R.S. Yang, and Z.L. Wang, Applied Physics Letters **89**, 093114 (2006).

[74] Y.J. Chen, Q.H. Li, Y.X. Liang, T.H. Wang, Q. Zhao, and D.P. Yu, Applied Physics Letters **85**, 5682 (2004).

[75] Z. Liu, D. Zhang, S. Han, C. Li, T. Tang, W. Jin, X. Liu, B. Lei, and C. Zhou, Advanced Materials **15**, 1754-1757 (2003).

[76] Q. Kuang, C. Lao, Z.L. Wang, Z. Xie, and L. Zheng, Journal of the American Chemical Society **129**, 6070-1 (2007).

[77] Q. Wan and T.H. Wang, Chemical Communications **30**, 3841 (2005).

[78] Y.J. Chen, L. Nie, X.Y. Xue, Y.G. Wang, and T.H. Wang, Applied Physics Letters **88**, 083105 (2006).

[79] T.H. Mamain, Nature **4736**, 493 (1960).

[80] R.W. Boyd, *Nonlinear Optics* (Academic Press, Inc., San Diego, 1992).

[81] P.A. Franken, A.E. Hill, C.W. Peters, and G. Weinreich, Physical Review Letters **7**, 118–119 (1961).

[82] A. DeMaria, D. Stetser, and H. Heynau, Applied Physics Letters **8**, 174–176 (1966).

[83] J. Shah, *Ultrafast Spectroscopy of Semiconductors and Semiconductor Nanostructures* (Springer Verlag, 1999).

[84] J.-C. Diels and W. Rudolph, *Ultrashort Laser Pulse Phenomena: Fundamentals, Techniques, and Applications on a Femtosecond Time Scale* (1996).

[85] C. Rulliere, *Femtosecond Laser Pulses: Principles and Experiments* (Springer, 2003).

[86] U. Morgner, F.X. Kärtner, S.H. Cho, Y. Chen, H. a Haus, J.G. Fujimoto, E.P. Ippen, V. Scheuer, G. Angelow, and T. Tschudi, Optics Letters **24**, 920 (1999).

[87] A. Baltuska, Z. Wei, and M.S. Pshenichnikov, Optics Letters 365-366 (1997).

[88] D. Kuizenga and A. Siegman, IEEE Journal of Quantum Electronics **6**, 694-708 (1970).

[89] R. Paschotta and U. Keller, Applied Physics B: Lasers and Optics **73**, 653-662 (2001).

[90] D.E. Spence, P.N. Kean, and W. Sibbett, Optics Letters **16**, 42-4 (1991).

[91] P.F. Moulton, Journal of the Optical Society of America B **3**, 125-133 (2002).

[92] A. Othonos, Journal of Applied Physics **83**, 1789 (1998).

[93] S. Link and M.A. El-Sayed, Annual Review of Physical Chemistry **54**, 331-66 (2003).

[94] G. Itskos, A. Othonos, T. Rauch, S.F. Tedde, O. Hayden, M.V. Kovalenko, W. Heiss, and S.A. Choulis, Advanced Energy Materials **1**, 802-812 (2011).

[95] A.M. Zheltikov, Physics-Uspekhi **49**, 605 (2006).

[96] A. Brodeur and S.L. Chin, Journal of the Optical Society of America B **16**, 637 (1999).

[97] G. Schweitzer, L. Xu, B. Craig, and F.C. DeSchryver, Optics Communications **142**, 283–288 (1997).

[98] Y.-S. Lee, *Principles of Terahertz Science and Technology* (Springer, 2009).

[99] P.C.M. Planken, C.E.W.M.V. Rijmenam, and R.N. Schouten, Semiconductor Science and Technology **20**, S121-S127 (2005).

[100] Y.C. Shen, P.C. Upadhya, E.H. Linfield, H.E. Beere, and A.G. Davies, Applied Physics Letters **83**, 3117 (2003).

[101] A. Rice, Y. Jin, X. Ma, X.C. Zhang, D. Bliss, J. Larkin, and M. Alexander, Applied Physics Letters **64**, 1324–1326 (1994).

[102] G.L. Dakovski, B. Kubera, and J. Shan, Josa B **22**, 1667–1670 (2005).

[103] H.P. Wagner, M. Kühnelt, W. Langbein, and J.M. Hvam, Physical Review B **58**, 10494 (1998).

[104] T.V. Gorkavenko, S.M. Zubkova, and L.N. Rusina, Semiconductors **41**, 641-650 (2007).

[105] Y. Shen, P. Upadhya, E. Linfield, H. Beere, and A. Davies, Physical Review B **69**, 1-4 (2004).

[106] A. Nahata and A. Weling, Applied Physics Letters **69**, 2321-2323 (1996).

[107] S. Casalbuoni, H. Schlarb, B. Schmidt, P. Schmüser, B. Steffen, and A. Winter, Physical Review Special Topics - Accelerators and Beams **11**, 1-18 (2008).

[108] Q. Wu and X. Zhang, **67**, 3523-3525 (1995).

[109] F. Blanchard, L. Razzari, H.C. Bandulet, G. Sharma, R. Morandotti, J.C. Kieffer, T. Ozaki, M. Reid, H.F. Tiedje, H.K. Haugen, and F.A. Hegmann, Optics Express **15**, 13212-20 (2007).

[110] B. Pradarutti, G. Matthaus, S. Riehemann, G. Notni, S. Nolte, and a Tunnermann, Optics Communications **281**, 5031-5035 (2008).

[111] P.C.M. Planken, H.K. Nienhuys, and H.J. Bakker, Josa B **18**, 313–317 (2001).

[112] P. Parkinson, J. Lloyd-Hughes, Q. Gao, H. Tan, C. Jagadish, M.B. Johnston, and L.M. Herz, Nano Letters **7**, 2162–2165 (2007).

[113] J.B. Baxter and C.A. Schmuttenmaer, The Journal of Physical Chemistry. B **110**, 25229-39 (2006).

[114] V.M. Axt and T. Kuhn, Reports on Progress in Physics **67**, 433-512 (2004).

[115] P. Mal`y, Czechoslovak Journal of Physics **52**, 645–667 (2002).

[116] M. Ghanassi, M.C. Schanne-Klein, F. Hache, a. I. Ekimov, D. Ricard, and C. Flytzanis, Applied Physics Letters **62**, 78 (1993).

[117] J. Tauc, *Amorphous and Liquid Semiconductors* (Plenum, New York, 1974).

[118] G. Welsh, N. Hunt, and K. Wynne, Physical Review Letters **98**, 3-6 (2007).

[119] G. Dakovski, B. Kubera, and S. Lan, Josa B **23**, 139-141 (2006).

[120] A. Sabbah and D. Riffe, Physical Review B **66**, 1-11 (2002).

[121] M.C. Downer and C.V. Shank, Physical Review Letters **56**, (1986).

[122] A. Walsh, J. Da Silva, and S.-H. Wei, Physical Review B **78**, 1-5 (2008).

[123] M. Nazeri and R. Massudi, Measurement Science and Technology **21**, 115601 (2010).

[124] H.J. Bakker, G.C. Cho, H. Kurz, Q. Wu, and X.-C. Zhang, Journal of the Optical Society of America B **15**, 1795 (1998).

[125] X. Xin, H. Altan, A. Saint, D. Matten, and R.R. Alfano, Journal of Applied Physics **100**, 094905 (2006).

[126] M. Tasumi, The Journal of Chemical Physics **46**, 755 (1967).

[127] M. Born and E. Wolf, *Principles of Optics* (Oxford:Pergamon, 1987).

[128] T.-R. Tsai, S.-J. Chen, C.-F. Chang, S.-H. Hsu, T.-Y. Lin, and C.-C. Chi, Optics Express **14**, 4898-907 (2006).

[129] L. Duvillaret and F. Garet, Selected Topics in Quantum **20**, 807-746 (1996).

[130] N.W. Ashcroft and N.D. Mermin, *Solid State Physics* (Thomson Learning Inc., 1976).

[131] N. Smith, Physical Review B **64**, 155106 (2001).

[132] W. Han, Science **277**, 1287-1289 (1997).

[133] G. Cheng, L. Zhang, Y. Zhu, G. Fei, and L. Li, Applied Physics **75**, 2455 (1999).

[134] T. Kuykendall, P. Pauzauskie, S. Lee, Y. Zhang, J. Goldberger, and P. Yang, Nano Letters **3**, 1063-1066 (2003).

[135] K. Bertness, A. Roshko, L. Mansfield, T. Harvey, and N. Sanford, Journal of Crystal Growth **300**, 94-99 (2007).

[136] W. Han, P. Redlich, F. Ernst, and M. Rühle, Applied Physics Letters **76**, 652 (2000).

[137] W.-Q. Han and A. Zettl, Applied Physics Letters **80**, 303 (2002).

[138] D. Ng, L. Tan, and M. Hong, Current Applied Physics **6**, 403-406 (2006).

[139] C.C. Tang, S.S. Fan, H.Y. Dang, P. Li, and Y.M. Liu, Applied Physics Letters **77**, 1961 (2000).

[140] X. Cai, A. Djurisic, and M. Xie, Thin Solid Films **515**, 984-989 (2006).

[141] J. Zhang and L. Zhang, Journal of Vacuum Science & Technology B: Microelectronics and Nanometer Structures **21**, 2415 (2003).

[142] Z. Dong, C. Xue, H. Zhuang, S. Wang, H. Gao, D. Tian, Y. Wu, J. He, and Y. Liu, Physica E: Low-dimensional Systems and Nanostructures **27**, 32-37 (2005).

[143] S.C. Lyu, O.H. Cha, E.-K. Suh, H. Ruh, H.J. Lee, and C.J. Lee, Chemical Physics Letters **367**, 136-140 (2003).

[144] K. Chang and J.-J. Wu, The Journal of Physical Chemistry B **106**, 7796-7799 (2002).

[145] L. Yu, Y. Ma, and Z. Hu, Journal of Crystal Growth **310**, 5237-5240 (2008).

[146] J.C. Wang, S.Q. Feng, and D.P. Yu, Applied Physics A: Materials Science & Processing **75**, 691-693 (2002).

[147] C.-H. Hsieh, L.-J. Chou, Y.-L. Chueh, and M.-T. Chang, Journal of Vacuum Science & Technology A: Vacuum, Surfaces, and Films **24**, 1635 (2006).

[148] C.-K. Kuo, C.-W. Hsu, C.-T. Wu, Z.-H. Lan, C.-Y. Mou, C.-C. Chen, Y.-J. Yang, L.-C. Chen, and K.-H. Chen, Nanotechnology **17**, S332-S337 (2006).

[149] J.A. Chisholm and P.D. Bristowe, Computational Materials Science **22**, 73–77 (2001).

[150] M. Zervos and A. Othonos, Nanoscale Research Letters **6**, 262 (2011).

[151] H.M. Chen, Y.F. Chen, and M.C. Lee, Physical Review B **56**, 6942-6946 (1997).

[152] A.. Polyakov, N.. Smirnov, A.. Usikov, A.. Govorkov, and B.. Pushniy, Solid-State Electronics **42**, 1959-1967 (1998).

[153] J.S. Colton, P.Y. Yu, K.L. Teo, and P. Perlin, Physica B: Condensed **274**, 75-79 (1999).

[154] I. Shalish, L. Kronik, G. Segal, Y. Rosenwaks, Y. Shapira, U. Tisch, and J. Salzman, Physical Review B **59**, 9748 (1999).

[155] C.B. Soh, S.J. Chua, H.F. Lim, D.Z. Chi, S. Tripathy, and W. Liu, Journal of Applied Physics **96**, 1341 (2004).

[156] B. Ha, S.H. Seo, J.H. Cho, C.S. Yoon, J. Yoo, G.-C. Yi, C.Y. Park, and C.J. Lee, The Journal of Physical Chemistry. B **109**, 11095-9 (2005).

[157] J. Yoo, Y.-J. Hong, S.J. An, G.-C. Yi, B. Chon, T. Joo, J.-W. Kim, and J.-S. Lee, Applied Physics Letters **89**, 043124 (2006).

[158] X.M. Cai, A.B. Djurišić, M.H. Xie, C.S. Chiu, and S. Gwo, Applied Physics Letters **87**, 183103 (2005).

[159] E.D. O'Sullivan, S. Hess, R.A. Taylor, and N.J. Cain, Physica B: Condensed **272**, 402-405 (1999).

[160] C.K. Sun, Y.L. Huang, S. Keller, and U.K. Mishra, Physical Review B **59**, 535-538 (1999).

[161] O. Aoudé, P. Disseix, J. Leymarie, A. Vasson, M. Leroux, E. Aujol, B. Beaumont, A. Trassoudaine, and Y. André, Physical Review B **77**, 1-8 (2008).

[162] J. Renard, B. Amstatt, C. Bougerol, E. Bellet-Amalric, B. Daudin, and B. Gayral, Journal of Applied Physics **104**, 103528 (2008).

[163] B. Chon, S.R. Ryu, Y.-J. Hong, J. Yoo, G.-C. Yi, T. Joo, and Y.M. Jung, Journal of Molecular Structure **883-884**, 209-215 (2008).

[164] C.-K. Sun, J.-C. Liang, X.-Y. Yu, S. Keller, U.K. Mishra, and S.P. DenBaars, Applied Physics Letters **78**, 2724 (2001).

[165] S.Y. Bae, H.W. Seo, J. Park, H. Yang, and B. Kim, Chemical Physics Letters **376**, 445-451 (2003).

[166] M.A. Reshchikov and H. Morkoç, Journal of Applied Physics **97**, 061301 (2005).

[167] C. Li, D. Zhang, S. Han, X. Liu, and T. Tang, Advanced **15**, 143-146 (2003).

[168] M.J. Zheng, L.D. Zhang, G.H. Li, X.Y. Zhang, and X.F. Wang, Applied Physics Letters **79**, 839 (2001).

[169] X.C. Wu, Chemical Physics Letters **373**, 28-32 (2003).

[170] P. Wu, Q. Li, C.X. Zhao, D.L. Zhang, L.F. Chi, and T. Xiao, Applied Surface Science **255**, 3201-3204 (2008).

[171] L. Dai, X.L. Chen, J.K. Jian, M. He, T. Zhou, and B.Q. Hu, Applied Physics A: Materials Science & Processing **75**, 687-689 (2002).

[172] M. Mazzera, M. Zha, D. Calestani, A. Zappettini, L. Lazzarini, G. Salviati, and L. Zanotti, Nanotechnology **18**, 355707 (2007).

[173] D. Calestani, M. Zha, A. Zappettini, L. Lazzarini, and L. Zanotti, Chemical Physics Letters **445**, 251-254 (2007).

[174] C. Liang, G. Meng, Y. Lei, F. Phillipp, and L. Zhang, Adv. Mater **13**, 1330–1333 (2001).

[175] S. Kar and S. Chaudhuri, Chemical Physics Letters **422**, 424-428 (2006).

[176] Y. Yan, Y. Zhang, H. Zeng, J. Zhang, X. Cao, and L. Zhang, Nanotechnology **18**, 175601 (2007).

[177] S.Q. Li, Y.X. Liang, C. Wang, X.Q. Fu, and T.H. Wang, Applied Physics Letters **88**, 163111 (2006).

[178] J. Zhang and F. Jiang, Journal of Physics D: Applied Physics **2046**, (2003).

[179] J. Zhang, X. Qing, F. Jiang, and Z. Dai, Chemical Physics Letters **371**, 311-316 (2003).

[180] Y.X. Liang, S.Q. Li, L. Nie, Y.G. Wang, and T.H. Wang, Applied Physics Letters **88**, 193119 (2006).

[181] M. Zervos, D. Tsokkou, M. Pervolaraki, and A. Othonos, Nanoscale Research Letters **4**, 491-7 (2009).

[182] S. Kodambaka, J. Tersoff, M.C. Reuter, and F.M. Ross, Physical Review Letters **96**, 1-4 (2006).

[183] L. Chen, W. Lan, R. Lin, H. Shen, and H. Chen, Applied Surface Science **252**, 8438-8441 (2006).

[184] F. Zeng, X. Zhang, J. Wang, L. Wang, and L. Zhang, Nanotechnology **15**, 596-600 (2004).

[185] M. Kumar, V.N. Singh, F. Singh, K.V. Lakshmi, B.R. Mehta, and J.P. Singh, Applied Physics Letters **92**, 171907 (2008).

[186] M. Wraback, H. Shen, A.V. Sampath, C.J. Collins, G.A. Garrett, and W.L. Sarney, Physica Status Solidi (a) **202**, 790-794 (2005).

[187] S. Wu, P. Geiser, J. Jun, J. Karpinski, J.-R. Park, and R. Sobolewski, Applied Physics Letters **88**, 041917 (2006).

[188] J.J. Baumberg and D.A. Williams, Physical Review Letters **78**, 3358-3361 (1997).

[189] C. Thomsen, H.T. Grahn, and H.J. Maris, Physical Review B **34**, (1986).

[190] S. Wu, P. Geiser, J. Jun, J. Karpinski, and R. Sobolewski, Physical Review B **76**, 1-8 (2007).

[191] B.R. Krishna and T. Subramanyam, Optical Materials (2000).

[192] P.G. Li, X. Guo, X.F. Wang, and W.H. Tang, Journal of Alloys and Compounds **479**, 74-77 (2009).

[193] Z.-J. Li, Z. Qin, Z.-H. Zhou, L.-Y. Zhang, and Y.-F. Zhang, Nanoscale Research Letters **4**, 1434-8 (2009).

[194] S. Budak, G.X. Miao, M. Ozdemir, K.B. Chetry, and A. Gupta, Journal of Crystal Growth **291**, 405-411 (2006).

[195] M.-R. Yang, S.-Y. Chu, and R.-C. Chang, Sensors and Actuators B: Chemical **122**, 269-273 (2007).

[196] M.C. Johnson, S. Aloni, D.E. McCready, and E.D. Bourret-Courchesne, Crystal Growth & Design **6**, 1936-1941 (2006).

[197] L. Mazeina, Y.N. Picard, J.D. Caldwell, E.R. Glaser, and S.M. Prokes, Journal of Crystal Growth **311**, 3158-3162 (2009).

[198] A. Kolmakov, Y. Zhang, G. Cheng, and M. Moskovits, Advanced Materials **15**, 997-1000 (2003).

[199] X. Jiang, Y. Wang, and T. Herricks, J. Mater. Chem. 695-703 (2004).

[200] D. Li, Y. Wang, and Y. Xia, Advanced Materials **16**, 361-366 (2004).

[201] P.G. Li, M. Lei, W.H. Tang, X. Guo, and X. Wang, Journal of Alloys and Compounds **477**, 515-518 (2009).

[202] G. Zhang, N. Liu, Z. Ren, and B. Yang, Journal of Nanomaterials **2011**, 1-5 (2011).

[203] J.X. Zhou, M.S. Zhang, J.M. Hong, and Z. Yin, Solid State Communications **138**, 242-246 (2006).

[204] F. Trani, M. Causà, S. Lettieri, A. Setaro, D. Ninno, V. Barone, and P. Maddalena, Microelectronics Journal **40**, 236-238 (2009).

[205] M. Zervos and A. Othonos, Journal of Crystal Growth **340**, 28-33 (2012).

[206] S. Luo, P.K. Chu, W. Liu, M. Zhang, and C. Lin, Applied Physics Letters **88**, 183112 (2006).

[207] F. Arlinghaus, Journal of Physics and Chemistry of Solids **35**, 931-935 (1974).

[208] D. Grischkowsky, S. Keiding, M. Van Exter, and C. Fattinger, J. Opt. Soc. Am. B **7**, 2006–2015 (1990).

[209] F.J. Garcia-Vidal and J.M. Pitarke, Physical Review Letters 4289-4292 (1997).

[210] H. Ahn, Y.P. Ku, Y.C. Wang, and C.H. Chuang, Applied Physics Letters **163105**, 10-13 (2007).

[211] E. Shanthi, V. Dutta, A. Banerjee, and K. Chopra, Journal of Applied Physics **51**, 6243–6251 (1980).

[212] D. Cooke, A. MacDonald, A. Hryciw, and J. Wang, Physical Review B 1-4 (2006).

[213] K. Button and C. Fonstad, Physical Review B **4**, 4539-4542 (1971).

[214] H. Němec, P. Kuzel and V. Sundstrom, Physical Review B 79, 115309 (2009).

[215] A.E. Taverner, C. Rayden, S. Warren, A. Gulino, P.A. Cox, and R.G. Edgel, Physical Review **51**, 6833-6837 (1995).

[216] J.M. Pitarke, V.M. Silkin, E.V. Chulkov, and P.M. Echenique, Reports on Progress in Physics **70**, 1-87 (2007).

[217] G.M. Turner and M.C. Beard, The Journal of Physical 11716-11719 (2002).

[218] L. Titova, T. Cocker, D. Cooke, X. Wang, A. Meldrum, and F. Hegmann, Physical Review B **83**, 1-9 (2011).

[219] A. Girlando and W. Knoll, Solid State Communications 895-898 (1981).

[220] M. Perner, P. Bost, U. Lemmer, and G.V. Plessen, Physical Review Letters **1**, 9-12 (1997).

[221] a Stella, M. Nisoli, De Silvestri S, O. Svelto, G. Lanzani, P. Cheyssac, and R. Kofman, Physical Review. B, Condensed Matter **53**, 15497-15500 (1996).

[222] T. Ahmadi and S. Logunov, Journal of Physical Chemistry **15**, 8053-8056 (1996).